Bilateral Swelling Self-inflating Tissue Expanders

Xue Min, Linacre College

A thesis submitted to the University of Oxford for the degree of

Doctor of Philosophy.

Abstract

Hydrogel tissue expander (HTE) self-inflates *in vivo* by gradually absorbing body fluid. It eliminates the regular injections required by the conventional balloon-type tissue expander and provides a more progressive stretching process to the tissue. Previously, the hot-compressed anisotropic HTE (A-HTE) has achieved the uniaxial swelling and could potentially match defects of anisotropy. This present work applied die-drawing as the solid-state processing to impart shape memory to the crosslinked copolymer of N-vinyl-pyrrolidone and methyl methacrylate, poly(VP-MMA) and successfully produced a novel self-inflating tissue expander with bilateral swelling properties.

This research is based on the assumption that A-HTE, especially bilateral swelling ones, could be more efficient, beneficial and convenient in the cases of anisotropic tissue expansion. In order to prove the concept, a mathematic model was established to study the tissue generation capacity of uniaxial (1D-Uni), bilateral (2D-Bi), and isotropic (3D-Iso) swelling HTEs. The simple syndactyly case was considered, and the complicated irregular anatomy was simplified into a regular geometry. The insertion mode was specifically designed in accordance with their primary swelling directions to achieve the optimal expansion efficiency for each type of HTE.

As the required tissue area for syndactyly reconstruction was fixed in the model, the correspondingly required swelling ratio and swollen volume of HTEs could be obtained. A few assumptions were made to constrain the model to obtain the analytical solutions, among which valid results were screened out using the critical buckling situation and swelling capacity of poly(VP-MMA) (VP:MMA 90:10, 0.2% crosslinker). The result showed that for generally 1D-Uni required the minimum swollen volume, however, 2D-Bi HTE provided the most comprehensive application possibility and generally required the minimum swelling ratio and the smallest incision size at implantation, compared to other HTEs.

With the proved advantages of 2D-Bi, the research was then focused on the development of the 2D-Bi poly(VP-MMA) HTE. The influence of processing parameters, including die angle,

drawing temperature, deformation ratio and drawing rates were examined using single-factor methods. It was found that poly(VP-MMA) rods (VP:MMA 90:10, 0.2% crosslinker) could be drawn through a converging conical die with a 5° to 10° semi-angle around its glass transition temperature of 145 ~ 180℃ at drawing rates of 0.1 to 6 mm/s. A maximum 3.7 times of elongation was achieved. The swelling rate and ratio of the die-drawn sample were significantly increased in the bilateral directions and greatly inhibited in the longitudinal (axial) direction. The extent of this anisotropy was tunable through the die-drawing deformation ratio. The preliminary study on the swelling rate control of die-drawn samples by polydimethylsiloxane showed an effective control in the swelling rate but simultaneously reduced the volume expansion prominently.

The characterization of die-drawn samples showed induced orientation but no evidence of crystallization. DSC analysis reflected an increased glass transition temperature of 168.8℃ compared to 163.1℃ of the isotropic sample. The optical microscope observed the aligned structure and elongated voids formation in the die-drawing direction on the lateral side of the die-drawn sample. The XRD data showed no noticeable differences between the die-drawn and the non-processed isotropic samples.

Acknowledgement

I am very grateful to my motherland China and China Scholarship Council for funding me and allowing me to pursue a DPhil degree in the University of Oxford.

I would like to thank my supervisor Professor Jan Czernuszka for his great help, guidance and inspiration. I would like to thank my colleagues, Yun Zhu, Jessica Smith, Qi Chen, Narjes Rashidi, Rabia Nazir, Maryam Tamddon, Yang Xu, Fang Li, Mu-huan Lee, Zamri Radzi and many others for idea-sharing and company. I also have obtained lots of help from the faculties and technicians at the Materials Department. Thank you all very much.

I am also very grateful to Linacre College, Oxford University and the beautiful Oxford city for providing me with wonderful and unforgettable learning and living experience in my life. Thank all my lovely friend met in Oxford and thanks for the love and forever support from my dearest friends in China.

Thank my parents for their continuous support, understanding and for having unconditional faith in me all the time. I would like to thank my 2 year old boy PiPi for giving me a chance to stop, and to restart for self-fulfilments. Finally, I would not be able to complete my DPhil without the enormous support from my husband Yang Cao, who had tried his best to allow me to have the greatest extent of freedom, time and morale to accomplish this task.

I would like to dedicate this work to my grandparents who gave me so much love and care.

Contents

List of Figures

List of Tables

List of Abbreviations

1D-Uni	**One dimensional (uniaxial-) swelling hydrogel tissue expander**
2D-Bi	Two dimensional (bilateral-) swelling hydrogel tissue expander
3D-Iso	Three dimensional (isotropically) swelling hydrogel tissue expander
3D-Iso-cy	Cylindrical isotropically-swelling hydrogel tissue expander
3D-Iso-cy(1D)	Cylindrical 3D-Iso to be placed as 1D-Uni tissue expander
3D-Iso-cy(2D)	Cylindrical 3D-Iso to be placed as 2D-Bi tissue expander
3D-Iso-sp	Spherical isotropically-swelling hydrogel tissue expander
AIBN	2,2'-azobisisobutyronitrile
AMA	Allyl methacrylate
CND	Continuous die-drawing procedure
DSC	Differentiate scanning calorimetry
DW	Distilled water
ECM	Extracellular matrix
EGF	Epidermal growth factor
EGFR	Epidermal growth factor receptor
HDPE	High density polyethylene

HEMA	Hydroxyethyl methacrylate
HTE	Hydrogel tissue expander
IMD	Intermittent die-drawing procedure
MMA	Methyl methacrylate
OM	Optical microscope
PAA	Poly(acrylic acid)
PCL	Polycaprolactone
PDMS	Polydimethylsiloxane
PEO (or PEG)	Poly(ethylene oxide) / Poly(ethylene glycol)
PE	Polyethylene
PET	Poly(ethylene terephthalate)
PID	Proportional-integral-derivative controller
PLA	Poly(lactic acid)
PLGA	Poly(lactic-*co*-glycolic acid)
PMMA	Poly(methyl methacrylate)
Poly(VP-AA)	Poly(N-vinyl-pyrrolidone-co-acrylic acid)
Poly(VP-MMA)	Poly(N-vinyl-pyrrolidone-*co*-methylmethacrylate)

POM	Polyoxymethylene
PTFE	Polytetrafluoroethylene
PU	Polyurethane
PVA	Poly(vinyl alcohol)
PVAc	Poly(vinyl acetate)
PVF	Poly(vinylidene fluoride)
SAXS	Small-angle X-ray scattering
SBF	Simulated body fluid
SEM	Scanning electron microscope
SMA	Shape memory alloy
SME	Shape memory effect
SMH	Shape memory hydrogel
SMP	Shape memory polymer
WAXS	Wide-angle X-ray scattering
XRD	X-ray diffraction
#A	Adhesive mode between tissue and tissue expander
#NA	Non-adhesive mode between tissue and tissue expander

#T	Top insertion mode: tissue expander inserted on one side of the finger bones
#TB	Top and bottom insertion mode: tissue expander inserted on both sides of the finger bones

1 Literature Review

1.1 Tissue Expansion

In this section, the history of tissue expansion and tissue expanders and the development of the anisotropic hydrogel-based tissue expanders will be briefly reviewed, followed by a discussion on the mechanism of tissue growth upon stretching.

1.1.1 Tissue Expansion and Tissue Expanders

Throughout human history, the enlargement of gravid females' abdomen and uterus with the growth of the foetus inside has long been the most intuitive example of the expansion potential of soft tissue. As early as 8000 BC, African tribes in Ethiopia, Sudan and other places have already utilized the stretching ability of the lip by inserting 'labret' into people's pierced lips as 'a visual key to social, cultural, political and cosmological concerns' [1]. Such custom is still circulating today in some cultures, such as the Mursi Tribe living in the lower valley of the Omo River in southwestern Ethiopia (Figure 1-1).

Figure 1-1 Mursi women and children (photo taken by Rod Waddington [2]).

With the development of medicine, tissue expansion technology shifted from a tribal tradition

to medical applications on reconstructive surgeries. However, in the early 1900s, doctors were still accustomed to using this technique according to their habits or empirical judgements. It was not until 1905 that Codivilla proposed to study the means of expanding the soft tissue rigorously to achieve the maximal lengthening of the tissue without altering its physiological functions in the treatment of limb deformity, particularly in the bone extension [3]. Even so, tissue expansion was a secondary concept depending upon the bone modification, and the knowledge of the extended tissue remained at a macroscopic level. Meanwhile, the apparatus involved in the operation was extracorporeal and bulky, as presented in Figure 1-2.

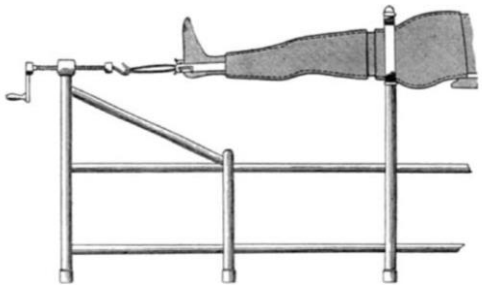

Figure 1-2 Godivilla's apparatus for femur lengthening and tissue expansion [3].

The idea lay dormant for another 50 years, during which time, the methods of skin grafts or pedicle flaps more prevailed in the surgeries with skin shortages[1]. In the annual meeting of American Society of Plastic and Reconstructive Surgeons (ASPRS) in 1956, Neumann first presented the subcutaneous-inserted inflatable rubber balloon, which was used to harvest extra

[1] In Google Scholar, there were 4630 results for the search: intitle: "skin graft" OR "skin grafts" OR "skin-graft" from 1905 to 1956. During the same period, the search: "tissue expander", "tissue expansion", tissue expander, tissue expanders, tissue expansion, tissue extension, tissue elongation, yielded no related literatures reporting the use of a device to expand human or animal skin tissue.

skin for the ear reconstruction of a male patient [4]. This device included a balloon and a reservoir. After the implantation, regular injections were needed to inflate the balloon to expand the skin. Whether or not the operation had achieved a high aesthetic standard, Neumann did generate ample and well-tolerated skin at the reconstruction sites. However, no further related clinical applications were reported for the next 20 years until Radovan rediscovered the idea of subcutaneous tissue expansion and balloon-type expander. Radovan eventually made the tissue expander concept known to a much larger group of audiences [5-10].

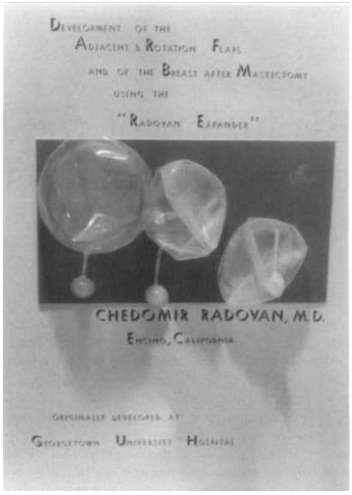

Figure 1-3 Radovan's poster display of his balloon-type tissue expander at the 1977 annual meeting of ASPRS.

Tissue expansion has several advantages over conventional operations as skin grafts. The skin grafts technique shows high complication rates on both donor site and graft site, including flap necrosis, hyperpigmentation, excessive hair growth, and hypertrophic scarring, infections and sensory disorder like pain paraesthesia, numbness [11, 12]. Tissue expansion solved these

problems in essence by generating the adjacent tissue in situ. One case reported expanded flaps had a mean survival length of 117% over the acutely raised random-pattern flaps and even improved vascularity [13]. Tissue expansion can also retain the original properties of the tissue, including its texture, colour and even functions, such as hair-growth ability [14, 15]. Figure 1-4 shows a boy who regained his hair-bearing scalp after tissue expansion by the balloon-type expander [15]. Other cases concerning muscles, especially those from the head and neck responsible for facial animation, have also been successfully rebuilt through tissue expansion in several clinical trials [16-18].

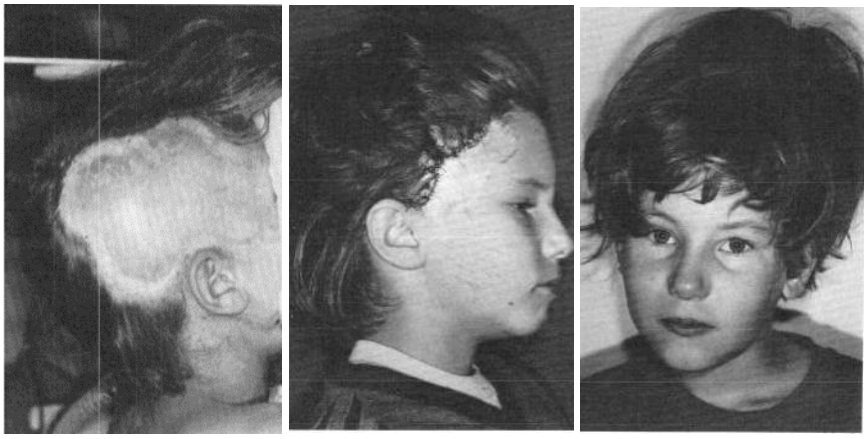

Figure 1-4 A successful case in scalp reconstruction [15].

Although it might have outperformed the skin graft techniques in many cases, tissue expansion is by no means a perfect method. Technically, the chronic balloon-type tissue expansion usually takes 6-12 weeks, which means the patients will have to bear the abnormal body configuration, risks of infection or inflammation and regular visits to the hospital for the injection of saline solvent during the expansion period.

The balloon-type expanders also have various complications, including 4 to 12 hours of transient pain and discomfort on every injection [19]; infections around both the valve and the balloon implant [19]; device extrusion induced inevitable tissue contamination [15, 20]; device leaks and rupture [21-24]; tissue ischemia and necrosis [15, 21, 25-27]. The solutions need to be found to reduce the complications. These findings suggest that a better device is needed to reduce the complications associated with the conventional tissue expansion techniques.

Austad et al. developed an osmotic-force-driven self-inflating implant: a semipermeable silicone envelope containing sodium chloride [28-30]. This new device could absorb extracellular fluid by osmosis without periodic injections and avoid using the valves. Gradual increase of device gives no acute pain to the patient, and it is useful for infants or whom a weekly injection is inconvenient. There was evidence that skin gained more proliferation during gradual expansion than the traditional increment expansion in the balloon method in a porcine model [31]. Nevertheless, the Austad device required 8-14 weeks of expansion and the osmotically driven device still had the potential breakage risk; the leaking of sodium chloride solvent might lead to severe tissue necrosis [30].

Later in 1992, Downes and Lavin first used a (hydroxyethyl methacrylate) (HEMA)-based hydrophilic expander for the enlargement of congenital anophthalmia socket [32]. However, due to the limited expansion capacity of the HEMA device (swelling ratio of 1.19), the first device had to be replaced with a new one after 3 days to achieve further expansion. The request for multiple procedures had significantly weakened the advantages of this novel type of tissue expander. The following year, Wiese published his article on the copolymer of methyl

methacrylate (MMA) and N-vinyl-2-pyrrolidone (VP) used as a tissue expander (Figure 1-5). With a swelling ratio of 20-30 in vitro, the MMA/VP based device eventually achieved a 2.5-3 swelling ratio in the rat model [33].

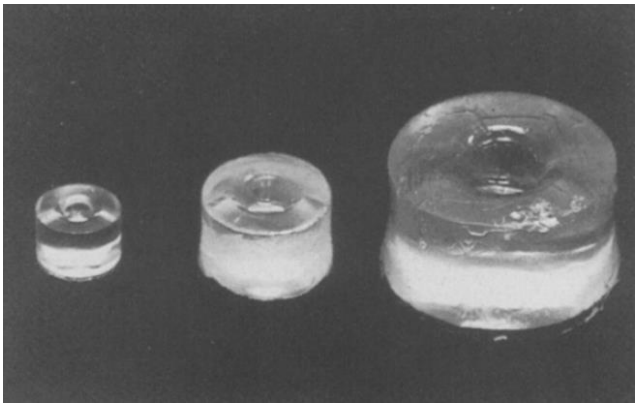

Figure 1-5 Hydrogel expanders with increased swelling ratios from left to right [33].

Further animal and clinical trials of hydrogel tissue expanders indicated that their uncontrolled rates might lead to high procedural complication rates [34, 35]. A second generation of the osmotic expander wrapped in a silicone membrane envelope was invented to slow down the swelling rates. According to the clinical data, the complication rates were reduced; however, minor complications, such as skin ischaemia and migration of the implant and wound dehiscence, still existed [34, 36-38].

The isotropic expansion may not be the best match for cases with the need for anisotropic tissue proliferation. The cases include but are not limited to the operations where skin growth in one (or two) specific directions is more favourable than the others, such as a cleft palate and syndactyly. Such potential requirement led to the efforts of researchers to endow the anisotropy to the hydrogel-based tissue expander.

Swan et al. suggested that a hydrogel expander with both controlled expansion rate and controlled swelling direction would reduce the risk of implant extrusion rate of the isotropic expanders in a confined anatomical reconstruction site [39]. Swan and co-workers successfully imparted the crosslinked isotropic poly(VP -MMA) hydrogel with the anisotropic swelling ability [39, 40]. Their work showed that in water or simulated body fluid, the hot-pressed hydrogels expanded more in the compressed direction than in other directions. The hot-pressing method was later applied in other polymeric systems, such as poly(vinyl pyrrolidone-acrylic acid) (poly(VP-AA)), the interpenetrating network of poly(lactic-*co*-glycolic acid) (PLGA) and poly(VP-MMA) and achieved similar anisotropic swelling properties [41, 42].

Studies were carried out to understand the compression process and its influence on the structure and swelling behaviour of the gel. Lee combined the results of birefringence and SEM images of the hot-compressed poly(VP-AA) gel and showed that its strain was unevenly distributed along the axial direction [41]. Smith et al. studied the role of friction between the mould and the dry gel and showed that the core-edge nonuniformity in the swelling of the compressed poly(VP-MMA) could be reduced by changing the aluminium to the polytetrafluoroethylene (PTFE) mould [43].

Furthermore, the anisotropic self-inflating poly(VP-MMA) has been implanted in porcine, sheep and horse models and all models demonstrated tissue proliferation. Swan and his co-workers found that uncoated anisotropic poly(VP-MMA) could cause minor complications in vivo [44]. The coated and uncoated expanders were implanted sub-mucoperiosteal in six pigs' hard palates for six weeks. The pigs operated with uncoated samples were acutely inflamed,

ulcerated and showed particulate foreign body contamination. In contrast, the pigs operated with coated samples were asymptomatic and uncomplicated during the six weeks and reached a 60% longitudinal increase and 120% transverse increase. However, the post-mortem showed the coated devices had left prominent indentation due to 'expander-mediated bony erosion'.

The later sheep and horse models were all done with coated anisotropic poly(VP-MMA). The horse model by Al-Majhali et al. showed that all six horses tolerated well during the 14 days tissue expansion process[1], and the anatomical location affected the outcome, including the modulus and strength of the expanded tissue. Manssor et al. applied the anisotropic hydrogel tissue expander in a sheep model for 4 weeks [45]. Both of the research mentioned no complications related to tissue expansion.

Such character could be advantageous in treating cleft palate, syndactyly and some wound closures in which the demand for the tissue at some parts or some directions is more than the others, particularly in a paediatric setting. However, no clinical data is yet available to confirm the advantages of anisotropic hydrogel tissue expanders over isotropic ones. Theoretical or modelling studies may be carried out to prove the concept before the clinical trials. The work of Swan et al. also brought forward the idea that the swelling of tissue expander could be directionally designable via different processing methods.

[1] The commercialized products Expanderm (Oxtex Ltd., UK) was used.

1.1.2 Other Anisotropic Tissue Expansion/Expanders

Tissue expansion ideas were not merely limited within the subcutaneous implant expander. Other available techniques apply external forces to achieve the tissue expansion, such as negative pressure cup, 'Nordström suture', as well as strap-based or adhesion wound closures devices.

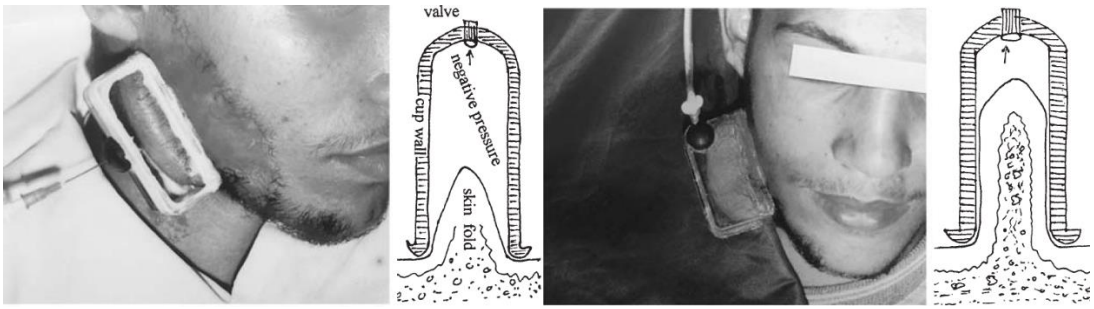

Figure 1-6 Negative pressure applied on the patient's facial tissue using a valved cup and corresponding schematic cross-sectional views; left: on the first day of cup application; right: after a week of cup application [46].

Lasheen and colleagues designed a negative pressure expansion device for the treating of scars. They applied a valved cup on the healthy skin next to the wound and stretched the skin by suction, as shown in Figure 1-6. However, the clinical trials were barely satisfactory as nearly half of the patients did not generate sufficient tissue and any excess pressure could result in ecchymosis, blisters and red spots [46, 47].

'Nordström Suture', shown in Figure 1-7, uses a medical-grade elastic silicone that can extend to up to four times its original length. It was first used in scalp reduction surgery to treat male

pattern baldness [48] and later more often adopted for the burns and other scars at scalps, abdominal and thigh regions [48, 49]. The suture is threaded onto the open edge of the cut and gradually tightens the lesions due to the elastic restoring force, consequently lessening the gap until the wound can be surgically closed.

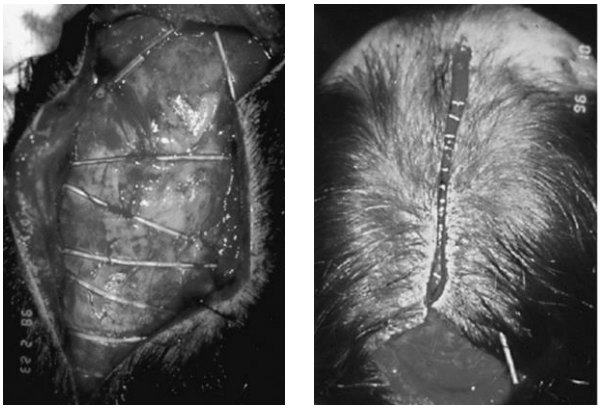

Figure 1-7 Nordström Suture used in scalp reduction for pattern baldness [48].

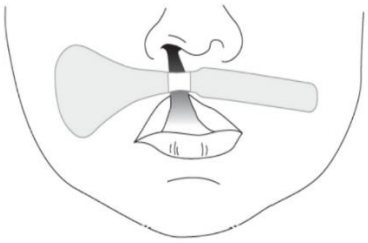

Figure 1-8 Schematic of DynaCleft® .

Based on similar ideas but with no percutaneous sutures, some devices use a set of adjustable straps or elastomeric adhesive elastic strips to bring the wound together, such as TopClosure®, DynaClose® and DynaCleft®. DynaCleft®, as demonstrated in Figure 1-8, is specially developed for cleft lip or cleft palate, intending to guide the soft tissue or bones to a proper

position before the surgery for improved aesthetic results. A significant limitation of such a device is that it requires adhesiveness between itself and the applied site. Thus, it cannot resolve the problem of tissue deficiency inside the mouth.

In all, these devices may avoid longitudinal tissue expansion at a transverse anatomical defect compared to the bulk tissue expanders. However, they all require a larger operational area than the defects and repeated tension adjustments in most cases. The applications for discrete anatomical locations by these 2D methods are yet not feasible, and the non-invasive adhesive methods may not be applied to some soft tissue with a moist surface, like oral mucosa. Therefore, more delicate devices are required to fill in the gap.

1.1.3 Mechanism of Tissue Expansion

Skin is an organ for us to sense the external environment. It is a core site for vitamin D synthesis, which is indispensable for calcium absorption. It plays a crucial role in temperature homeostasis, which is vital for human survival. At the same time, the skin is one of the main organs for our perception of the external environment and the first physical barrier to excessive water loss and external pathogens, microbial, chemical, physical, thermal and radiation damages.

Figure 1-9 shows the histology of normal skin, consisting primarily of epidermis and dermis. The epidermal layers consist of stratum corneum, stratum lucidum, stratum granulosum, stratum spinosum and stratum basale. Dermal layers consist of papillary dermis and reticular dermis. The skin consists of a series of closely interrelated networks which determine its

biomechanical properties [50]. Collagen and elastin account for 77% and 4% fat-free dry weight of the skin and contribute to the skin tensile strength and elasticity, respectively.

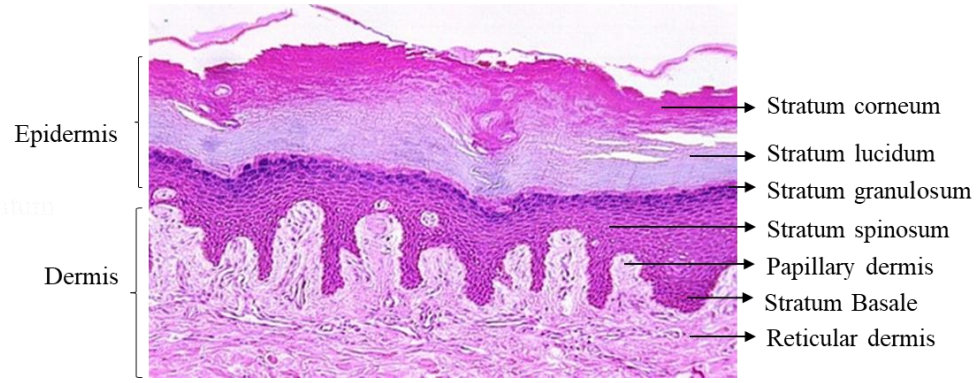

Figure 1-9 Histology of normal human skin (reproduced from [51]).

In the 1960s, Lorber and Milobsky studied the cell mitosis of the stretched mouse skin under 36 hours of tension and found that adjacent epidermal cells were separated and basal cells increased under slight to moderate tension while decreased under further stretching [52]. Francis and Mark found the autoradiograph labelling index (indicative of epidermal mitotic activity) of the guinea pig skin expanded by a gel prosthesis was three times higher than that of the sham-operated group [53]. Squier implanted a specially designed spring, initially in its compressed state, onto the back of the mouse and recorded the relaxation degree of the spring over four days [54]. He compared the results with the sham-operated and unoperated groups and found that the stretching has significantly increased the cell mitosis of the epidermis and resulted in the hyperplasia of all cell layers after four days.

The laboratory studies on the expanded guinea pig tissue by the osmotic silicone expander showed no significant differences in guinea pig epidermal thickness but significant thinning

of dermis and panniculus carnosus[1] between the expanded group and the sham-operated group [29]. The researchers speculated the non-thinning of the epidermis to the increased mitosis activities or a decreased cell maturation rate. In comparison, Manders et al. considered that the resulting capsule[2] after the implantation might contribute to the non-thinning of the expanded tissue [15].

Evidence showed that moderate tissue expansion might also increase the blood flow in the expanded tissue. The microangiograms of the pig flaps showed increased vascularity of expanded skin flaps compared to the control group [13]. And the microsphere perfusion studies revealed an altered microcirculation of the expanded skin [13, 15, 29, 55]. It has also been proved that exposure to mechanical stimuli can preserve the skin's functionality and structure over several generations with no observations of malignant changes [56].

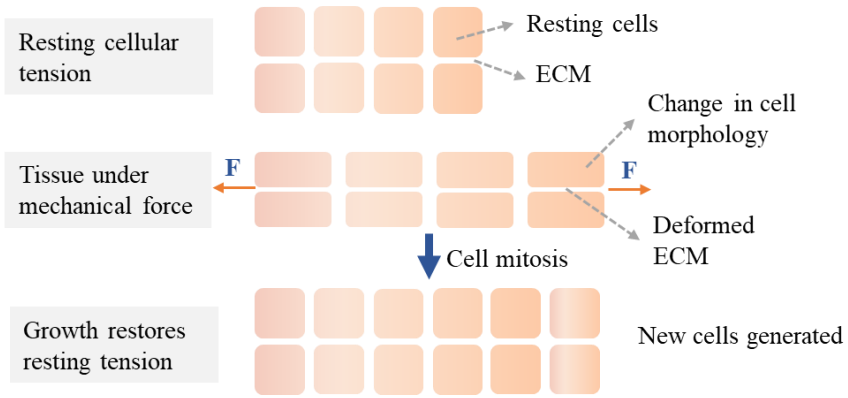

Figure 1-10 Schematic of biological creep in tissue expansion, reproduced from [56].

[1] Panniculus carnosus is a layer of muscle in vertebrates, but does not widely exist in human's tissue. It allows the skin to move independently of deeper muscles, especially upon wounding.

[2] A fibrous capsule normally occurred a few days after the implantation of tissue expander and will completely surround the expanders eventually.

Upon mechanical stimuli, resting skin cells extracellular matrix (ECM) deform and then mitosis activities are initiated and new skin cells are generated.

De Filippo and Atala intuitively represent tissue expansion as in Figure 1-10 [56]. The mechanical force will initiate the morphologic changes of the extracellular matrix, leading to the perturbance of the plasma membrane as well as the integrin, which communicates between ECM and cytoplasmic protein. The integrin will transmit external force-proportional mechanical signals into the cytoplasm of the cells [57-59]. The force will also induce the rearrangements in the actin filament, which further modulates the cell shape and cause morphologic changes in the cell, and the member ruffling can be observed [60]. Moreover, membrane ruffling is a typical phenomenon occurring before the cell division resulting from the epidermal growth factor (EGF) proliferation [61]. This indicates the external stress ultimately induced the cell mitosis by the actin-binding filament pathways.

In vitro models demonstrated the direct effect of mechanical stretch applied to the cell would increase epidermal growth factor (EGF) and epidermal growth factor receptors (EGFR) [62]. Mechanical strain was also reported to affect plasma membrane and organelle to increase intracellular DNA synthesis [63]. Moreover, due to stretch stimuli, the ions migrate through the mechanically-sensitive ion channels on the cell membrane [63-65]. It has been shown that the conformational changes in cell promotes the Ca^{2+} influx and lead to the depolarization of the cell and cell contraction [66-72].

In brief, the mechanical stimuli initiate a cascade of cell signalling pathways that ultimately

activate the cell proliferation. The converging pathways involves multiple types of growth factors, the protein kinases, secondary messengers, ion channels which all have important roles in the cell mitosis. Therefore, the skin has a natural property to proliferate under proper mechanical stimuli, and such property has laid out the foundation of the tissue expansion technique.

1.2 Hydrogels

Since the research object is the hydrogel-based tissue expander, this section will give an introduction on the characteristics and application of hydrogel and preliminarily discuss hydrogel as a shape memory material.

1.2.1 A Brief Introduction on Hydrogel

Since the debut of hydrogel in the 1960s, researchers and engineers have intensively excavated and remarkably developed the application potential. Nowadays, with significantly improved inflation capacity, excellent mechanical properties, bespoke functionalities, hydrogels are almost everywhere in the biomedical world. With the mature of its related technologies, hydrogel has also deeply bonded with our daily life and become an indispensable part of modern livings.

It can be used as the wound dressing for its flexibility, durability and permeability to water [73, 74], the coating for medical devices such as urinary catheters for their smooth and lubricating properties [75, 76], the controlled-releasing drug vehicle for good biocompatibility and the

designable environment-sensitive functional groups [77-79]; the scaffold for tissue engineering for their structural similarity to the macromolecular based components in the body [80, 81]; the gastric retentive dosage form/ tissue expander/ embolization device for its expandability [82-84] and the bioactuator used as soft robotic locomotor and manipulation grippers for its stimuli-response properties [85, 86]. From the contact lenses with high oxygen permeability and water content to the superabsorbent particles in the disposable nappies and sanitary pads, the commercialized hydrogels had considerably improved our quality of life.

1.2.2 Hydrogel Chemistry and Structure

Hydrogels can be made from natural polymers such as gelatine, chitosan, alginate, or synthetic polymers, such as poly(acrylic acid), poly(ethylene oxide) or poly (vinyl alcohol), or the combination of the two. Broadly, hydrogels can be classified into 'chemical' gel and 'physical gel' according to their structural forms. Chemical gels, or so-called 'permanent gels', are cross-linked by covalent bonding and therefore have structurally stable networks. On the other hand, the 'physical gel' is crosslinked through physical bonds, such as, molecular entanglements, secondary forces including van der Waals interactions, hydrogen bonds, and also ionic attractions [77, 80, 87].

There are various kinds of macromolecule structures that are possible for hydrogels. In the view of monomeric composition, these structures can be classified into the following categories: homopolymer, copolymer, polyrotaxanes, interpenetrating polymer networks (IPNs) [40, 88]. Homopolymers, formed by a single species of monomer, can either be

chemically crosslinked or physically entangled, taking poly(2-hydroxyethyl methacrylate) (PHEMA) and the mixture of PEO/PVA as an example, respectively [89-91]. Co-polymer comprises two or more monomer species on a single chain, and at least one of the monomers is hydrophilic. Polyrotaxanes are a variant of sliding gels [92, 93]. IPNs have two independent crosslinked polymeric networks, which are partially interlaced [94-96].

1.2.3 Swelling and Diffusion

1.2.3.1 Swelling process

Hydrogels can absorb water that is from tens to hundreds of times of their dry weight. The swelling behaviours of hydrogels are controlled by their chemical nature, physical structure, and solvent diffusion properties.

In an aqueous environment, water molecules around the hydrogel will first bind to its most polar hydrophilic groups [77]. These water molecules are often referred to as 'primary bound water'. Then the hydrated hydrophilic groups give rise to the exposure of some hydrophobic groups, leading to the occurrence of hydrophobically bound water, or 'secondary bound water'. Primary and secondary bound water makes the 'total bound water'. After that, the system imbibes water as a function of osmotic potential and swells against the resistance of covalent or physical crosslinks exerting elastic network retraction force until reaching the final equilibrium of forces. The absorbed water at this stage is termed as 'free water' [77, 97]. The driven and counteracting forces are respectively osmotic pressure (π) and elastic retraction force (ρ). The swelling pressure P is the difference between π and ρ:

$$P = \pi - \rho \tag{2.1}$$

Hence the final equilibrium of swelling can be achieved when P equals zero, or $\pi = \rho$.

1.2.3.2 Swelling ratio

For tissue expanders, the swelling property may be one of the most critical factors. The swelling property of hydrogel expanders could be measured in terms of the change between hydrogel and xerogel in mass or volume. Xerogel is the anhydrous form of hydrogel. The swelling degree for a hydrogel is usually described by the increase of weight, volume, and dimensions in hydrogel at the time of measurement. The maximum degree of swelling is usually reached at an equilibrium state.

In practice, the change in particular directions may be of more interest for the anisotropic expanders. For an isotropic hydrogel expander, the volume change is the ratio of final volume over the volume of xerogel; for an anisotropic hydrogel expander, the size change may primarily occur in length (or area) of a particular direction (or surface). Therefore, the characterization of swelling properties varies with different anisotropic swelling properties.

1.2.3.3 Influential factors of swelling behaviours

In general, factors that increase the chain flexibility or the volume between the chains will contribute to the water diffusion. It can then be generalized that the equilibrium of the swelling is mainly subject to the nature of the component of the hydrogel, the concentration of the crosslinker and the physical interaction (H-bonding, Van der Waals interaction) between the

polymer chains and the solvent [77].

As crosslinked poly(VP-MMA) copolymer is the material used for this project, it is of more interest to specifically investigate this polymer. The swelling ratio of poly(VP-co-MMA) is determined primarily by the proportion of hydrophilic polymer within the system and the amount of crosslinker. Previous studies showed that increasing the VP content would result in increased swelling [40]. In addition, the amount of crosslinker is positively correlated with the hydrogel's mechanical strength and Young's modulus, and negatively correlated with its swelling capability. Furthermore, the presence of functional groups on the crosslinker may also influence the swelling response. Crosslinkers with great hydrophobicity can also decrease hydrogel swelling [40].

1.2.4 Hydrogels as shape-memory polymers

The shape memory material can remember at least two shapes, a permanent shape (P) and a temporary shape (T). It is made initially to be of shape P and then processed to shape T. When being exposed to specific physical or chemical environments, it can recover from shape T to P without any external stress applied.

Common shape materials are shape memory alloy (SMA) and shape memory polymer (SMP). The former is a widely known concept, whereas the latter has attracted more attention in recent years. Behl and Lendlein termed the process that makes an SMP from shape P to T as 'programming' [98]. The typical three steps of 'programming' are: raise the temperature to make the material flexible, apply stress to deform the material to T, and cool the material to

fix the temporary shape. Liu et al. suggested that SMPs have two components at the molecular level: crosslinks that identify the P shape and the switching segments that determine $T_{critical}$ [99]. The crosslinks of SMP could be either chemical or physical and the switching segments could be the hydrogen interaction.

The most widely applicable approach to Initiate the material recovery from T to P is to raise the temperature to at or above a critical point, $T_{critical}$. $T_{critical}$ could be the glass transition temperature, the thermal transition temperature (T_g) of an amorphous SMP or the melting point, T_m of an SMP with the crystalline feature. For this case, the temperature is regarded as the stimulus or trigger for the shape memory effect (SME). Depending on the materials' unique properties, there could be a wide range of triggers and one SMP could have multiple triggering factors. SMPs may be classified according to their different triggering mechanisms, such as, heating, hydration, pH, electric stimulus, magnetic field [100]. Based on the nature of crosslinking and polymeric networks, Liu et al. had categorized the SMP into four categories [101]: covalently crosslinked glassy thermoset networks, e.g. poly(VP-MMA)- PEO semi IPN [99]; covalently crosslinked semi-crystalline network, e.g. crosslinked polycaprolactone (PCL) [102]; physically crosslinked glassy copolymers, e.g. miscible blend systems: poly(vinyl acetate) (PVAc) with poly(lactic acid) (PLA) [103]; physically crosslinked semi-crystalline block copolymers, e.g. physically crosslinked polyurethane (PU) multiblock copolymer with PCL [104].

Shape-memory hydrogel (SMH) is a cross-linked material having a hydrophilic fraction that can be swelled in water and hydrophobic sections with reversible order-disorder SME

controlled by temperature or other stimuli [101]. The copolymer of acrylic acid and n-stearyl acrylate developed by Osada and Matsuda was a typical temperature-dependent SMH that presents SME in its swollen state with constant volume [105]. The swollen gel was heated to 50°C and coiled and then cooled to RT and retained its coiled shape. When it was heated to 50°C again, it recovered its original straight shape. There are also SMHs that showed SME in terms of the volume change. The SMH developed by Li et al. exhibits volume change by three orders of magnitude in response to external stimulation, such as temperature and pH [106].

PMMA is a typical SMP material [107]. Liu mentioned covalently crosslinked PMMA of high molecular weight (>10^6 g/mol) to exhibit SME and that poly(VP-MMA) does not present SME below 100 ˚C [101]. Swan et al. tested the T_g of poly(VP-MMA) (wt % 90:10) to be around 160 ˚C [40]. The structure of the crosslinked poly(VP-MMA) system was a typical SMH, with PVP as its hydrophilic section and PMMA worked as the switching segment. The shape memory effect (SME) of crosslinked poly(VP-MMA) was not comprehensively studied as an SMP, possibly due to its high $T_{critical}$ (or T_g in this case), as most of the studies were interested in the SMP that perform at a relatively lower temperature, preferably around body temperature for biomedical applications. Intrinsically, the triggering mechanism of poly(VP-MMA) should be increasing the temperature. However, due to the hydrophilic groups on the PVP segments, moisture may be utilized as the second triggering mechanism. Due to the expandable character of poly(VP-MMA) as a hydrogel, overwhelmed moisture, e.g. immersing the material into water, may simultaneously increase the volume and shape recovery at the same time [108].

This work aims to impart the anisotropic inflating feature to hydrogel copolymers. As been

previously stated, the anisotropic-swelling can be realized by the shape memory feature of some specific hydrogels, and one memory-endowing method is solid-state processing. Therefore, the next section will be providing some potentially viable solid-state processing methods for polymers.

1.3 Solid-state processing of polymers

In the 1960s, academia and industry started to look into the possibility of introducing a high level of oriented polymeric structure to improve the polymer mechanical property [109]. Various metal processing methods were introduced to the polymer world, e.g., compression, tensile drawing, extrusion, moulding and die-drawing. In this section, the tensile drawing, extrusion and die-drawing will be specifically reviewed as they should be mostly related to the objective of this thesis.

1.3.1 Free Drawing

The drawing (or free-drawing) involves uniaxially stretching a solid polymer with the tensile testing machine and may be regarded as the earliest uniaxial processing route. Ward et al. first used the cold-drawing to produce the polyethylene terephthalate (PET) with anisotropic optic and mechanical properties and high-density polyethylene (HDPE) with increased Young's modulus [110, 111], indicating the success of solid state deformation in changing the polymer molecular orientation. Ward et al. did not recognise that a few years earlier, Takayanagi et al. had summarised their work on drawing some crystalline polymers and concluded that the best

processing temperature to obtain the material with the highest orientation and modulus should be close to the temperature at which the crystalline dispersion takes place [112, 113]. Later on, various research groups carried out the polymer drawing at a raised temperature and successfully improved the products' mechanical properties [114, 115].

However, the results showed that such a method has a few limitations. For instance, the product renders a 'natural draw ratio' (or drawing ratio, deformation ratio, 'R') achieved by the 'necking' during the process. The natural draw ratio is affected mainly by the material intrinsic property and temperature [111]. Therefore, the free drawing method does not allow for product modification through the control of process parameters. In addition, the necking is subject to strain hardening [116]. The strain hardening is a dynamic process in the drawing since it increases with the ever-increasing molecular orientation, leading to rapid increasing drawing stress that may eventually exceed the strength of the material. As a result, free drawing has a natural limitation in achieving polymers with high orientation.

1.3.2 Extrusion

Because of the free drawing limitations, extrusion was introduced to the polymer from metal processing. Tensile stress is absent from extrusion as it is a process of pushing a sample through a converging metal die to achieve the desired orientation or cross-sectional profile. Extrusion can be divided into hot extrusion and cold extrusion according to the processing temperature or into the hydrostatic extrusion and ram extrusion based on the pressure source.

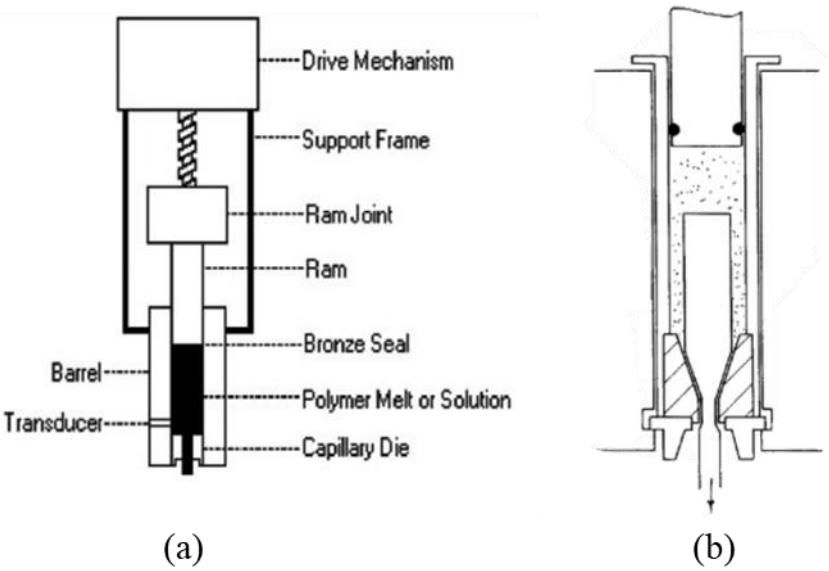

Figure 1-11 Schematic of (a) capillary rheometer as a ram extrusion apparatus [117] and (b) hydrostatic extrusion apparatus [118].

Southern and Porter first applied a capillary rheometer to extrude HDPE around its T_m (130~136°C) and obtained crystalised HDPE[2] [119, 120]. The schematic of the capillary rheometer is shown in Figure 1-11 (a). It can be considered a ram extruder. Unlike the above work that used the PE melts, Imada et al. used the PE billets in a similar piston-cylinder device with a converging die at a lower temperature of 80~110°C and the extrudate had Young's modulus of 30 GPa [113].

Compared to the ram extrusion, hydrostatic extrusion has the advantage of reduced friction between the die wall and the billet because the pressurised fluid will follow the sample into

[2] The work using the capillary rheometer to extrude the polyethylene (PE) should not be classified as the solid-state processing.

the die and act as a lubricant [109]. A typical apparatus of the hydrostatic extrusion is presented in Figure 1-11 (b). Williams first introduced the hydrostatic extrusion for processing polypropylene (PP) and achieved the maximum Young's modulus of 16 GPa [118]. Ward and his colleagues later followed the work of William and produced the PE extrudates with Young's modulus of up to 46 GPa and a deformation ratio of 25 [121]. This was prominently larger the cold drawn product of PE, which has a maximum modulus of 0.25 GPa with a natural deformation ratio of 15 [111].

The extrudate usually has a deformation ratio determined by the dimension of the sample (or limited by the inner diameter of the pressure vessel) and die exit, which means the process can effectively control the deformation ratio. However, extrusion also has some disadvantages. First, extrusion is a 'batch process' in which only one discrete billet can be loaded into the pressure vessel [122]; thus, the continuous processing seems infeasible. Second, Coates and Ward revealed that the strain rate is constantly increasing with the ever-increasing deformation ratio in the die [123]. Thus, the solid state extrusion presents very high flow stresses as the billet reaches the die exit, resulting in the demand for high extrusion pressure, the axial component of which may exceed the material's ultimate strength and cause fracture. In addition, such a processing route was reported with limited extrusion rates (the axial production speed) of 0.15 mm/s [124]. For some materials, the high stress also restrains the deformation ratio in some cases, such as polyoxymethylene (POM). The hydrostatic extrusion of POM (D500, $\overline{M_n}$ = 45000) could only achieve a much smaller deformation ratio (6~10) compared to the free drawing process (12~25) at a processing temperature of 140~160°C [114,

125].

Note that for the extrusion process, there exists the nominal deformation ratio (R_N) and the actual deformation ratio (R_A). R_N is defined as the ratio of the billet cross-sectional area (before processing) to the die exit cross-sectional area. While R_A is the ratio of the billet cross-sectional area to the actual product/extrudate cross-sectional area. For extrusion, R_A is usually smaller than R_N due to the 'die swell'. The 'die swell' is defined as $die\ swell = \frac{product\ diameter - die\ exit\ diameter}{die\ exit\ diameter}$ [125].

1.3.3 Die-drawing

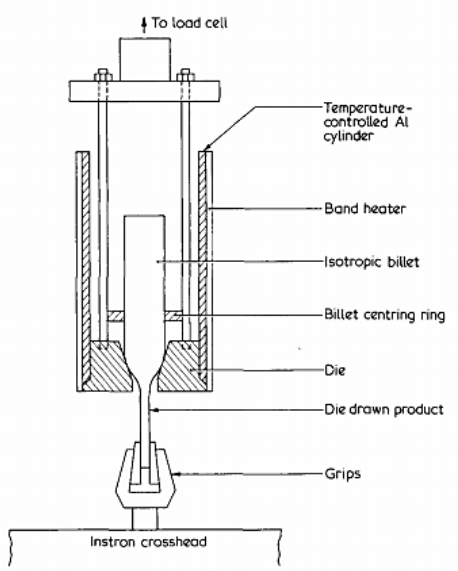

Figure 1-12 Schematic of a die-drawing apparatus [122].

Die-drawing involves drawing a solid polymer through a converging die at a suitable temperature. It is a method that integrates free drawing and extrusion to overcome the intrinsic limitations of both methods. The schematic of a small scale die-drawing device designed by

Coates and Ward is shown in Figure 1-12 [122].

The die of conical or other shapes is wrapped around by a band heater and mounted onto the Instron tensile testing machine. The billet is placed inside the die with a 'tag' sticking out the die exit. In the experiment, the crosshead of the tensile machine will move upwards while the clamp grips the tag to realise the billet deformation under both the tensile stress from stretching and the compression from the die. The method has been extensively tried on various polymers, including PE [122, 126-128], PP [123, 129-132], POM [127, 133-135], PET [136], PVF (poly(vinylidene fluoride)) [137], PLA [138, 139] and even wood composites [140], and the influence of processing parameters were studied. Analytical and modelling studies have been carried out to understand the mechanism of the die-drawing process [141-145].

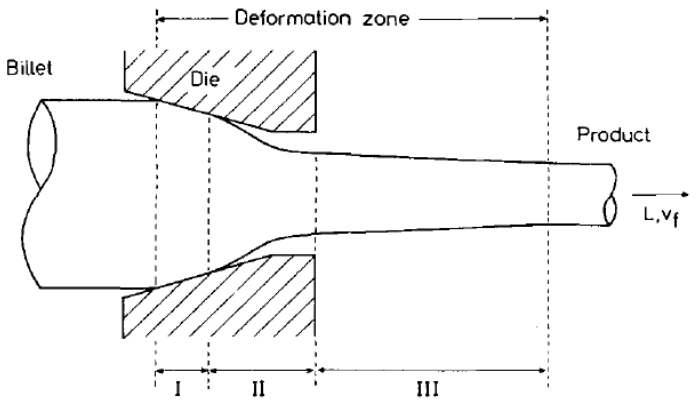

Figure 1-13 Schematic diagram of the deformation zone in a die-drawing process [133].

The die-drawing also has the nominal deformation ratio R_N and the actual deformation ratio R_A defined the same as in section 1.3.2. Gibson et al. depicted the three deformation zones of the die-drawing: (I) conical die flow, (II) isothermal tensile flow, (III) non-isothermal tensile

flow, as shown in Figure 1-13 [126]. As the necking of the billet continues in zone II and III, R_A tends to be larger than the R_N after the die exit in the die-drawing.

1.3.4 Comparison of the processing routes

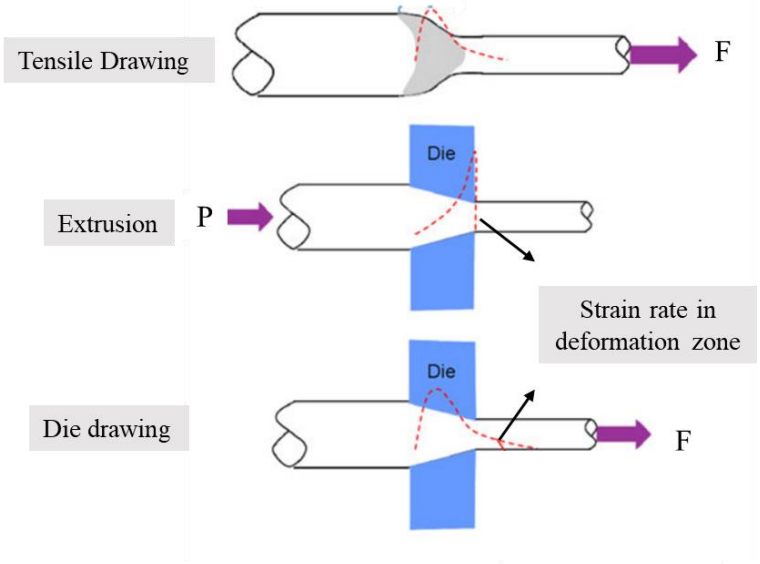

Figure 1-14 Schematic of three uniaxial processing routes to impart high strains to solid polymers, reproduced from [124].

Figure 1-14 illustrates the processing paths and strain rate–- strain curve of free drawing (tensile drawing), hydrostatic extrusion (and processing with similar setting) and die-drawing [124] and Figure 1-15 presents the true stress-strain-strain rate ($\sigma - \varepsilon - \bar{\varepsilon}$) of these three uniaxial processings in a 3D graph. In both figures, the strain rate curves imply that the hydrostatic extrusion has the highest strain rate at the die-exit, while the die-drawing, similar to the free-drawing, has the maximum strain rate that occurred within the die when the deformation ratio of the sample is lower than the ultimate deformation ratio. Therefore, the

maximum stress required by extrusion was much higher than die-drawing and tensile drawing, as shown in Figure 1-15.

Take POM as an example; the D500 POM experienced axial pressure of 180mPa (hydrostatically extruded at 164°C with the extrusion rate of ~0.25 mm/min and $R_N = R_A$ = 8.9, zero 'die swell') [125] compared to the die-drawing axial pressure of 70~100 mPa (die-drawn at 158°C with the die-drawing rate of ~10 mm/min and R_A = ~9) [133].

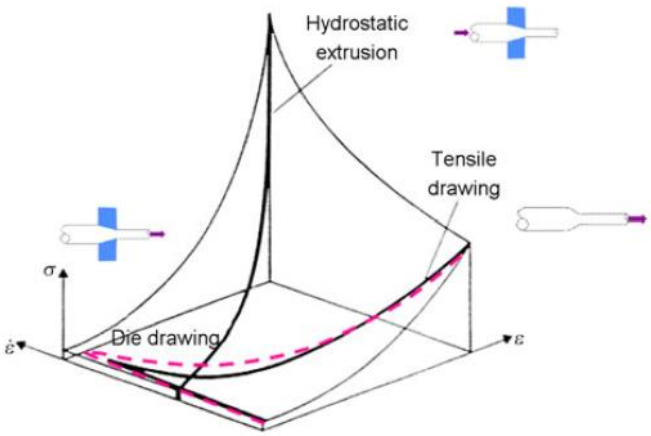

Figure 1-15 Deformation 'path' across the true stress-strain-strain rate surface [124].

Moreover, the extrusion pressure increases rapidly with the extrusion rate [125]. As mentioned earlier, the extrusion rates are generally limited to 0.15 mm/s (9 mm/min). Extruding POM at the same rate as the die-drawing would very likely cause a further drastic increase of the extrusion stress and end up with the POM fracture. If eliminating the extra help from the pressure-transmitting fluid to reduce the friction between the die and the sample, the extrusion process will require even greater axial pressure to push the billet out of the die.

The die-drawing, reported by Gibson and Ward in the processing of PE and PP, exists a 'steady-state' at some point, in which the sample billet deformation ratio (diameter) shows little fluctuation, in comparison with the ever-increasing necking during the free drawing process [126]. During the 'steady-state', the drawing load remains constant with a constant drawing rate.

Table 1-1 Features of three uniaxial processing routes.

	Tensile drawing	**Hydrostatic extrusion**	**Die-drawing**
Stress	■ Absence of compression ■ Axial stress depends on the material nature and temperature	■ Absence of tensile stress ■ Higher flow stress ■ Higher extrusion force required ■ The requirement reaches the highest at the die exit	■ Have both compression and tensile stress ■ Lower flow pressure and axial stress
Strain	■ The highest strain occurs in the neck at comparatively low strains ■ Uncontrolled 'natural draw ratio'	■ Limited deformation ratio ■ Stable and controllable deformation ratio	■ The highest strain rate encountered at low levels of plastic deformation ■ Stable products deformation ratio at steady-state
Scale	■ Only for a small section	■ Large section products ■ One batch production ■ Limited production rates	■ Large section products ■ Continuous production ■ Reasonable production rates.

Therefore, die-drawing combined the advantages of free drawing (low axial stress, high drawing rates/ high production rates) and extrusion (controllable deformation ratio), offers greater potentials for polymer solid state processing. Table 1-1shows the advantages and disadvantages of three different processing routes in terms of processing stress, strain and scale. The following sub-sections will focus on the retrospective studies on the die-drawing

parameters and their effects on the products.

1.3.4.1 Die geometry and die angle

The converging die used in the die-drawing can be of various shapes, e.g., conical die, wedge-shaped die and curved dies. The conical die is primarily used in the die-drawing of polymers due to its easy to make and axis-symmetric feature. The core feature of a conical die is the die angle (or half-angle). Mirza et al. simulated the die-drawing of POM through dies with different half-angle (5°, 8°, 10°, 15°) and showed that the higher the angle, the higher the R_A and higher drawing stress (also axial load) [143]. They attributed the result to the higher strain rate caused by a more sharply converging die (under the same drawing rate and temperature condition). The higher strain rate gives rise to a more significant drawing load, leading to more free drawing in deformation zone III in Figure 1-13. In addition, they also found that the deformation of the core and surface reflected much higher uniformity in the 5° half-angle die than in the 15° half-angle die. It seems that without considering the production efficiency, a smaller die angle could be more beneficial.

1.3.4.2 Die-drawing temperature

Temperature, which ultimately influences the mechanical behaviour of the polymer chains, is of vital importance in the die-drawing process. The temperature needs to be considered in two situations: the initiation of the die-drawing process in the die and the cooling/quenching process to accelerate the strain hardening or facilitate the fixation of the polymer after exiting the die.

In principle, any temperature that provides sufficient molecular mobility for processing can be used as the temperature of die-drawing. For most polymers, the processing could be conducted at a temperature between the glass transition temperature T_g and the melting points T_m [109, 124]. In the die-drawing of copolymers of POM, Hope et al. found that the drawing load significantly reduced with the increasing temperature, and samples with larger initial diameter could be successfully drawn at relatively higher temperatures [133].

In addition, Kukureka et al. reported analytical modelling of the temperature distribution along the die using both activated rate theory and uniaxial tensile test data. Both approaches show that the billet temperature (both surface and core) will rise along the axial direction of the die due to the mechanical work done as the progress of die-drawing [141]. The raised temperature gives rise to the flow stress reduction and may essentially influence the mechanical process.

The additional cooling procedure is absent from most of the polymer die-drawing process, possibly because these polymers' strain-hardening feature allows for the 'steady-state' of drawing and the progressive cooling process outside die in return strengths the effect of strain-hardening. However, material that undergoes elastic deformation inside the die or does not show strain-hardening effect may require additional cooling to prevent excessive spring back tendency.

1.3.4.3 Deformation ratio

The deformation ratio reflects the final strain extent of the sample. In literature, different nominal deformation ratios were commonly achieved by die-drawing samples with various

initial diameters through the same die. The alternative was to die-draw the sample with identical initial diameters through the dies with different exit diameters [142]. Coates and Ward showed that the actual deformation ratio was affected by the drawing rates as the deformation continued after exiting the die due to the tensile stress, and the maximum deformation ratio that could be achieved increased with the drawing rates [122]. They reported the R_A could be almost three times of the R_N value for a die-drawn PP at a drawing rate of ~8 mm/s. Despite the significant difference between the R_A and R_N, the relations between R_A and drawing rates were steady, in comparison with the free drawing process, in which the neck could be constantly propagating.

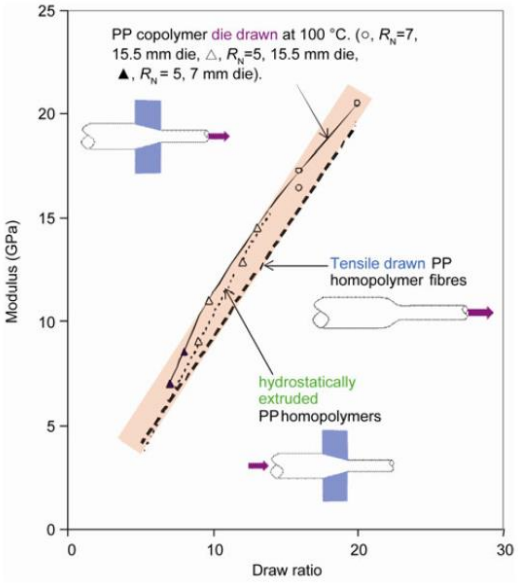

Figure 1-16 Young's modulus–- draw ratio (deformation ratio) of PP processed by different processing routes [124] (as a reproduction of work by Coates and Ward in 1979 [122]).

However, such a feature is only applied to polymers that process sufficiently strain hardening behaviour [123]. The early work of Hoffman and Sachs showed that the die-drawing of metal,

which is lack of strain hardening effect, tends to end up with 'unstable or catastrophic neck' when the deformation ratio is higher than 2.72 [146]. Another example would be PVF, which also shows no strain hardening. Its R_A was found to be very close to R_N and was independent from the drawing rates [137].

The majority of previous works have suggested that the deformation ratio (final strain) has a strong correlation with the orientation of the materials and hence is a crucial factor in the level of modulus or strength achieved. On the contrary, the choice of processing routes (free-drawing, extrusion and die-drawing) only shows a minor effect on the material strength, as shown in Figure 1-16.

1.3.4.4 Die-drawing rates

The die-drawing rate was generally defined as the haul-off velocity or the crosshead speed. On the other hand, the strain rate more accurately reflected the rate of material deformation. Although the actual strain and the strain rate in the die vary from place to place, the drawing rate is considered a reasonable representation of the average strain rate of the material.

As mentioned earlier, increasing drawing rates generally leads to increased R_A and such relation was confirmed by the die-drawing of various polymers, including POM [133, 135], PP [130], PE [126], and PLA [138]. Some exceptions, such as PVF, did not show the dependence of the deformation ratio on the drawing rates [137].

Furthermore, the drawing rates' influence on the axial stress or axial load also varies from

polymer to polymer and varies for the same sample with different ranges of deformation ratio. For example, the axial load of low molecular PE changes little [126] while POM and PP tend to increase significantly [130, 133] with the increasing drawing rates, possibly because PP and POM have intrinsically higher crystallinity. Richardson et al. reported that the axial stress of PVF (when R_N = 6) decreases with the drawing rates at first and sees a turning point after drawing rate reached ~0.7 mm/s [137].

1.3.4.5 Characterisation for the oriented polymers

As the aim of the polymer processing by die-drawing is to obtain the oriented polymers with improved mechanical properties, the characterization of the products usually consists of the determination of the mechanical properties, crystallisation and morphologies. General characterisation methods included density and tensile tests for the mechanical properties, thermal analysis, birefringence, X-ray diffraction (XRD) for orientation and crystallization calculation, optical microscope (OM), scanning electron microscope (SEM) for the morphology observation.

The die-drawing was found to influence the macroscopic properties, including density and strength. Studies of isotropic and die-drawn POM revealed that the density of material decreases with R_A, resulted from the die-drawing-induced voids [135]. Similar density reductions were found on other polymers PP, PVF, PE [129, 130, 137].

The morphological changes of the oriented polymer could be observed through eyes, OM SEM. Various polymers lost their transparency after die-drawing and the SEM images confirmed the

generation of voids [134, 135]. The area ratios of voids were calculated via the image analysis software and increased with the actual drawing ratios. SEM images of die-drawn polymers also generally show a high degree of fibre orientation [133, 147]. Figure 1-17 shows the example of SEM images for the isotropic and die-drawn POM.

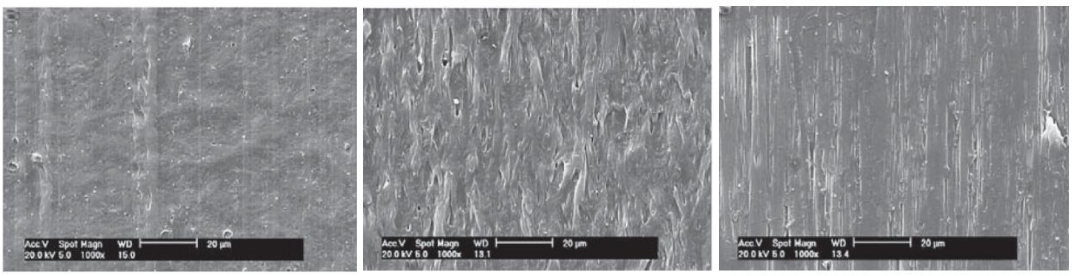

Figure 1-17 SEM of POM isotropic and die-drawn samples (longitude direction) [135].

The DSC measurement of die-drawn PP from Chaffey et al. shows an increased melting temperature and the melting enthalpy, thus confirming the existence of orientation or alignment [131]. Mohanraj et al. also used DSC endotherms and the heat of POM crystal fusion to obtain the die-drawn POM crystallinity. The lamellar thickness of the crystallized samples were calculated through the Gibbs-Thomson equation[3] [135].

Richardson et al. used both wide-angle and small-angle X-ray scattering (WAXS/SAXS) to identify the effect of processing variables on the crystal phase composition of die-drawn PVF.

[3] $T_m = T_m^0\left(1 - \frac{2\sigma_e}{\Delta h_0 l}\right)$, in which T_m^0 is the equilibrium melting temperature; σ_e is the free surface energy of the end faces lamellar that is associated with the crystallization process; Δh_0 is the thermodynamic enthalpy of fusion per unit volume of the crystalline phase. In the cited journal article, Mohanraj et al. assumed the value of T_m^0, σ_e and Δh_0 for POM to obtain the lamellar thickness l.

The XRD patterns indicate the crystalized content, and diffractometry calculation yielded the composition and orientation angle of the crystal phase [137]. Mohanraj's WAXS study of die-drawn POM shows a strong peak at (100) reflection over isotropic POM, suggesting that the crystal α axis is preferentially oriented perpendicular to the draw direction of a small portion of isotropic materials [135].

1.4 Summary

This chapter first reviewed the evolution of tissue expansion techniques, especially the development of tissue expanders, to show the application potential of expanders in plastic reconstruction surgery and the necessity of further research on the control of direction for the self-inflating tissue expanders. As the self-inflating tissue expanders are based on a hydrogel system, hydrogels' chemistry, applications and properties were introduced. Poly(VP-MMA), as a very promising biocompatible gel in tissue expansion, was reviewed for this thesis. The last part of this survey introduced some typical processing methods for polymer and pointed out that die-drawing, which combines free drawing and compression, and the force direction of which might meet the requirement of producing a bilateral swelling tissue expander, was perhaps the most feasible processing route for this current project.

Based on the reviews of the die-drawing experiments on other polymer systems, the author developed a unique processing route for poly(VP-MMA) and the properties of the die-drawn product were studied and characterized. The detail of the work will be presented in chapters 3 and 4. However, as mentioned earlier, the advantages of anisotropic hydrogel tissue expanders

compared to isotropic ones have not been reported in the literature. Therefore, the author decided to use a simplified mathematical model to describe the tissue generation capacity of anisotropic tissue expanders in the simple syndactyly case, hoping to quantitively determine whether the anisotropic tissue expander will be able to outperform the isotropic expander in some aspects. The modelling work may provide a theoretical basis for the research and development significance of anisotropic tissue expander and will be presented in Chapter 2.

2 Mathematical Modelling of Self-Inflating Tissue Expanders

List of Parameters (Chapter 2)

$\boldsymbol{R}$	The radius of the simplified cylindrical phalanx
$\boldsymbol{L}$	The length of the simplified cylindrical phalanx
$\boldsymbol{A_g}$	The area of tissue generated by the hydrogel tissue expanders (HTE)
$\boldsymbol{A_r}$	The area of tissue required by a syndactyly reconstructive surgery
$\boldsymbol{r}$	The radius of a fully expanded cylindrical expander
$\boldsymbol{r_0}$	The initial radius of a cylindrical expander before swelling
$\boldsymbol{a}$	The ratio of r to R
$\boldsymbol{H}$	The length of a fully expanded cylindrical expander
$\boldsymbol{H_0}$	The initial length of a cylindrical expander before swelling
$\boldsymbol{b}$	The ratio of H to R
$\boldsymbol{m_{1D}}$	The swelling ratio of the uniaxial swelling expander (1D-Uni) $m_{1D} = H/H_0$
$\boldsymbol{m_{2D}}$	The swelling ratio of the bilateral swelling expander (2D-Bi) $m_{2D} = a/a_0$
$\boldsymbol{m_{3D}}$	The ratio of the isotropic swelling expander (3D-Iso) $m_{3D} = a/a_0 = H/H_0$
$\boldsymbol{n}$	The number of expanders on one side of the phalanx
$\boldsymbol{\lambda}$	The slenderness ratio of a cylinder: $\lambda = H/r = b/a$
$\boldsymbol{\lambda_{1D}}$	The slenderness ratio of 1D-Uni and 3D-Iso-cy(1D)
$\boldsymbol{\lambda_{1D}}$	The slenderness ratio of 2D-Bi and 3D-Iso-cy(2D)
$\boldsymbol{\lambda_{critical}}$	The critical slenderness ratio as a stability criterion
$\boldsymbol{\lambda_{critical\_1D}}$	The critical (maximum) slenderness ratio of 1D-Uni and 3D-Iso-cy(1D)
$\boldsymbol{\lambda_{critical\_2D}}$	The critical (maximum) slenderness ratio of 2D-Bi and 3D-Iso-cy(2D)
$\boldsymbol{m_{prac}}$	The practical swelling ratio of poly(VP-MMA) as a capability criterion
$\boldsymbol{m_{prac\_1D}}$	The practical swelling ratio of 1D-Uni and 3D-Iso-cy(1D)

m_{prac_2D}	The practical swelling ratio of 2D-Bi and 3D-Iso-cy(2D)
m_{prac_3D}	The practical swelling ratio of 3D-Iso-sp
V_i	The individual volume of each device for one insertion model
V_t	The total volume of all the expanders for one insertion model
M	The required volume swelling ratio of HTE
M_{1D}	The required volume swelling ratio of 1D-Uni; $M_{1D} = m_{1D}$
M_{2D}	The required volume swelling ratio of 2D-Bi; $M_{2D} = {m_{2D}}^2$
M_{3D}	The required volume swelling ratio of 3D-Iso-sp; $M_{3D} = {m_{3D}}^3$

2.1 Introduction

Downes et al. used hydroxyethyl methacrylate (HEMA) based material for the enlargement of the congenital anophthalmic socket in 1992, pioneering the application of the self-inflating hydrogel tissue expander (HTE) [32]. The defects of specific applications could require more tissue in a particular direction than in other directions. The conventional isotropically swelling HTE may generate unnecessary tissue in other directions or even cause tissue punctures or necrosis. In these cases, an anisotropic swelling hydrogel may be preferable to optimise the geometry of tissue generated and improve tissue generation efficiency.

Swan et al. developed an anisotropic-inflating poly(VP-co-MMA) hydrogel disc by hot-pressing the cylinder material rod at its glass transition temperature [40]. The main expansion direction of the treated poly(VP-co-MMA) hydrogel was opposite to the compressing direction, showing a one dimensional (1D) expansion characteristic. Such an idea revealed the feasibility of controlling the swelling directions by rearranging the microstructure of HTE through heat

treatment. Hence not limited to the 1D expansion, HTE may potentially be processed to have a two-dimensional expansion (2D). A typical 2D HTE example could be an HTE of cylinder shape that swells entirely or mostly in its radial direction while its height barely changes. Such a device will be beneficial for cases where extra tissue is required merely in a plane area (e.g., syndactyly and cleft palate). For instance, in a syndactyly case, a 2D HTE rod could be inserted lengthwise underneath the web (along the length of fused fingers). Ideally, the 2D HTE will merely make up for the absent tissue between the fingers without growing needless tissue on either end of the finger. Moreover, the orientation of tissue generated under such circumstances would naturally coincide with the local defects, and the final closure of the defects could avoid unnecessary cutting, shaping or stretching of the tissue flaps.

Table 2-1 Schematic of isotropic and anisotropic tissue expanders.

Expanders / Swelling State	Isotropic HTE	Anisotropic HTE	
	3D-Iso	1D-Uni	2D-Bi
Before Swelling			
After Swelling (Arrows represent the swelling direction)			

This chapter presents a general model that examines the effect of several materials design parameters on the successful application(s) of HTEs with controlled or uncontrolled expansion directions. The three potential swelling types of HTE are presented in Table 2-1: the untreated

isotropic swelling HTE (3D-Iso), the hot-pressed uniaxially swelling HTE (1D-Uni), and the bilateral swelling HTE (2D-Bi), which has not been reported in the literature. The mathematic modelling aimed to compare the tissue generation efficiency of 1D-Uni, 2D-Bi and 3D-Iso in the same scenario – a simple syndactyly case (Figure 2-1). Even with simple syndactyly, there could be many possible cases if considering the differences in the number of expanders, insertion position, and shape of the expander. Therefore, specific cases that could optimise the use of HTE and possibly improve surgical convenience were selected for the discussion.

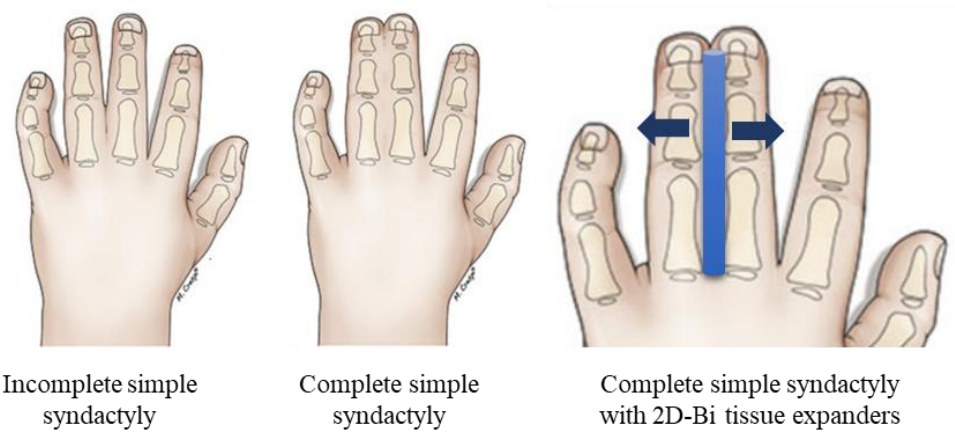

Figure 2-1 Illustrations of simple syndactyly cases and a potential insertion method for a 2D-Uni HTE (syndactyly images were reproduced from [148]).

In detail, the simulation process consisted of the following steps: (1) determined the fundamental structure of the model, which was that the tissue generated should equal the tissue required; (2) built up the geometric model by setting the parameters (e.g., diameters and lengths) of finger bones and the geometry and the swelling ratio of HTE as variables; (3) determined the necessary assumptions and conditions; (4) respectively conducted the expression of the area of tissue generated (using the HTE related variables) and the expression

of the area of the tissue required in the reconstruction (using finger bones related variables); (5) used the relationship between the variables to obtain the analytical solutions of these variables. The results revealed the hydrogel's dimensions and required swelling ratios for each case under a particular geometry of the finger bones.

However, some of the analytical solutions were not valid in reality. The feasible ranges of the HTE swelling ratio, mechanical property, and the critical buckling slenderness ratio of poly(VP-MMA) (VP: MMA, 90:10 w/w) were used to eliminate invalid results. The results of required volume, volume swelling ratio and incision size of 1D-Uni, 2D-Bi and 3D-Iso HTEs were compared to determine the pros and cons between the anisotropic and the isotropic swelling HTE.

Due to the machinable nature of HTE, the surgeon can select the right isotropic or anisotropic HTE and customise them to appropriate dimensions based on the structural features of a patient's hand. One significance of this modelling is to provide a simple reference for these surgeons. In addition, with a modified geometric model, this method can be extended to other conditions of reconstructive surgery.

2.2 Modelling in a Simple Syndactyly Case

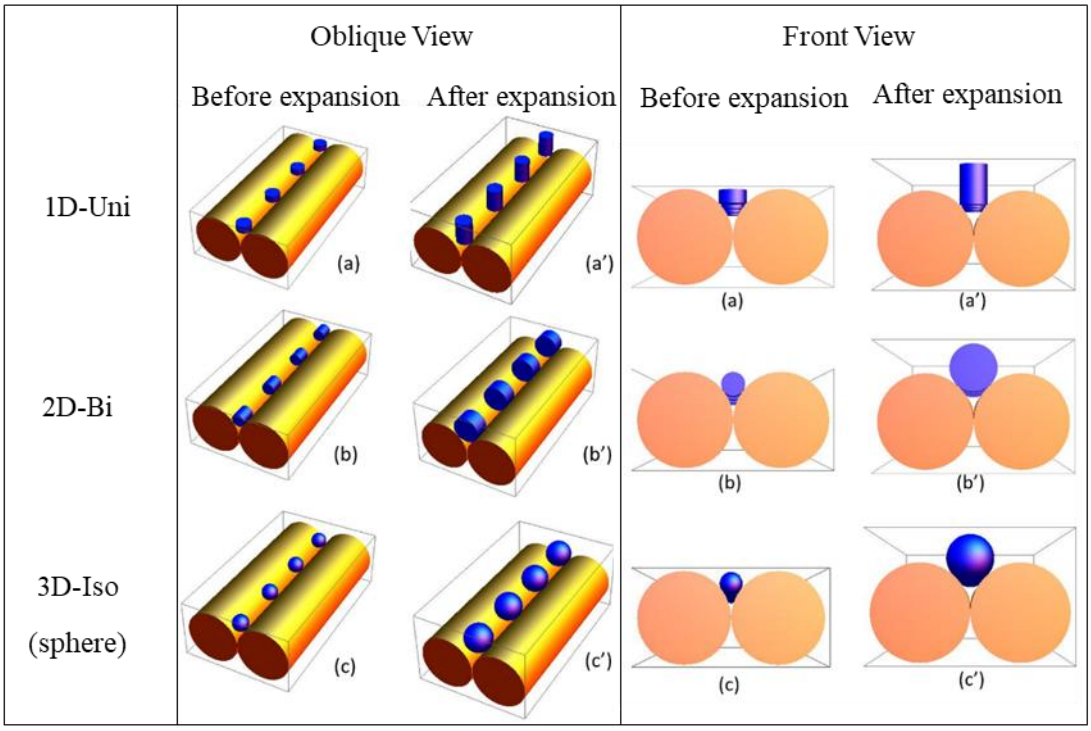

Figure 2-2 3D illustrations for the model of HTEs expansion on the phalanxes (without tissue). Note that (a') case also applies to horizontally-placed cylindrical 3D-Iso and (b') applies to the vertically-placed cylindrical 3D-Iso.

Simple syndactyly is when the soft tissue of two adjacent fingers joins together without the fusion of phalanxes. The current model simplified a section of fused fingers into two cylinders bound with a layer of tissue with zero thickness. The inserted HTE under the tissue should swell to an adequate volume to generate sufficient extra tissue for reconstructive operations. The schematic swelling diagrams of 1D-Uni, 2D-Bi and 3D-Iso are presented in Figure 2-2. The required volume for 1D-Uni, 2D-Bi and 3D-Iso HTE could be calculated to reveal the tissue generation efficiency. The model will be described in this section.

2.2.1 Assumptions

The general assumptions for this work were introduced to simplify and regulate the model.

For the finger bones and tissue:

(A1) The model applied to the simple syndactyly case[4].

(A2) A segment of the fused fingers was abstracted to a cylinder.

(A3) Regardless of the elasticity of the tissue.

(A4) The generated skin areas are valid for syndactyly reconstructive surgery.

In addition, the preconditions for HTE were specified as follows:

(B1) The HTE would expand only along its primary swelling direction(s).

(B2) The insertion of dehydrated HTEs would not deform the original layer of soft tissue (as illustrated in Figure 2-6 on p51.

(B3) The shapes of HTEs were limited to basic geometric shapes of cylinder and sphere.

Assumption (B2) is consistent with the operating principle of reducing patient discomfort and also reduces the suture/wound tension after the initial insertion of dehydrated HTEs. Urschel et al. found that moderate distracting forces are beneficial for wound healing, but excessive stress is harmful [149, 150]. The physical significance behind such precondition is to provide a minimum extent of initial deformation of the dorsal finger skin to minimise the patient's discomfort while utilizing the gradual stress increase due to the HTE swelling to benefit its

[4] Merely the soft tissue on two adjacent fingers joined together, and the fusion of phalanxes was not in the domain of discussion.

healing.

2.2.2 Fundamental Equation

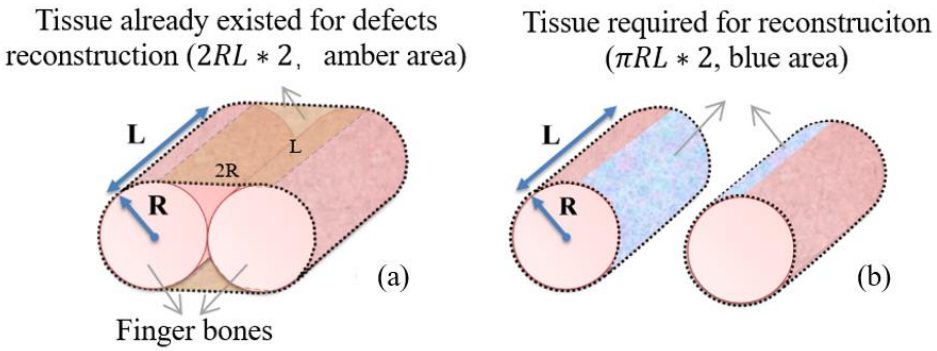

Figure 2-3 Simplification of (a) simple syndactyly and (b) fingers with tissue after the reconstructive surgery. R and L is the radius and length of the finger bone.

As mentioned before, a segment of two phalanxes was simplified into two cylinders with a radius of R and a length of L. The core equation of this model was to make the area of the needed tissue A_r, equal to the area of generated tissue A_g, as presented in Eq. (2.1). A_r was the tissue area difference between the normal fingers and the fused fingers, therefore could be expressed as a simple function of the geometric parameters of phalanxes (R, L), as given in Eq. (2.2). The value of A_g depended on not only items related with finger bones (R, L), but also parameters of the swollen hydrogel, such as the radius and length of a swollen cylindrical HTE (r, H). Hence it could be regarded as a function of multiple variables as given in Eq. (2.3).

$$A_r = A_g \tag{2.1}$$

$$A_r = 2 * \pi RL - 4RL \tag{2.2}$$

$$A_g = f(r, R, L, H \ldots) \tag{2.3}$$

2.2.3 Tissue Adhesiveness: The Boundary

Theoretically, the boundary conditions between tissue and HTE can be anything between the completely non-adhesive state (#NA) and the completely adhesive state (#A). #NA and #A cases are shown in Figure 2-4 (a) & (b). In the #NA case, grown tissue attaches to the phalanxes and expanders like a tight rope cross-section (or a tight membrane in a 3D view). Whereas under the #A condition, it adheres to the expander periphery like a vacuum film. Wiese reported that the in vivo expansion of tissue was 'tightly related to the gel cylinder' as shown in Figure 2-5 (a) & (b) [33]. The X-ray photos of tissue expansion by 1D-Uni HTE on a sheep limb in Figure 2-5 (c) & (d)) showed that the HTE-tissue attachment was closer to #NA just after the insertion, and it eventually became #A after the full expansion of HTE [151].

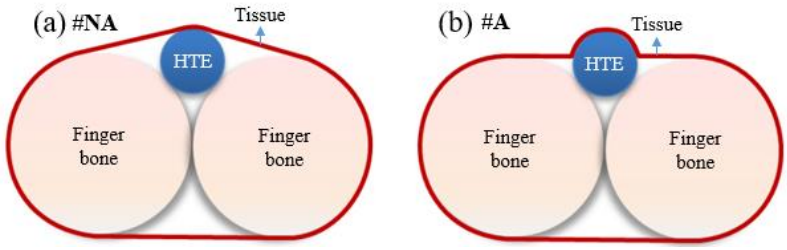

Figure 2-4 Possibilities of tissue adhesiveness: the cross-sectional views of (a) #NA case, (b) #A case.

Since the calculation of generated tissue area in this work was based on the final swollen state of HTE, #A mode was selected for the final discussion. The expressions for the #HA cases are still provided in Appendix I.

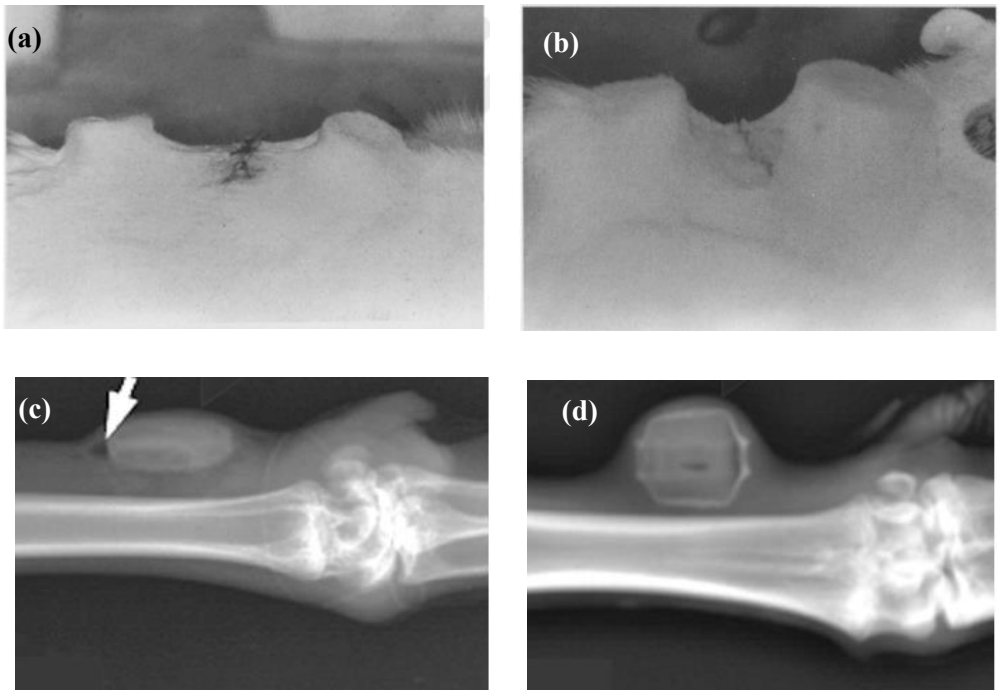

Figure 2-5 Images of tissue expanders in vivo. Top: photos of tissue expander in the rat back tissue (a) just after the implantation, (b) swelling for 3 days [33]. Bottom: X-ray of sheep front leg under tissue expansion (c) after the insertion of HTE, (d) with fully swollen HTE [151].

2.2.4 Discussion of the Insertion Modes

The insertion patterns directly determine the geometry relations of HTEs, finger bones and the covering tissue, thus affecting the final calculation results. It is essential to discuss how the HTEs are to be placed on the defective sites. In this work, the initial insertion mode of each

case was determined by three aspects: (1) the shapes of HTEs and corresponding preferred placement orientation on the finger bones; (2) the number of HTEs; (3) the location of HTEs and the intervals between HTEs.

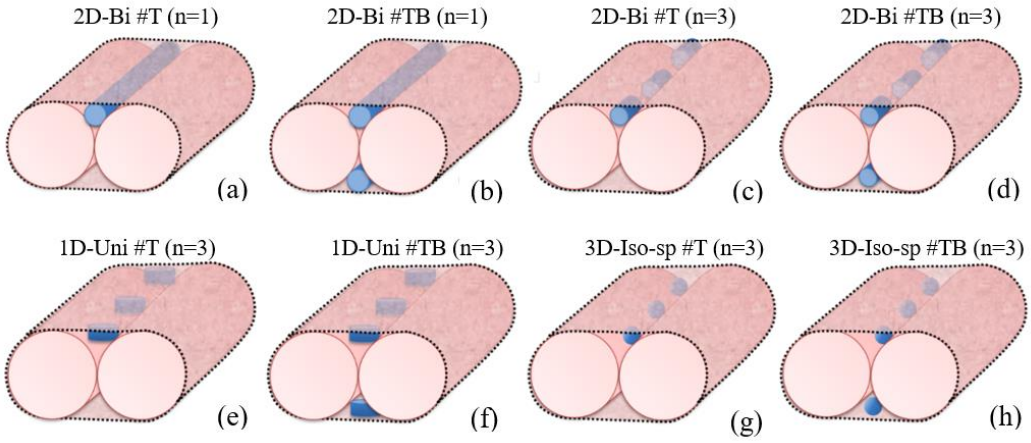

Figure 2-6 Schematic of example insertion patterns: (a)(b)(c)(d) for 2D-Bi HTEs (axis parallel with the phalanxes);I)(f) for 1D-Uni HTEs (axis vertical to the phalanxes); (g)(h) 3D-Iso sphere expanders (3D-Iso-sp); Noted that (a-f) are also schematic cases for cylindrical 3D-Iso, and the sizes of and intervals between HTEs may not reflect the actual cases.

Table 2-1 demonstrates the schematic swelling behaviours of three types of expanders. The cylinder shape conforms to the shape of the syndactyly defect to a certain extent and is also a commercially available shape of HTE (particularly for poly(VP-MMA)). Therefore, we chose the cylinder as the universal shape for 1D-Uni, 2D-Bi and 3D-Iso (marked as 3D-Iso-cy) to make a fair comparison. In addition, a spherical shape was assigned to 3D-Iso (marked as 3D-Iso-sp) to coordinate with its isotropic swelling properties. Furthermore, the differences in

their primary swelling directions will lead to variations of their preferable insertion modes. It is more practical to place 1D-Uni with its axis (height) vertical to the fingers, see Figure 2-6 (e) & (f); and to place 2D-Bi parallel with the fingers, see Figure 2-6 (a)-(d).

The number of devices also influences the final relations of HTE and generated tissue. We considered the possibility of inserting multiple discrete expanders (1 to 9 expanders) of HTE on one or each side of the phalanxes. Figure 2-6 (a) & (b) stand for insertion with single HTE. The rest of the images illustrate insertion with three HTEs.

The cases of placing HTE solely on one side were named 'top insertion' (#T case), and those on both sides were 'top and bottom insertion' (#TB case). For #T and #TB cases, n and $2n$ were used to describe the numbers of HTEs, respectively. Figure 2-6 (a), (c), (e), (g) indicate #T cases; Figure 2-6 (b), (d), (f), (g) represent #TB cases. Furthermore, if multiple HTEs were implanted, the final interval between two adjacent swollen expanders equalled either the height or the radius (whichever is in parallel with the finger bones) of the swollen HTE, and the first and the last HTE aligned up with the edge of both ends of phalanxes. Illustrations of this design are shown in Figure 2-7 (b), Figure 2-8 (b), Figure 2-9 (b) and details will be discussed in section 2.2.5.

2.2.5 Calculation

A total of 90 cases were obtained regarding all the insertion modes[5]. As mentioned earlier, each case had its own expression for Eq. (2.1). It was then ready to use all the geometric parameters and assumptions to express the area of generated tissue for each case. All the equations are provided in Appendix I. In order to obtain the analytical results of these fundamental functions, we further investigated the relations between the parameters of dry HTE, swollen HTE and the segment of phalanxes for each type of HTE. Ratios were used to simplify the excessive variables. Size ratios in Eq. (2.4) and Eq. (2.5) were used to replace the parameters of dry HTE and phalanxes.

$$a = \frac{r}{R} \tag{2.4}$$

$$b = \frac{H}{R} \tag{2.5}$$

in which, r represents the radius for the cylindrical and spherical device; H stands for the height of cylindrical devices; R is the phalanx radius. Simultaneously, a linear swelling ratio was used to connect the parameters of the dry HTE and the swollen HTE. Details will be

[5] There are 5 types of HTEs: 1D-Uni, 2D-Bi, 3D-Iso-cy(1D), 3D-Iso-cy(2D), 3D-Iso-sp. For each type, there are 18 cases: 9 for #T mode and 9 for #TB mode. In total there are 9×2×5=90 cases.

provided in the subsections as the meaning of the linear swelling ratio varied between HTEs.

In the end, we assumed the phalange length was ten times its radius ($\frac{L}{R} = 10$) to obtain the numerical results of a, b and m required for each case. In terms of the average phalangeal size of 0.5-2 years old infant, whose age is suitable for reconstructive surgery for syndactyly, L/R = 10 was a reasonable value according to the literature [148, 152-154].

2.2.5.1 Bilateral swelling tissue expanders: 2D-Bi

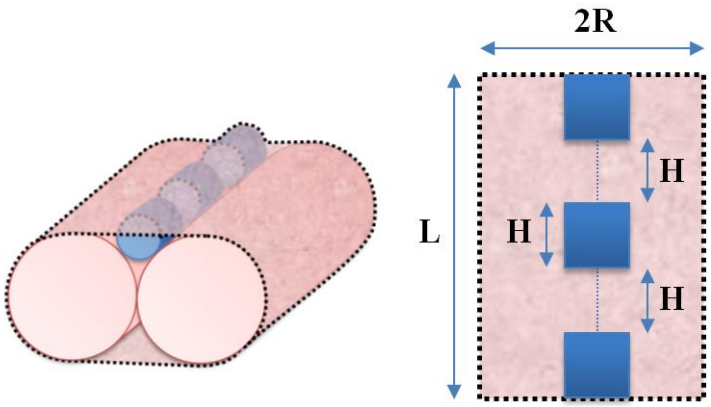

(a) Standard View (b) Top View

Figure 2-7 Schematic of 2D-Bi #A insertion case ($n = 3$).

Based on the complete adhesion (#A) between the tissue and device, Eq. 6.7 (Appendix I) was established to represent the fundamental equation for the #T cases and Eq. 6.9 (Appendix I) for #TB cases.

As seen in Figure 2-7, the interval between two adjacent 2D-Bi HTEs was equal to the length (H) of the device itself, and the distal device was aligned with the edge of phalanxes. The

length of the phalanx (L), can thus be described by H and the number of devices (n)[7]:

$$L = (2n - 1)H \tag{2.6}$$

Note that the tissue at the intervals will inevitably grow less than the tissue directly attached to the devices. However, according to assumption (A4), such an effect will be ignored, and the generated tissue area will all be considered as the effective area for closing up the syndactyly defect.

Because 2D-Bi was assumed to swell only in the radial directions, a linear swelling ratio described in Eq. (2.7) was introduced[8]:

$$m_{2D} = \frac{r}{r_0} \tag{2.7}$$

With the a & b defined in Eq. (2.4) and Eq. (2.5), Eq. 6.7 and Eq. 6.9 could be simplified to Eq. 6.8 & Eq. 6.10 (Appendix I), which contain only a as the variables[9]. Assigning the positive integrals to n ($n = 1, 2, 3 \ldots 9$), we obtained the results of a, b, m for each case. All the results are shown in Table 2-2.

The results of m in Table 2-2 represent the required swelling capacity of the expander. The values of a & b would be used to calculate the HTE volume required for the further

[7] According to the assumption (B1), only the radius of 2D-Bi will increase during the expansion and the height will remain unchanged. Hence, the height of a swollen 2D-Bi equaled the height of its anhydrous state ($H = H_0$).
[8] According to the assumption (B2), the radius of the dry 2D-Bi HTE was fixed to r_0 =0.25R as $(R + r_0)^2 = R^2 + (R - r_0)^2$.
[9] In the function, b was not considered as variables because by dividing R on both side of Equation (2.6), we have $\frac{L}{R} = (2n - 1)b$. Since we assumed $\frac{L}{R}$ =10, we had $b = \frac{10}{2n-1}$. In addition, n =1, 2, 3…9.

comparison between each type of HTEs.

Table 2-2 The calculation results of 2D-Bi #A insertion ($L = 10R$)*

	n	**1**	**2**	**3**	**4**	**5**	**6**	**7**	**8**	**9**
#T	$\boldsymbol{b}$	10	3.33	2.00	1.43	1.11	0.91	0.77	0.67	0.59
	$\boldsymbol{a}$	0.74	0.82	0.79	0.75	0.72	0.69	0.66	0.64	0.62
	$\boldsymbol{m_{2D}}$	2.96	3.27	3.15	3.01	2.87	2.75	2.65	2.56	2.48
#TB	$\boldsymbol{b}$	10	3.33	2.00	1.43	1.11	0.91	0.77	0.67	0.59
	$\boldsymbol{a}$	0.54	0.59	0.58	0.56	0.54	0.52	0.50	0.49	0.48
	$\boldsymbol{m_{2D}}$	2.16	2.36	2.31	2.22	2.14	2.07	2.01	1.96	1.91

* For #TB mode, n is the number of expanders on each side; for 2D-Bi, values of b are the same for #T and #TB modes.

2.2.5.2 Uniaxial swelling tissue expanders: 1D-Uni

The cylindrical 1D-Uni HTEs were designed to be placed as in Figure 2-8 (a), with their swelling direction perpendicular to the axis plane of two phalanxes to prevent tissue penetration at both ends of the phalanxes, as shown. Similar to the assumption in Eq. (2.6), we assumed the interval between 1D-Uni HTEs was equal to the diameter of the anhydrous device, as illustrated in Figure 2-8 (b). If n expanders inserted, the relationship of r (r_0), n and L will be[11]:

$$L = (2n - 1) * 2r \tag{2.8}$$

[11] According to the assumption (B1), the radius of the dehydrated 1D-Uni equals the radius of the swollen device ($r_0 = r$).

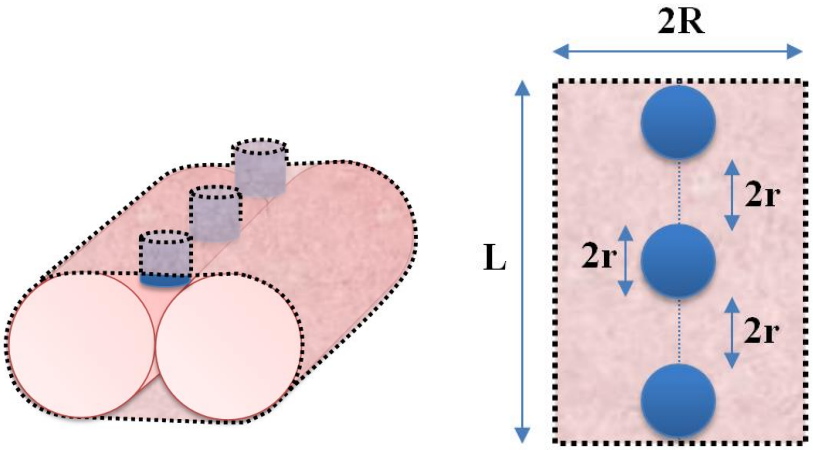

(a)Standard View (b) Top View

Figure 2-8 Schematic of 1D-Uni #A insertion case ($n = 3$).

For 1D-Uni, H is related to the initial height of the dehydrated device, H_0, by a proportion of m_{1D}, as defined in Eq. (2.9). m_{1D} represents the swelling capacity in the primary swelling direction of 1D-Uni. In addition, due to the assumption– (B2) - no initial deformation of tissue, the relations of H_0, r_0 (r), and R will follow Eq. (2.10) based on the Pythagorean theorem.

$$m_{1D} = \frac{H}{H_0} \tag{2.9}$$

$$(R - H_0)^2 + (R - r_0)^2 = R^2 \tag{2.10}$$

With Eq. (2.4), (2.5), (2.9) and (2.10), Eq. (2.11) can be derived:

$$b = m_{1D}(1 - \sqrt{2a - a^2}) \tag{2.11}$$

The fundamental equations for the #T and #TB insertion of 1D-Uni #A cases were established as Eq. 7.19 and Eq. 7.21 (Appendix I). The two equations were then simplified using the above

relations. The resulting Eq. 7.20 and Eq. 7.22 (Appendix I) merely have m as the variables. The corresponding a, m, b were hence solved. The results are demonstrated in Table 2-3.

Table 2-3 The calculation results of 1D-Uni #A insertion ($L = 10R$)*.

	n	4	5	6	7	8	9
#T	a	0.71	0.56	0.45	0.38	0.33	0.29
	b	1.31	1.41	1.49	1.56	1.62	1.66
	m_{1D}	31.51	13.56	9.23	7.37	6.35	5.71
#TB	a	0.71	0.56	0.45	0.38	0.33	0.29
	b	0.68	0.76	0.83	0.89	0.94	0.98
	m_{1D}	16.26	7.28	5.12	4.19	3.68	3.35

* For #TB mode, n is the number of expanders on each side; for 1D-Uni, values of a are the same for #T and #TB modes. And according to Eq.(2.8), $a = L/[2(2n\text{-}1)R]$. When $L/R = 10$, $a = 5/(2n-1)$. In addition, $a \geq 1$ leads to $r \geq R$, meaning the insertion of HTEs will deform the initial layer of tissue, which violates the assumption (B2). Therefore, for 1D-Uni, $n = 1, 2, 3$ are beyond the discussion under the precondition of $L = 10R$.

2.2.5.3 Isotropic expanding tissue expanders

Cylindrical 3D-Iso expander (3D-Iso-cy)

When 3D-Iso was cylindrical (3D-Iso-cy), its long axis should align with the axis of the fingers either as 2D-Bi (Figure 2-7) or perpendicular to the finger axis as 1D-Uni (Figure 2-8).

3D-Iso-cy placed as 2D-Bi, marked as 3D-Iso-cy(2D) would share the same final required size of r, H of 2D-Bi, meaning the value of a and b in Table 2-2 also apply to 3D-Iso-cy(2D). In addition, due to the no-initial deformation assumption (B2), m_{2D} in Table 2-2 would be

considered as the minimum swelling ratios required for 3D-Iso-cy(2D). For 3D-Iso, m is the linear swelling ratio of all directions, which means the 3D-Iso-cy(2D) would have a smaller starting height ($H_0 = H/m_{2D}$) than 2D-Bi ($H_0 = H$).

Similarly, 3D-Iso-cy placed as 1D-Uni, marked as 3D-Iso-cy(1D) would share the same final required size of r, H of 1D-Uni, meaning the value of a and b in Table 2-3 also apply to 3D-Iso-cy(1D). The corresponding m_{1D} is the minimum swelling ratio required for 3D-Iso-cy(1D). 3D-Iso-cy(1D) would have a smaller starting radius ($r_0 = r/m_{1D}$) than 1D-Uni ($r_0 = r$).

Spherical 3D-Iso expander (3D-Iso-sp)

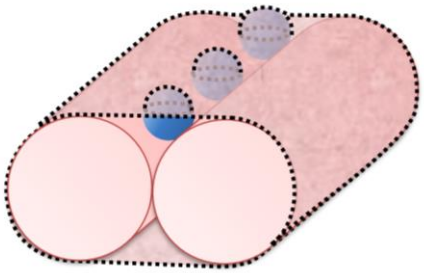

Figure 2-9 The spherical model of 3D-Iso ($n = 3$).

For the #A mode, the tissue area at the final state should be the total area of the spherical crowns above the original tissue plane, shown in Figure 2-9. The interval setting was the same as the 1D-Uni in Figure 2-8 (b). The equations for both #T and #TB cases are listed in Eq. 6.23 and Eq. 6.25 in Appendix I, and the corresponding simplified equation is given as Eq. 6.24 and Eq. 6.26. When $L = 10R$, the results are shown in Table 2-4.

Table 2-4 The results of a & m for 3D-Iso-sp cases.

	n	1	2	3	4	5	6	7	8	9
#T	a	1.45	1.08	0.92	0.82	0.76	0.71	0.68	0.65	0.62
	m_{3D}	5.82	4.32	3.68	3.29	3.04	2.85	2.70	2.58	2.49
#TB	a	1.04	0.79	0.69	0.62	0.58	0.55	0.53	0.51	0.49
	m_{3D}	4.14	3.16	2.75	2.50	2.33	2.21	2.11	2.04	1.97

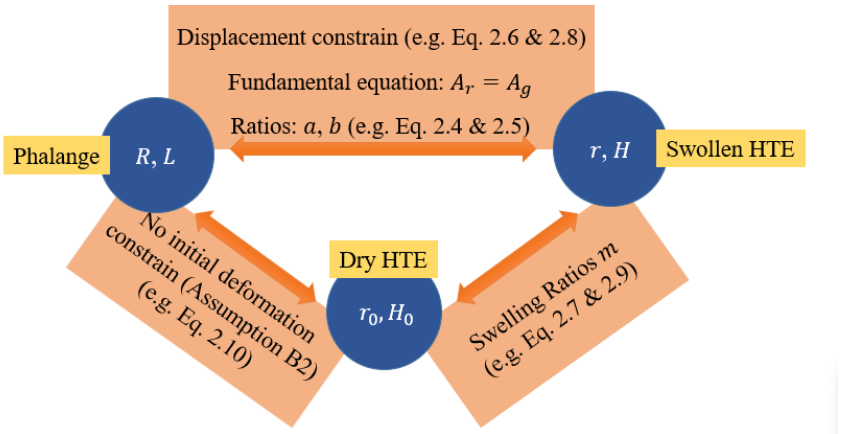

Figure 2-10 The relations between the parameters used in the modelling.

To summarize, the size ratios and required swelling ratios of 1D-Uni, 2D-Bi, 3D-Iso-cy(1D), 3D-Iso-cy(2D) and 3D-Iso-sp were obtained based on the relations between the dimensions of phalanges, dry HTEs and swollen HTEs, as presented in Figure 2-10.

2.3 Result and Discussion

Despite the results given in Table 2-2 to Table 2-4 being the numerical solutions of the fundamental equations, not all have practical significance. In addition, the expanded tissue has a reaction force on the expanding HTE, suggesting a potential buckling risk if the final cylinder is either too slim for 1D-Uni placement or too flat for 2D-Bi placement. Moreover, the linear

swelling ratio of HTE for each case may not be practical. Therefore, it is necessary to use the limitations of mechanical and swelling properties of the actual HTE to screen out reliable results. As mentioned in the introduction, this work has taken poly(VP-MMA) HTE as an example to analyse the modelling results.

After discussing the feasibility in 2.3.1, the HTEs were compared in several aspects. 2.3.2 discusses the swollen volume of HTEs to obtain the most volume-wise efficient device; 2.3.3 investigates the required overall volume swelling ratios for viable cases to determine the HTE that requires minimum swelling capacity; 2.3.4 studies the incision sizes required by each case to acquire the cases with the minimum initial wound. Finally, 2.3.5 demonstrates an example of simple syndactyly to provide a more intuitive image of the application of this mathematical modelling.

2.3.1 Feasibility Analysis: Stability and Capability

To further investigate the results of expander volume, stability index λ（the structural ratio of the swollen HTE) and capability index m (required linear swelling ratio) will be studied for each case.

2.3.1.1 Stability indexes λ

Stability indexes for each case

During the expansion, the compressive stress is continuously applied to a long thin cylindrical expander laterally (for 2D-Bi) or axially (for 1D-Uni) given by the overlying tissue. Structural instability may result in device buckling before the compression reaches the maximum stress

that the materials can bear, as shown in Figure 2-11 for 2D-Bi and Figure 2-12 for 1D-Uni. Note that considering the stability of a spherical 3D-Uni-sp was unnecessary, as a solid sphere would not be subject to buckling, while the 3D-Uni-cy should subject to the same buckling criterion as their 2D-Bi or 1D-Uni counterpart.

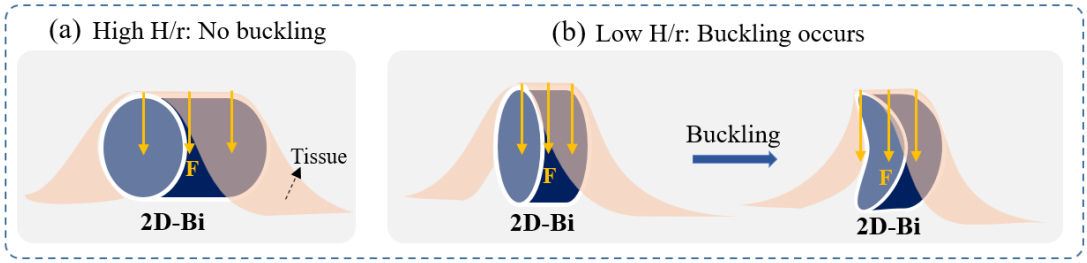

Figure 2-11 Conditions of 2D-Bi HTE under skin pressure: (a) no buckling when 2D-Bi has relatively high H/r; (b) buckling occurs when 2D-Bi has relatively low H/r. Note that such conditions also apply to 3D-Iso-cy(2D), and the schematic is only for illustration purposes and does not accurately reflect the adhesive condition assumed previously in section 2.2.3.

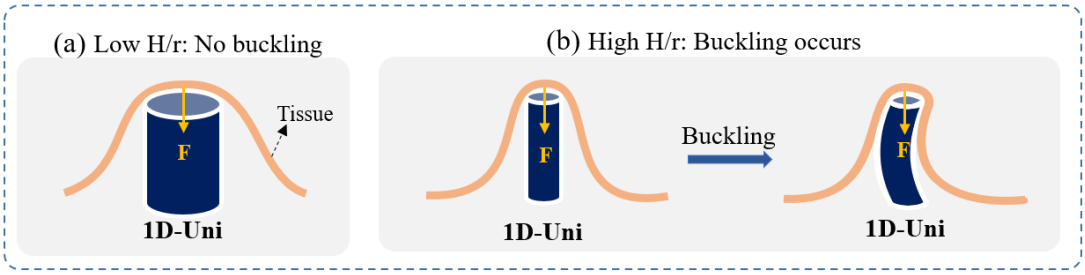

Figure 2-12 Conditions of 1D-Uni HTE under tissue pressure: (a) no buckling when 1D-Uni has relatively low H/r; (b) buckling occurs when 1D-Uni has relatively high H/r. Note that such conditions also apply to 3D-Iso-cy(1D); the tissue is presented as a line for simple illustration and its adhesion condition assumed in 2.2.3 is not demonstrated of accuracy.

Buckling was related to the slenderness ratio λ (for instance, H/r), the load (axial or lateral) and Young's modulus (E) of the material. If a fully swollen HTE can avoid buckling under maximum stress that is possibly applied, it is considered stable during the whole swelling process since, for both 2D-Bi and 1D-Uni, stability decreases as the HTE swells and the fully swollen HTE is the least stable.

Stability criterion: critical slenderness ratio $\lambda_{critical}$

$\lambda_{critical}$ is the critical slenderness ratio that results in buckling at maximum stress that possibly applies. It was found that the maximum stress applied by tissue during the swelling of poly(VP-MMA) (90:10 w/w) HTE was 64 kPa, and the Young's modulus of a fully swollen poly(VP-MMA) HTE was 140 kPa [155]. The $\lambda_{critical}$ could be therefore obtained using the classic empirical buckling formulas. In addition, buckling experiments on the fully swollen poly(VP-MMA) HTE were carried out and $\lambda_{critical}$ were deducted based on the experimental data. Both results are listed in Table 2-5 and whichever offered more strict conditions was chosen as the final stability criterion.

For both 2D-Bi and 1D-Uni, λ is a function of the fully swollen length and diameter and can be calculated using the ratio data (a, b) in Table 2-2 and Table 2-3. Λ for each case is shown in Figure 2-14 (a) for 2D-Bi (λ_{2D}) and Figure 2-15 for 1D-Uni (λ_{1D}). It is worth noting that since 2D-Bi and 3D-Iso-cy(2D) shared the same numerical results of a & b, they had the same λ. This was also true for 1D-Uni and 3D-Iso-cy(1D).

Moreover, for 2D-Bi, as seen in Figure 2-11, the higher λ, the more stable the HTE. Therefore,

cases with $\lambda_{2D} \geq \lambda_{critical}$ were valid. Similarly, for 1D-Uni(Figure 2-12), cases with $\lambda_{1D} \leq \lambda_{critical}$ are valid. Detailed calculations of λ and $\lambda_{critical}$ are shown in the subsections.

Stability criterion for 2D-Bi and 3D-Iso-cy(2D)- $\lambda_{critical\_2D}$

2D-Bi HTE was horizontally placed and primarily under lateral stress (Figure 2-11). This is similar to the symmetrical bending of a lateral-loaded circular plate, the critical buckling stress (N_{cr}) of which had been given by Brush et al. [156], as in Eq.(2.12).

$$N_{cr} = 14.68\frac{EH^3}{12(1-v)r^2} \tag{2.12}$$

in which E is the Young's modulus of the material, v is the Poisson's ratio.

The above equation leads to $\lambda_{critical\_2D} = \frac{H^3}{r^2} = \frac{12(1-v)N_{cr}}{14.68E}$, where N_{cr} = 64 kPa and E = 140 kPa. v of a hydrogel generally ranged from 0.25 to 0.49 [157]. $\lambda_{critical\_2D}$ based on the Brush equation is 0.19~0.28. However, for this model, $\lambda_{2D} = \frac{H^3}{r^2} = \frac{b^3R}{a^2}$.[20] For one group of a, b values, λ_{2D} would vary if R is assigned with different values. As a result, it is unrigorous to compare the R-dependent λ_{2D} with a constant $\lambda_{critical\_2D}$.

Alternatively, a buckling experiment on the swollen poly(VP-MMA) HTE under lateral load was carried out (details given in 4.3.2). It showed that the buckling stress was linearly related to H/r and $\lambda_{critical\_2D}$ = 1.56 for the critical buckling stress of 64 kPa. For 2D-Bi or 3D-Iso-

[20] The results of λ calculated based on the Brush equation are given in Figure 6-1 in Appendix II.

cy(2D), $\lambda_{2D} = H/r$ needs be larger than $\lambda_{critical\_2D}$ to avoid buckling.

Stability criterion for 1D-Uni and 3D-Iso-cy(1D) – $\lambda_{critical\_1D}$

1D-Uni HTEs were designed to be parallelly placed and primarily under axial stress. Leonhard Euler derived a classic buckling formula for a homogeneous, linear stress-strain behavioural, perfectly straight, axially loaded column [158, 159]:

$$\sigma_{critical} = \frac{\pi^2 E}{(K \cdot H/r)^2} \tag{2.13}$$

Where $\sigma_{critical}$ is the critical buckling stress and K is the column effective length factor (E, H and r are the same as previously defined). K corresponds to different constants for different end conditions of the column, as shown in Figure 2-13. In the 1D-Uni case, the space between the phalanxes where the bottom of the HTE is located can be regarded as a fixed end as it has no degree of freedom. The skin attached at the top of the device still offers some extent of flexibility and can therefore be considered as a pinned end. Hence K = 0.7 and based on Eq. (2.12), $\lambda_{critical\_1D} = \frac{\pi}{0.7}\sqrt{\frac{E}{\sigma_{critical}}}$ = 3.25.

On the other hand, Maneepairoj showed that the Euler buckling formula could predict the buckling condition of 1D-Uni poly(VP-MMA) HTE if a safety factor was considered, and his experimental data on the poly(VP-MMA) (90:10 w/w) showed that $\lambda_{critical\_1D} \approx 3.0$ [155].

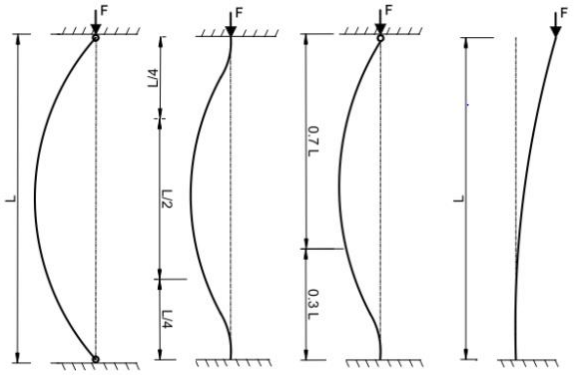

Figure 2-13 Euler column: end condition factors and buckling, reproduced from [160]: K = 1 for column pinned in both ends; K = 0.5 for both ends fixe; K = 0.7 for one end fixed, the other end pinned; K = 2 for one end fixed, one end free.

The deviation of the practical result to the theoretical prediction could be due to the imperfect geometry and the non-linear stress-strain behaviour of the materials. In this research, $\lambda_{critical\_1D}$ = 3 was used to justify the stability of 1D-Uni (also 3D-Iso-cy(1D)) and $\lambda_{1D} \leq \lambda_{critical\_1D}$.

2.3.1.2 Swelling capability indexes m

Note that the capability index m was also the required linear swelling ratio mentioned earlier (m_{1D}, m_{2D}, m_{3D}). We compared m with the possible ranges of poly(VP-MMA) linear swelling ratio (m_{prac}) to see if the required swelling capacity was feasible. The three types of HTEs within the discussion shared the same raw material but underwent different anisotropic treatment (or no treatment). Previously, it was proved that in 1D-Uni, such treatment merely changed the linear swelling capacity in specific directions instead of the overall volume swelling capacity [40]. And it is assumed that the conclusion can also be applied to 2D-Bi

HTE. Therefore, for the range of m_{prac}, we always have $m_{prac\_1D} \geq m_{prac\_2D} \geq m_{prac\_3D}$ for the poly(VP-MMA) of the same composition.

Equilibrium swelling case & Un-equilibrium swelling case

The practical equilibrium swelling ratio of poly(VP-MMA) 1D-Uni HTE was reported to be between 6 and 8 ($6 \leq m_{1D\_prac} \leq 8$) [40]. As $m_{1D} \in m_{1D\_prac}$, we have $6 \leq m_{1D} \leq 8$. For 3D-Iso, the swelling ratio, $m_{3D\_prac} = 2 \pm 0.1$ (i.e., $m_{3D} \approx 2$). The possible range of the required swelling ratio of 2D-Bi was hence $2 < m_{2D} < 6$[21]; the lower bound was the upper limit of the swelling ratio of 3D-Iso expanders, and the upper bound was the lower limit of 1D-Uni expanders.

In practice, however, the HTEs could be taken out before reaching their maximum/equilibrium swelling ratio once sufficient tissue has been generated. There should be no lower limit for the swelling capacity in this case. Therefore, $m_{1D} \leq 8$, $m_{2D} < 6$[22], $m_{3D} \leq 2.1$ were set as the final criterion for the swelling capacity index.

2.3.1.3 The feasible cases

Figure 2-14 to Figure 2-15 plotted two indexes and corresponding critical points for 2D-Bi and 1D-Iso HTEs. The experiment results in Figure 2-14 (a) give more strict conditions than the result deduced from the Brush equation (shown in Figure 6-1, Appendix II). In Figure 2-14

[21] The experimental data in Figure 4-12 on p140 showed $2 < m_{2D\_prac} \leq 3.7$.

[22] The experimental data indicated $m_{2D\_prac} \leq 3.7$ and such criterion does not change the results.

(b), all points meet m_{2D} < 6. To sum up, 2D-Bi HTEs require $n \leqslant 5$ for #T and $n \leqslant 7$ for #TB mode (for all #TB cases, n represents the number of devices in one row).

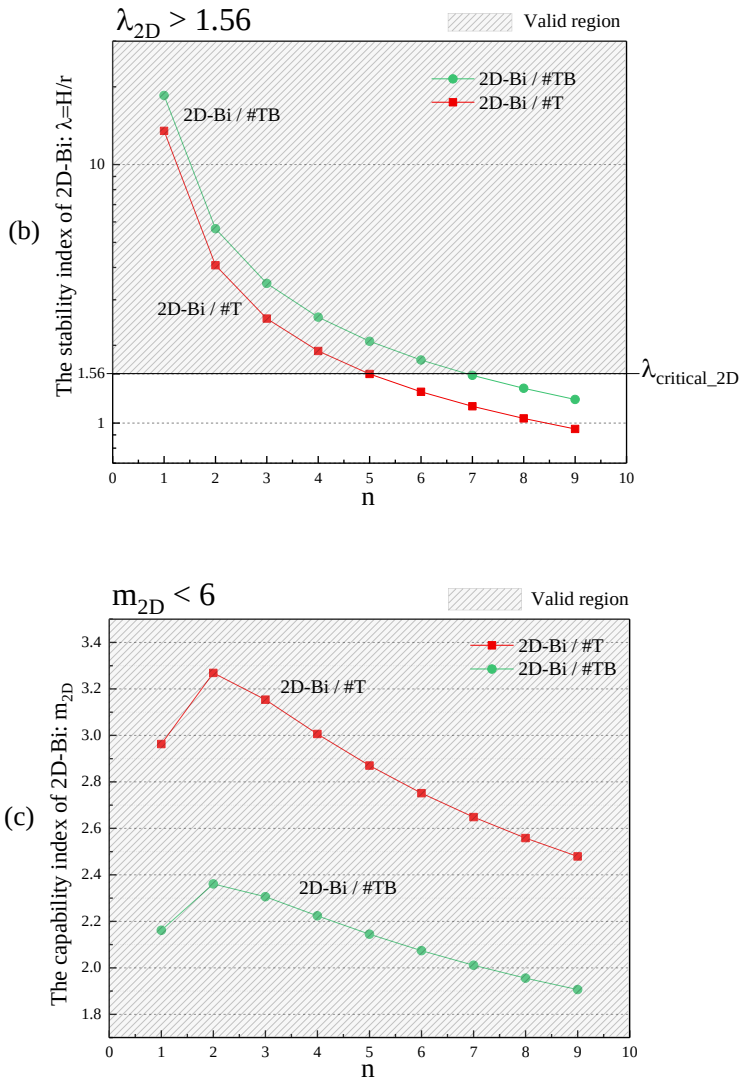

Figure 2-14 Stability and capability index of 2D-Bi: (a) stability index based on experimental data: $\lambda_{2D} = {}^{H}/_{r}$; (c) capability index m_{2D} for 2D-Bi HTEs.

Similarly, for 1D-Uni, we had the criterion of $\lambda_{1D} < \lambda_{critical\_1D} = 3$ and $m_{1D} \leq 8$. Based on the results in Figure 2-15, the feasible cases are n = 5-8 (#TB).

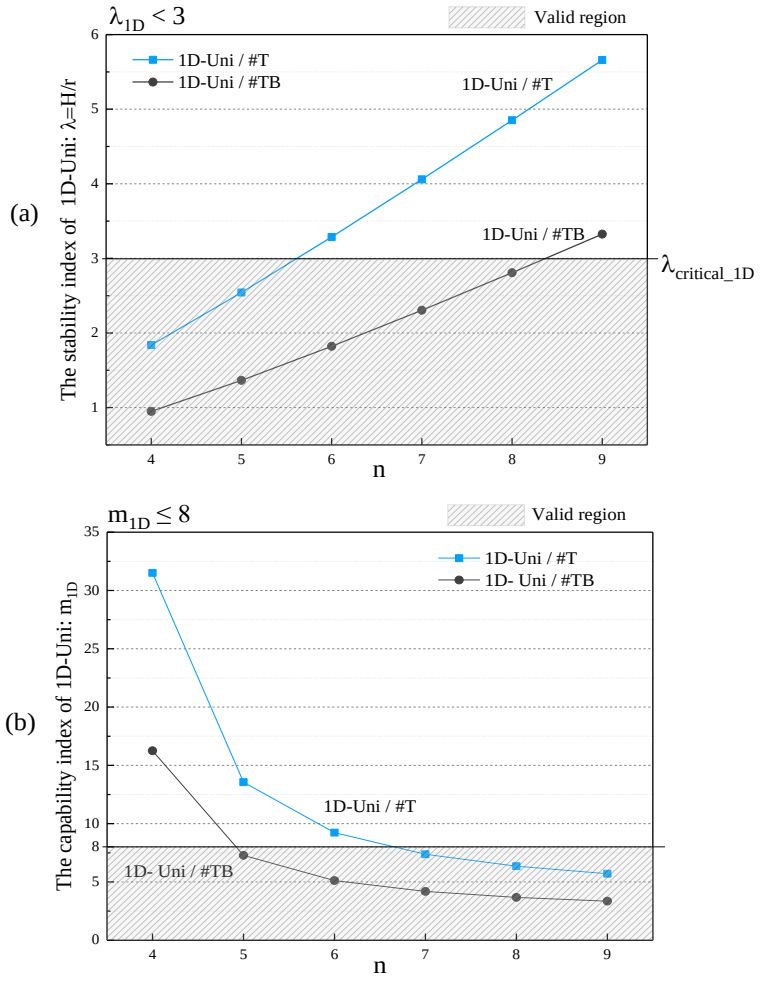

Figure 2-15 The (a) stability index λ, and (b) capability index m_{1D} of 1D-Uni HTEs.

3D-Iso-cy(2D) shares the same data in Figure 2-14. The $\lambda_{critical}$ is the same as 2D-Bi in Figure 2-14 (a), while the capability criterion is $m_{3D} \leqslant 2.1$. As a result, no cases could be considered practical to meet both criteria. In the same manner, 3D-Iso-cy(1D) shares the data of 1D-Uni in Figure 2-15 but with a different capability criterion. The m (i.e., m_{3D}) in Table 2-4 of the viable cases for 3D-Iso-sp should also subject to the $m_{3D} \leq 2.1$.

Table 2-5 presents the criterion and the corresponding applicable n for each type of HTE and the qualified n satisfying both the stability and swelling capacity requirements.

The λ and m revealed an upper limit of the possible number of the inserted cylindrical HTEs. For the condition $L = 10R$, the maximum n on one side of the phalanges is 8. The degree of freedom of the patient fingers would increase with the number of devices, but the surgeon's operation convenience may be the opposite. We may conclude that the 2D-Bi has the most expansive space for the selection of devices numbers (1~5 for #T and 2~14 for #TB cases[23]). For 1D-Uni, there seems to be a contradiction between the required slenderness ratio and swelling capacity, resulting in a relatively small applicable range. For 3D-Iso-cy(2D) and 3D-Iso-cy(1D), the core conflict is that their practical swelling ratio cannot achieve sufficient swelling to meet up the assumption of no initial deformation of the web tissue (assumption B2). Furthermore, the application of spherical 3D-Iso-sp is also restrained for a similar reason. It may be feasible to use more than 9 devices for 3D-Iso-sp. However, too many expanders could be complicated in procedures, and the frequent displacement may lead to a transversion of the device-tissue relation from #A mode (full adhesion) to #NA mode (non-adhesion).

[23] n_{TB} = 7 corresponds to 7 expanders on one side of the finger bones. So, a total of 14 expanders are actually considered for this case.

Table 2-5 The valid $\boldsymbol{n}$ for 3 types of expanders (including equilibrium and un-equilibrium swelling cases);"-" means no valid case.

	2D-Bi		**1D-Uni**		**Cylindrical 3D-Iso**				**Spherical 3D-Iso 3D-Iso-sp**	
					3D-Iso-cy(2D)		**3D-Iso-cy(1D)**			
Limit of λ and the suitable n	$\lambda_{2D} > \lambda_{critical\_2D}$ = 1.56		$\lambda_{1D} < \lambda_{critical\_1D}$ = 3		$\lambda_{2D} > \lambda_{critical\_2D}$ = 1.56		$\lambda_{1D} < \lambda_{critical\_1D}$ = 3		Stable	
	n_T = 1-5	n_{TB} = 1-7	n_T = 4-5	n_{TB} = 4-8	n_T = 1-5	n_{TB} = 1-7	n_T =4-5	n_{TB}=4-8	n_T = any	n_{TB} = any
Limit of m and the suitable n	$m_{2D} < 6$		$m_{1D} \leq 8$		$m_{3D} \leq 2.1$					
	n_T = 1-9	n_{TB} = 1-9	n_T = 7-9	n_{TB} = 5-9	–	n_{TB} = 6-9	–	–	–	n_{TB} = 8-9
The qualified n considering both λ and m	**n_T = 1-5**	**n_{TB} = 1-7**	–	**n_{TB} = 5-8**	–	**n_{TB} = 6-7**	–	–	–	**n_{TB} = 8-9**

2.3.2 Required HTE Volume for Sufficient Tissue Expansion

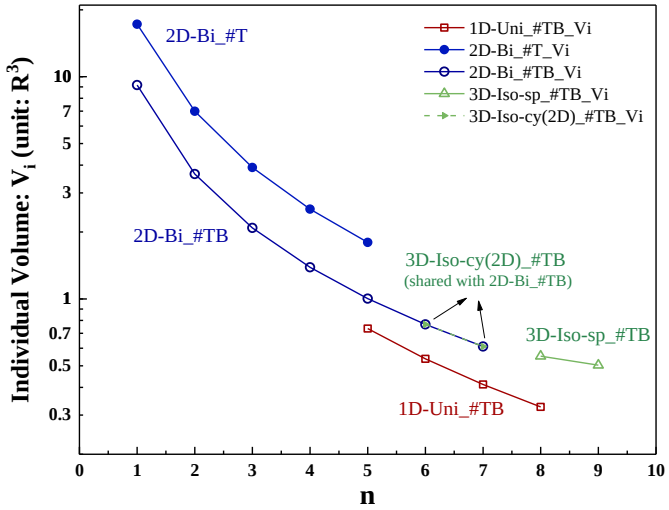

Figure 2-16 The swollen individual device volume for all valid #T and #TB cases.

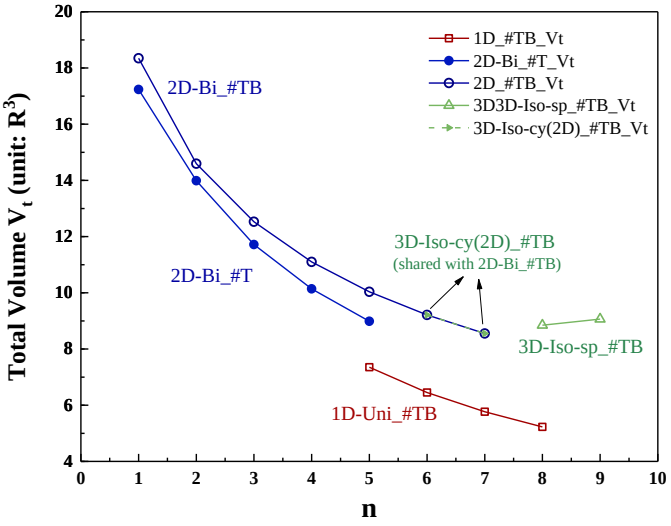

Figure 2-17 The total volume of all inserted swollen devices for all valid cases in #T and #TB modes.

Solid symbols represent all the #T cases and hollow symbols for all the #TB cases.

The individual volume V_i in Figure 2-16 shows the required volume of each HTE to achieve

sufficient tissue for the reconstruction surgery. The total volume, V_t, in Figure 2-17 was the product of V_i and the number of HTEs in each case. The former represented the final individual device size which might influence patients' comfort and convenience, while the latter was more related to the material cost. Points that did not meet the stability and capability criteria were eliminated from the figures. The result for all cases without considering the stability and capability criterion is provided in Figure 6-2 and Figure 6-3 in Appendix II.

Both figures showed that the more anisotropic HTEs inserted, the smaller volume was required, suggesting that smaller devices were generally preferable in terms of both cost-efficiency and the feeling of patience. For isotropic expander 3D-Iso-sp, more expanders resulted in smaller V_i but larger V_t. 1D-Uni has both smaller V_i and V_t than 2D-Bi and 3D-Iso. 2D-Bi (n_{TB} = 7) shows a smaller V_t than 3D-Iso-sp (n_{TB} = 8, 9)[24]. It should be noted that points of 2D-Bi (n_{TB} = 6-7) in Figure 2-16 and Figure 2-17 shared the same results with the 3D-Iso-cy(2D).

Consistent with our initial approximations, 2D-Bi under #TB modes had a smaller V_i (Figure 2-16) and a larger V_t (Figure 2-17) compared to the #T modes, since the absolute numbers inserted under #TB modes were $2n$. Figure 2-18 considered the absolute number of 2D-Bi inserted for each case. Both V_i and V_t of #TB modes were larger than those of #T modes (comparable only when the range of n is 2~7) possibly due to the #TB design of displacement

[24] In Appendix II, 2D-Bi (n_{TB} = 8, 9) had smaller V_i and V_t than 3D-Iso-sp (n_{TB} = 8, 9) as shown in Figure 6-1 and Figure 6-2. However, they may be prone to buckle due to relatively low H/r (1.36 for n_{TB} = 8 and 1.23 for n_{TB} = 9).

allowed for a better utilization of the finger edge for #T modes.

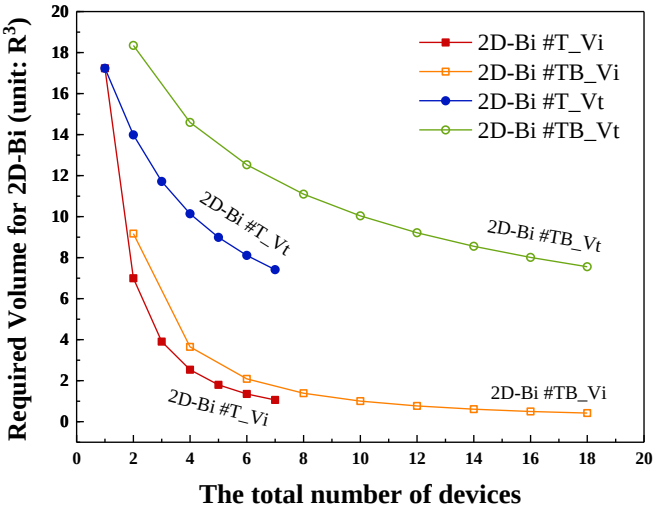

Figure 2-18 The individual and total volume of swollen 2D-Bi vs total number of devices in each case. The total number of devices equals n in #T and $2n$ in #TB cases.

The results indicated that the way of placing 1D-Uni HTEs might be the most efficient. However, the efficiency of the devices cannot simply be determined by the final volume of the devices. It is also a matter of the required swelling ratios. The high volume-wise efficiency could be a result of the high requirement of volume swelling ratios. Details will be discussed in the next section.

2.3.3 Required HTE Volume Swelling Ratios *M*

The initial setting of the model considered the linear swelling ratio m as a variable instead of the fixed value. The m acquired from the fundamental equation could be seen as the requirement to achieve the tissue generation target for each case. However, the actual swelling ability of HTE is

determined by its material nature.

As mentioned in 2.3.1.2, anisotropic processing is supposed not to change the overall volume swelling ability [40, 108] and this assumption is confirmed again by the experimental results shown in Figure 4-8 (d) and (e) in Chapter 4. For instance, if the isotropic swelling 3D-Iso and the treated anisotropic swelling 1D-Uni share the same material, their equilibrium volume swelling ratios (M) will also be the same.

Thereby, for each case, the required linear swelling ratio m can be converted into the required volume swelling ratio M, representing the requirement for the inherent swelling capacity of the material. The larger the M is, the higher demand for the swelling ability of the material. In other words, if a case requires a higher M, it means that the expansion efficiency of the HTE under this specific insertion mode is relatively low.

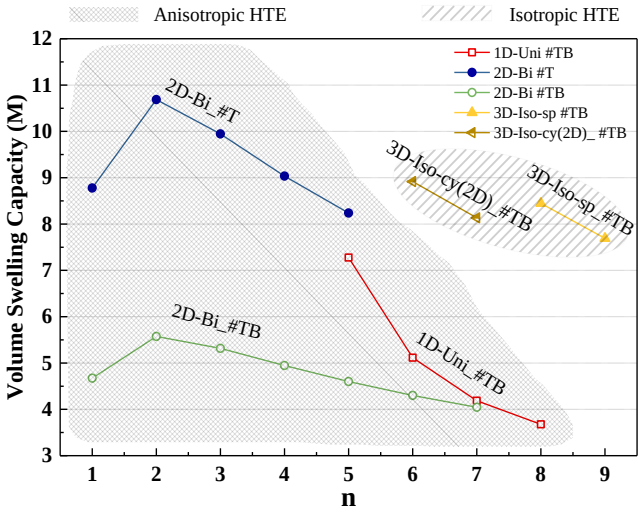

Figure 2-19 Volume swelling capacity M required for each valid case.

For 1D-Uni, which swells only in one linear direction, $M = m_{1D}$. For 2D-Bi, which swells uniformly in two linear directions, its volume swelling ratio is the square of its linear swelling ratio, $M = {m_{2D}}^2$. For 3D-Iso, which expands isotropically in the three dimensions, its volume swelling ratio is the cubic of its linear swelling ratio, i.e., $M = {m_{3D}}^3$.

Therefore, based on the values of m given in Table 2-2 to Table 2-4, we calculated the corresponding required volume swelling ratio M for each case. The results are shown in Figure 2-19. Taken together, 1D-Uni (n = 8, #TB) requires the minimum volume swelling ratio and 2D-Bi (#TB) showed very prominent tissue generation efficacy in the broader application range. In addition, despite that the 2D-Bi partially shares the result with 3D-Iso-cy(2D) in terms of the swollen dimensions (diameter, height and volume) of the HTEs, the required volume swelling ratio of 3D-Iso-cy(2D) is much higher than its 2D-Bi counterpart.

The above conclusions are valid even without considering the capability and stability criteria. Figure 6-4 in Appendix II shows that for both #T and #TB cases, $M_{2D} < M_{1D} < M_{3D}$ (when n = 8, 9, $M_{2D} > M_{1D}$ but with close values). Furthermore, $M_{3D-cy(2D)} < M_{3D-sp} < M_{3D-cy(1D)}$ indicates displacing the 3D-Iso HTEs as the 2D-Bi result in a reduced requirement for the material's intrinsic volume swelling ratio.

Based on the results of V_i, V_t and M, it can be concluded that the anisotropic ally swelling HTEs have higher expansion efficiency than the isotropic HTE. Furthermore, although 2D-Bi showed a larger swollen volume required compared to that of 1D-Uni, it has the lowest demand for the intrinsic swelling capacity of the material.

2.3.4 Required Incision Size for HTE Insertion

It would be interesting to know the initial device size as a dry gel and determine the incision size for each insertion mode. The incision is usually a linear cut. For 2D-Bi, the incision plane is a circle (diameter: $2r_0$), and the incision should be equal to $\frac{1}{2}\pi * 2r_0$ if the elasticity of the incision is negligible. For 1D-Uni or cylinder 3D-Iso placed as 1D-Uni, the incision plane is a rectangle (lateral size: $2r_0$ & h). We assumed the skin has no elasticity and the incision could be wide open; therefore, twice the incision length would equal the cross-sectional perimeter of the device (a circle for 2D-Bi and 3D-Iso-sp, and a rectangle for 1D-Uni). The required incision size is therefore πr_0 for 2D-Bi and 3D-Iso-sp and $2r_0 + H_0$ for 1D-Uni. The incision size for each case is shown in Figure 2-20. It shows that both 2D-Bi and 3D-Iso-sp have smaller incisions than 1D-Uni under the insertion fashion designed in the experiments.

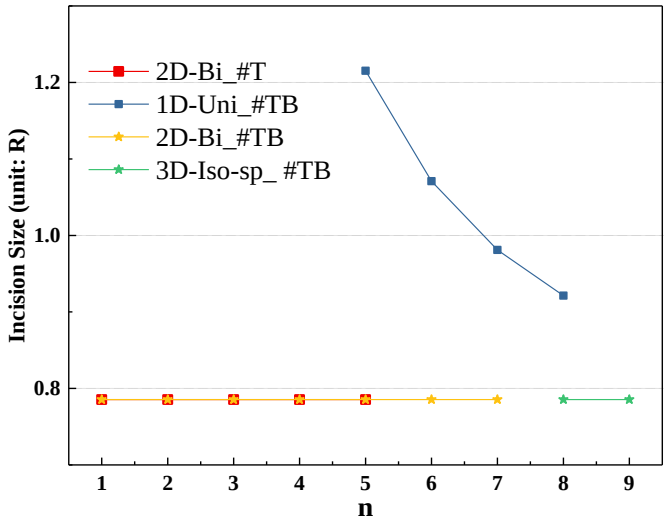

Figure 2-20 Required incision size for each valid case.

2.3.5 An Example

This section depicts an infant syndactyly case, and the corresponding device initial size, incision size, final swollen dimension and the required material swelling ratio are presented. This defect is 30mm long (L = 30 mm) and has a mean phalangeal radius of 3 mm (R = 3 mm). The parameters of the defect site match the ratio of L/R used. Table 2-6 to Table 2-8 respectively shows results for 2D-Bi, 1D-Uni and 3D-Iso-sp.

Table 2-6 Device size for 2D-Bi (L = 30, R = 3, r_0 = 0.75, incision = 2.36); unit: mm.

n	**1**	**2**	**3**	**4**	**5**	**6***	**7***
H_0 (H)	30.00	10.00	6.00	4.29	3.33	2.73	2.31
r_T	2.22	2.45	2.37	2.25	2.15	-	-
m_T	2.96	3.27	3.15	3.01	2.87	-	-
r_{TB}	1.62	1.77	1.73	1.67	1.61	1.56	1.51
m_{TB}	2.16	2.36	2.31	2.22	2.14	2.07	2.01

*3D-Iso-cy(2D) shares the results of 2D-Bi for #TB when n = 6-7.

Table 2-7 Device size for 1D-Uni (L = 30, R = 3); unit: mm.

n	**5**	**6**	**7**	**8**
r_0 (r)	1.67	1.36	1.15	1.00
H_{0_TB}	0.31	0.49	0.64	0.76
H_{TB}	1.29	1.47	1.65	1.80
m_{TB}	7.28	5.16	4.19	3.35
Incision	3.65	3.21	2.94	2.76

Table 2-8 Device size for 3D-Iso-sp (L = 30, R = 3, r_0 = 0.75, incision = 2.36), unit: mm.

n	**8**	**9**
r_{TB}	1. 56	1.53
m_{TB}	2.10	2.03

Table 2-9 Device size for 3D-Iso-cy(2D) (L = 30, R = 3, r_0 = 0.75); unit: mm.

$\boldsymbol{n}$	**6**	**7**
$\boldsymbol{H_0}$ $(\boldsymbol{H})$	2.73	2.31
$\boldsymbol{r_{TB}}$	1.56	1.51
$\boldsymbol{m_{TB}}$	2.07	2.01

For 2D-Bi and 3D-Iso-sp, its initial radius is 0.75mm as $r_0 = 0.25R$ to make the most of the space and its length depends on the number of expanders inserted. Based on the minimum required final volume, the best model among all the suitable cases should be the insertion of nine 1D-Uni on both sides of the phalanges (#TB). However, the increased number of expanders will decrease the interval between each expander, potentially changing the contact mode between tissue and expanders (small intervals may result in less adhesion between tissue and expanders). On the contrary, fewer expanders ($n \cong 1\sim2$) inserted may constrain the mobility of phalanges, such as bending. As a result, inserting 3-5 2D-Bi HTEs may be the most suitable choice for practical applications and swelling efficacy.

2.3.6 A Brief Discussion on L/R

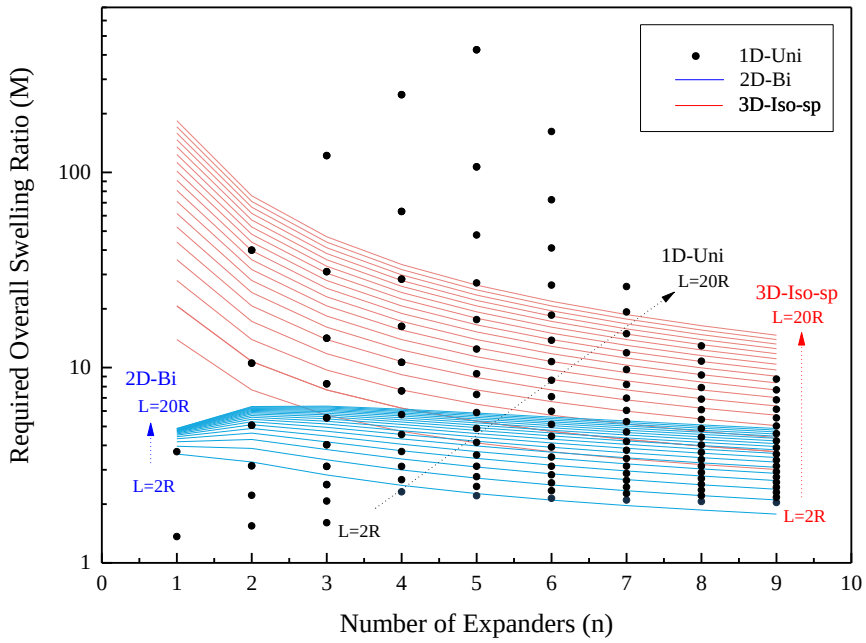

Figure 2-21 Required volume swelling ratio (M) of 3D-Iso-sp (#TB), 1D-Uni (#TB) and 2D-Bi (#TB).

Apart from L/R = 10, all integral values from 2 to 20 were assigned to investigate the influence of L/R ratio on the results of the m, λ, V_i and V_t. It turned out the general trend of m, λ, V_i and V_t with n would not be affected by increasing L/R (except for the m of 2D-Uni changing from monotonically increasing to first increasing and then decreasing). The results are provided in Figure 6-5 (2D-Bi #T), Figure 6-6 (2D-Bi #TB), Figure 6-7 (1D-Uni #T), Figure 6-8 (1D-Uni #TB), Figure 6-9 (3D-Iso-sp #T) to Figure 6-10 (3D-Iso-sp #TB) in Appendix II. Noted that 1D-Uni #T, 3D-Iso-cy(1D) #T, 3D-Iso-cy(1D) #TB, 3D-Iso-cy(2D) #T have no valid cases. 3D-Iso-cy(2D) #TB has very limited valid cases. In the general view, 2D-Bi is

suitable for all the cases from $L = 2R$ to $20R$ with plenty of choices for the numbers of expanders to be inserted. 1D-Uni is suitable for $L= 2R$ to $19R$ in the #TB insertion, but the overall choices of expander number are limited. 3D-Iso-sp is valid when $L= 2R$ to $12R$.

shows the required volume swelling ratios (M) of 3D-Iso-sp (#TB), #1D-Uni (#TB) and 2D-Bi (#TB) of all cases without the consideration of the capability and stability. It shows that 2D-Bi in general has the minimum required M.

2.4 Summary

In this chapter, the author compared the tissue generation efficiency (required swollen volume and volume swelling ratio) and incision size of three types of hydrogel tissue expanders with uniaxial, bilateral and isotropic swelling capacity through a simplified syndactyly case.

The core of this modelling work was based on the fundamental relationship that the tissue required for reconstructive surgery should equal the tissue generated by HTEs. The former was a function of phalanx geometry, while the latter was determined by the shape, number, dimensions and placement (direction, location and interval) of the swollen HTEs. With the assumptions and boundary conditions, the dimension information and the swelling ratio of the HTE were obtained. Then the stability and capability of each case were discussed, and valid cases were selected for further comparison.

1D-Uni will be more favourable if small final volumes of the HTE are of more necessity as it

has the smallest individual and total volume when n = 5~8. 3D-Iso-cy is not applicable for all the cases as it fails to meet the swelling ratio requirement. 3D-Iso-sp has good stability with a spherical shape (the rolling along the phalange is not considered), but it is only applicable when more than 8 expanders are inserted, and it requires a relatively high volume swelling ratio compared to the anisotropic HTEs. 2D-Bi HTE has the advantages of the smallest incision size and the lowest requirement of material intrinsic volume swelling ratio when n_{TB} = 1~7. 2D-Bi also has the smallest final volume among all the HTEs when n = 1~4. Furthermore, 2D-Bi offers the widest range of choices in the number of expanders to be inserted.

In addition, the results also provided some suggestions in terms of the insertion fashion. Inserting HTEs on both sides of the fingers (#TB) required a smaller individual device volume and volume swelling ratio but greater total volume than inserting on one side (#T). For anisotropic expansion, inserting more discrete expanders seems to be a more efficient way in both volume-wise and volume swelling ratio-wise. However, the upper limits in this case (L = $10R$) was n_{TB} = 7 for 2D-Bi and n_{TB} = 8 for 1D-Uni.

In the end, an example was given to show what this study may offer, and a brief discussion on the effect of L/R showed that within the range of 2~20, the results did not show significant differences from the results under the condition of L/R = 10 and 2D-Bi generally has the lower requirement for the material intrinsic volume swelling ratio.

There are many limits to this study: all the results were based on the contrarians that the

insertion of HTEs should not deform the initial plane of the phalanx plane, which may not be the primary concern for an actual situation. In addition, the property of tissue (spring-back after the removal of the expanders), the size change of the non-primary swelling direction of HTEs and a more factual syndactyly environment were ignored in this study but could be introduced in the future to improve the modelling.

In all, this chapter has depicted the feasible shapes, expansion directions, and the number of devices for typical HTEs as in syndactyly and verified tissue generation efficiency of the anisotropic HTEs and showed the bilateral swelling self-inflating tissue expander (2D-Bi) has various advantages over the other HTEs. The next chapter is devoted to exploring the development of a 2D-Bi HTE.

3 Developing a Bilateral Swelling Self-Inflating Tissue Expanders

List of Parameters (Chapter 3)

Mechanical Analysis

$\boldsymbol{D_0}$	Diameter of a sample before die-drawing
$\boldsymbol{D}$	Diameter of a sample slab in the die
$\boldsymbol{D_f}$	Diameter of a sample after die-drawing
$\boldsymbol{P_n}$	The compressive stress from die to sample ($\perp$ die wall)
$\boldsymbol{\tau_f}$	The friction stress from die to sample ($/\!/$ die wall)
$\boldsymbol{\sigma_z}$	The axial stress of a sample slab
$\boldsymbol{\sigma_r}$	The radial stress of a sample slab
$\boldsymbol{\sigma_{n=1,2,3}}$	Principle stress (n = 1, 2, 3) of a sample slab
$\boldsymbol{\sigma_v}$	The yield stress of the sample material
$\boldsymbol{\mu}$	Friction coefficient
$\boldsymbol{\alpha}$	The semi-angle (half-angle) of the die
$\boldsymbol{B}$	The ratio of μ over $\tan\alpha$
$\boldsymbol{\phi}$	The redundant work factor
$\boldsymbol{\Delta}$	The delta factor $\Delta = \sin\alpha * \frac{D_0+D_f}{D_0-D_f}$

Processing Parameters

$\boldsymbol{D_i}$	Diameter at grid i before die-drawing
$\boldsymbol{D_o}$	Average diameter of the sample before die-drawing, $D_0 = \frac{1}{n}\sum_{i=1}^{n} D_i$
$\boldsymbol{H_i}$	Distance between the grid i-1 and i before die-drawing, $H_i \approx$ 5mm
$\boldsymbol{H_0}$	Average distance between grids before die-drawing, $H_0 = \frac{1}{n}\sum_{i=1}^{n} H_i$
$\boldsymbol{D_i'}$	Diameter at grid i after die-drawing
$\boldsymbol{D_f}$	Average diameter of the die-drawn sample (#Die-drawn), $D_f = \frac{1}{n}\sum_{i=1}^{n} D_i'$
$\boldsymbol{H_i'}$	Distance between the grid i-1 and i after die-drawing
$\boldsymbol{H_f}$	Average distance between grids of #Die-drawn, $H_f = \frac{1}{n}\sum_{i=1}^{n} H_i'$
$\boldsymbol{D_e}$	Diameter of die exit, D_e = 7 mm
$\boldsymbol{R_N}$	Nominal deformation ratio, $R_N = \left(\frac{D_o}{D_e}\right)^2$
$\boldsymbol{R_D}$	Nominal deformation ratio, $R_D = \left(\frac{D_o}{D_f}\right)^2$
$\boldsymbol{R_H}$	Nominal deformation ratio, $R_H = \frac{H_f}{H_0}$
$\boldsymbol{S}$	Displacement of the crosshead/die
$\boldsymbol{S_r}$	Relative displacement of the sample ‘bulb’ end to the die
$\boldsymbol{S'}$	Displacement of the crosshead when sample ‘bulb’ is just pulled out of the die
$\boldsymbol{L_0}$	Original length of the sample
$\boldsymbol{\Delta L}$	Actual elongation of the sample, $L = S - S_r$

$\boldsymbol{L}$	Length of the die-drawn sample
$\boldsymbol{\varepsilon}$	Engineering strain of the sample, $\varepsilon = \frac{L-L_0}{L_0} = \frac{\Delta L}{L_0}$
$\boldsymbol{t}$	A certain time point during die-drawing
$\boldsymbol{t'}$	The whole die-drawing time (without pausing)
$\boldsymbol{v_d}$	Drawing rate, $v_d = \frac{dS}{dt}$
$\dot{\boldsymbol{\varepsilon}}$	Engineering strain rate, $\dot{\varepsilon} = \frac{v_d}{L_0} - \frac{dS_r}{dt \cdot L_0}$
$\bar{\dot{\boldsymbol{\varepsilon}}}$	Average engineering strain rate of the whole die-drawing process, $\bar{\dot{\varepsilon}} = \frac{v_d}{L_0} - \frac{1}{t'}$
$\boldsymbol{A_o}$	Cross-sectional area of sample before die-drawing, $A_o = \pi\left(\frac{D_o}{2}\right)^2$
$\boldsymbol{F}$	Axial load recorded by the load cell at time t
$\boldsymbol{A}$	Cross-sectional area of sample at die-drawing time t
$\boldsymbol{\sigma}$	Engineering stress, $\boldsymbol{\sigma} = \frac{F}{A_o}$
$\boldsymbol{\sigma_t}$	True stress, $\boldsymbol{\sigma} = \frac{F}{A}$
$\boldsymbol{\sigma_{max}}$	The maximum engineering drawing stress in the die-drawing process
$\boldsymbol{\sigma_{ave}}$	The average engineering drawing stress at a steady-state
$\boldsymbol{\varepsilon_t}$	True strain, $\boldsymbol{\varepsilon_t} = \ln(1+\varepsilon) = \ln\frac{L}{L_0}$

3.1 Introduction

Hydrogel-based tissue expanders (HTE) can be implanted subcutaneously and swell by absorbing the body fluid to stimulate tissue growth [161, 162]. Compared to the conventional balloon-type tissue expander, HTE does not require regular injections through an injection port. An anisotropic swelling HTE can be suitable for cases where isotropic expansion would be more likely to cause punctures or generate surplus tissue in unnecessary directions [163].

Swan et al. hot-pressed the poly（VP-MMA) cylinder stub into a disc. The processed sample gained a more significant swelling in the previously compressed direction and a restrained swelling in the radial direction. Based on the work of the one-directional compression of the hydrogel, it is of interest and necessity to further explore the processing to achieve the two-dimensional swelling of HTE. The all-around control of the hydrogel swelling direction achieved by the comprehensive manipulation of the hydrogel could be beneficial in reconstructive surgeries for geometrically anisotropic defects.

The processing-stress and swelling direction relations revealed in the previous work [163] naturally led to the idea of using lateral compression and/or axial tensile force on the heated anhydrous HTE to achieve the lateral swelling, as illustrated in Figure 3-1. Drawing, extruding or die-drawing a sample through a conical die satisfies such requirement of the force directions. However, as mentioned in the literature review, die-drawing, which combines the advantages of free drawing and extrusion, became the processing routes of most potentials.

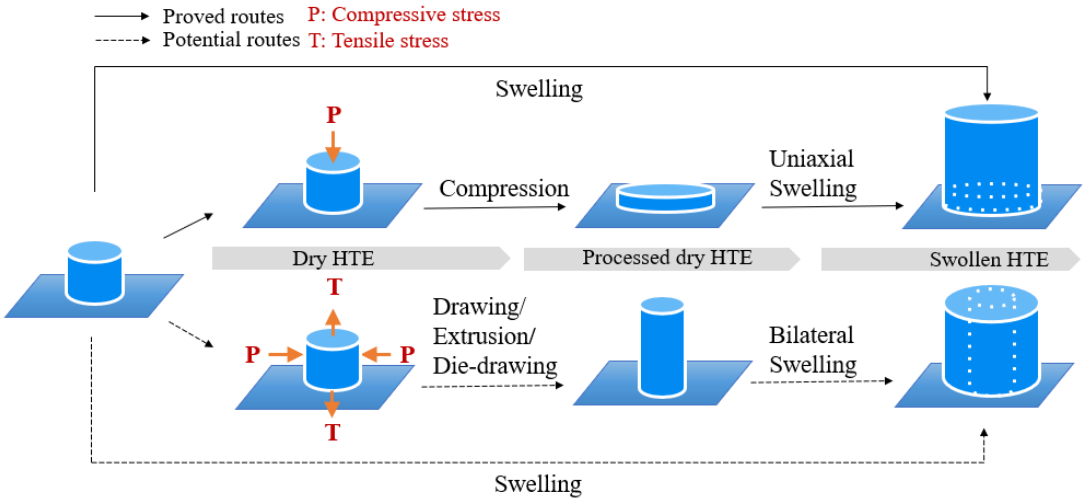

Figure 3-1 Top: the mechanism of making unidirectional swelling hydrogel tissue expander (1D-Uni); bottom: the idea of making bilateral swelling hydrogel tissue expander (2D-Bi).

The die-drawing has been widely studied as a polymer processing route. The die-drawn polymer showed axial orientation with improved modulus [114, 115]. Such a method was primarily used for the processing of thermoplastic materials. However, its applications on the gel have not been reported in the literature. On the other hand, the shape memory feature of poly(VP-MMA) has been presented and studied via a compression method. The main task of this chapter is to introduce die-drawing processing to the material poly(VP-MMA), and obtain bilateral swelling properties through its shape memory properties.

Based on the die-drawing device designed by Coates and Ward, the author developed a die-drawing method for poly(VP-MMA). Original isotropic poly(VP-MMA) rods were drawn through the die under different protocols and processing parameters, such as deformation ratio, temperature, drawing rate, aiming to generate a uniform, intact elongated material. This

current work investigated the influences of processing parameters on the die-drawing process and the swelling behaviours of the HTE. The results will be discussed in this and the next chapters.

3.2 Materials

The raw materials used in the experiments were isotropic Poly (VP-MMA) rods (Ø14mm×140mm) manufactured by Polymeric Sciences Ltd Sussex UK. The rods were synthesised by the pharmaceutical grade methyl methacrylate (MMA) and N-vinyl-2-pyrrolidone (VP) (VP: MMA = 90:10 w/w) upon the addition of allyl methacrylate (AMA, 0.2 wt.%) as the crosslinking agent and 2,2'-azobisisobutyronitrile (AIBN, 0.2 wt.%) as the free radical initiator. Sample were generally stored in a desiccator with 2.5 – 6mm silica granules as the desiccant.

3.3 Die-drawing System Design and Processing Protocol

The die-drawing device was essential to achieve the successful die-drawing of the poly(VP-MMA). This section first discusses the geometry of the die, then explains how to combine the die with the temperature control device and the existing tensile testing machine to establish a complete die-drawing system, and finally presents the general processing protocol of a poly(VP-MMA) die-drawing process.

3.3.1 Die Geometry

The dies used for die-drawing are commonly conical [123, 126, 133], wedge [138, 164], or profiled [165]. The conical die was chosen for the poly(VP-MMA) to keep consistency with the shape of the raw materials. The die design included the geometry of the conical slope, including the entrance diameter, the exit diameter, and the half cone angle (α) and the length of the exit. An extra cylindrical part at the exit can avoid an abrupt ending with an acute angle and reduce the chance of wearing.

The approximate range of the die half-angle was obtained through the axisymmetric drawing model based on the ideal plastic rigid body in section 3.3.1.1. With the theoretical results, previous studies in literature, and the consideration of the size and shape of the raw material, the die design was determined and presented in the following section.

3.3.1.1 Mechanical analysis of axisymmetric drawing

Although the heated poly(VP-MMA) is not the ideal plastic, it is beneficial to utilise the approximated model to understand the mechanical process and estimate the possible range of the die geometry.

Slab method to determine the maximum reduction ratio

The slab method is widely applied in engineering problems to get an approximate solution for plastic forming. Basic assumptions of the slab method for die-drawing include but are not

limited to: (1) uniform deformation: the cylindrical surface remains cylindrical and has the same cylinder axis before and after deformation; (2) principal stress: the normal stress on the unit surface is uniformly distributed principal stress; (3) negligible influence of shear force and friction shear on von Mises yield criterion.

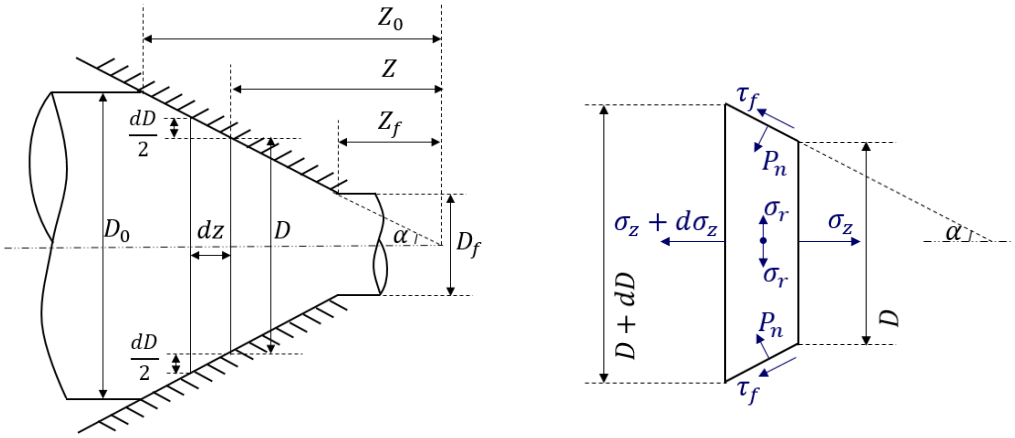

(a) (b)

Figure 3-2 Stress analysis for material in the die-drawing process: (a) geometry of a die and material, (b) stress analysis of a slab chosen from the rod with a thickness of dz.

Assume half cone angle is α, the original diameter of the rod is D_0, and the final diameter of the die-drawn sample is D_f. In the cylindrical coordinate system, a unit of dz thickness is selected from the deforming body. The unit has two parallel cross-sections with a diameter of D and $D + dD$ respectively, as shown in Figure 3-2 (a). Figure 3-2 (b) introduces the stresses occurring in the unit section. In Figure 3-2 (b), σ_z is the principal stress along the z-axis direction where the rod has a diameter of D or where $z = Z$; σ_r is the internal stress perpendicular to the z-axis; τ_f is the frictional shear stress between the die and the rod; P_n is the normal stress from the die wall; τ_f is assumed to obey Coulomb's law of friction, where

$\tau_f = \mu P_n$.

We can establish two equations based on static equilibrium via $\sum F_z = 0$ and $\sum F_r = 0$. The equations are given as Eq.(3.1) and Eq. (3.2), respectively.

$$(\sigma_z + d\sigma_z)\frac{\pi(D+dD)^2}{4} - \sigma_z\frac{\pi D^2}{4} + \tau_f\frac{\pi D dz}{\cos\alpha}\cos\alpha + P_n\frac{\pi D dz}{\cos\alpha}\sin\alpha = 0 \tag{3.1}$$

$$\sigma_r \pi D dz - \tau_f\frac{\pi D dz}{\cos\alpha}\sin\alpha + P_n\frac{\pi D dz}{\cos\alpha}\cos\alpha = 0 \tag{3.2}$$

With the geometric relationship $dD = 2\tan\alpha\, dz$ and the Coulomb's law of friction $\tau_f = \mu P_n$, we can simplify the above equations into Eq. (3.3) and Eq. (3.4).

$$2\left[\sigma_z + P_n\left(1 + \frac{\mu}{\tan\alpha}\right)\right]dD + Dd\sigma_z = 0 \tag{3.3}$$

$$P_n = \frac{\sigma_r}{\mu\tan\alpha - 1} \tag{3.4}$$

According to the von Mises yield criterion, when only principal stresses (σ_1, σ_2, σ_3) dominate, the yield stress of materials, σ_v, can be expressed by:

$$\sigma_v = \sqrt{\frac{1}{2}[(\sigma_1 - \sigma_2)^2 + (\sigma_2 - \sigma_3)^2 + (\sigma_3 - \sigma_1)^2]} \tag{3.5}$$

In the case of a conical die, which is of rotation asymmetry, $\sigma_z = \sigma_1$ and $\sigma_r = \sigma_2 = \sigma_3$.

Therefore, the von Mises criterion can be simplified into Eq. (3.6).

$$\sigma_v = \sigma_z - \sigma_r \tag{3.6}$$

Then take such relationship into Eq. (3.3) and Eq. (3.4), P_n can be expressed by σ_z and σ_v, as shown in Eq.(3.7).

$$P_n = \frac{\sigma_v - \sigma_z}{1 - \mu \tan \alpha} \approx \sigma_v - \sigma_z \tag{3.7}$$

Substitute P_n in Eq. (3.3) with the above formula and Eq. (3.8) can be obtained.

$$2\frac{dD}{D} = \frac{d\sigma_z}{B\sigma_z - (1+B)\sigma_v} \tag{3.8}$$

where $B = \frac{\mu}{\tan \alpha}$. Integrate on both sides of Eq. (3.8).

$$D^{2B} = C[B\sigma_z - (1+B)\sigma_v] \tag{3.9}$$

where C is a constant. When the surface tension is zero, $D = D_0$, $\sigma_z = 0$, C can be deduced:

$$C = -\frac{{D_0}^{2B}}{(1+B)\sigma_v} \tag{3.10}$$

The expression of the principle drawing stress at the point is, therefore:

$$\sigma_z = \frac{1+B}{B}\sigma_v\left[1-\left(\frac{D}{D_0}\right)^{2B}\right] \tag{3.11}$$

If the reduction ratio is defined as in Eq. (3.12), σ_z can also be expressed as Eq. (3.13).

$$R_r = \frac{{D_0}^2 - D^2}{{D_0}^2} \tag{3.12}$$

$$\sigma_z = \frac{1+B}{B}\sigma_v[1-(1-R_r)^B] \tag{3.13}$$

For ideal plastic solid, which does not experience strain-hardening in the plastic deformation, σ_z has the maximum stress σ_{z-max} when the maximum deformation ratio R_{D-max} is reached, as shown in Eq. (3.14) and σ_{z-max} should equal the yielding stress of the material, σ_v. This can render the R_{r-max} in an ideal situation in Eq. (3.15).

$$\sigma_{z-max} = \frac{1+B}{B}\sigma_v[1-(1-R_{r-max})^B] \tag{3.14}$$

$$R_{r-max} = 1 - \frac{1}{(1+B)^{\frac{1}{B}}} \tag{3.15}$$

As we have $\lim_{B\to 0}(1+B)^{\frac{1}{B}} = e$,

$$\lim_{B\to 0} R_{r-max} = 1 - \frac{1}{e} \approx 0.632 \tag{3.16}$$

$B \to 0$ represents the case of $\mu \to 0$. So, the maximum limit of R_{r-max} will only exist for a

non-friction case. In the general situation, the maximum reduction ratio cannot exceed 0.632. This could be a reference for the design of the die. It should be noticed that for non-ideal plastic solid, the R_{r-max} could be either larger or smaller than the value deducted.

Redundant work method to determine the angle of the die

The deduction of the redundant work method is based on the ideal plastic solid for which the deformation stress can be expressed by:

$$\sigma = \sigma_v \tag{3.17}$$

where σ_v is still the yield stress of the material. The draw stress can then be expressed by

$$\sigma_z = \int \sigma \, d\varepsilon = \sigma_v \varepsilon = 2\sigma_v \ln \frac{D_0}{D_f} \tag{3.18}$$

If we take the friction force and the redundant work into account, the drawing stress will be [166]:

$$\sigma_z = 2\phi\sigma_v \ln \frac{D_0}{D_f}(1 + \mu \cot \alpha) = \phi\sigma_v \ln \frac{1}{1-r}(1 + \mu \cot \alpha) \tag{3.19}$$

where ϕ is the redundant work factor, where $\phi \propto \tan \alpha$. As shown by Eq.(3.18), the ideal work of homogeneous plastic deformation is irrelevant to α. The work used to overcome the friction (item contains μ) decreases with increasing α ($0 \leq \alpha \leq \pi$), while the redundant work

increases with the increasing α [167]. Hence the curve of total work required, or the maximum draw stress, should have a minimum value at some optimum die angle α^*. In order to obtain α^*, the delta factor, which can define the die geometry, has been introduced [168].

$$\Delta = \sin\alpha \frac{D_0 + D_f}{D_0 - D_f} \approx \frac{\sin\alpha}{R_r}(1 + \sqrt{1 - R_r})^2 \tag{3.20}$$

Also, according to experimental studies, the delta factor has the optimum value:

$$\Delta_{opt} \approx \left[\frac{\mu}{\ln 1/(1 - R_r)}\right]^{1/2} \tag{3.21}$$

The corresponding optimum α (in radians) can be expressed by

$$\alpha^* \approx \arcsin\left[\frac{R_r\sqrt{\mu}}{\left(1 + \sqrt{1 - R_r}\right)^2} \cdot (\ln\frac{1}{1 - R_r})^{-\frac{1}{2}}\right] \tag{3.22}$$

As discussed previously, R_{r-max} = 0.632. Therefore, the range of optimum semi angle of the die (in radians) can be obtained when the friction coefficient is provided:

$$\alpha^* \leq \arcsin 0.245\sqrt{\mu} \tag{3.23}$$

Assume that the friction coefficient between poly(VP-MMA) and aluminium/steel mould is

close to that of PMMA and aluminium/steel mould, which is between 0.15 to 0.76[26] [169], then $\alpha^* \approx 5.45 \sim 12.33°$. The retrospective review showed that the half-angle for die-drawing general polymer generally ranged from 5° to 15° [122, 129-131, 133, 137, 142, 147]. Based on these results, two conical dies with 10° (α = 10°) and 5° (α = 5°) half-angle were selected for the trials of die-drawing poly(VP-MMA) and were marked as 10°Die and 5°Die respectively.

3.3.1.2 Practical limitations of the die

The cross-sectional 3D viewings, perspective 3D viewings, and engineering drawings of the two dies are shown in Figure 3-3, and the die parameters are listed in Table 3-1. The diameter of raw materials (D_0 = 14 mm) restrained the diameter of the die entrance from being greater than 14mm. The diameter of the die exit was designed to be Ø7mm (D_e = 7 mm). The maximum reduction ratio would be smaller than $R_{r-max} = 1 - \left(\frac{D_e}{D_0}\right)^2 = 0.73$ in this design, which was larger than the theoretical result of 0.632. This would allow for subsequent experiments to explore the maximum deformation of (VP-MMA). The potential reduction ratio could be varied by slimming down the diameter of the raw material rod. In addition, an extra cylindrical part was added to the end of the tapered die to avoid an abrupt ending with an acute angle and reduce the chance of die wearing.

---

26 0.15 is the dynamic friction coefficient between PMMA and dry aluminium/steel. 0.76 is the dynamic friction coefficient between dry rubber (as a simulation of heated rubbery PMMA) and dry aluminium/steel.

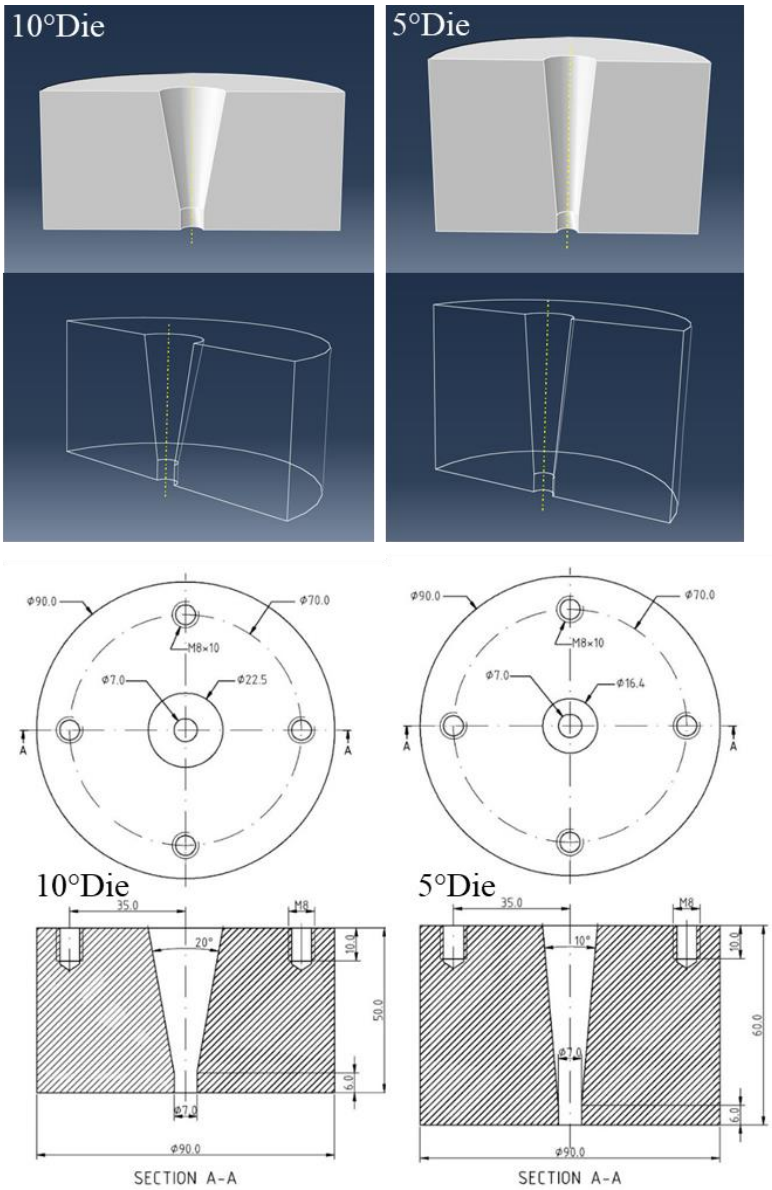

Figure 3-3 The cross-sectional 3D view (top), perspective 3D view (middle) and the engineering drawing (bottom) of the die with half-angle 10° (left) and 5° (right).

Table 3-1 Die parameters.

Part	Parameters	10°Die	5°Die
Die Body (Cylindrical)	Diameter	90.0mm	90.0mm
	Length	50.0mm	60.0mm

Conical Mould	Inner diameter at entrance	22.5mm	16.4mm
	Half cone angle	10°	5°
	Vertical Length	44.0mm	54.0mm
Die Exit	Diameter	7.0mm	7.0mm
	Length	6.0mm	6.0mm

3.3.2 Die-drawing System

As temperature and force are the two essential elements of die-drawing, the system is composed of a mechanical system and a temperature control system.

3.3.2.1 Mechanical system

Depending on the movement of the die, die-drawing can be categorised into two ways: (1) the horizontal way (die still) that clamps and pulls the materials through the die; (2) the vertical way (sample still) that fixes the sample but pulls the die to squeeze the material through [122]. This study selected the latter approach as it was suitable for small scale production and could be carried out directly on the tensile testing machine in the laboratory. The mechanical system of this study (Figure 3-4) consisted of the *power part* that provided the drawing force and controlled the drawing rate and procedures, the *deforming part* that controlled the material deformation, and the *gearing part* that connected the above.

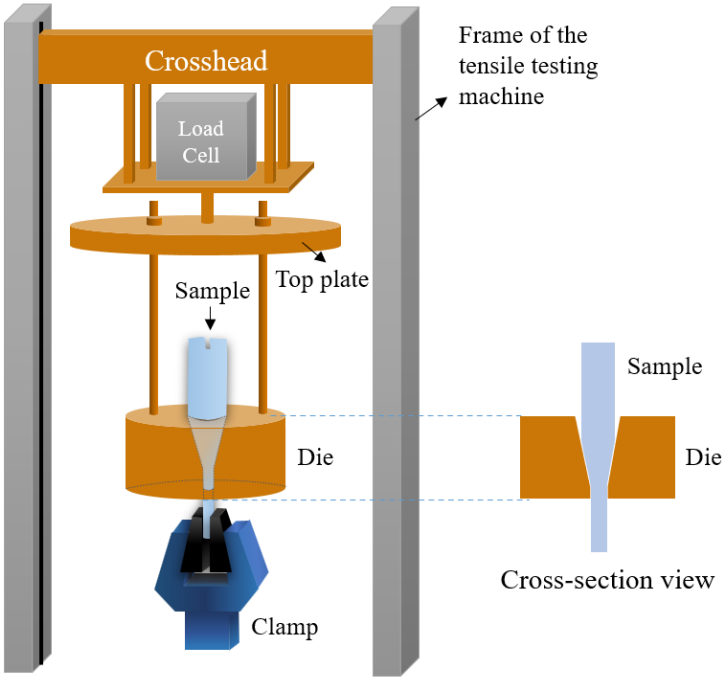

Figure 3-4 Schematic of the mechanical system with perspective die core.

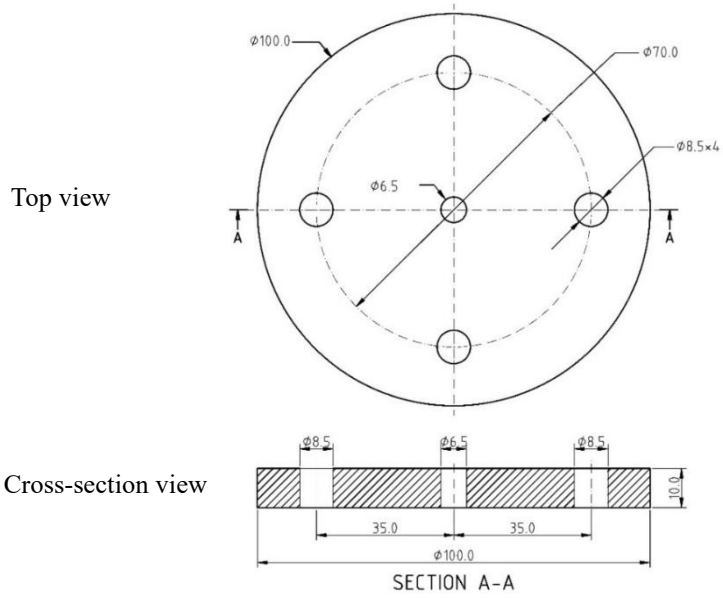

Figure 3-5 The engineering drawing of the top plate of the die (unit: mm).

The *power part* was basically the tensile testing machine, and the *deforming part* discussed in the previous section primarily consisted of the die. For the *gearing part*, a plate was required to transfer the driving force to the die from the tensile tester. The plate was connected to the die using the screws and nuts via four see-through holes (Ø8.5mm). The engineering drawing of the plate is given in Figure 3-5. Another screw in the centre of the plate was attached to the sensor of the load cell.

3.3.2.2 Temperature control system

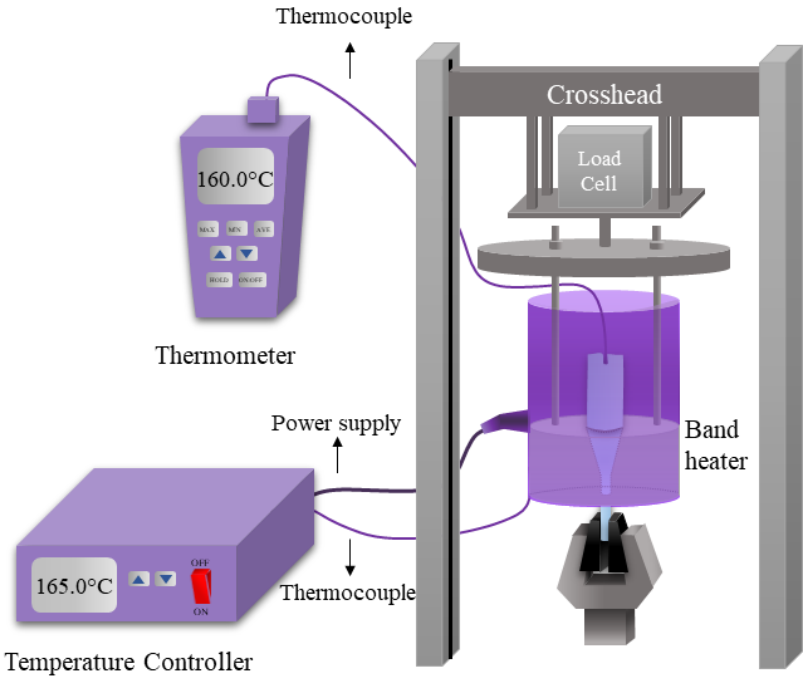

Figure 3-6 The die-drawing set-up with a thermal system.

Previous work by Swan et al. showed that poly(VP-MMA) is deformable around its glass transition temperature and becomes rigid when it cools down to room temperature [163]. A

thermal system is indispensable for triggering the flexibility of the poly(VP-MMA) chain. Following the design of Coates and Ward [122], the die was bound by an adjustable band heater, as shown in Figure 3-6. The wall of the bespoke heater was higher than the die to ensure a heated atmosphere for the sample. The thermocouple between the band heater and the die would feed the die surface temperature back to the temperature controller[28]. Additionally, the temperature of the sample was monitored by a separate thermometer so that the set value of the controller can be adjusted accordingly, hence ensuring a suitable heating process. Before the processing, the glass transition temperature of poly(VP-MMA) was obtained using the differentiate scanning calorimetry (DSC) and heating time required was determined.

Glass transition temperature

From the heat flow – temperature curve of DSC given in Figure 3-28, the glass transition temperature (T_g = 163.1 °C) of the isotropic poly(VP-MMA) (#Iso) was obtained. Since the two inflexions on the DSC curve indicated the change of poly(VP-MMA) from glassy state to rubbery state, temperatures within these two inflexion points (123°C and 188°C) were considered for processing experiments. Moreover, initial trials showed that the stretching of poly(VP-MMA) under 135°C was difficult, and browning was likely to occur above 185°C. Therefore, a smaller temperature range of 145°C~180°C was taken for the subsequent

28 It was found that putting the probe close to the die centre would give rise to a delayed response and cause the overheating of the die.

experiments.

Heating time requirement

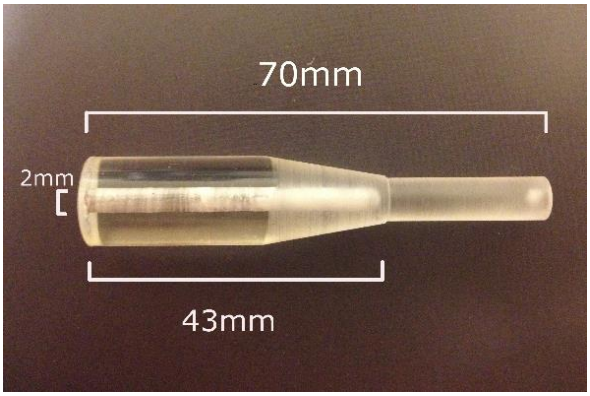

Figure 3-7 Sample prepared for the temperature profile.

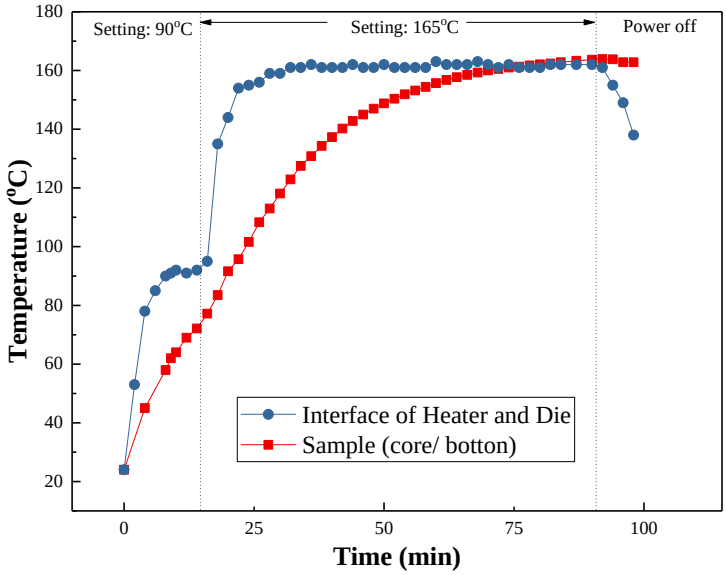

Figure 3-8 Temperature profile of the die and sample.

A 43mm depth of the hole was drilled at the 'bulb' centre of a 14mm diameter poly(VP-MMA) rod (Figure 3-7), and the thermometer thermocouple probe was inserted into the bottom of the

hole to monitor the core temperature of the sample. Meanwhile, the thermocouple probe of the temperature controller was left between the band heater and the die to monitor the die surface temperature. The heating temperature was initially set as 90°C and then to 165°C to prevent the overheating of the sample. The temperature change of the die and the sample was plotted as a function of time in Figure 3-8. The die surface reached ~160°C in about 20 minutes, while the 14mm sample took around 65 minutes to reach the processing temperature.

3.3.2.3 Equipment models

Table 3-2 List of equipment models and supplier information

Devices	Model	Provider
Tensile testing machine	DMG universal tensile testing machine	Dension Mayes Group (Leeds, UK)
Operating system	Rubicon digital control system	
Load cell	SM-100 force transducer Capacity 100 lbf (≈445N)	Interface, Inc. (Scottsdale, Arizona, USA)
Band heater	Mica band heater Ø89.3×155mm/ 1000mm A/B/C leads/ maximum working temperature 280°C	Elmatic Ltd. (Cardiff, UK)
Thermocouple 1 (band heater /temperature controller)	RS K Type Thermocouple Stainless Steel/ 1×150mm Probe/ -100 → +1000 °C	Parts all provided by RS Component Ltd (Corby, UK)
Temperature controller	Eurotherm 2166 proportional-integral-derivative controller (PID) 48*96mm/ 85-264V supply voltage	Circuits built up by technician Bob Lloyd (Materials, University of Oxford)
	Solid state relay (SSR) 10A rms/ 24-280Vac	All assembled by the

	Electronic enclosure 2U×178D×203W	author
Thermocouple 2 (materials/thermometer)	Testo K Type Thermocouple Fibreglass/ 1.5×812.8mm Probe/ -50 → +399 °C	
Thermometer	RS 1319A digital thermometer	
10°Die	Cylinder (Ø90.0×50.0mm) with a conical channel (entrance/exit: Ø22.5/Ø7.0mm, 10° half cone) and a cylindrical die exit (Ø7.0×6.0mm) in the centre. Made with stainless steel.	Materials provided by Mechanical Workshop, Materials Department, University of Oxford Machined by the author under the supervision of technician Laurie Walton (Materials, University of Oxford)
5°Die	Cylinder (Ø90.0×60.0mm) with a conical channel (entrance/exit: Ø16.4/Ø7.0mm; 5° half cone) and a cylindrical die exit (Ø7.0×6.0mm) in the centre. Made with aluminium.	
Top plate	Aluminium Plate (Ø90.0×10.0mm)	
Holding sticks	M8×130mm steel screws	
Lathe	XYZ 1440 centre lathe	XYZ Machine Tools Ltd. (Tiverton, UK)

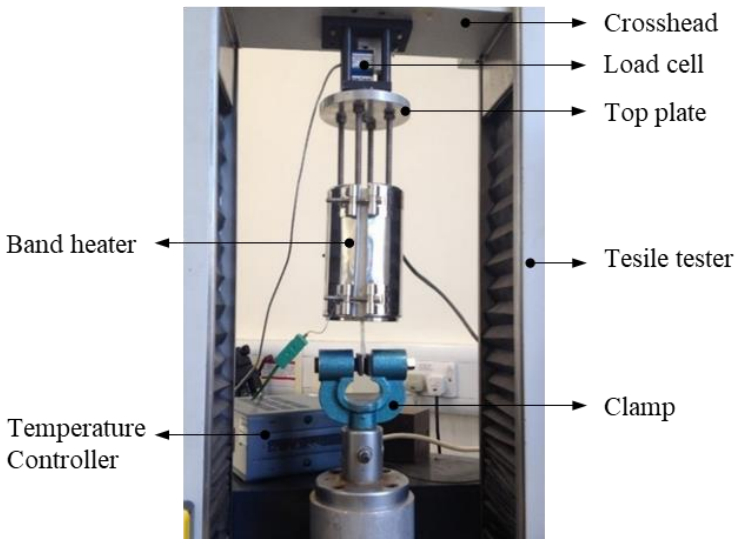

Figure 3-9 Photo of the die-drawing system (the thermometer is not shown).

The equipment information is provided in Table 3-2 and a photo of the die-drawing system is presented in Figure 3-9.

3.3.3 Die-drawing Processing

The section demonstrates the workflow of the die drawing process, including the sample preparation, die drawing and post die-drawing. The protocol of each step will be elaborated in the subsection.

3.3.3.1 Sample preparation

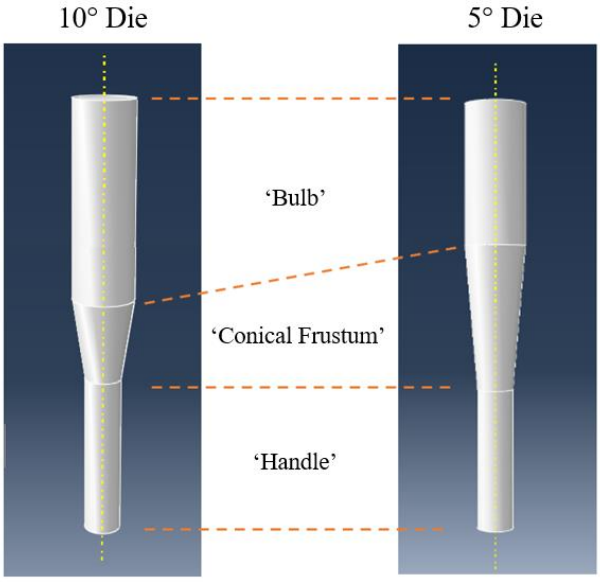

Figure 3-10 Illustrations of lathed samples for 10°Die and 5°Die.

Consistent with previous works on the die-drawing of polymers, trials by the author showed the necessity of forming a billet 'nose' before die-drawing for the clamp to hold. Coates et al. mentioned in their first die-drawing article that the nose could be made either extruding the

sample or having an isotropic billet with stepped diameter along its length [122]. Others reported pre-machined samples with a tag and a tapered part [126, 133]. The tag was smaller than the die exit to allow for the initial gripping. The tapered part had an angle 1/3 of the die (e.g., a 5° semi-angle sample for a 15° semi-angle die) to facilitate the die-drawing at the beginning.

The hydrostatic extrusion was considered unsuitable for the poly(VP-MMA) as the pressure liquid might contaminate the material. The ram extrusion was proved impractical by several failed attempts. The poly(VP-MMA) rod extruded out of the die immediately recovered its original shape due to the stress-free condition and the retained high temperature. The short and bulky end of the sample was unfavourable for the gripping. Furthermore, buckling of billet tended to occur upon more significant extrusion pressure. Therefore, the pre-machining method was adopted in the present study.

The cylindrical rod (approx. Ø14×140mm) was lathed into a ‘torch’ shape of the same semi-angle to fit the conical die. It contained a larger cylinder (‘bulb’), a taper region in the middle (‘conical frustum’) and a slimmer cylinder (‘handle’). The length of ‘conical frustum’ and ‘bulb’ varied with the cone angle and the ‘bulb’ diameter, while the ‘handle’ had a fixed size of Ø6.5×25mm, as shown in Figure 3-10. The length was to ensure a firm grip of the ‘handle’. Moreover, the ‘bulb’ was pre-machined to different diameters for each die to achieve different deformation ratios. A small hole (Ø2×5mm) was drilled in the centre of the ‘bulb’ end to place the thermocouple probe of the thermometer. The samples were then cured in a vacuum oven

at 110˚C for 1 hour.

Then a ‘gripping mark’ was drawn 6 mm from the ‘handle’ end. Parallel marks (vertical to the sample axis of symmetry) were drawn at 5mm constant spacing on the ‘bulb’, and the dimensions at the marks were measured. The samples were again kept in the desiccator and ready for die-drawing processing.

3.3.3.2 Die-drawing protocol: heating, drawing and cooling

After the system assembly, the sample was inserted through the die with its ‘bulb’ on top. The die was repositioned via the tensile machine’s crosshead so that the grip could align with the ‘gripping mark’ and hold the ‘handle’ appropriately. Then it was crucial to move the die further down for 2-3mm to detach the die and the sample before heating[29].

The thermocouple probe of the thermometer was placed in the ‘bulb’ hole to monitor the instant temperature of the sample centre. Then the temperature controller was switched on, and its set temperature was usually 5-10°C higher than the targeted temperature of the sample

[29] The small air gap could prevent uneven heating and reduce the initial friction. Direct contact heating of the sample with the die caused increased friction force, leading to immediate sample breaking when drawing began. The mechanism behind the scene remains unknown, but possibly due to the slightly expanded material in the die (resulted from the heating) and the extended contact-heating time had enhanced the interaction of the die material and poly(VP-MMA) at a molecular level. It could be either a heat- and force-induced interfacial chemical bonding between the two materials or a strengthened physical coupling of the tiny ‘sawtooth’ on the interface.

due to the heat dissipation in the open system of the band heater[30]. The heating procedure was usually set to 60 minutes based on the temperature profile of a Ø14mm sample.

During the heating, the drawing parameters (drawing rate, drawing distance or time, pausing period[31], the safety boundaries) were programmed through the Rubicon software. These parameters and the experimental design will be further discussed in section 3.4.1. When the sample reached the target temperature, a command was given to the tensile machine to drive the die upwards as previously set in the Rubicon.

After the sample was pulled out of the die and naturally cooled, it was stored in the desiccator to remove excess moisture. The deformation was then examined through the grid lines marked previously. Finally, the samples were cut into small stubs for characterization and swelling experiments.

3.4 Experimental Design

The current study used the single-factor method to investigate the influence of process parameters on the die drawing of poly(VP-MMA). In addition, the die-drawn products were

[30] As mentioned earlier in section 3.3.2.2, the die was pre-heated to ~90°C under a set temperature of 90°C first.

[31] In some cases, occasional pauses were necessary because samples required additional time to cool down and set. The timing and duration of pauses varied according to different drawing rates, reduction rates and temperatures. The pauses-involved IMD process will be further discussed in section 3.5.1.3 on p94.

characterised by differential scanning calorimetry (DSC), X-ray diffraction (XRD) and the optical microscope (OM) to examine the change of sample before and after die-drawing and to discuss the influence of parameters further.

3.4.1 Die-drawing Parameters

Table 3-3 Experimental design: die-drawing parameters

Variable	Variable Parameter	Control Parameter
Die angle	Die angels (5° half-angle die, 10° half-angle die)	T=160°C 1, 2, 3, 4 mm/s Drawing rate #11 Sample (⌀11.0mm original diameter)
Deformation ratio	'Bulb' diameters of the original sample rods (⌀9.0mm, ⌀9.5mm, ⌀10.0mm, ⌀11.0mm, ⌀12.0mm, ⌀13.0mm, ⌀14.0mm)	5° half-angle die T=160°C 4 mm/s Drawing rate
Drawing rate/Strain rate	Speed of crosshead movement (0.3mm/s, 0.5mm/s, 1mm/s, 2mm/s, 3mm/s and 4mm/s)	5° half-angle die #9.5 Sample/ v_d = 0.3, 0.5, 2, 3, 4 mm/s (T=145°C) #10 Sample/ v_d = 0.3, 0.5,1 mm/s (T=145°C); #11 Sample/v_d = 1, 2, 3, 4 mm/s (T=160°C)
Drawing temperature	Processing temperatures (145°C, 160°C, 180°C)	5° half-angle die #9.5 Sample 4 mm/s Drawing rate

Table 3-3 reflects the drawing parameters designed in this experiment. The definition, calculation of the parameters will be further discussed in the subsections.

3.4.1.1 Die angle (α)

At the same temperature (T=160°C) and drawing rates (v_d = 1~4 mm/s), samples with the same original 'bulb' size of ⌀11.0mm were die-drawn in the 10°Die & 5°Die, respectively.

In addition, before die-drawing, initial shaping was done for the purchased poly(VP-MMA) rods (Ø14×140mm). Only the volume of the 'bulb' on such rod accounts for the effective die-drawing. The total wastage volume included the lathed off material, the 'conical frustum' and the 'handle'. Figure 3-10 (p107) showed that the effective ('bulb') length of a 10°Die sample was longer than a 5°Die sample. In order to intuitively compare the material utilization efficiency of the two dies, the efficiency rate and the loss rate were calculated. The results are shown in section 3.5.1.1.

3.4.1.2 Deformation ratios (R)

In order to explore the influence of drawing ratio on processing, all the rods were lathed to the same 'handle' size and the half-angle of the conical frustum, but different 'bulb' diameters (⌀9.0mm, ⌀9.5mm, ⌀10.0mm, ⌀11.0mm, ⌀12.0mm, ⌀13.0mm, ⌀14.0mm with an error of ±0.2mm). These samples were drawn through the 5°Die at 160°C with a drawing rate of 4 mm/s. The die-drawn rods were marked as #size according to their initial diameters (e.g., #11 represents the die-drawn sample previously lathed to ⌀11mm). The deformation ratios were calculated based on the following definitions.

Calculation of the deformation ratios

Figure 3-11 (a) illustrates how the original sample was grid-marked with fixed interval of 5mm. Figure 3-11 (b) shows the samples after die-drawing; the mark would extend with the stretching of the sample. Measurements of the diameters at the grid marks and the lengths between the grids were done before and after processing. For diameter, $D_0 = \frac{1}{n}\sum_{i=1}^{n} D_i$, $D_f = \frac{1}{n}\sum_{i=1}^{n} D_i'$; and for length, $H_0 = \frac{1}{n}\sum_{i=1}^{n} H_i \approx 5mm$, $H_f = \frac{1}{n}\sum_{i=1}^{n} H_i'$ (n represents the serial number of grid marks). Previously, the reduction ratio ($R_r = \frac{{D_0}^2 - D^2}{{D_0}^2}$) were defined in Eq. (3.12). For the die-drawn samples, length measurements (H_i') were consistently performed on the same side of the widened marks, as presented in Figure 3-11 (b).

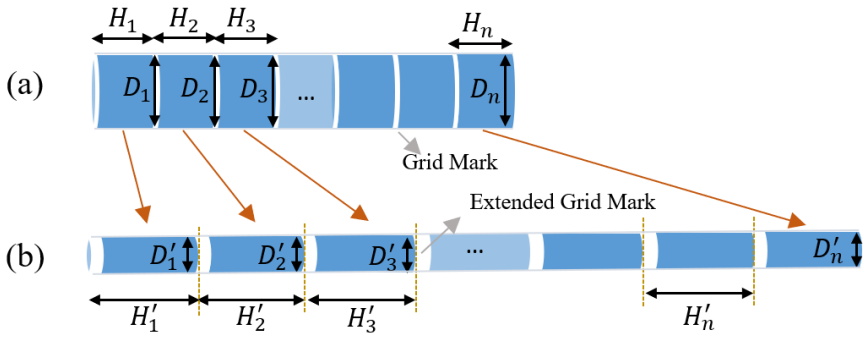

Figure 3-11 Schematic of measurements before die-drawing (a) and after die-drawing (b).

In this section, various deformation ratios are defined and discussed to depict the deformation extent of the die-drawn sample. The nominal deformation ratio, R_N is the ratio of initial cross-section area over that of the die exit, which equals the square ratio of initial diameter (D_o) to the diameter of the die exit (D_e). D_f is the diameter of the die-drawn product. Accordingly, the actual area deformation ratio, R_D is the ratio of initial cross-section area over that of the die-

drawn products, and R_H is the ratio of die-drawn sample height to that of unprocessed sample. R_{Ave} is the average of R_D and R_H. The four deformation ratios R_N, R_D, R_H and R_{Ave} are expressed in Eq. (3.24) to Eq. (3.27) respectively and the calculated values will be presented in 3.5.1.2.

$$R_N = \left(\frac{D_o}{D_e}\right)^2 \tag{3.24}$$

$$R_D = \left(\frac{D_o}{D_f}\right)^2 \tag{3.25}$$

$$R_H = \frac{H_f}{H_0} \tag{3.26}$$

$$R_{Ave} = \frac{1}{2}\,(R_D + R_H) \tag{3.27}$$

Note that $R_D = R_H$ implies that the volume remains constant before and after the process, while $R_D < R_H$ ($R_D > R_H$) indicates a volume increase (decrease) after processing.

3.4.1.3 Drawing rate (v_d) & strain rate ($\dot{\varepsilon}$)

The isotropic samples were drawn through the 5°Die at the same temperature with various drawing rates (v_d = 0.3 ~ 4 mm/s) to examine the effect of drawing rates on the die-drawing process. Trials showed that v_d > 6mm/s would cause difficult control of the drawing system and largely increase the chance of sample breaking. For #9.5, v_d = 0.3, 0.5, 2, 3, 4 mm/s (T=145°C); for #10, v_d = 0.3, 0.5,1 mm/s (T=145°C); for #11, v_d = 1, 2, 3, 4 mm/s (T=160°C).

Definition of drawing rate v_d and strain rate $\dot{\varepsilon}$

Within this study, drawing rate (v_d) is the displacement rate of the crosshead/die. Its value was set through the Rubicon system, v_d = 0.1~4 mm/s.

Figure 3-12 demonstrates the relationship of S, S_r L_0, L and ΔL (S is the crosshead or die displacement, S_r is the relative movement of the 'bulb' end to the die; L_0 is the original length of the sample; L is the length of the die-drawn sample; $\Delta L = L - L_0 = S - S_r$ is the actual elongation of the sample). Therefore, v_d can be expressed as the displacement of the crosshead over the drawing time t, as shown in Eq.(3.28).

$$v_d = \frac{dS}{dt} = \frac{d(\Delta L + S_r)}{dt} \tag{3.28}$$

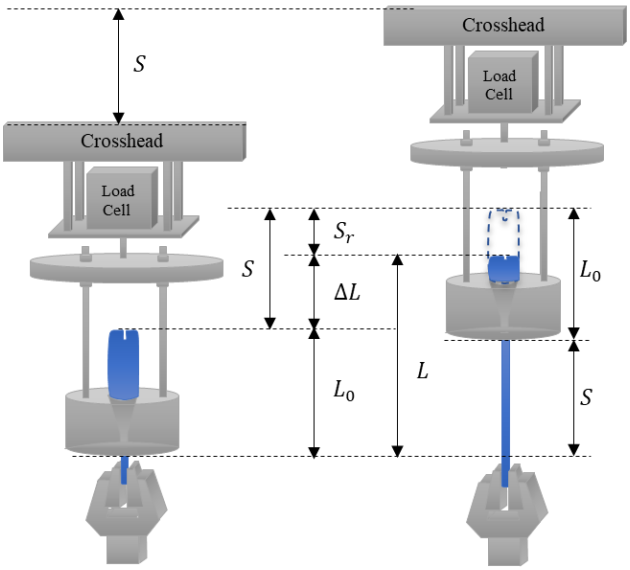

Figure 3-12 Relations between die movement and sample elongation.

ε is the engineering strain of the material, $\varepsilon = \frac{\Delta L}{L_0}$. Strain rate ($\dot{\varepsilon}$) is the change in material strain relative to time. As the sample in the die was merely gripped at the 'handle' end while the 'bulb' end was free, $\dot{\varepsilon}$ was related to S_r and was different from the v_d. As a result, the relation between v_d and $\dot{\varepsilon}$ is expressed by Eq. 3.29.

$$\dot{\varepsilon} = \frac{d\varepsilon}{dt} = \frac{d\frac{\Delta L}{L_0}}{dt} = \frac{d(S - S_r)}{dt \cdot L_0} = \frac{v_d}{L_0} - \frac{dS_r}{dt \cdot L_0} \tag{3.29}$$

If, during the whole process, the crosshead has moved an overall distance of S' over time t' with a constant speed v_d to pull the sample just outside the die ($S_r = L_0$), the average strain rate ($\bar{\dot{\varepsilon}}$) of such a process would be:

$$\bar{\dot{\varepsilon}} = \frac{\int_0^{\varepsilon} d\varepsilon}{\int_0^{t} dt} = \frac{\int_0^{\frac{S'-L_0}{L_0}} d\frac{\Delta L}{L_0}}{t'} = \frac{S' - L_0}{L_0.t'} = \frac{v_d}{L_0} - \frac{1}{t'} \tag{3.30}$$

Therefore, $\bar{\dot{\varepsilon}}$ were calculated through v_d, L_0 and t' and will be discussed in 3.5.1.3.

3.4.1.4 Processing temperature (*T*)

As previously mentioned in 3.3.2.2, T_g of isotropic poly(VP-MMA) determined by DSC was 163.1°C. According to these results, the experiment was designed to draw #9.5 sample through a 5°Die with v_d = 4mm/s at 145°C, 160°C and 180°C, respectively, to study the influence of temperature on the die drawing process.

3.4.1.5 Stress-strain curve for die-drawing

Axial stress is an essential mechanical characterization of materials in the process of die drawing. It reflects the principal stress of materials in the drawing direction under specific tensile conditions. The drawing force was recorded by the load cell for each trial and converted to the drawing stress defined in the subsection. The maximum drawing stress (σ_{max}) reflects the engineering stress when the highest drawing load occurred, while the average drawing stress (σ_{ave}) was calculated via the average force during the steady drawing state. In the experiment, σ_{max} corresponded to the maximum stress recorded in the whole die-drawing process for a sample, while σ_{ave} was the average force between the bulb entering the die and the end of the bulb leaving the die. An example will be given in Figure 3-19. The relations between σ_{max} (or σ_{ave}) and α, R_{Ave}, v_d, $(\bar{\varepsilon}), T$ are provided in section 3.5.1 to discuss the effect of parameters on the die-drawing process.

Definition of drawing stress

Stress is the force exerted per unit area of material, and strain reflects the deformation extent of the material. Engineering stress (σ, or nominal stress) is the load (F) divided by the cross-sectional area of the original unprocessed sample (A_0). True stress (σ_t) is the load (F) divided by the area of the instant cross-section (A) at which the load is applied. Engineering strain (ε, or nominal strain) is the change of materials per unit length which is the quotient of elongation (ΔL) over the original length of the sample (L_0). True strain is the (ε_t) is the natural logarithm of the ratio of the real-time length (L) over the original length (L_0). σ, σ_t, ε and ε_t are

expressed in Eq. (3.31) to (3.34), respectively.

$$\sigma = \frac{F}{A_0} \tag{3.31}$$

$$\sigma_t = \frac{F}{A} \tag{3.32}$$

$$\varepsilon = \frac{\Delta L}{L_0} \tag{3.33}$$

$$\varepsilon_t = \ln(1+\varepsilon) = \ln\frac{\Delta L + L_0}{L_0} \tag{3.34}$$

In this research, σ equalled the drawing force divided by the original 'bulb' cross-sectional area and ε was approximated as the crosshead displacement divided by the original length of the sample. Note that the actual engineering strain was less than the value calculated from the crosshead displacement because the sample had one free 'bulb' end that constantly migrated in the die with the die-drawing progression.

3.4.2 Characterisation of Die-drawn Samples

Previous studies showed that the die-drawn polymers had increased orientation compared to their unprocessed counterpart [109, 131, 135]. The structural alignment changed the molecular interaction, which further led to the alteration of the thermal and optical properties of the material.

In order to investigate the influence of die-drawing on poly(VP-MMA) and the properties of

the die-drawn products, the original isotropic poly(VP-MMA) (#Iso) and the die-drawn samples (#Die-drawn) were analysed by differential scanning calorimetry (DSC), X-ray diffraction (XRD) and the optical microscope (OM).

3.4.2.1 DSC

Differential scanning calorimetry (DSC) is one common thermal analysis technique that can detect the specialized thermal transition for the polymer. In DSC analysis, the sample and the reference material are placed in separate calorimeters/sample furnaces. The difference of energy required to equal the temperatures between the sample and reference material is measured as a function of temperature.

The heat flow - temperature curve obtained by DSC could reflected T_g of poly(VP-MMA). The difference in T_g between #Iso and #Die-drawn could be substantial evidence of polymer structure alteration. The DSC equipment used was Perkin Elmer PYRIS Diamond Differential Scanning Calorimeter. Both #Iso and #die-drawn (#11) DSC samples were prepared as tiny chips. In the analysis, ~2 mg sample was placed in the sample chamber, which was heated up in a nitrogen atmosphere at a scanning rate of 50°C/min. The heat flow - temperature curves measured by the calorimeter were plotted in Figure 3-28 in 3.5.2.1.

3.4.2.2 XRD

X-ray diffraction (XRD), could measure the orientation quantitatively by utilising parameters resulting from the interaction between electromagnetic radiation and the molecular system

[170]. XRD is a technique to investigate the crystal structure of a material. The Bragg's Law ($2d \sin\theta = n\lambda$, where d is the distance between diffracting planes, θ is the incident angle of the beam, n is any integral number, and λ is the wavelength of the beam) indicates that the cleavage faces of crystals appear to reflect X-ray beams at certain angles (θ). Hence if the rotating the crystal material against a steady X-ray beam, the detector positioned at 2θ can receive the reflected X-ray. Such characteristic angles exhibit the crystallinity of the material.

The original poly(VP-MMA) was isotropic and amorphous [40]. XRD could be applied to determine whether the die-drawing process would alter the material structure and induce any crystallinity. In this study, the XRD analysis of #Iso and #Die-drawn (#11 and #13) was carried out on Malvern PANalytical Empyrean X-ray diffraction system with a Cu-Kα radiation, 45kV voltage and 50mA current at room temperature in the 2Θ range from 5° to 70°.

3.4.2.3 Optical microscope

OM technique uses a set of convex lenses to form a magnified virtual image. The optical microscope, Zeiss Axioskop 2 MAT, fitted with Axiocam digital colour camera, was used to examine the morphologies of the lateral side and cross-section of #Iso and #Die-drawn (#11, #12 and #13) with 20× and 100× magnification.

3.5 Results of Die-drawing Experiments

In this section, the first half will discuss the effects of die-angle (α), deformation ratio (R_H.

R_N, R_D, R_H and R_{Ave}), drawing rate (v_d)/strain rate ($\bar{\dot{\varepsilon}}$), and temperature (T) on the die-drawing process, while the second half will demonstrate the characterisation results of the die-drawn poly(VP-MMA).

3.5.1 Influence of Die-drawing Parameters

The photo of the die-drawn #9.5 sample is shown in Figure 3-13. The die-drawn sample can be divided into four zones: a 'bulb' tail, the die-drawn 'bulb', 'conical frustum', and the partially drawn 'handle'. Die-angle, deformation ratio, temperature, drawing rate and drawing protocols all played essential roles in the die-drawing process. The details of how they had affected the die-drawing process and results will be discussed in this section.

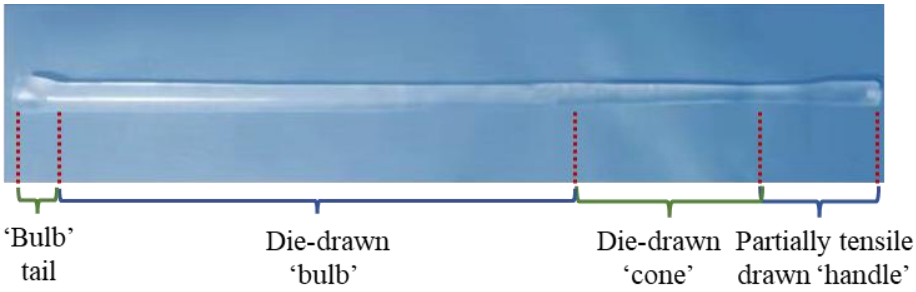

Figure 3-13 The image of a typical die-drawn sample (#9.5)[32].

3.5.1.1 Die angle (α)

The maximum and average drawing loads of the #11 with different v_d are shown in . The

[32] The image combined two separate photos of one #9.5 sample to avoid the distortion of perspective effect. The original photos are given in Figure 6-11 in Appendix III.

10°Die increased the maximum and average drawing force significantly by 79% and 57%, respectively, compared to the 5°Die (considering the average force for all v_d).

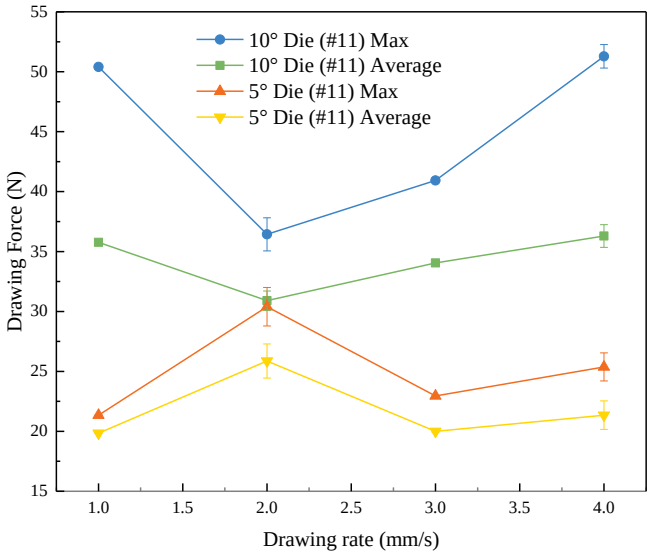

Figure 3-14 The drawing force of #11 die-drawn from 10°Die/5°Die using various drawing rates (T = 160°C).

In addition, the maximum diameter of rods that could be drawn through a 10°Die was around 12mm. However, laminar cracks occurred to this sample during swelling, indicating the drawing force had damaged the sample's internal structure (presented in Figure 4-11).

For the 5°Die, the largest sample that could be pulled out of the die was #13 (⌀13.0), and the die-drawn sample survived the swelling tests. It seemed that the 5°Die significantly reduced the overall work required to elongate per unit length of #11, which meant the redundant work and the work to overcome friction were lower than that in a 10°Die.

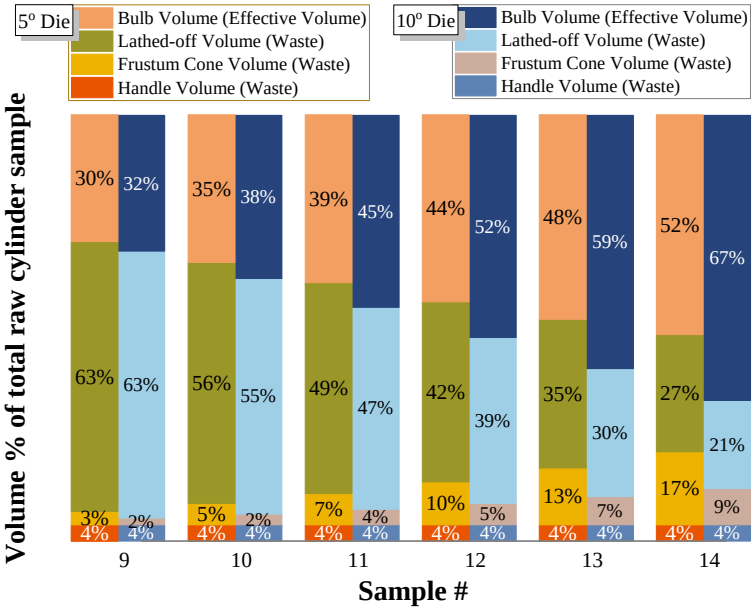

Figure 3-15 Effective and waste volume percentage of samples lathed for 5°Die and 10°Die.

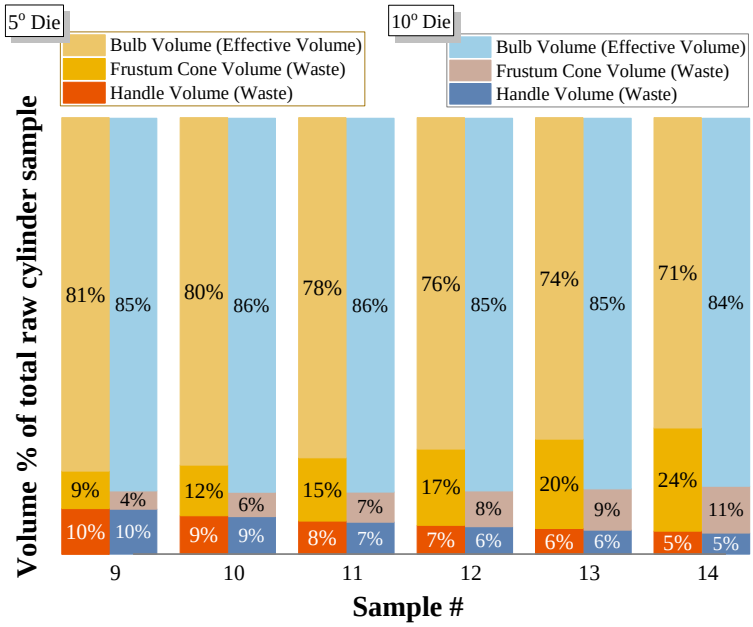

Figure 3-16 Effective and waste volume percentage of samples for the 5°Die and 10°Die if directly synthesised in a torch-shape mould.

Figure 3-15 presents the ratio of effective and wastage material volume in terms of the total volume. The material wastage of a 10°Die sample was less than a 5°Die sample, and the difference increased with the sample diameter.

It is theoretically possible to directly polymerise poly(VP-MMA) in a torch shaped mould to eliminate the necessity of lathing. By doing so, the effective percentage of a whole sample will increase for both dies, as shown in Figure 3-16. Due to the angle size, the frustum volume of a 5°Die sample would always be about twice that of a corresponding 10°Die sample, as the volume ratio equals $\frac{\tan 10°}{\tan 5°}$ = 2.015.

Although the 5°Die required more material waste than the 10°Die, it had advantages such as increased maximum drawing ratios, reduced overall work, and lower failure rates. Further with the practical experiences, the author suggested that 5°Die was more favourable than the 10°Die in the die-drawing process, and the following discussion will be focused on the 5°Die.

3.5.1.2 Deformation ratio (R)

The dimensions of the sample before and after die-drawing are given in **Error! Not a valid bookmark self-reference.**. The corresponding R_N, R_D, R_H and R_{Ave} were calculated and plotted in Figure 3-17. The plot of σ_{max} vs R_{Ave} and σ_{ave} vs R_{Ave} are provided in Figure 3-18. n is the number of samples on which the average value is based.

It shows that both R_D and R_H were larger than R_N as the actual die-drawn diameter D_f was always smaller than the I.D of die exit D_e (Ø7mm). Compared to the die-drawing of

thermoplastic materials, for which the actual deformation ratio could be 150% to 500% of R_N [123, 126], the R_D (or R_H) in this study only had a relatively small variance from R_N (maximum difference was 8% of R_N).

Table 3-4 Sample size before and after die-drawing (drawing rate 4mm/s, T=160 ℃).

Sample No.	Before Drawing (mm)		After Drawing (mm)	
	$D_0(\pm 0.2)$	$H_0(\pm 0.2)$	D_f	H_f
#9	9.0	5.0	6.91±0.26	8.79±0.78
#9.5	9.5	5.0	6.76±0.21	10.12±0.49
#10	10.0	5.0	6.59±0.29	11.56±1.09
#11	11.0	5.0	6.82±0.11	14.47±1.65
#12	12.0	5.0	6.58±0.12	15.99±1.47
#13	13.0	5.0	6.69±0.19	18.05±1.22

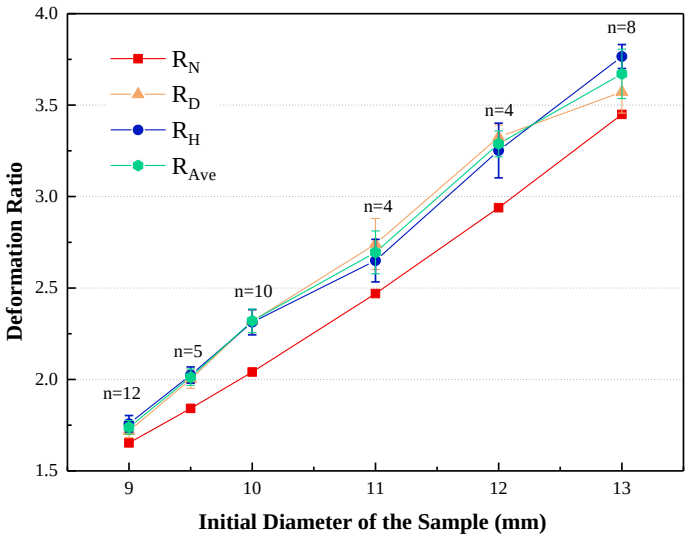

Figure 3-17 The actual and nominal deformation ratios (5°Die, v_d=4mm/s, T=160°C).

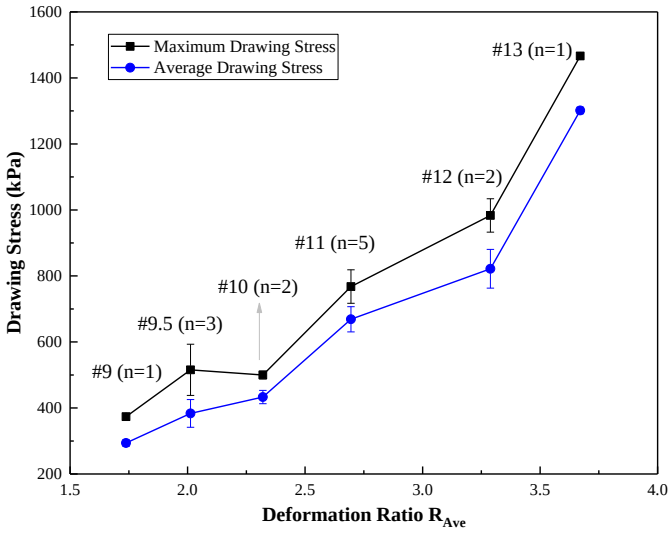

Figure 3-18 Relations between drawing stress and R_{Ave} (5°Die, v_d=4mm/s, T=160°C).

This was possibly due to the regular pausing applied at relatively high drawing velocity, which had frozen out the sample to prevent further deformation. Moreover, the difference between the $R_D/R_H/R_{Ave}$ and R_N increased with the deformation ratios as more severe free necking occurred under higher drawing stress.

R_H was prominently larger than R_D (i.e., $H_f D_f^2 > H_0 D_0^2$) when v_d > 3.5, representing a volume increase after the die-drawing process. This might be because of the extra voids introduced by stretching. The voids were observed through the optical microscope and will be further discussed (3.5.2.3). The average of R_D and R_H (R_{Ave}) will be used to represent the actual drawing ratio for each case in the following discussion.

In addition, both σ_{max} and σ_{ave} generally increased with the R_{Ave}. This was consistent with findings in the die-drawing of many thermoplastic polymers such as PE, PP, POM, PET [122, 129, 133, 136], as discussed in the section 1.3.4.3. A larger R_{Ave} was equivalent to a larger

initial diameter in the current experimental set-up, which meant more material would be squeezed through the die.

3.5.1.3 Drawing rate (v_d) & strain rate ($\dot{\varepsilon}$)

As the poly(VP-MMA) does not have a strain-hardening effect, sufficient cooling was important to initiate the hardening of material to stabilize the die-drawing process. The preliminary test showed that continuous die-drawing at high v_d led to the sample breaking caused by the localized catastrophic necking after the die exit. Periodic pauses were therefore introduced into the process to give the sample extra cooling time. In this case, the sample was successfully pulled at relatively higher v_d. Interestingly, after further exploring, the author found that the process could be exempt from regular pauses at sufficiently low v_d. In this section, the intermittent die-drawing and continuous die-drawing are introduced prior to the discussion of the effects of v_d on the die-drawing process.

Discussion on the drawing modes: intermittent (IMD) and continuous (CND) die drawing

The intermittent die-drawing (IMD) referred to the die-drawing process with occasional pauses. The continuous die-drawing (CND) was a smooth process without pauses. The trials showed that IMD was essential for a higher range of $v_d \approx$ 2mm/s ~ 6mm/s, to allow a sample to cool adequately, while CND drawing was feasible at lower v_d ($\leq$ 0.5 mm/s), and when the $R_{Ave} \leq 2.25$. The typical crosshead displacement vs time curves of IMD and CND are

presented in Figure 3-19.

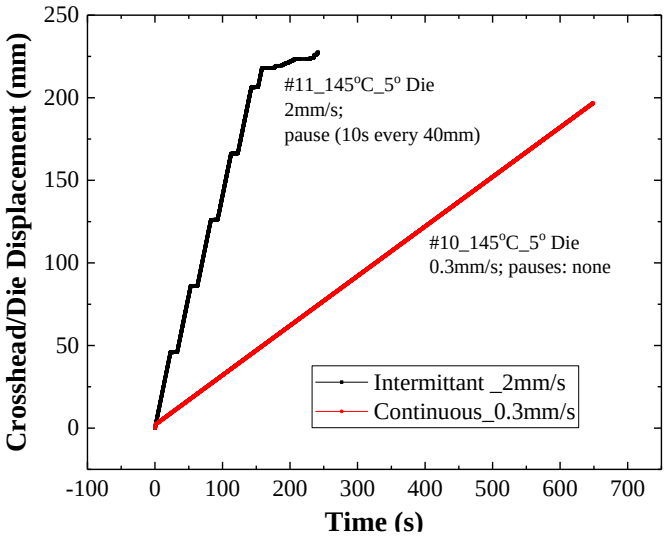

Figure 3-19 Two drawing modes for the die-drawing of poly(VP-MMA).

The slope of the curve represents the v_d. For the IMD, the short plateaus represent the pauses, which was 10s for the current case. The displacement between each pause was generally between 40~60mm. The required pausing was also the nominal deformation ratio (R_N) and temperature (T). One empirical function was generated to provide a rough suggestion of pausing time (t_{pause}) for the die-drawing under different processing parameters:

$$t_{pause} = 0.6\sqrt{v_d}(T - 140) \cdot R_N \tag{3.35}$$

Note that the unit of t_{pause} is second and Celsius value should be used for T in this equation, and this equation is suitable for a similar scale of poly(VP-MMA) die-drawing. The required pausing time extended with the increase of R_N, v_d and T.

When the drawing rate was adequately low, the drawing process could be regarded as a

combination of infinite pauses. Hence, the material had enough time to achieve the elongation and relaxation simultaneously, and the part exiting the die will also have ample cooling time to fix the deformation.

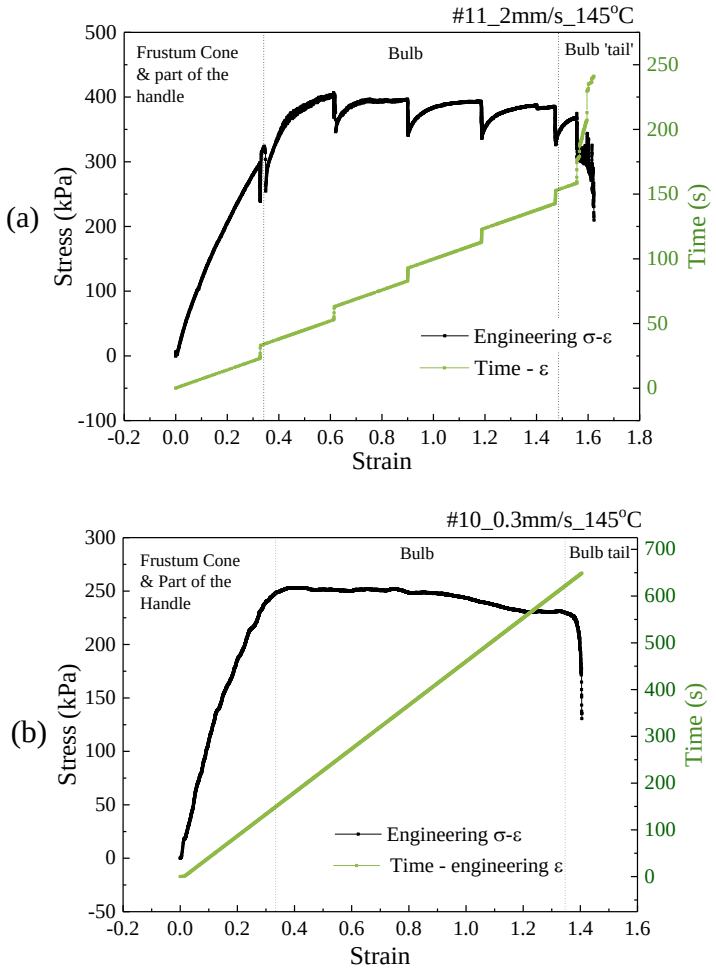

Figure 3-20 The engineering stress-strain & time-strain plots of (a) IMD and (b) CND.[33]

[33] For both IMD and CND modes, the maximum stress σ_{max} was the peak stress in the curve; and the average stress σ_{ave} was the average of stress data points in the "bulb" and the "bulb end" (excluding the last rapid stress drop) regions.

The typical stress-strain curves (σ-ε) of IMD and CND are given in Figure 3-20 (a) and (b), respectively. The corresponding drawing stages of different die-drawn parts (Figure 3-13) are marked with dotted lines in Figure 3-20. The die-drawing of 'conical frustum' and partial 'handle' corresponds to the curve before the first pause/stress drop for IMD in Figure 3-20 (a) and the slope before the plateau for CND in Figure 3-20 (b). The die-drawing of 'bulb' corresponds to the IMD middle fluctuant curve and the CND plateau. The die-drawing of the 'bulb tail' corresponds to the final incomplete stress wave for IMD and the final stress declining part on the CND curve.

For the IMD process, Figure 3-20 (a) shows multiple time-dependent decreases in the stress under a constant strain, and each decrease corresponds to one pause. The stress decaying phenomenon, which reflects a molecular chain relaxation inside the matrix due to stress dissipation, is a characteristic behaviour of the viscoelastic polymer, reflecting the decreasing tendency of the polymer to recover its original shape upon the removal of the stress [171].

During the die-drawing of the 'bulb', the stress rose initially and then gradually flattened out for each crosshead active period of IMD and the whole CND process. This was very similar to the 'steady-state' reported by Gibson and Ward in their early work on the die-drawing of PE and PP [126].

It should be noted that the plateaus in both IMD and CND declined slightly with the progression of the process. This could be possibly due to several reasons: (1) as the die-drawing went on, the material left in the die gradually decreased, hence the required force to

overcome the gravity of the material reduced; (2) the temperature of the material might have raised due to: more heat was transferred from the sample surface to the core (considering the initial heating was not thorough)/ or more heat transferred to unit volume of sample from the heating system (considering the constant work rate of the heating module and constant heat dissipation for the open system)/ or the mechanical work-induced accumulation of heat; (3) when approaching the end of the die-drawing, the free 'bulb' end entered the converging die, the overall contact area between the die and the sample started to decrease, leading to reduced friction force and therefore the axial load required was also reduced. The die-drawing of #9.5 did not see an apparent decline in the drawing stress over time, further supporting the above assumptions. Due to a smaller 'bulb' diameter, the gravity influence was more negligible; uniform temperature distribution might be reached at an earlier stage; the reduced compression from the die also lessened the friction.

Strain rate ($\bar{\dot{\varepsilon}}$) calculation

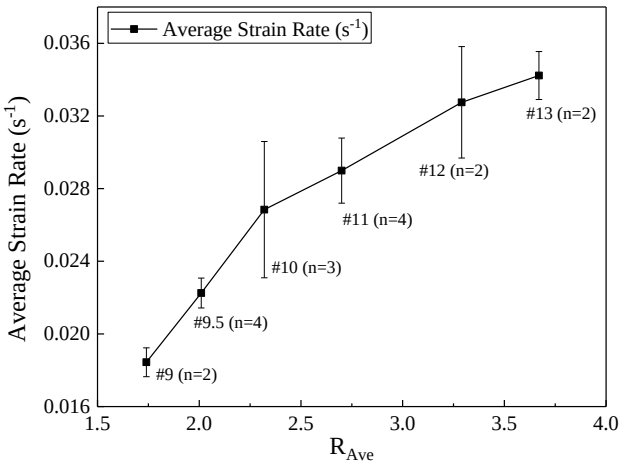

Figure 3-21 Average strain rates of samples with different deformation ratios (5°Die &

v_d=4mm/s, T=160°C)[34].

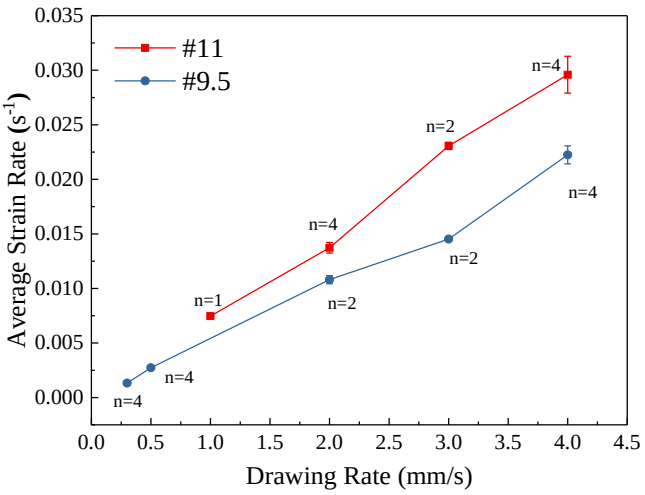

Figure 3-22 $\bar{\dot{\varepsilon}}$ of samples #11 and #9.5 with different v_d (5°Die).

With the experimental data, the $\bar{\dot{\varepsilon}}$ for each case were obtained through Eq. (3.30) on p116. The strain rates of samples with R_{Ave} are plotted in Figure 3-21. $\bar{\dot{\varepsilon}}$ for #9.5 and #11 with different v_d are shown in Figure 3-22. The $\bar{\dot{\varepsilon}}$ increased with deformation ratios and drawing rates.

The influence of v_d and $\bar{\dot{\varepsilon}}$

Previously showed the v_d in relation to the average drawing force for sample #11 with 5°Die and 10°Die. Similar to , the plots of $\sigma_{max}/\sigma_{ave}$ vs v_d of #9.5 and #10 in Figure 3-23. Reports showed various results of uniaxial load - v_d relations as previously discussed in section 1.3.4.4. Gibson and Coates showed the die-drawing of PE and PP was not v_d-sensitive [123, 126]. Hope et al. showed the axial load of POM die-drawing increased at relatively low v_d and

[34] For #9 and #13, samples that were not successfully drawn out of die but achieved partial drawing have also been taken into consideration.

gradually flattened out or even declined at higher v_d range [133]. Richard et al. showed the load of die-drawing PVF could first decrease and then increase with v_d when R_N=6, while for R_N=2 or 4, the load remained constant at a lower v_d but experienced an upturn when v_d exceeded 1.3 mm/s [137]. Therefore, σ-v_d relation seems to be determined by the properties of the material itself, and for the same material, different deformation ratios could show various σ-v_d relations.

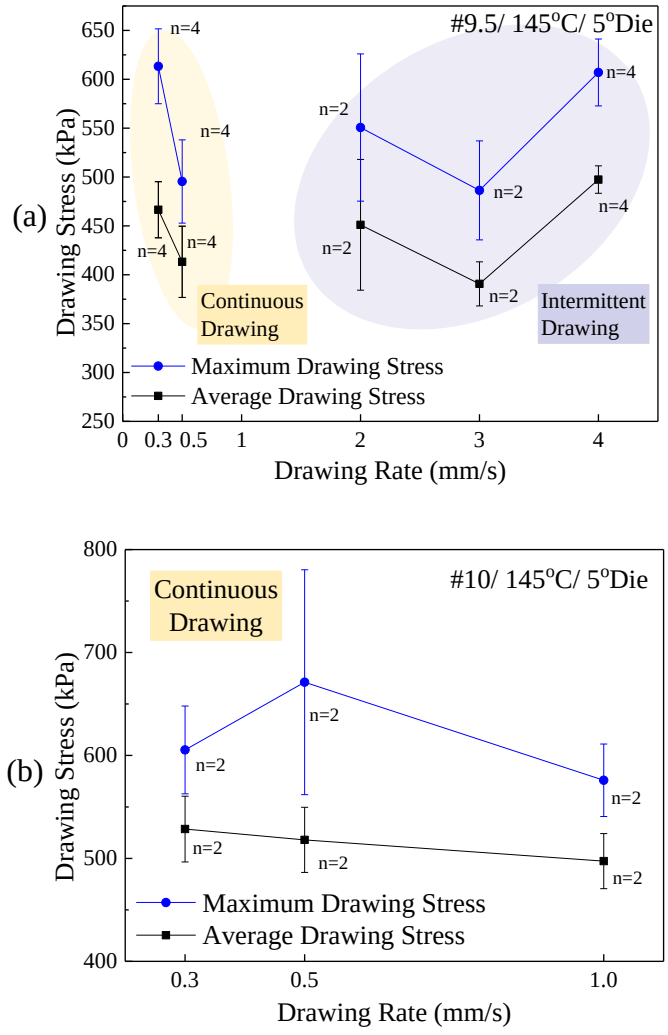

Figure 3-23 Stress-drawing rate plots of (a) #9.5 (b) #10.

Both Figure 3-23 (a) and (b) showed the σ_{ave} decrease with the v_d at the low range (v_d<1 mm/s) for the CND. Previously, showed that at higher range of drawing rates ($v_d \geqslant 1$ mm/s), in which the IND was applied, #11 showed a minimum σ at v_d = 2 mm/s for the 10°Die and maximum σ at the same v_d for the 5°Die. For #9.5, minimum σ appeared at v_d = 3mm/s for the 5°Die. It should be noted that varied pauses in the IND might influence the results. More data needs to be collected to draw a further conclusion for poly(VP-MMA).

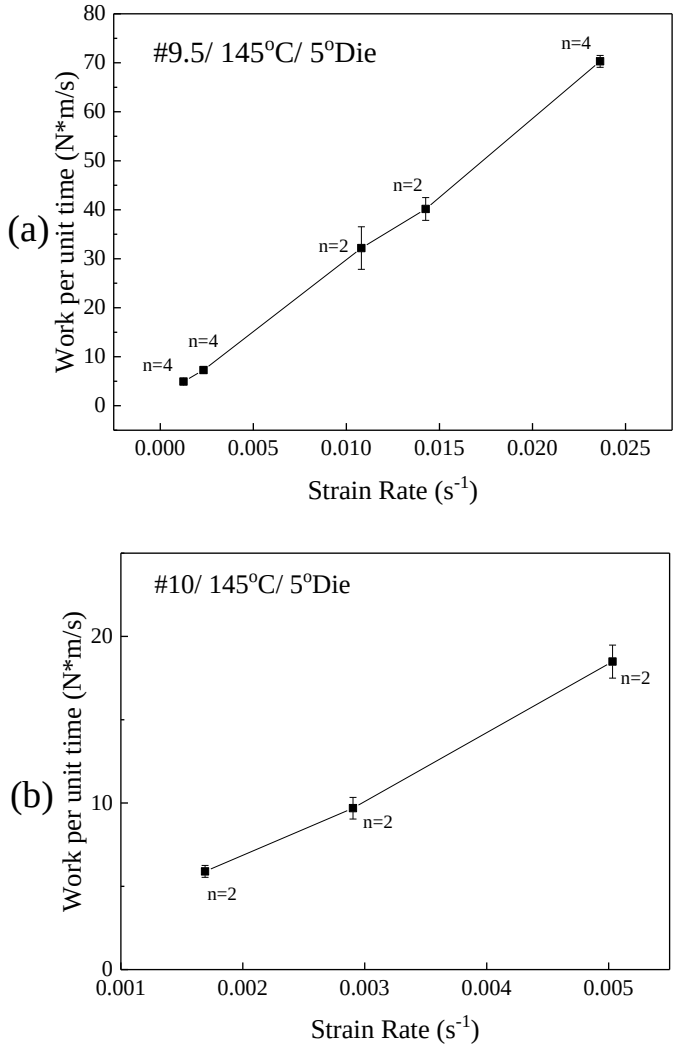

Figure 3-24 Work (per unit time)-strain rate plots of (a) #9.5 (b) #10.

According to Figure 3-22, an increased v_d represents an increased $\bar{\dot{\varepsilon}}$, meaning more material deformation per unit time, which should require a higher rate of work. The average rate of work in each case was calculated using the average force times the corresponding v_d and showed in Figure 3-24. It reveals a monotonical relationship with the strain rate for both #9.5 and #10.

3.5.1.4 Processing temperature

As shown in Figure 3-25, raising the temperature has significantly reduced the axial drawing stress of #9.5. The flexibility of polymer chains increases with temperature, therefore prominently reducing the force required to stretch the material.

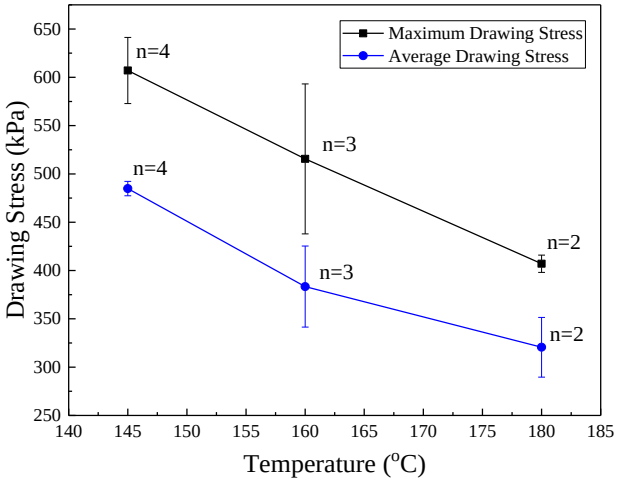

Figure 3-25 The temperature - drawing stress relations (IMD/#9.5/5°Die/v_d=4 mm/s).

The average drawing ratio of different cases are shown in Figure 3-26 (a). It was found that the samples drawn at higher temperature tends to have a larger drawing ratio than at a lower temperature. The standard error was observably more significant in the 180°C than those in

the 145°C and 160°C. Moreover, samples drawn at 180°C had higher opacity than those drawn at a lower temperature, possibly due to the expanding of the trapped gas after heating (Figure 3-27).

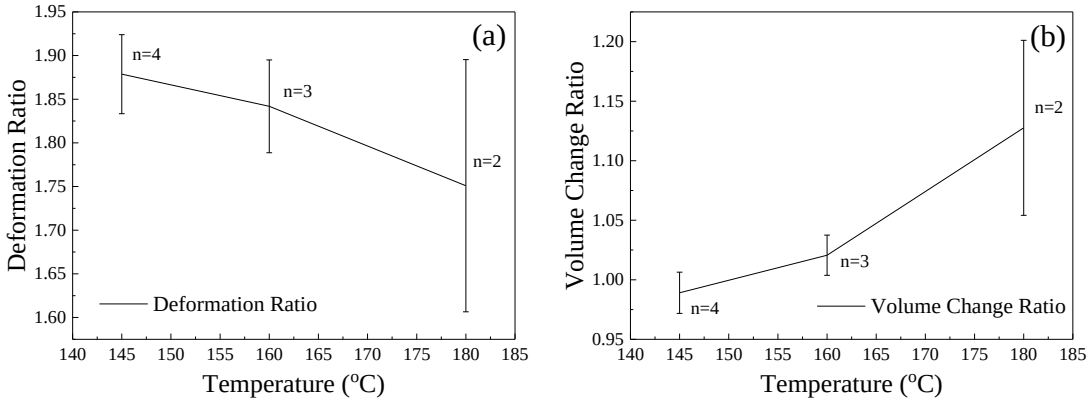

Figure 3-26 The (a) actual drawing ratios (b) volume ratios of #9.5 die-drawn at various temperatures.

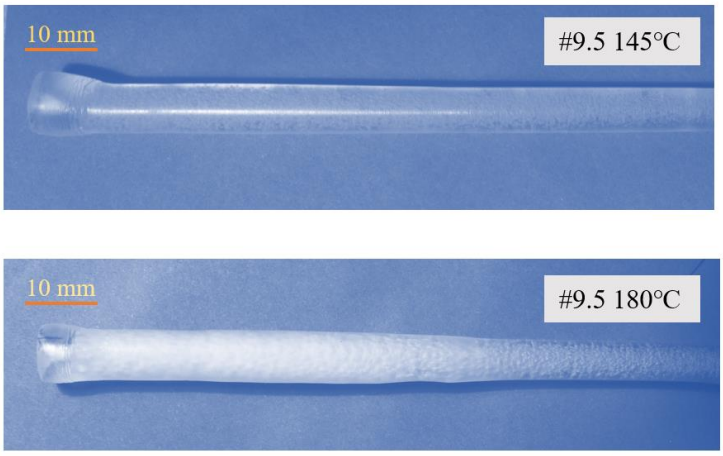

Figure 3-27 Photos of two die-drawn samples.

The volume change of the sample before and after drawing was hence studied. Figure 3-26 (b) shows that 180°C samples had a non-negligible volume increase, which confirmed the

possibility of heat-induced bubble generation. The initiator AIBN was a possible source of bubbles as the radical initiation process involved nitrogen releasing. The high temperature might have initiated the reaction of residual AIBN.

3.5.2 Characterisation Result of Die-Drawn Poly(VP-MMA)

In this section, DSC, XRD and OM results are provided. The differences in characterization between the #Die-drawn and #Iso samples will be discussed.

3.5.2.1 DSC result

DSC analysis was performed on the #Iso and #Die-drawn poly(VP-MMA) samples. The heat flow – temperature data are plotted in Figure 3-28 (a). The 1st order derivative of the heat flow curve is given in Figure 3-28 (b) and its maxima peak of the plot represents the glass transition temperature (T_g) of the sample [172].

As displayed on the graph, T_g of #Iso and #11 are approximately 163.1℃ and 168.8℃. As the T_g is inversely proportional to the flexibility of the chains and directly proportional to the intermolecular force, the increased T_g of die-drawn sample indicated a reduced flexibility of the polymeric chains and increased intermolecular force resulting from the die-drawing process. Therefore, the DSC result showed that the die-drawing process increased the polymeric order of the poly(VP-MMA) possibly by aligning the polymeric chains in the die-drawing directions.

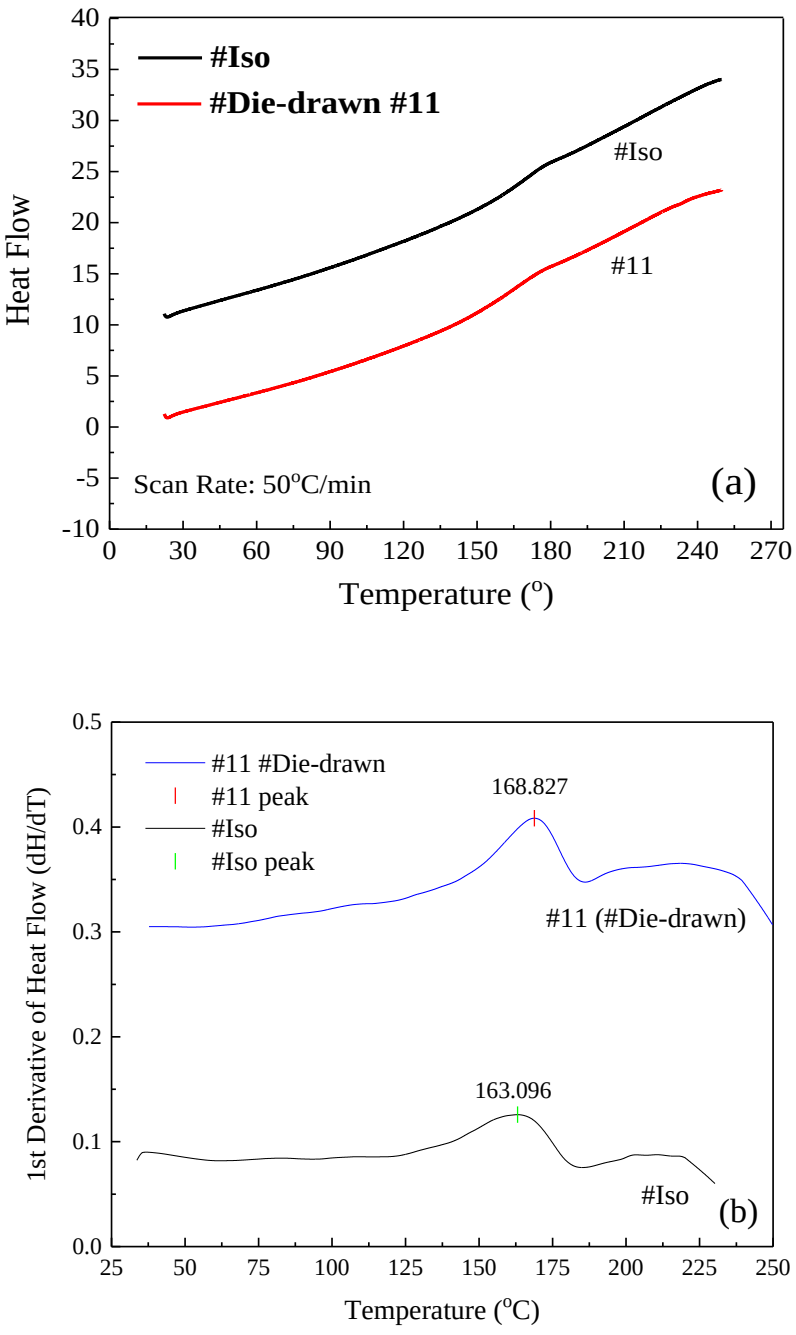

Figure 3-28 (a) The DSC profile of #Iso and #Die-drawn poly(VP-MMA) samples; (b) 1st order derivative of heat flow (dH/dT) – both smoothed with Lowess function.

3.5.2.2 XRD result

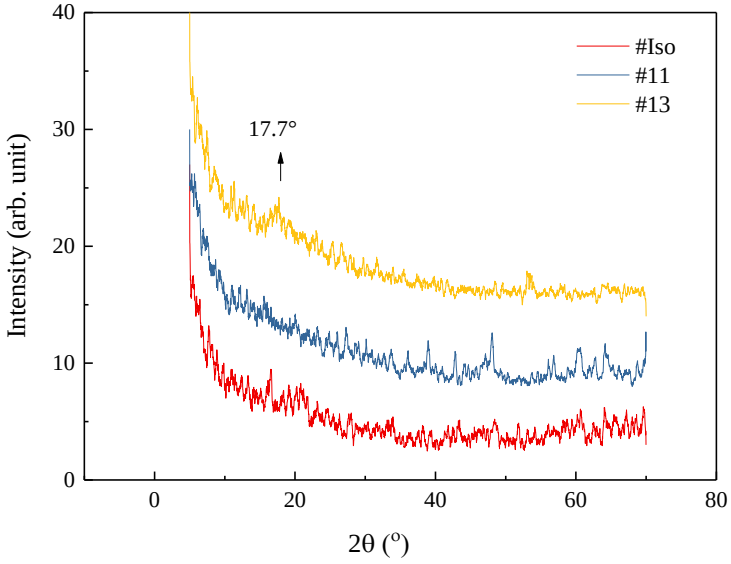

Figure 3-29 XRD of #Iso and #Die-drawn (#11 and #13).

Previous studies confirmed the amorphous nature of pure PMMA, pure PVP, PMMA/PVP blends and poly(VP-MMA) copolymer. There are slight variations between differnet work, but in general, broad diffraction peak was found at 20° ~ 25° for PVP [173-175] and PMMA tends to show most intense halo peaks at 2θ values of 10° ~ 30° [176, 177]. In addition, Devikala compared the PMMA/PVP blends with different compositions and found that increased PVP content will decrease the peak intensity and the increase in the bandwidth with the increase of PVP concentration [178].

Figure 3-29 shows the XRD results of isotropic and die-drawn poly(VP-MMA) samples. #Iso and #Die-drawn poly(VP-MMA) showed a broad diffraction band under 2Θ ~ 30°, reflecting its amorphous nature. The high VP content (90%) in the poly(VP-MMA) #Iso and #Die-drawn

may have led to increased bandwidth and the disappearance of identifiable peaks, which was inconsistent with the findings of Devikala [178]. #13 did present a weak broad peak at 2Θ~17°, which may indicate a subtle increase of crystallinity compared to #Iso and #11. However, as the differences between the #Iso, #11 and #13 were subtle and the background noise was significant, no certain conclusion can be generated from the current XRD result.

3.5.2.3 Optical microscope photos

Compared to the isotropic sample, #11, #12, #13 all have parallelly aligned patterns on the lateral walls, as presented in the 20× magnified Figure 3-30 and 100× magnified Figure 3-31.

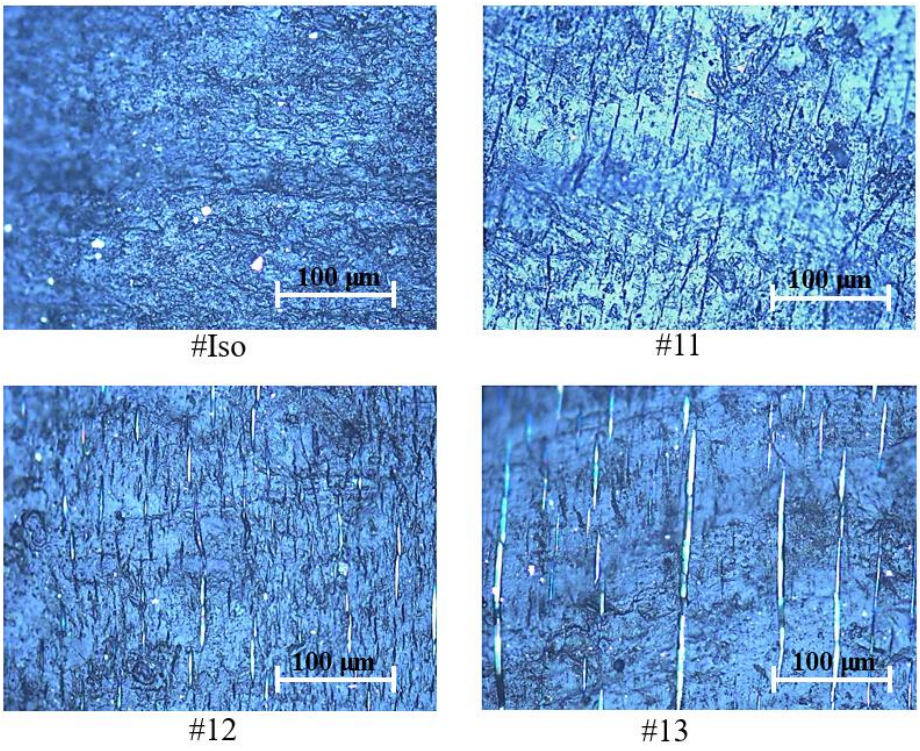

Figure 3-30 Optical microscope images of sample lateral sides (20× magnification); the vertical direction is the die-drawing direction of #Die-drawn (#11, #12, #13).

The width, length and area of the strip-shaped pattern vary from the samples with different deformation ratios. In literature, the voids induced by die-drawing are very common. Hope et al. reported the ladder-like voids on the SEM micrographs of die-drawn POM [133]. The patterns in the present work are very similar to the voids found on the SEM images of both the die-drawn and extruded POM samples by Mohanraj et al. [135] and thus were possibly the voids induced during the die drawing process.

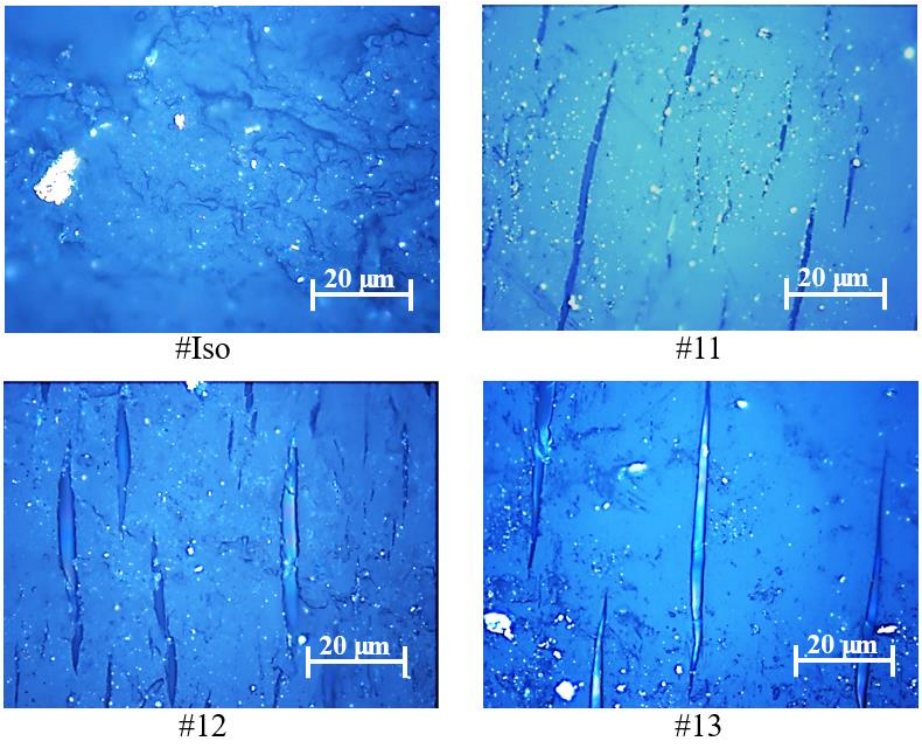

Figure 3-31 Optical microscope images of sample lateral sides (100× magnification); for the #Die-drawn (#11, #12, #13), the vertical direction is the die-drawing direction.

It was reported that the voids aspect ratio increases linearly with the actual deformation ratio, and the value is greater in a die-drawn sample than its extrudate counterpart, possibly because of the tensile nature of the stress in the die-drawing process [135]. However, the drawing ratio

in the present work was comparatively low (<~4) compared to the drawing ratio mentioned in the literature (<~9); therefore, the presence of the voids was not prominent.

In addition, we can observe from Figure 3-31 that some relatively large voids of #12 and #13 samples demonstrate light pattern inside the voids. Such phenomenon uniquely observed by the OM could be a result of light diffraction and interference from the voids or a reflection of the residual stress of material around the voids. The isochromatic lines were vaguely seen to be vertical to the die-drawing directions, indicating the direction of the residual stress was paralleled with the die-drawing directions.

ImageJ was used to calculate the total area, average length and width of these voids for each case and the result were shown in Figure 3-32. As presented in Figure 3-32 (a) and (b), the total area of voids and voids aspect ratio increase linearly with the R_{Ave}, which showed a similar trend as that of die-drawn POM by Mohanraj et al. [135]. Interestingly, Figure 3-32 (c) shows that the total voids number decreases linearly with the R_{Ave}. Combining the result of the average area per void in Figure 3-32 (d), it indicates the growth of voids might have been realized by the merging of neighbouring smaller voids. Both the length and width of voids, as shown in Figure 3-32 (e) and (f), seem to be positively related with R_{Ave}, despite the length increase of #12 sample (R_{Ave} = 3.29) was not very significant.

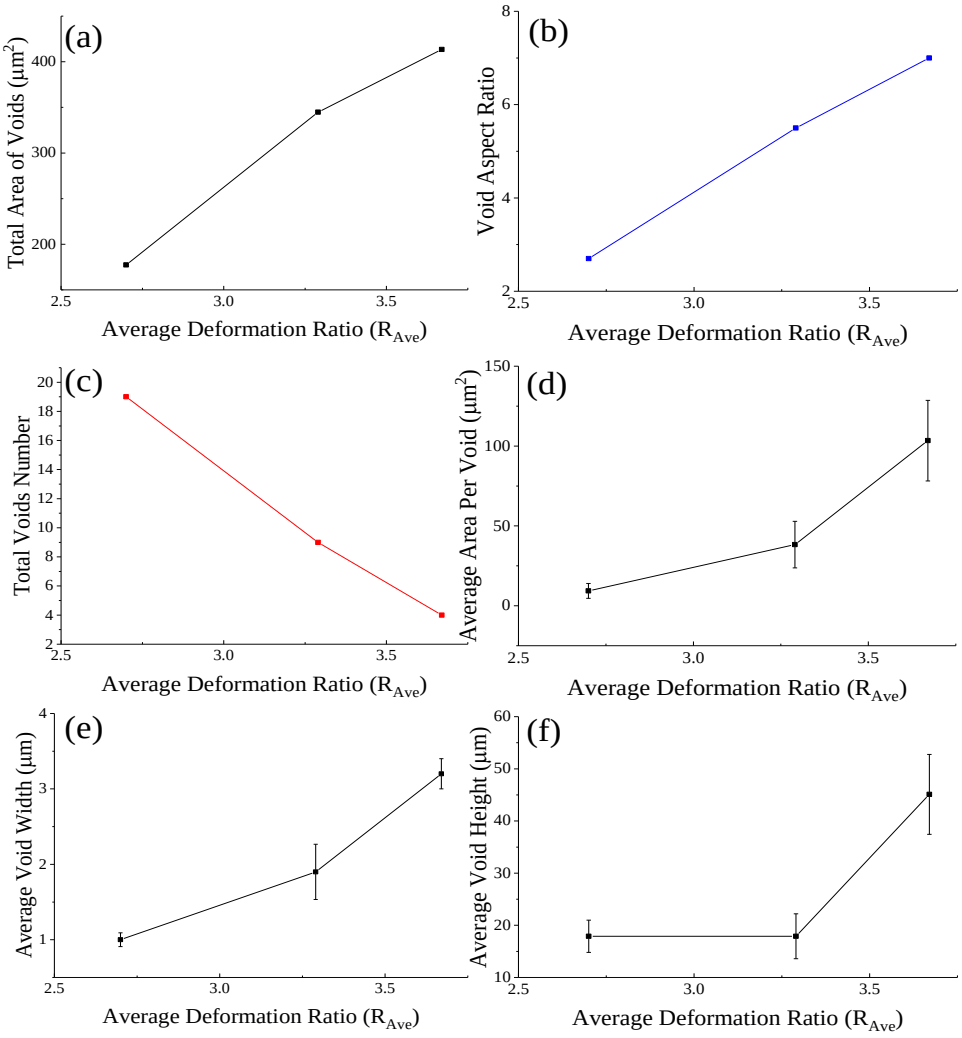

Figure 3-32 The relations of void with deformation ratio using data generated from ImageJ: (a)total area of voids in the OM image; (b) void aspect ratio; (c) the number of voids; (d) per void area; (e) average void width and (f) average void length.

Figure 3-33 shows the difference between the OM pictures taken at the lateral side and the cross-sectional area of die-drawn #13. The cross-sectional area does not contain the aligned pattern. The paralleled ridges shown in the cross-sectional figure resulted from the turning. The small dark round dots with a diameter of approx. 10um may be the cross-section of the

aligned polymeric clusters. The lateral pictures of #12 also showed similar morphology as #13.

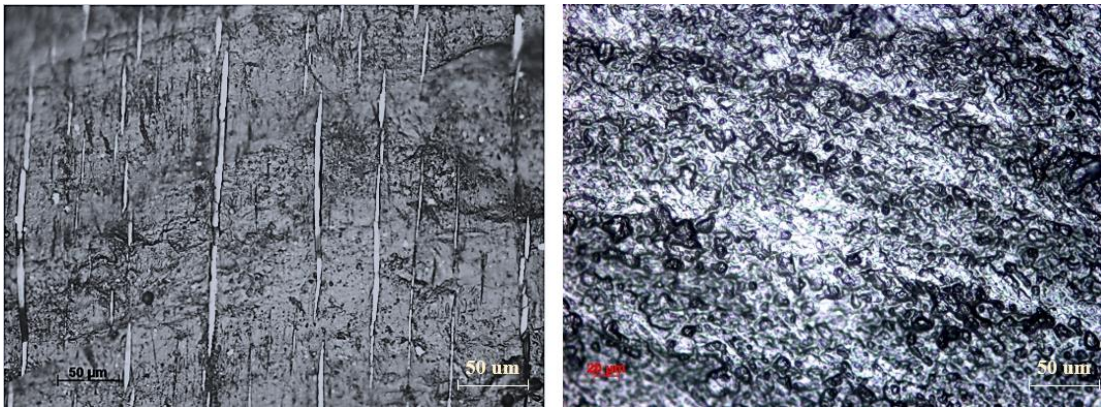

(a) (b)

Figure 3-33 OM images of #13 (a) lateral side; (b) cross-sectional surface (20× magnification).

3.6 Summary

In this section, the method of die-drawing poly(VP-MMA) through a conical die was presented, and the influences of processing parameters including die angle, drawing rate, ratio and temperature on the die-drawing process have been investigated to optimise the process.

The polymers used in the conventional die-drawing processing were mostly thermoplastic material, which becomes flexible upon reasonable heating and fixes again when cooling. These materials, commonly with a linear polymeric structure, undergo plastic deformation at higher temperatures; hence, regardless of the cooling progress, they present no natural tendency to return to their original shape when they leave the die. Although the slightly cross-linked poly(VP-MMA) shows a very similar behaviour of thermoplastic since it becomes malleable

at a raised temperature, its deformation in the die is elastic rather than plastic.

This explains why the extrusion did not work for poly(VP-MMA) in the current experiment setting. Once the extruded material came out of the die, the free-of-force state would immediately initiate the recovery (returned to its 'bulb' size) of the material unless a super-efficient cooling system was attached to the die exit. In the study, to overcome the recovery tendency at the die exit, an intermittent die-drawing (IMD) protocol was developed for relatively high drawing rates and meanwhile, the continuous die-drawing (CND) was found feasible for a low temperature and low drawing rate setting.

The experiments showed that the die-drawing of poly(VP-MMA) could achieve a broader deformation range and an increased success rate using a 5° half-angle die compared to a 10° half-angle die. The maximum deformation ratio achieved in the current study was 3.7 (#13) for the 5°Die and 2.7 (#11) for 10°Die (#12 die-drawn through 10°Die broke in the swelling tests). The feasible temperature ranged from around 145℃ to 180℃. Higher temperatures within the range resulted in an increased sample volume and visible bubbles (despite that, most of the bubbles eventually disappeared in the swelling). Excessively high temperatures (above 180℃) would result in browning and breaking of the sample. Drawing rates of 0.3-6mm/s were proved to be feasible for the die-drawing of poly(VP-MMA). Drawing stress during the die-drawing increased with the deformation ratio and die-angle, decreased with the drawing temperature and showed non monotonically relations with the drawing rates. The average work done per unit time was monotonically related to the drawing rates and was proportional to the

strain rate.

Differential Scanning Calorimetry (DSC), X-ray Diffraction (DSC) and optical microscope have been used to determine how the die-drawing process has influenced the structure of the poly(VP-MMA). DSC showed that the die-drawn poly(VP-MMA) had a slightly increased glass transition temperature, indicating the potential of an increased alignment of polymer chains. The XRD showed that the die-drawing process did not change the amorphous nature of poly(VP-MMA). The optical microscope pictures presented voids on the lateral side of die-drawn while no similar patterns were observed on the cross-section of the die-drawn or the lateral side of an isotropic sample. The total voids, the average area per void, and the average width of the voids (except the number of voids) all increased with the deformation ratio. These aligned patterns further supported the DSC and XRD results.

4 Swelling Behaviour of Die-drawn Hydrogel

List of Parameters (Chapter 4)

$\boldsymbol{m_0}$	Mass of die-drawn xerogel (the die-drawn sample before swelling)
$\boldsymbol{m_t}$	Mass of die-drawn hydrogel (#Die-drawn) at time t
$\boldsymbol{m_\infty}$	Mass of #Die-drawn at equilibrium swelling state
$\boldsymbol{S_m}$	The mass swelling ratio of #Die-drawn, $\boldsymbol{S_m} = \frac{m_t - m_0}{m_0}$
$\boldsymbol{S_{m-\infty}}$	The equilibrium mass swelling ratio of #Die-drawn, $\boldsymbol{S_{m-\infty}} = \frac{m_\infty - m_0}{m_0}$
$\boldsymbol{d_0}$	Diameter of #Die-drawn xerogel
$\boldsymbol{d_t}$	Diameter of #Die-drawn at time t
$\boldsymbol{d_\infty}$	Diameter of #Die-drawn at equilibrium swelling state
$\boldsymbol{S_d}$	The diameter swelling ratio of #Die-drawn, $\boldsymbol{S_d} = \frac{d_t - d_0}{d_0}$
$\boldsymbol{S_{d-\infty}}$	The equilibrium diameter swelling ratio of #Die-drawn, $\boldsymbol{S_{d-\infty}} = \frac{d_\infty - d_0}{d_0}$
$\boldsymbol{h_0}$	Height of #Die-drawn xerogel
$\boldsymbol{h_t}$	Height of #Die-drawn at time t
$\boldsymbol{h_\infty}$	Height of #Die-drawn at equilibrium swelling state
$\boldsymbol{S_h}$	The height swelling ratio of #Die-drawn, $\boldsymbol{S_h} = \frac{h_t - h_0}{h_0}$
$\boldsymbol{S_{h-\infty}}$	The equilibrium height swelling ratio of #Die-drawn, $\boldsymbol{S_{h-\infty}} = \frac{h_\infty - h_0}{h_0}$
$\boldsymbol{v_0}$	Volume of #Die-drawn xerogel
$\boldsymbol{v_t}$	Volume of #Die-drawn at time t
$\boldsymbol{v_\infty}$	Volume of #Die-drawn at equilibrium swelling state
$\boldsymbol{S_v}$	The volume swelling ratio of #Die-drawn, $\boldsymbol{S_v} = \frac{v_t - v_0}{v_0}$
$\boldsymbol{S_{v-\infty}}$	The equilibrium volume swelling ratio of #Die-drawn, $\boldsymbol{S_{h-\infty}} = \frac{v_\infty - v_0}{v_0}$

$\boldsymbol{d_0}'$	Diameter of random isotropic xerogel (#Iso)
$\boldsymbol{d_f}'$	Diameter of fully swollen #Iso
$\boldsymbol{S_{d-\infty}}'$	The equilibrium diameter swelling ratio of #Iso, $\boldsymbol{S_{d-\infty}}' = \frac{\boldsymbol{d_f}' - \boldsymbol{d_0}'}{\boldsymbol{d_0}'}$
$\boldsymbol{h_0}'$	Height of random isotropic xerogel (#Iso)
$\boldsymbol{h_f}'$	Height of fully swollen #Iso
$\boldsymbol{S_{h-\infty}}'$	The equilibrium height swelling ratio of #Iso, $\boldsymbol{S_{h-\infty}}' = \frac{\boldsymbol{h_f}' - \boldsymbol{h_0}'}{\boldsymbol{h_0}'}$

4.1 Introduction

Based on the hot-pressed poly(VP-MMA) can swell primarily in the compressed direction, this project is designed to use die-drawing to achieve the bilateral swelling of poly(VP-MMA) (Figure 3-1). This chapter examines the swelling behaviours of the die-drawn poly(VP-MMA) (#Die-drawn) to verify the design.

The poly(VP-MMA) rods processed under different die-drawing conditions were cut into short columns and left in distilled water to identify the directional swelling features. The different swelling properties were correlated with their different processing parameters (R_{Ave}, v_d and T).

Considering the #Die-drawn expansion properties (decreased ratio of height to diameter with the progress of swelling) and its potential placement in the practical situation (the tissue exerting a force on the lateral side of the swelling #Die-drawn), it may encounter buckling

during the swelling. This project studied the buckling stress and critical slenderness ratio of complete swollen poly(VP-MMA).

Smith reported that the poly(VP-MMA) has a shape memory feature as the compressed sample swelled back to the shape as its unprocessed state [108]. This study tried to prove such a feature applied to the #Die-drawn samples as well.

Lastly, the research had a preliminary study of the swelling rate control of the #Die-drawn poly(VP-MMA). In previous works, a semipermeable silicone membrane was used to envelop the gel to control its swelling rate [40, 41, 108], because the uncontrolled swelling of poly(VP-MMA) caused higher complication rates in the tissue expansion compared to the controlled ones [35, 38]. The #Die-drawn swells even faster in some directions compared to #Iso. Therefore, the swelling rate control was of importance. The #Die-drawn were dip-coated with multiple layers of polydimethylsiloxane (PDMS, silicone) membrane to explore the controlled swelling behaviour.

4.2 Swelling Properties of #Die-drawn

This section will introduce the method of investigating (1) the swelling dimensions/ directions/ force, (2) the influence of die-drawing parameters on the swelling behaviours and (3) the buckling situations of #Die-drawn.

4.2.1 Anisotropic Swelling of #Die-drawn

The intact die-drawn rods were cut into stubs (~14 mm length) for the swelling experiments. The stubs were further marked with water-insoluble ink to determine the measuring position over the swelling period. After the measurement of the mass (m_0), diameter (d_o) and height (h_0), dehydrated stubs were immersed in the distilled water (DW) and stored in a constant temperature incubator (N30, Memmert GmbH., Germany) at 37˚C. DW was used in the swelling experiments, as Swan et al. proved that DW was an adequate approximation of simulated body fluid (SBF) for poly(VP-MMA) [163]. At designed intervals, samples were taken out from DW, dried using filter papers until no water could be observed on the surface. Then measurements of mass (m_t), diameter (d_t) and height (h_t) were taken at time t. $t \approx$ 1, 2, 3, 5, 8, 12, 24 (day 1), 48 (day 2)…, and 216 hours (day 9). In addition, the isotropic poly(VP-MMA) #Iso, were also lathed to small stubs of identical size with #Die-drawn and underwent the same swelling tests.

In this research, S_m, S_v, S_d, S_h were used to represent the mass, volume, diameter, and height swelling ratio of the die-drawn poly(VP-MMA) at swelling time t, respectively. S_m, S_v, S_d, S_h were defined as follows:

$$S_m = \frac{m_t - m_0}{m_0} \tag{4.1}$$

$$S_v = \frac{v_t - v_0}{v_0} \tag{4.2}$$

$$S_d = \frac{d_t - d_0}{d_0} \tag{4.3}$$

$$S_h = \frac{h_t - h_0}{h_0} \tag{4.4}$$

In addition, $v_0 = \frac{1}{4}\pi {d_0}^2 h_0$ and $v_t = \frac{1}{4}\pi {d_t}^2 h_t$. Note that the lower-case d & h, etc., describe the size of material in the swelling compared to the upper-case D & H mentioned previously in Chapter 3 for the dimensions of the sample before and after mechanical processing. Theoretically, $D_f = d_0$.

Table 4-1 #Die-drawn samples for the swelling experiments

Processing Parameters	**Variables**	**Controlled processing conditions**
Deformation ratio	#Iso (R_{Ave}=1) & #Die-drawn with R_{Ave}=1.74, 2.01, 2.32, 2.70, 3.29, 3.67 (i.e., #9, #9.5, #10, #11, #12, #13)	5° Die T=160°C v_d = 4 mm/s
Drawing rate	v_d = 2, 3 and 4 mm/s	5° Die T=145°C R_{Ave} = 2.01 (#9)
Drawing temperature	T =145, 160, 180 °C	5° Die R_{Ave} = 2.01 (#9) v_d = 4 mm/s

The equilibrium swelling state of the hydrogel occurred when no more mass gaining in 48 hours. The corresponding mass (m_∞), volume (v_∞), diameter (d_∞) and length (h_∞) swelling ratio for this state was marked as $S_{m-\infty}$, $S_{v-\infty}$, $S_{d-\infty}$ and $S_{h-\infty}$ respectively. The impact of process parameters (R_{Ave}, v_d and T) on the swelling behaviours of #Die-drawn were

investigated, and the experiment design is given in Table 4-1.

4.2.2 Buckling Experiments

The potential buckling phenomenon has been discussed for the mathematic model of the 1D-Uni, 2D-Bi and 3D-Iso HTEs previously in Chapter 2. In this chapter, the buckling conditions for the #Die-drawn (i.e., 2D-Bi) are further examined through experimental studies.

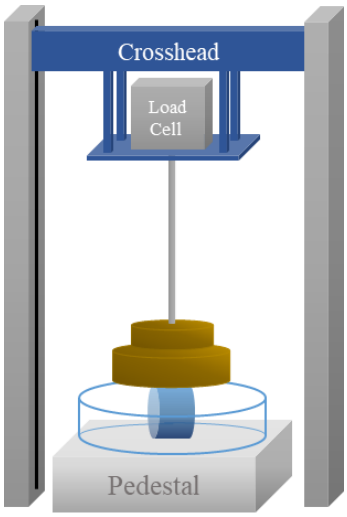

Figure 4-1 Schematic for buckling test set-up.

The setting of the buckling experiments shown in Figure 4-1. A stainless steel plate (Ø30mm) was attached to the load cell（Interface Inc., USA）of a tensile testing machine (Denison Mayes Group, UK). A thin layer of nitrile film was wrapped around the plate to prevent corrosion by water and oxygen. A petri dish was placed on top of a pedestal and a fully swollen poly(VP:MMA) samples was placed in the centre of petri dish. The fully swollen #Die-drawn would have the lowest Young's Modulus and the smallest slenderness ratio compared to its

dry or nonequilibrium swelling states. Therefore, the fully swollen state is when the buckling is most likely to happen. Samples with the same equilibrium diameter and different lengths were prepared so that each sample possessed different slenderness ratios. The plate was designed to move downwards at a steady speed of 50 μm/s, simulating the top-down tissue compression. The buckling of each sample could be directly observed in the experiment or presented on the force-displacement curve. To define the critical stress at the buckling, we calculated the corresponding contacting area between the sample and the plate based on the assumption that the radius and height of the cylinder (r & h) remained the same during the compression.

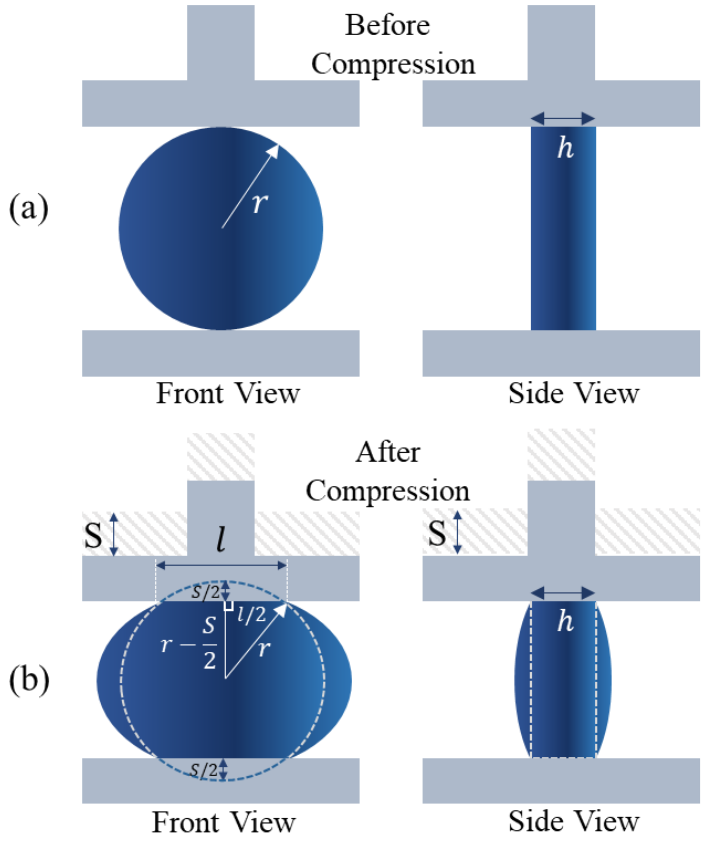

Figure 4-2 Diagram of constant radius/height assumption: (a) before compression; (b) after

compression. r is radius of the sample; h is the height/length of the sample; S is the crosshead displacement at buckling; l is one lateral of the compression area.

As shown in Figure 4-2, the radius (r), half length of the compressed region ($l/2$), and the difference of the radius and the displacement of the compression head ($r - \frac{d}{2}$) are subject to the Pythagorean theorem. The contact area $A_b = l \times h = 2\sqrt{r^2 - (r - \frac{S}{2})^2} \times$ h. The stress at the buckling was $\sigma_b = \frac{F_b}{A_b}$, in which F_b is the critical load for buckling. The relationship between the critical buckling stress and the slenderness ratio (either H/r or H^3/r^2) will be shown in section 4.3.2.

4.2.3 Swelling Rate Control

The tissue expansion using conventional balloon type of expanders typically require 6-12 weeks [179], and a few studies confirmed the feasibility of rapid expansion of 2 to 4 weeks, but the tissue generated was only 1/3 of the chronic tissue expansions [55, 180]. Both the processed and unprocessed poly(VP-MMA) swelled to its maximum within two weeks, and 80% of swelling was achieved in a few days [40, 108]. In the porcine trial of the hot-compressed poly(VP-MMA), the hard posterior palates of the two pigs implanted with uncoated samples showed ulceration and local inflammation at day 12, and the implanted tissue expander was partially broken, while the group using polydimethylsiloxane (PDMS) coated samples showed no complications over 6 weeks [44]. The #Die-drawn samples used for the coating were #9.5 made with CND mode at 145℃.

PDMS is a biocompatible material generally considered inert, non-toxic, and non-flammable. The chemical structure of PDMS is provided in Figure 4-3. It is widely used in cosmetic products, the food industry and medical devices, e.g., surfactant, antifoaming agent, contact lens materials.

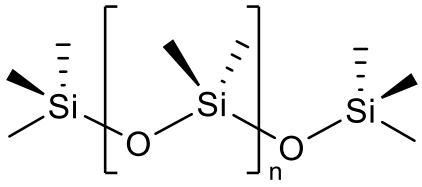

Figure 4-3 Chemical structure of PDMS.

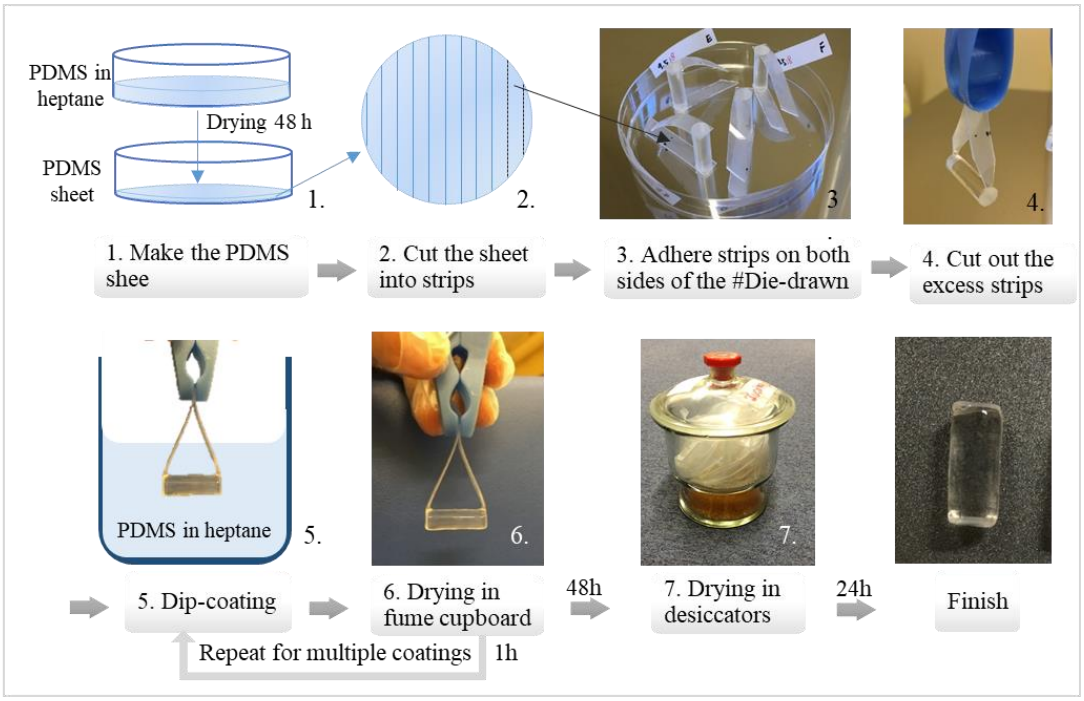

Figure 4-4 The dip-coating procedure for #Die-drawn poly(VP-MMA).

PDMS (MED6-6606, originally in heptane, NuSil Polymer Systems Technology Ltd., UK) was used as a semipermeable coating to restrain the rapid expansion of uniaxially compressed

poly(VP-MMA) and showed successful control of the swelling rate [163]. Samples of approximately the same size as the previous swelling experiments (Ø6.5×14mm) were coated with various layers of PDMS and swelled in DW. A dip-coating method for the #Die-drawn stubs was developed, and the protocol is shown in Figure 4-4 and described as follows.

1-2. *Making the PDMS strips*. Heptane is toxic and vaporises at room temperature[35]. Hence the procedure was carried out in the fume cupboard. PDMS/heptane solution was poured into a polystyrene petri dish (Ø90mm) to a depth of 6 mm. The petri dish was left in the fume cupboard for two days to evaporate heptane and form a translucent PDMS sheet of ~0.3mm thickness. The sheet was cut into strips with a size of 7×30~40 mm and peeled off from the petri dish.

3-4. *Adhering strips to the sample*. As the swelling character of die-drawn poly(VP-MMA), it was beneficial to coat the lateral side of expanders to be of consistent thickness. Therefore, two PDMS strips were glued to the sample circular ends with the PDMS/heptane solution as the 'glue'[36]. The excess strip material around the sample was cut off while a small portion remained for the handling. The two strips were held together by a peg. The length of the strips required proper adjusting so that the sample central axis was as level as possible when the peg

---

[35] The equilibrium vapour pressure of heptane is 5.3 kPa at 20°C; atmosphere pressure is 100.5 kPa at Oxford altitude and 20°C.

[36] Method: around 5μl PDMS/heptane solution was dripped at one end of the strip to form a droplet (Ø2~3mm). Then one circular end of the sample was immediately attached to the 'glue' droplet and was held under gentle pressure for 5 to 10s until a firm attachment. The sample with one strip attached was left in the fume hood for 2 hours for the glue to cure.

was hung on a rack to ensure an even and balanced coating.

5-6. *Dip-coating and Drying*. The sample was then completely immersed in the PDMS/heptane solution and held for 2 seconds before being taken out[37]. Then the sample was hung on a rack to dry in a fume hood for 1 hour. The process was repeated multiple times for multiple layers of PDMS coating.

7. *Further drying and finish*. After applying the target amount of coating layers, the samples were dried for 48h. Then the strips that protruded out of the sample was removed. The sample was kept in the desiccator with granular silica gel for another 24h to remove the heptane further.

PDMS had several roles in the coating procedures: the accessorial strips that held the sample to implement dipping, the glue between the strip and the sample and primarily, the coating material. As the strips will be unavoidably coated simultaneously with the sample, the multi usages of PDMS retained the coating consistency.

In the experiments, 1, 2, 3, 4, 6, 8 and 10 coatings were tried for the #Die-drawn. The total coating thickness of each sample was measured, and the average thickness per coating was calculated to discuss the consistency of the dip-coating methods. The coated samples were left in the DW for about 20 weeks to see how the PDMS coating would influence the swelling

[37] Excess liquid was scraped off against the beaker wall to ensure only a thin layer of the membrane was coated onto the sample. Otherwise, PDMS solution would accumulate at the lower lateral of the sample and form a hump during drying. Such hump would build up after several layers and eventually led to an uneven lateral coating.

behaviour.

4.2.4 Shape Memory Feature

Smith discussed the shape memory feature of the hot-pressed poly(VP-MMA) [108]. He revealed that the uniaxial compressed the poly(VP-MMA) gel still 'remembered' its original shape. If the same feature applies to the samples in this study, the #Die-drawn will swell to the same dimensions as its unprocessed isotropic counterpart.

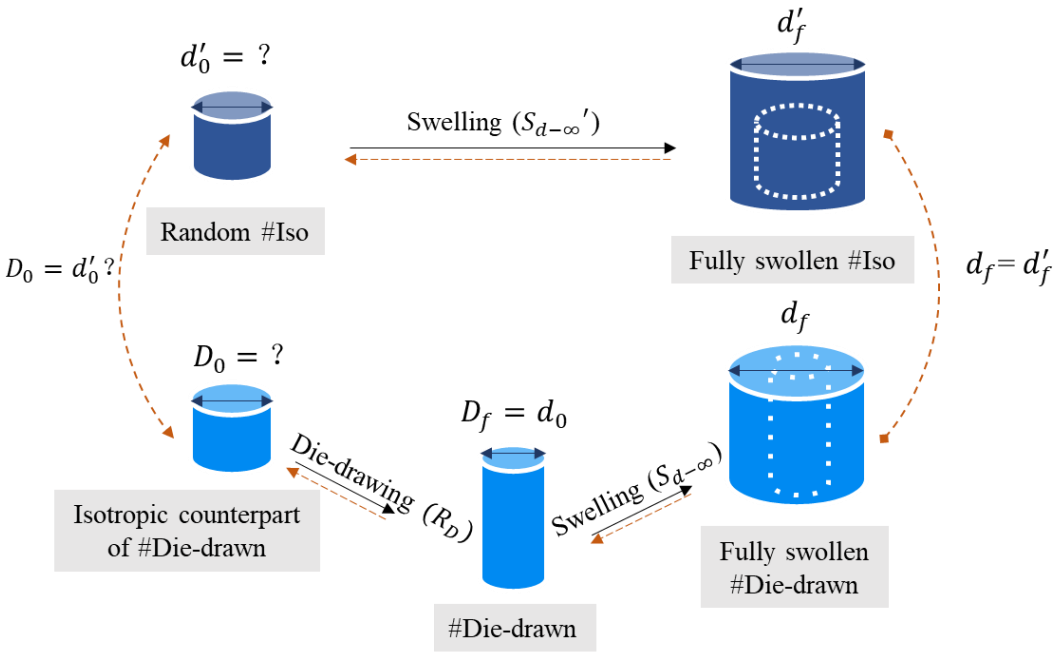

Figure 4-5 Schematic of the shape memory feature of poly(VP-MMA) (black arrows: processing and swelling routes; orange arrows: shape memory effect deduction.

Figure 4-5 illustrates a possible way of proving the shape memory feature of #Die-drawn poly(VP-MMA). Assuming a #Die-drawn and a random #Iso achieve the same dimensions after swelling ($d_f = d_f'$). If we work backwards and derive that the diameter of the #Die-

drawn before die-drawing (D_0) equals the diameter of this #Iso before swelling ($d_0{}'$), we can prove that this random #Iso is of the same size as the isotropic counterpart of the #Die-drawn, and hence prove that the #Die-drawn can memorize the shape of its isotropic counterpart. Based on this idea, $\frac{d_0{}'}{D_0}$ was expressed by the deformation ratio and swelling ratio of the #Die-drawn and #Iso. Because these ratios were available from the experiments, the value of $\frac{d_0{}'}{D_0}$ could be calculated.

The deduction of expression $\frac{d_0{}'}{D_0}$

As it was assumed that $d_f{}' = d_f$. For the #Die-drawn:

$$S_{d-\infty} = \frac{d_f - d_0}{d_0} = \frac{d_f{}' - d_0}{d_0} \tag{4.5}$$

$$R_D = \left(\frac{D_o}{D_f}\right)^2 = \left(\frac{D_o}{d_o}\right)^2 \tag{4.6}$$

For the random #Iso sample:

$$S_{d-\infty}{}' = \frac{d_f{}' - d_0{}'}{d_0{}'} \tag{4.7}$$

The expression of $\frac{d_o{}'}{D_0}$ was obtained by eliminating d_0 and $d_f{}'$ in the above three equations:

$$\frac{d_o{}'}{D_0} = \frac{S_{d-\infty} + 1}{\sqrt{R_D}\,(S_{d-\infty}{}' + 1)} \tag{4.8}$$

Then the experimental data of $S_{d-\infty}$, $S_{d-\infty}{}'$ and R_D were assigned to Eq. (4.8) to obtain the value of $\frac{d_o{}'}{D_0}$. Similarly, we can deduce the height relations of this random #Iso ($h_o{}'$)and the

#Die-drawn isotropic counterpart (H_0): $\frac{h_o{}'}{H_0} = \frac{R_H(S_{h-\infty}+1)}{S_{h-\infty}{}'+1}$, and $S_{h-\infty}$, $S_{h-\infty}{}'$ and R_H were assigned to obatin the ratio of $\frac{h_o{}'}{H_0}$. If both $\frac{d_o{}'}{D_0}$ and $\frac{h_o{}'}{H_0}$ equal 1, it means that the isotropic counterpart of #Die-drawn and the random #Iso are identical. The results are given in 4.3.4.

4.3 Results and Discussion

4.3.1 Anisotropic Swelling Properties of #Die-drawn

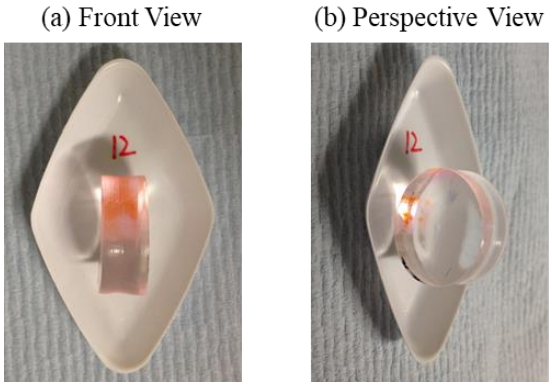

Figure 4-6 Photos of #12 at 6 hours of swelling: (a) front view, (b) perspective view.

Photos of all samples were taken from a front view with a weighing boat as the background, as shown in (a). A perspective view in (b) may provide more intuitive idea of how the #Die-drawn was placed on the weighing boat. Figure 4-7 shows the photos of swelling #Iso and #Die-drawn in chronological order (a more comprehensive photo set is provided in Figure 6-12 in Appendix). Note that the #Iso was placed parallel to the weighing boat long axis while #Die-drawn parallel to the weighing boat short axis. All the samples started as stubs about the same size.

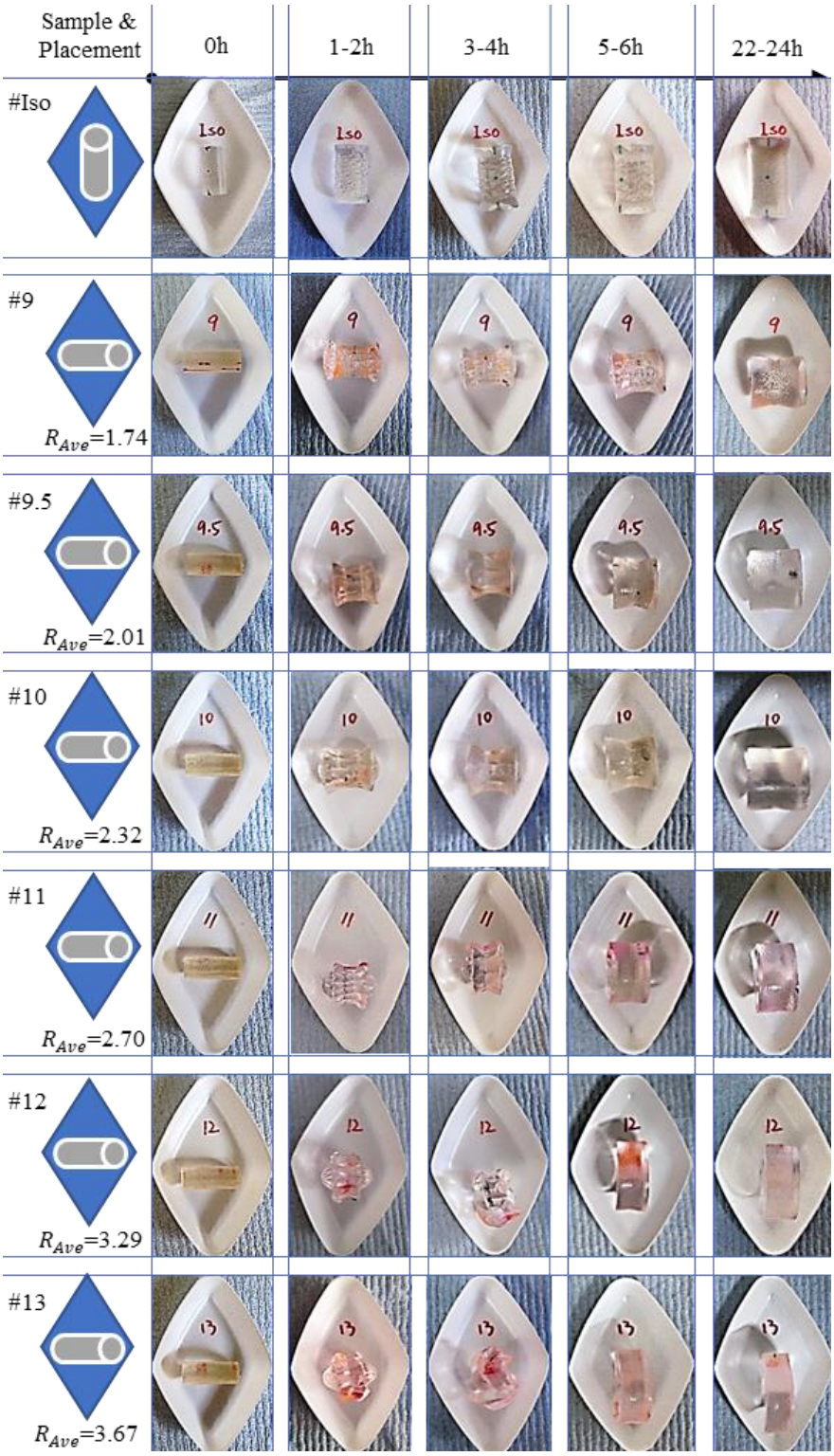

Figure 4-7 Photos (front view) of the swelling #Iso and #Die-drawn with various deformation ratios R_{Ave}.

In the swelling process, the size of #Iso increased in proportion to the original shape, however, the #Die-drawn deformed relative to the original shape during the volume increase. Notably, samples with higher R_{Ave} experienced more significant shape change - more considerable diameter increase and height decrease.

Figure 4-8 plots the diameter, height, surface area, mass, and volume swelling ratios of #Iso and #Die-drawn over 9 days. Figure 4-9 displays the diameter and height swelling in the first 12 hours.

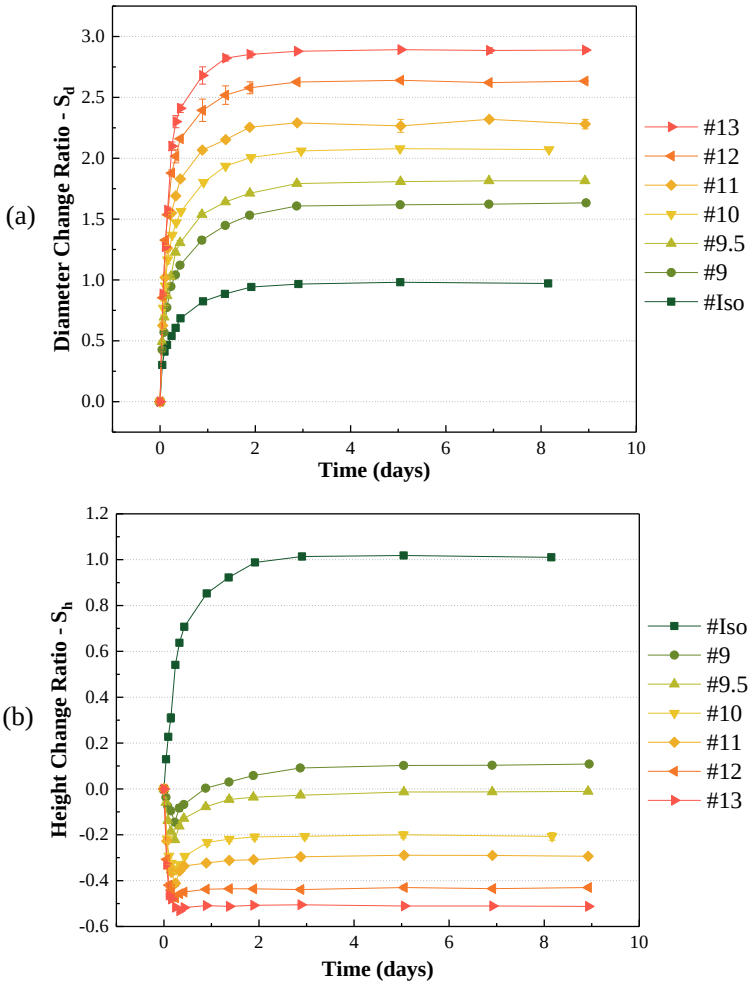

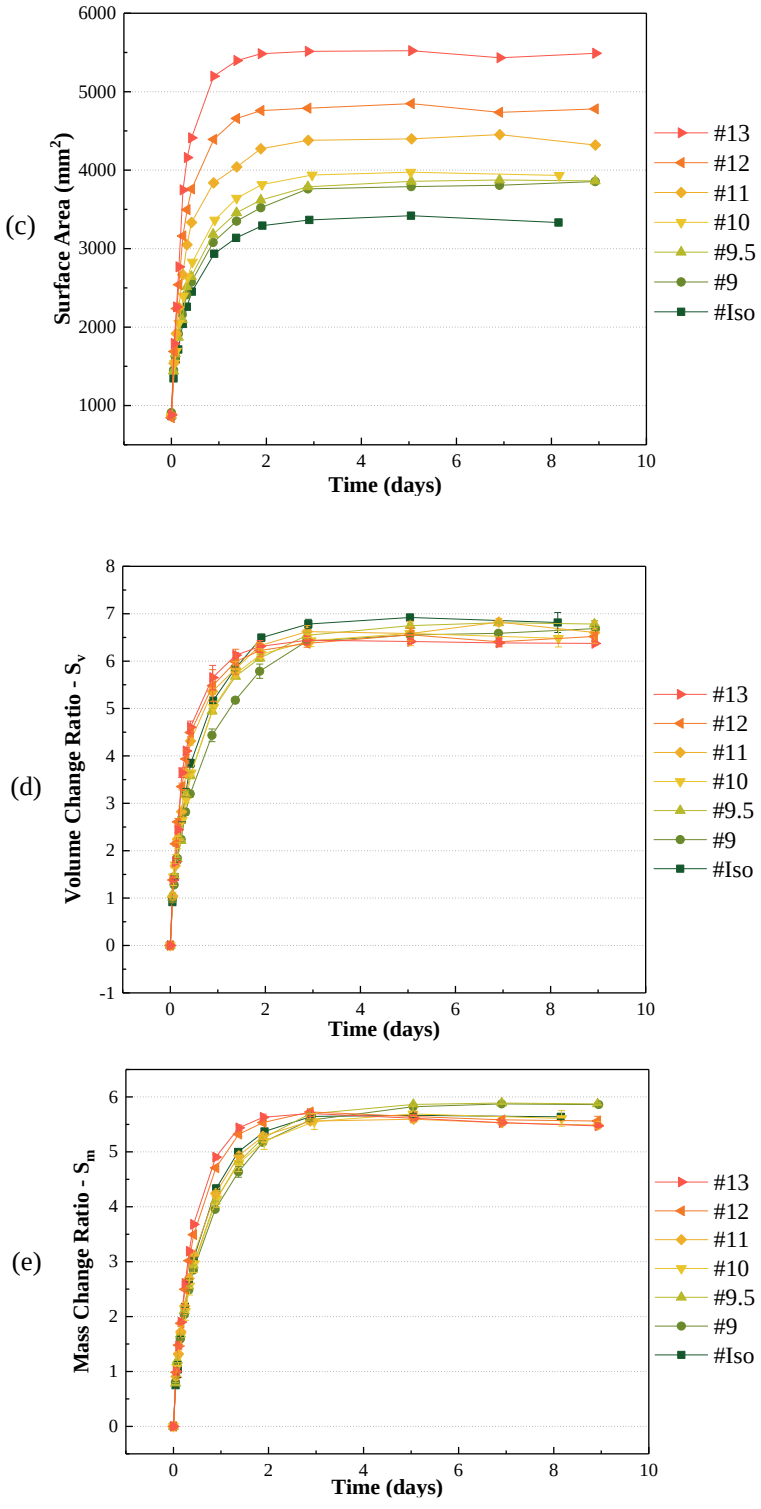

Figure 4-8 The (a) diameter, (b) height, (c) surface area, (d) volume, and (e) mass swelling ratios of #Iso and #Die-drawn with different deformation ratios (n = 3).

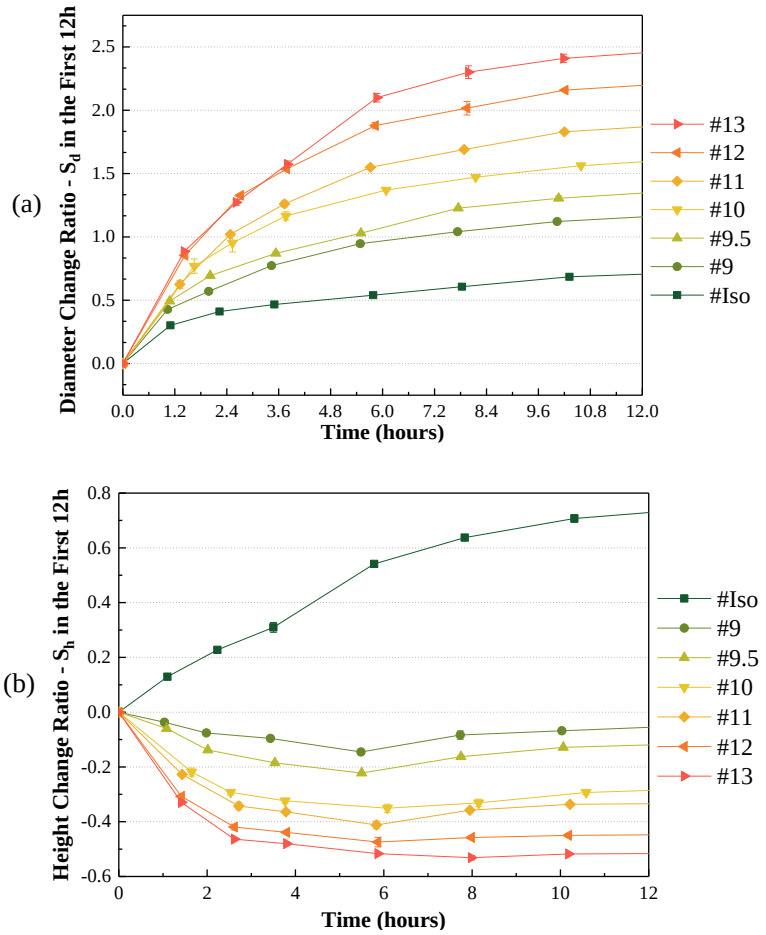

Figure 4-9 The swelling ratios of #Iso and #Die-drawn in first 12 hours (n = 3): (a) diameter swelling ratio S_d and (b) height swelling ratio S_h.

Figure 4-8 (a) and Figure 4-9 (a) show that the #Die-drawn swelled faster and more prominent in the bilateral direction (i.e., diameter) than #Iso, and the diameter swelling rate and ratio positively correlated to the deformation ratio. While #Iso eventually doubled its diameter at its fully swollen state ($S_{d-\infty} \approx 1.0$), #Die-drawn reached a 163.1±0.5% to 288.8±1.4% diameter increase ($S_{d-\infty} \approx 1.6$~2.9).

As presented in Figure 4-8 (b), #Die-drawn experienced entirely different swelling in the

height direction from #Iso. The height of #Iso increased with time and the S_h almost shared the same increasing pattern as S_d, showing the isotropic swelling performance. However, the height of all #Die-drawn experienced a sharp reduction initially and then re-expanded after around 6 hours (#13 re-expansion occurred after 8 hours). Moreover, the #Die-drawn equilibrium swelling ratios, $S_{h-\infty}$, ranged from -0.5 to 0.1, suggesting that the height swelling of #Die-drawn was significantly impaired, and the swollen height might even become smaller than the dry state. Specifically, for #9.5, $S_{h-\infty} \approx 0$ and $S_{d-\infty} \approx 0.75$, meaning the fully swollen #9.5 achieved bilateral swelling with no expansion in the height direction compared to its beginning dimensions.

Figure 4-8 (c) indicates that with the increase of R_{Ave}, the surface area of the sample increased to a greater extent and at a greater rate, indicating that more severe deformation provided a larger contact area for the water and accelerated the swelling. This might explain the phenomenon in Figure 4-9 (a) and (b) that the swelling/deforming rates increased with higher R_{Ave}.

In Figure 4-8 (d) and (e), the S_v and S_m curves of these samples nearly coincide at the end, implying that the mechanical processing did not significantly change the ultimate water absorption capacity of the poly(VP-MMA) sample, which could be evidence that the nature of #Die-drawn samples did not change by the mechanical processing. #12 and #13 die-drawn samples had a slightly faster S_v and S_m increase in the first few hours than the samples with smaller deformation ratios and #Iso. This could be explained again by the surface area results

in Figure 4-8 (c). Furthermore, #12 and #13 showed slightly smaller final volume change ratio ($S_{V-\infty}$). This could be due to a larger void aspect ratio of #12 and #13 resulted from die-drawing, as shown in Figure 3-32 (b). The voids preoccupied some volume space before swelling, therefore reducing the final volume increase capacity of the gels.

4.3.1.1 An explanation for the swelling pattern of #Die-drawn

Initial height decrease: competitive effects in the height direction

As described earlier, all #Die-drawn experienced an initial sharp reduction first and then a re-expansion after a few hours. An explanation of this phenomenon could be the 'competition' assumption. One competitor was the hydrogel's tendency to swell in water due to its natural hydrophilic property. The other competitor was the recovery tendency of material. As the cooling down under tension stored the residual stress in the polymer network (reversibly fixed the temporary shape), #Die-drawn tends to release the stress upon critical conditions. For the hydrogels, the critical conditions can be an increased temperature, which directly increases the flexibility of the polymer chain, or a humid environment, where water diffuses into the polymer network and acts as a plasticizer.

Figure 4-10 is an illustration of the 'competition' assumption. Figure 4-10 (a) and (b) show the stress applied to the sample during the die-drawing process and the corresponding recovery tendency when swelling. The recovery was opposite to the stress direction.

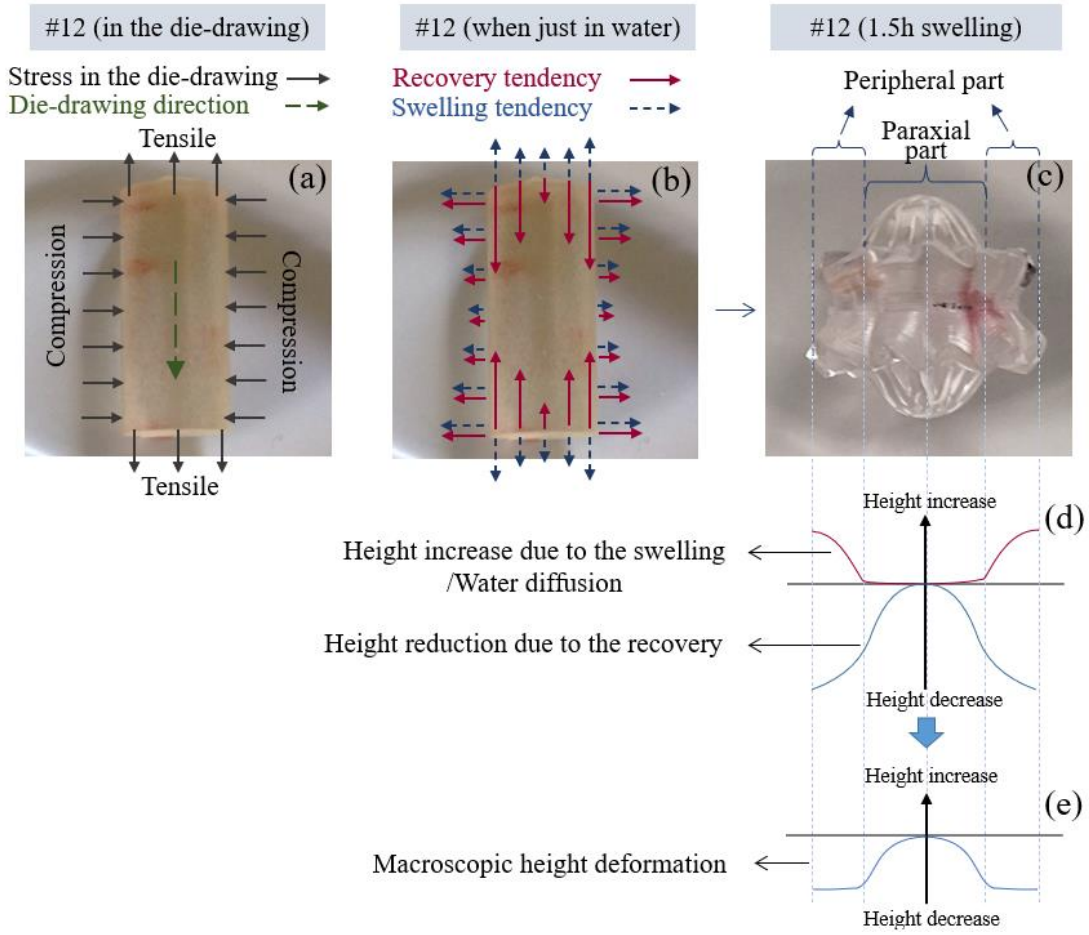

Figure 4-10 Illustration of the competitive/collaborative effects between the recovery tendency and swelling tendency of a #Die-drawn: (a) the stress applied to the sample during the die-drawing process; (b) the recovery and swelling tendency of the sample at the beginning of swelling; (c) the photo of #12 after 1.5 hours of swelling; (d) schematic of the heigh change caused by water diffusion and recovery deformation; (e) schematic of the overall macroscopic height change.

The likely reason behind this phenomenon was that only a limited amount of water diffused into the system in the first place. Because the amount was insufficient to support the expansion of the hydrogel skeleton, the water acted more as a plasticizer, and the hydrogel thus mainly

presented the deformation opposite to the die-drawing direction. Such explanation was consistent with the observations from the photos of #Die-drawn in Figure 4-7 (columns 2 and 3) and the swelling of #12 in Figure 4-10 (c): the peripheral part of the sample contracted more than the paraxial part as the water diffused gradually from the peripheral part to the core.

Moreover, Figure 4-10 (c) shows that the degree of recovery reduction in height increased with the off-axis distance in the paraxial part, while in the peripheral part, the height of the sample showed relative consistency along the radial direction. Figure 4-10 (d) and (e) illustrate the possible reason for such a difference. The height increase due to swelling should be directly related to the amount of water diffused into the system. In the paraxial, the recovery dominated as it was much more sensitive to water. In the peripheral part, the difference between the recovery decrease and swelling increase became relatively stable.

Enhanced lateral swelling: collaborative effects in the radial direction

The enhanced lateral swelling could also be explained using Figure 4-10 (b). In the radial direction, the swelling and recovery were in the same direction. Therefore, they were sharing a collaborative relation. The collaboration of these two tendencies led to the swelling rate increase of #Die-drawn compared to the #Iso.

4.3.1.2 Breaking in the swelling

Samples that had been successfully die-drawn without breaking may not necessarily result in intact swelling. Some #Die-drawn experienced lamellar rupture during the swelling. Photos in

Figure 4-11 recorded the lamellar fracture of #12 (die-drawn from the 10°Die) during the swelling. Before being completely broken, the #12 sample presented a flower shape after 3 hours of swelling.

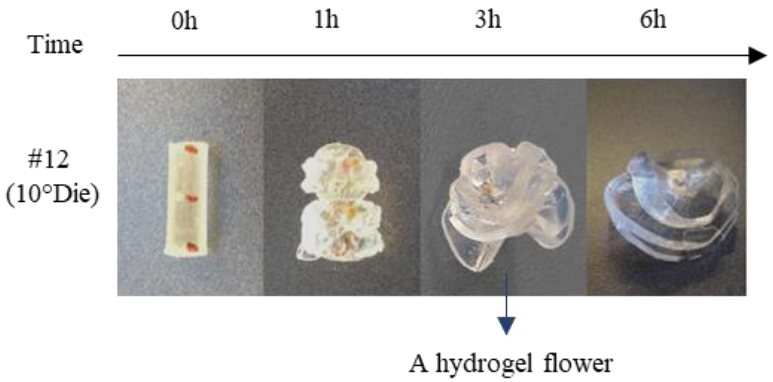

Figure 4-11 The swelling path of #12 (10°Die, 160°C, v_d=4mm/s).

The mechanism for the breaking during swelling remained to be confirmed. One possible reason was that although the maximum drawing stress did not exceed the ultimate breaking strength of the material, the shear stress from the die wall was approaching the critical shear strength of the material and might have caused tiny cracks on or near the surface. The crack was quickly frozen as the sample came out of the die, preventing further breaking.

During the swelling, the crack end material expanded larger and faster than those surrounding the crack tip as the crack itself contributed to a larger surface area. As a result, the expanded crack end started to push each other and led to the crack tip propagation further towards its surrounding, resulting in two (or more) separately hydrogel layers. If the core was already in a swollen state when the tip reached the core, the tip growth might stop, and the core was still

able to connect the partially fractured layered, as shown in Figure 4-11. Otherwise, the tip growth will continue and lead to the complete fracture of the hydrogel lamellas.

4.3.1.3 The influence of processing parameters: a further discussion

Deformation ratios R

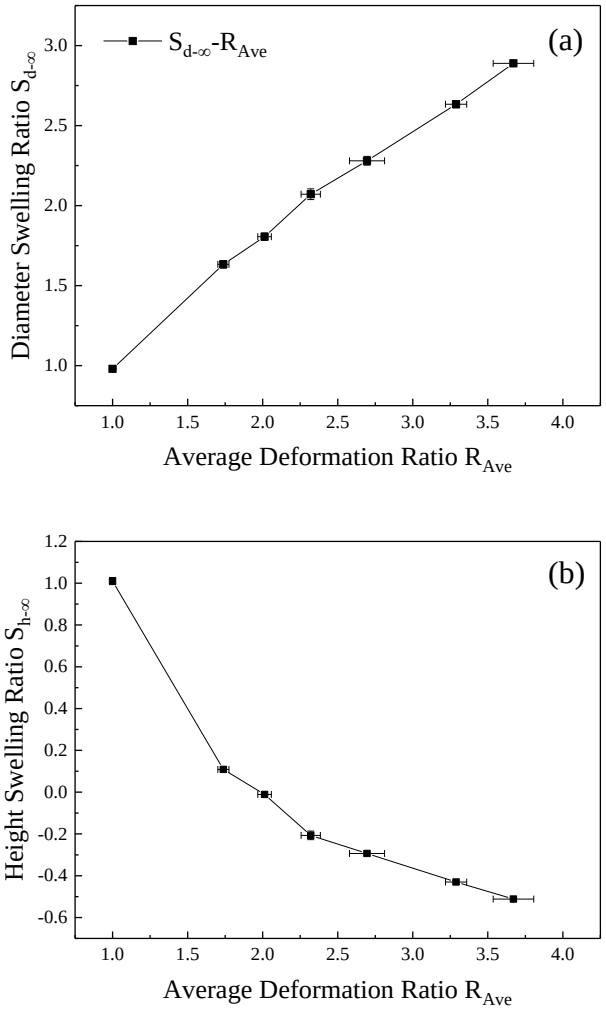

Figure 4-12 The plot of (a) equilibrium diameter swelling ratio ($S_{d-\infty}$) with R_{Ave} (n = 3); (b) equilibrium height swelling ratio ($S_{h-\infty}$) with R_{Ave} (n = 3).

Figure 4-12 (a) presents the relationship of deformation ratio R_{Ave} and the equilibrium diameter swelling radio ($S_{d-\infty}$). $S_{d-\infty}$ is monotonically increasing with R_{Ave}. Figure 4-12 (b) plots the $S_{h-\infty}$ vs R_{Ave}. Contrary to the trend of $S_{d-\infty}$-R_{Ave}, $S_{h-\infty}$ was monotonically decreasing with R_{Ave}.

Based on the same raw material and the consistent processing parameters (die-angle, v_d and T), the deformation ratios determined the diameter and height swelling of the samples.

Drawing rates v_d

#Die-drawn with different v_d did not show significant differences in the swelling performance, as shown in Figure 4-13. The small variations between the samples may be the error caused by the different actual deformation ratios.

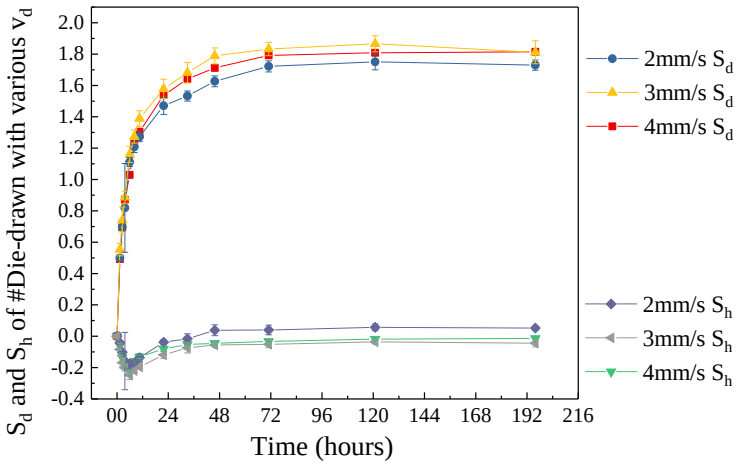

Figure 4-13 Diameter and height swelling ratios (S_d and S_h) of #Die-drawn with different v_d (#9.5 die drawn with 5°Die at 145°C, v_d= 2, 3, 4 mm/s, n = 3).

Temperatures (T)

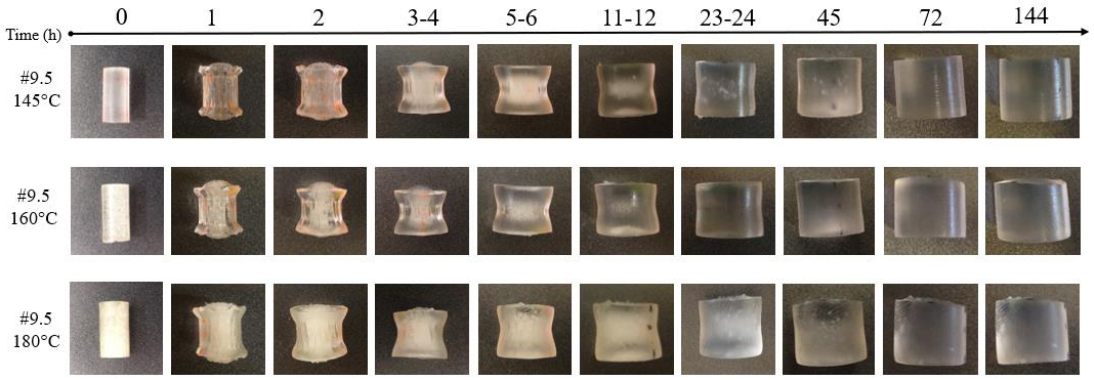

Figure 4-14 Front view photos of the swelling #9.5 die-drawn at various temperatures (photos taken at 0, 1, 2, 3-4, 5-6, 11-12, 23-24, 45, 72, 144 hours after swelling).

Figure 4-14 shows the photos of swelling #9.5 previously die-drawn at different temperatures. The opacity of anhydrous samples increased with the die-drawing temperatures (t = 0) and visible bubbles could be seen in #9.5 (160°C and 180°C). The bubbles disappeared from the front view after 24 hours of swelling.

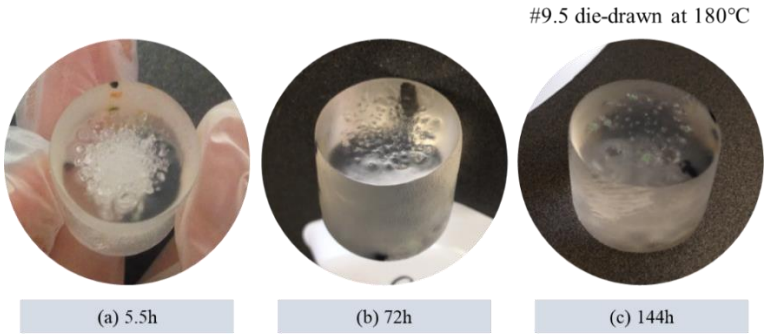

Figure 4-15 Photos of #9.5 (180°C) after (a) 5.5h, (b) 72h, and (c) 144h of swelling.

However, while the 145°C and 160°C samples eventually ended up with a smooth surface, the

cross-section surface of the 180°C samples presented tiny pits, as shown in the photos in Figure 4-15.

One explanation was that the intensive bubbles in 180°C samples had led to thin bubble walls, and these fragile walls inevitably encountered brittle fracture when the rod was cut into stubs. The bubble wall fragments during cutting may be the material that initially belonged to the hole.

Figure 4-16 shows that samples die-drawn at 145℃ and 160℃ presented no significant differences in S_d, S_h, S_m and S_v. However, sample die-drawn at 180°C showed a smaller S_d in Figure 4-16 (a) possibly due to its larger R_{Ave} (Figure 3-26 (a)).

Figure 4-16 (b) also shows a significantly decreased S_v of 180℃ samples compared to other samples. As previously shown in Figure 3-26 (b), the 180℃ #Die-drawn had a larger initial volume. Therefore, the dry180℃ samples with bubbles could be considered as a partially pre-expanded sample by the medium air. Such pre-expansion occupied a portion of volume expansion that the water could originally achieve. The S_m in Figure 4-16 (c) indicates that the existence of the bubble did not change the ultimate water absorption capacity of the hydrogel. It also means that for the 180℃ sample, there was an amount of water entering the pre-existing bubbles without contributing to the volume increase.

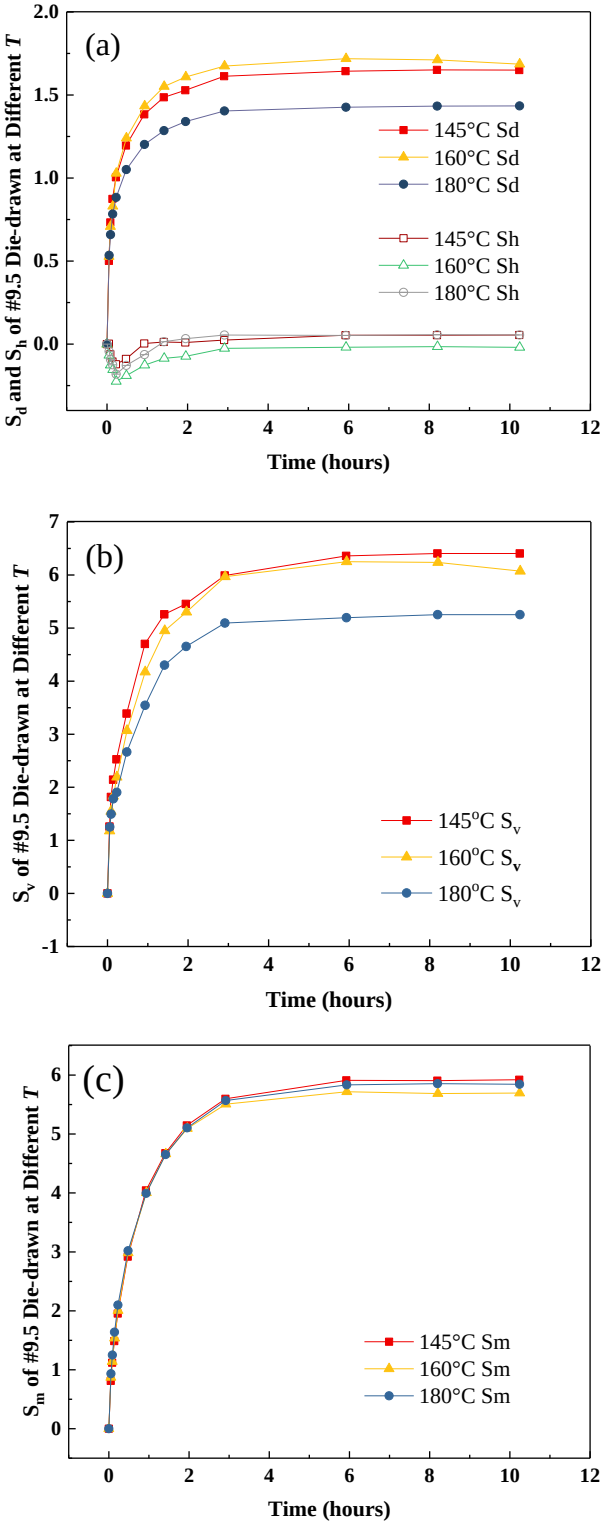

Figure 4-16 (a) Diameter, (b) volume, (c) mass swelling ratio of #9.5 die-drawn at different temperatures (with 5°Die and v_d = 4mm/s, n = 3).

4.3.2 Buckling Experiments

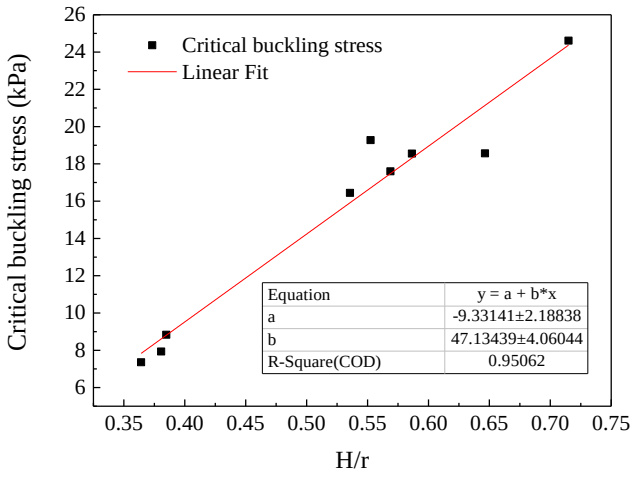

Figure 4-17 The relationship of critical buckling stress vs slenderness ratio H/r.

The critical buckling stress ($\sigma_{critical}$) was acquired and plotted against the slenderness ratio H/r and showed in Figure 4-17. The $\sigma_{critical}$ - H^3/r^2 relation were plotted and shown in Appendix III. The linear fitting shows a relationship: $\sigma_{critical} = 47.13\frac{H}{r} - 9.33$. It implies that when $H/r < 0.20$, the buckling will likely happen even without stress and for the $\sigma_{critical} = 64$ kPa (Maneepairoj found that poly(VP-MMA) (w/w 90:10), has E =140 kPa and a maximum swelling stress of 64 kPa (i.e., N_{cr}) in a skin mimic device [155], the corresponding $\frac{H}{r} = 1.56$.

4.3.3 Swelling Rate Control

In the experiment, samples coated with less than four layers of PDMS showed early puncture in the initial 72 hours for most of the cases, indicating that the mechanical strength of the thin

coating was insufficient to support the expansion of the internal hydrogel. The thinner the coating, the lower the mechanical strength of the coating and the faster the water diffuses. In addition, a thinner coating meant a greater coating thickness difference between the circular part and the lateral part of the sample due to the embedded PDMS strips. The difference might deteriorate the unbalanced swelling of the hydrogel. As a result, the discussion will focus on the samples coated with 4, 6, 8, 10 layers of coatings in this section. The result will be compared to the non-coated die-drawn samples.

Coating thickness

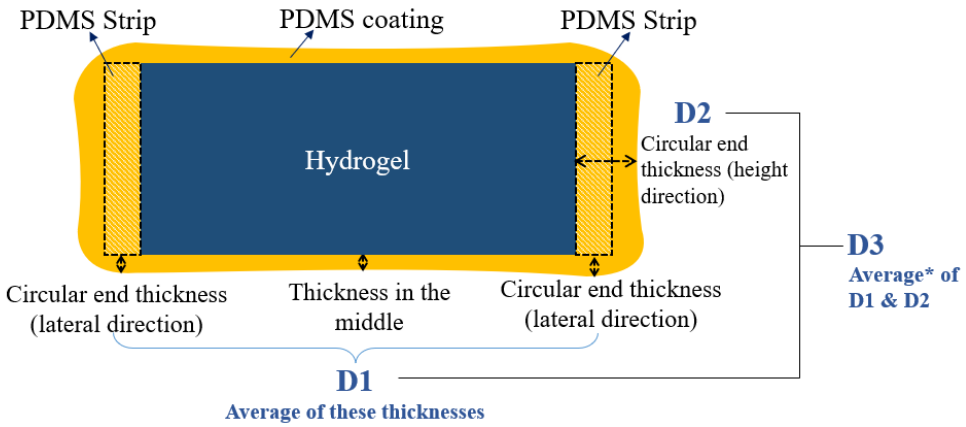

Figure 4-18 Illustration of a coated #Die-drawn stub (*D3 is the sum of D1 and D2 times their corresponding area proportions).

Figure 4-18 is a schematic of a PDMS-coated #Die-drawn. Figure 4-19 shows the mass difference of the sample before and after coating. The total mass followed a relatively good linear trend as the layers increased, and the mass of per-layer coating remained reasonably consistent. The influence of strips at the circular ends used before the dip-coating process

seemed to be negligible.

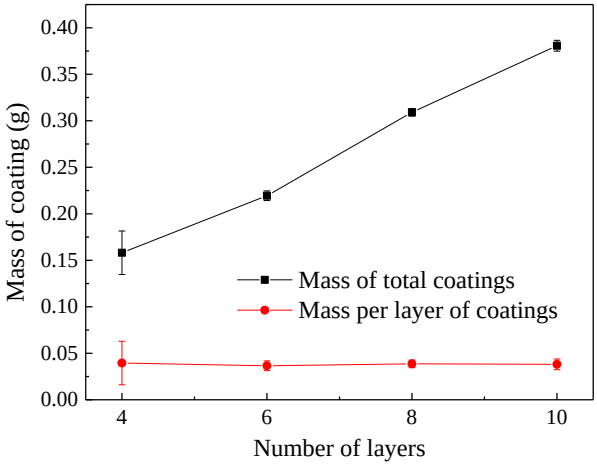

Figure 4-19 The mass of total coatings and mass per layer (n = 3).

Figure 4-18 also shows that the coating thickness could be different in different areas of the sample. In order to study the influence of local coating thickness on #Die-drawn expansion, D1, D2 and D3 were introduced to distinguish axial, lateral and overall coating thickness. D1 was the average lateral thickness (the average of middle and two circular ends thickness in diameter/lateral directions); D2 was the total circular end thickness in height/axial direction; D3 was the overall average of the sample. D3 was the sum of D1 and D2 times their corresponding area proportions, D3 ≈ 0.89×D1+0.11×D2[38] for each case. The values of D1,

[38] The area of a cylinder consists of area of the lateral $2\pi r \times h$ and the area of the circular ends $2 \times \pi r^2$. Hence, the lateral thickness (D1) should contribute to $2\pi r \times h/(2\pi r \times h + 2 \times \pi r^2)$ proportion of the overall thickness D3 and the circular thickness (D2) should contribute to $2 \times \pi r^2/(2\pi r \times h + 2 \times \pi r^2)$ percentage of D3. r and h were measured for each case before coating and the proportions of D1 and D2 were calculated accordingly. Considering all the data points, the range of the proportion for D1was 0.885 to 0.895 and for D2 was 0.105 to 0.115. Therefore, it is concluded D3 ≈ 0.89×D1+0.11×D2.

D2, D3 and the corresponding per-layer thickness are given in Figure 4-20 (a) and (b).

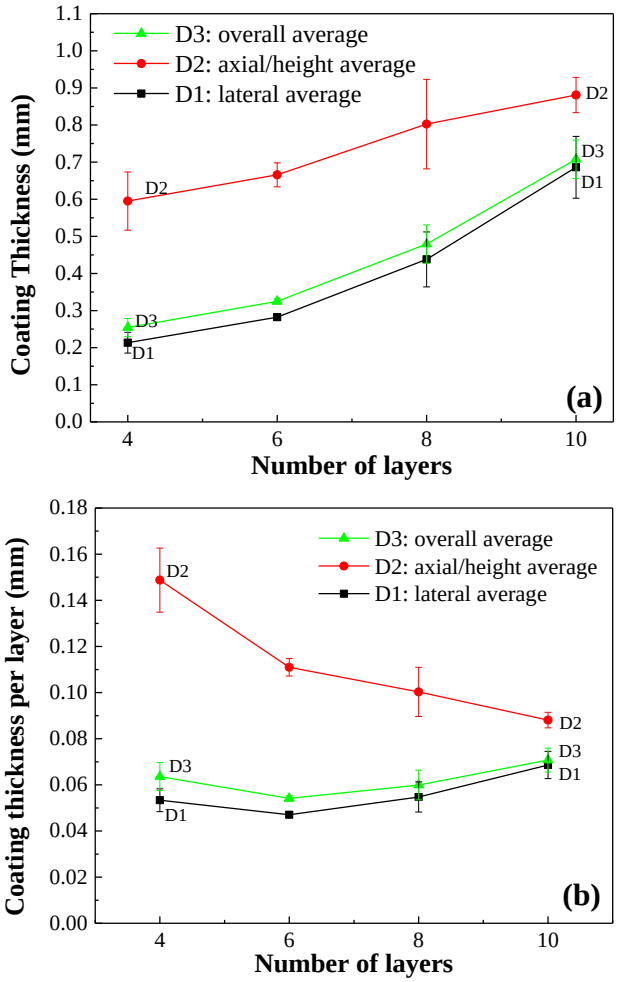

Figure 4-20 PDMS coatings: (a) accumulated thickness, (b) thickness per layer (n = 3).

Figure 4-20 (a) shows that the increase rate of D1 accelerated with the number of layers, reflecting the accumulation of PDMS at the circular ends increased with the repeating times of the process. In Figure 4-20 (b), the per-layer thickness of D2 got closer to D1 as the weight of the strip thickness lessened with the increment of total coating thickness. As the proportion of lateral thickness (D1) is larger than the axial thickness (D2) in the total coating (D3), D3 is closer to D2 in both figures. In addition, D3 should represent the equivalent perfectly uniform

coating thickness for each case. The average per-layer thickness of the PDMS coating ranged from 0.054 to 0.071 mm.

Figure 4-19 and Figure 4-20 altogether reflected that the coating operation was relatively consistent from layer to layer. The dip-coating method developed in this research required lots of manual procedures. It was inefficient manufacturing-wise but provided relatively good consistency and did not rely on extra equipment.

Coating thickness vs swelling behaviour

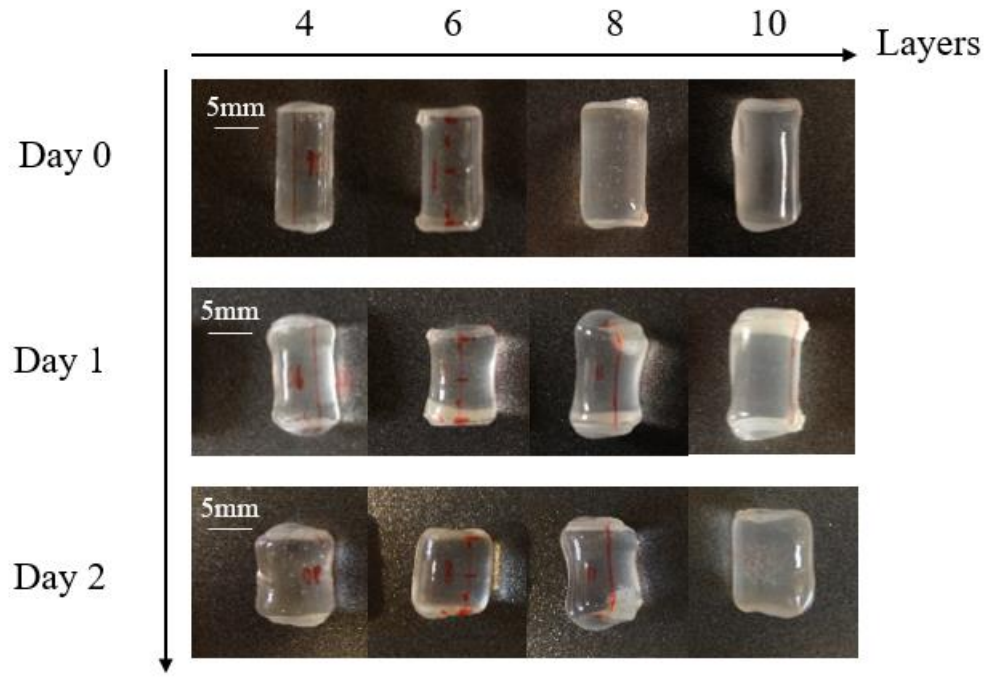

Figure 4-21 Photos of PDMS-coated #Die-drawn during the first three days of swelling.

Figure 4-21 shows the photos of coated sample in its dry state (day 0) and swelling after 1-2 days. The surface waviness observed in the initial swelling of the uncoated samples (as seen

in Figure 4-7, Figure 4-10 and Figure 4-14) did not occur on the coated sample. PDMS membrane essentially reduced the water penetration rate, leading to a smaller amount of water and a smaller gradient of water diffusion distribution in the sample compared to the uncoated samples. Therefore, the more water-sensitive recovery tendency dominated the material deformation initially, and the swelling (volume expansion) was significantly limited.

Figure 4-22 demonstrates the swelling behaviour (diameter, height, volume and height change) of the coated #Die-drawn. Compared to the uncoated #9.5 in Figure 4-8, PDMS coating has significantly reduced the swelling capacity in diameter, height, volume and mass in Figure 4-22. The S_d at day 150 (S_{d-150}) of the coated samples reached 0.47 to 0.69 compared to $S_{d-\infty}$ = 1.81 of the uncoated sample.

In height-wise, the uncoated #9.5 achieved nearly the same height as the dry gel ($S_{h-\infty}$ = 0), while the uncoated samples showed a 22% (10 layers) to 26% (4 layers) deduction after 150 days.

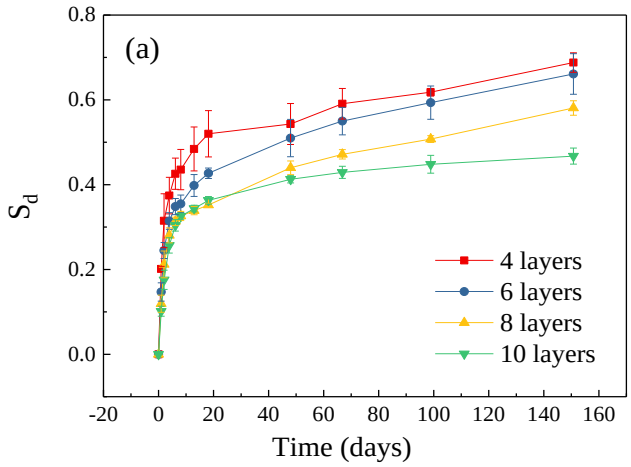

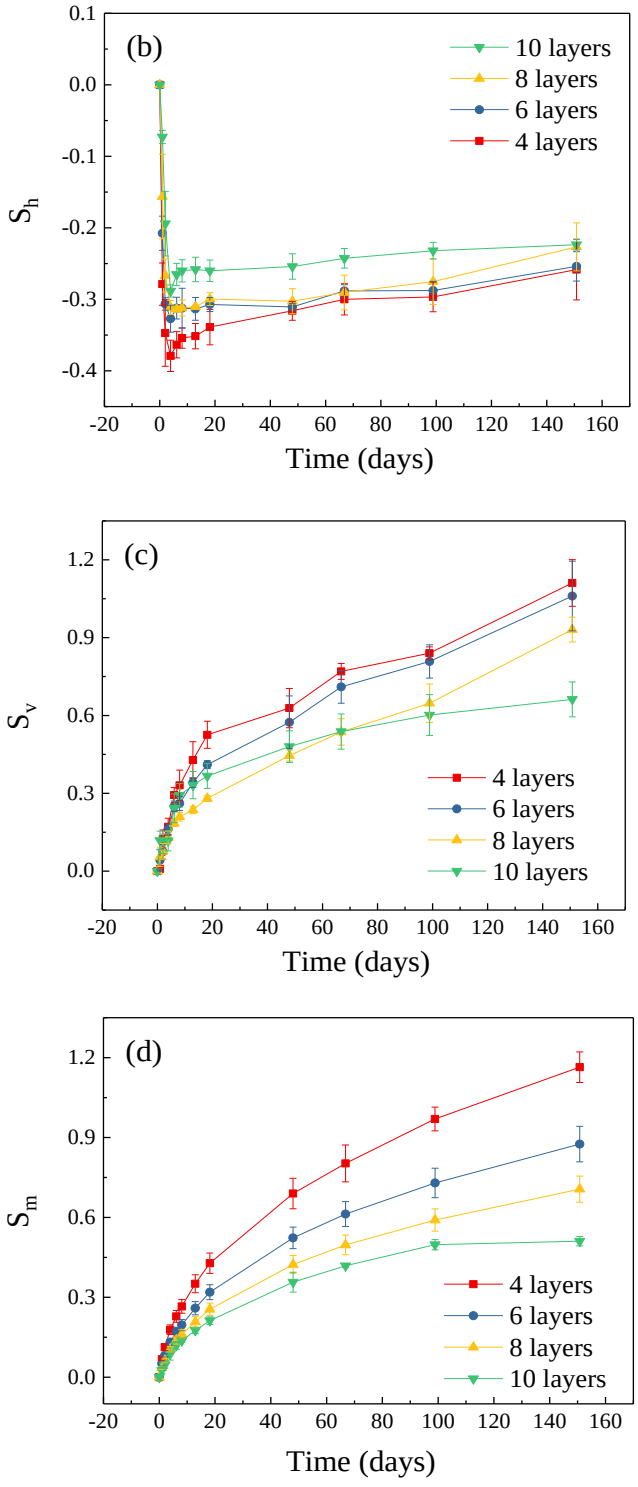

Figure 4-22 Diameter(a), height(b), volume(c) and mass(d) swelling of #Die-drawn coated with different layers of PDMS.

The mass increment of the coated sample achieved only 9% (10 layers) to 20% (4 layers) of the uncoated #9.5 sample, and the volume increase was 10% (10 layers) to 17% (4 layers) of the uncoated ones. In addition, Figure 4-8 (d) shows a plateau for the S_m of the 10-layer-coated samples, indicating that the expansion force of the hydrogel has already reached a balance with the tension of PDMS coating. The other samples with less coating seemed to have remaining expansion potential.

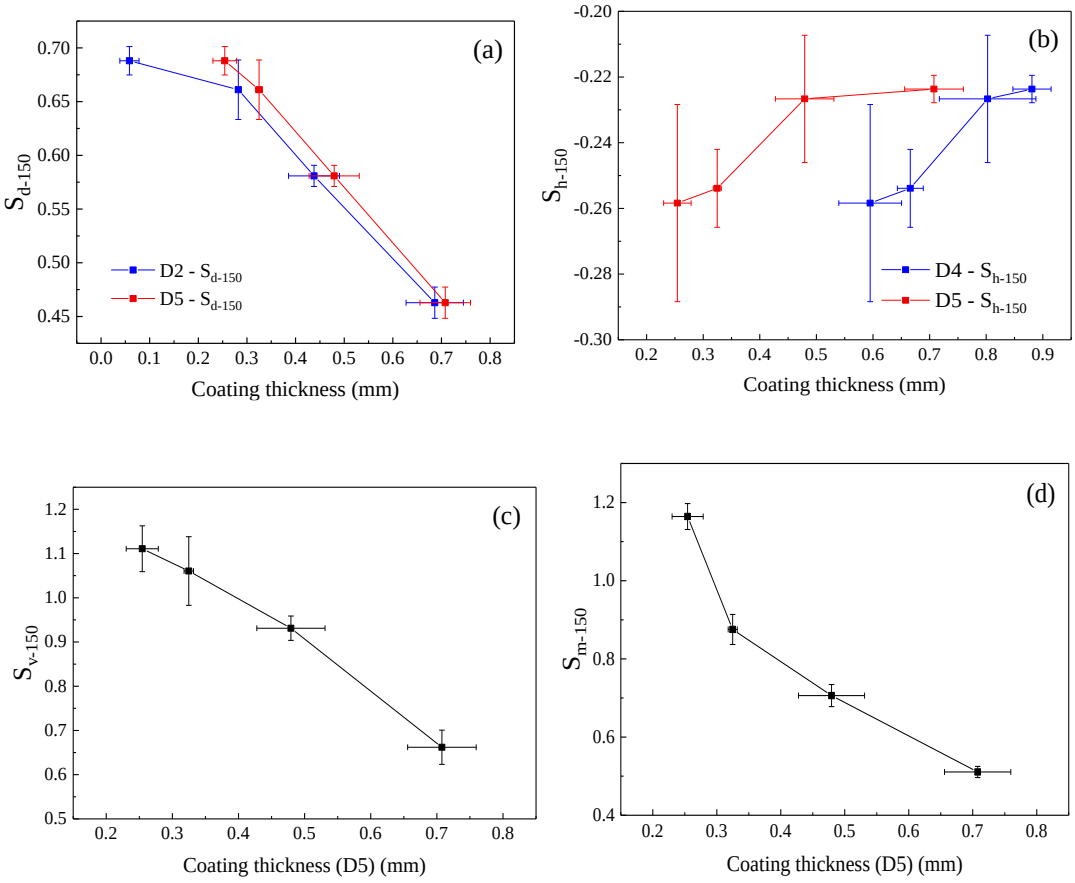

Figure 4-23 The (a) diameter, (b) height, (c) volume and (d) mass swelling ratio at day 150 vs the coating thickness of the samples (n = 3).

Figure 4-23 plots the swelling ratios at day 150 vs the coating layers thickness (D1/D2/D3).

To study whether the unevenness in the coating will influence the directional swelling, D1 was particularly used for the S_{d-150} and D2 for S_{h-150}.

In general, the swelling capacity and rate of the coated samples were primarily dependent on the number of coating layers or coating thickness. Figure 4-23 (a) to (d) show that the S_{d-150}, S_{v-150} and S_{m-150} were all negatively correlated with D3 and the S_{h-150} was positively correlated with D3. In Figure 4-23 (a), D3 presents a better linear fit for the S_{d-150} than D1, suggesting the long-term diameter swelling ratio was more depended on the overall thickness of the sample rather than the local thickness. However, in Figure 4-23 (b), S_{h-150} is better linear-fitted with D2 than D3[39], possibly because the existence of the PDMS strips has provided extra mechanical restrain in the height direction.

Previously, a silicone sheet perforated with laser ablation was used for the hot-compressed poly(VP-MMA). The enveloped sample reached 60-70% of the mass swelling capacity of its uncoated version [40]. The current coating strategies restrained the mass swelling ratio to at least 20%. Improvement needs to be done based on this work, or a new coating method/material should be used in future work to provide sufficient swelling rate control without greatly comprising the swelling capacity. However, the overall swelling capacity reduction will be inevitable unless the membrane can degrade at a reasonable pace.

[39] The linear relationship for D2-S_{h-150} and D3-S_{h-150}: D2: S_{h-150} = 0.134*D2-0.341 (R^2 = 0.9745) and D3: S_{h-150} = 0.073*D3-0.275 (R^2 = 0.9225).

4.3.4 Shape Memory Feature of #Die-drawn

Table 4-2 Data of $S_{d-\infty}$, R_D, $S_{h-\infty}$ and R_H (for #Iso, $S_{d-\infty}{}'$ = 0.98; $S_{h-\infty}{}'$ = 0.99).

Sample	**#9**	**#9.5**	**#10**	**#11**	**#12**	**#13**
$S_{d-\infty}$	1.63	1.81	2.07	2.28	2.63	2.89
R_D	1.72	2.00	2.32	2.74	3.33	3.57
$S_{h-\infty}$	0.11	-0.02	-0.21	-0.29	-0.43	-0.51
R_H	1.76	2.02	2.31	2.65	3.25	3.77

Table 4-3 Value of $d_o{}'/D_0$ ($\frac{d_o{}'}{D_0} = \frac{S_{d-\infty}+1}{\sqrt{R_D}\,(S_{d-\infty}{}'+1)}$) and $h_o{}'/H_0$ ($\frac{h_o{}'}{H_0} = \frac{R_H(S_{h-\infty}+1)}{S_{h-\infty}{}'+1}$).

Sample	**#9**	**#9.5**	**#10**	**#11**	**#12**	**#13**
$\boldsymbol{\frac{d_o{}'}{D_0}}$	1.01	1.00	1.02	1.00	1.01	1.04
$\boldsymbol{\frac{h_o{}'}{H_0}}$	0.98	0.99	0.92	0.95	0.93	0.93

The data obtained from the experiments are listed in Table 4-2. These data yielded the value of $d_o{}'/D_0$ and $h_o{}'/H_0$ in Table 4-3. The average of $d_o{}'/D_0$ and $h_o{}'/H_0$ approximately equal 1, meaning the isotropic counterpart of #Die-drawn and the random #Iso are almost identical, proving that the #Die-drawn memorised its original shape in the unprocessed state.

In detail, although $d_o{}'/D_0$ are close to but slightly larger than 1, $h_o{}'/H_0$ are smaller than 1, meaning the recovery of #Die-drawn (especially the samples with larger deformation ratios) was more than 100%. This might be due to systematic error, or it may indicate that the initial

competition/collaboration between the recovery tendency and swelling tendency eventually led to a final swollen state with internal tension: the polymeric chains in the diameter direction was overstretched due to the synergistic effect of recovery and swelling, resulting in the passive compression of those chains in the height direction.

4.4 Summary

This chapter primarily focused on the swelling properties of the #Die-drawn samples. The #Die-drawn samples achieved significantly increased diameter swelling ratios and restrained height swelling while roughly maintaining the volume and mass swelling ratios compared to the #Iso. As a result, we may conclude that the die-drawing, which applied lateral compression and axial stretching to the hydrogel, achieved our initial hypothesis to increase the lateral swelling and decrease the axial swelling of the material.

The swelling path of the sample was mainly related to the deformation ratio and had no direct relations with the die angle, the drawing rate and the temperature. The higher the deformation ratio, the greater the sample deformation during the subsequent expansion. In the exploration of the shape memory property of #Die-drawn, it was found that the sample remembered its original unprocessed shape.

The whole swelling process of #Die-drawn could be regarded as either cooperation or competition between the recovery trend to its original morphology and the expansion trend to a larger dimension/volume. At the initial stage of swelling, the recovery and expansion of the

die-drawn sample in diameter were towards the same direction; thus, their relation was synergistic and showed a more prominent and rapid swelling than #Iso. At the same time, the recovery and expansion in height were in opposite directions, thus showing the competitive relation. Moreover, the recovery tendency was more prominent at first and outperformed the expansion tendency later, so macroscopically, the height decreased first and then increased. On the other hand, the phenomenon also indicated that the water diffused into the sample acted more as a plasticizer at the beginning, which softened the sample chain and allowed residual stress release. Then gradually, water started to fill and support the hydrogel structure, and the sample manifested the expansion.

Since both the initial swelling force and swelling rate of the #Die-drawn was larger than #Iso, it was necessary to control the swelling rate of #Die-drawn to minimize the complications rates. This work followed the swelling control method of previous work and made a preliminary study on the swelling control of #Die-drawn by a PDMS coating. A modified dip-coating method was developed for the #Die-drawn sample to provide a relatively consistent per-layer coating thickness. The minimum average layer thickness that withstood the swelling force of a Die-drawn sample was around 0.2mm. Although the coating successfully reduced the swelling rate, it also significantly reduced the swelling ratio. After 150 days, the thinnest coated sample reached a diameter swelling of merely 39% of its uncoated counterpart.

5 Summary and Future Work

5.1 Summary

Based on the previous work on the hot-pressing of poly(VP-MMA) and the die-drawing experience of thermoplastic polymers, This present work used the die-drawing processing to impart shape memory feature to the poly(VP-MMA) hydrogel and successfully produced a novel bilateral swelling self-inflating tissue expander.

In the processing, the cylindrical poly(VP-MMA) was die-drawn through a conical die at/around its glass transition temperature. The processing parameters, including die angle, drawing temperature, deformation ratio, and drawing rate, were explored to provide a protocol for the successful die-drawing of poly(VP-MMA). The drawing stress significantly increased with the die-angle and was positively correlated with the deformation ratios. For a 5° semi-angle die, the maximum elongation (deformation ratio) in the die-drawing process was 3.7, the drawing rates suitable was 0.1 to 6 mm/s and the temperature was 145-180°C.

In addition, a mathematic model based on the simple syndactyly case was established to study the tissue generation capacity of uniaxial (1D-Uni), bilateral (2D-Bi), and isotropic (3D-Iso) HTEs. Based on the assumption of phalanx radius (R) was 1/10 of its length (L), it was proved that 2D-Bi overall requires the shortest incision at insertion site, has most valid cases in terms of stability and swelling capability and the lowest requirement of material intrinsic swelling ratio compared to 1D-Uni and 3D-Iso HTE. Moreover, the results can be extended into much broader range of L/R values (2~20). In terms of the required individual and total swollen volume, 1D-Uni outperformed the others and was the most cost-efficient HTE. In all, the

anisotropic HTE showed considerable advantages over the isotropic ones.

The die-drawn product with different R_{Ave} (#Die-drawn) and the unprocessed isotropic gel (#Iso) were characterized by differential scanning calorimetry (DSC), X-ray diffraction analysis (XRD) and the optical microscope (OM). DSC data showed that #Die-drawn has a slightly increased glass transition temperature compared to #Iso, reflecting reduced chain mobility of the processed sample. OM showed elongated voids occurred exclusively on the lateral side of #Die-drawn while were absent on the cross-sections of the #Die-drawn and the #Iso. The void area and width increase with the deformation ratio, suggesting that a higher R_{Ave} and correspondingly higher axial drawing stress had resulted in a more prominent orientation along the drawing direction. However, the XRD results showed no conclusive evidence of increased crystallization after the die-drawing process. More analysis on the #Die-drawn may be done to determine the extent of crystallization and orientation.

In the #Die-drawn swelling experiments, the expansion rate, ratio and force of the cylindrical #Die-drawn sample were increased in the diameters but inhibited in the longitudinal (axial) direction. The extent of this anisotropy was tunable and with specific R_{Ave} = 2.0, the #Die-drawn could merely have radial expansion (diameter increase) at equilibrium without height change compared to its dry state. In addition, with appropriate processing parameters, the processed material could expand to the same shape as the untreated material suggesting its shape memory properties. The swelling rate and force of #Die-drawn were faster and larger than #Iso, which led to a preliminary study on the swelling rate control. Polydimethylsiloxane

(PDMS) was used as the coating material. While the coating significantly reduced the swelling rate of #Die-drawn, it simultaneously restrained its overall swelling capacity. #Die-drawn coated with 0.22 mm PDMS achieved 40% of the uncoated sample's diameter swelling and 20% in the water mass intake.

In summary, this present study mathematically proved the advantages of bilateral swelling self-inflating tissue expanders over uniaxial swelling tissue expanders and the isotropic tissue expanders, and further proved the idea of using die-drawing to achieve the shape memory feature of poly(VP-MMA) and obtained hydrogel tissue expander with tunable anisotropic swelling capacities.

The bilateral expansion of materials by means of moulding provides a new dimension for the expansion control of hydrogels. Theoretically, materials with similar shape memory types can achieve biaxial (bilateral) expansion by means of this method. Therefore, according to the characteristics of the application object, by choosing the hydrogel base material with appropriate strength and swelling properties, the application of this processing route could be extended to a much wider field, such as some specific congenital defects and endovascular embolization for various diseases.

5.2 Future Work

There are many unfulfilled tasks in this work. The quantitative study of the material orientation has not been carried out, and the swelling rate control was not satisfied. The animal studies on

the coated die-drawn poly(VP-MMA) have not been done to provide valuable data on how the bilateral swelling HTE will influence the growth of skin/tissue compared to the #Iso and uniaxial swelling anisotropic samples.

New coating methods or new coating materials may be explored to provide a suitable swelling rate and sufficient swelling ratio at the same time. Spray coating may be used to provide a more uniform coating; appropriate proliferation of the coating may be done to accelerate the water penetration; coating materials with lower Young's modulus but higher shear strength may be applied. Alternatively, if the existence of the membrane cannot achieve the full expansion of the #Die-drawn, raw material with higher intrinsic swelling capacity can be used.

A few improvements could also be made in the die-drawing process, and the potential for the large-scale production of the #Die-drawn poly(VP-MMA) could be investigated. The samples could be synthesized into a torch shape with the rightful diameter to be more effective. The temperature control system could be improved to provide faster and more controllable in-die heating and out-die cooling environments. The mechanical system could be rotated to a horizontal fashion to facilitate a longer-term die-drawing process. For the large scale production of #9.5 die-drawn poly(VP-MMA), a furnace of 30-40cm length could be mounted onto the motor-driven drawing machine with two special-designed alternative moving clamps and a cutting tool installed at the die-exit. If the die-drawing process is carried out at 145°C under continuous mode (CND) with a 0.30 mm/s drawing rate, the #9.5 can possibly achieve a smooth heating and die-drawing process. Such a die-drawing process should be able to

produce a die-drawn rod at 20 cm per minute consistently. This might be much faster than the hot pressing process as the hot-pressing, in which a batch of product may take 100 to 120 min. The mechanism of hot-pressing determines that the sample must wait for the mould to cool down before being taken out.

There are also other potential applications for die-drawn shape-memory hydrogel/polymers. The bilateral swelling ability could be imparted on other materials for a broader application field. For instance, a die-drawn hydrogel with fast-swelling properties (possibly achieved by porous structures, e.g., superporous hydrogel) and exhibits a degree of viscosity on the vascular walls can be used as an endovascular occlusion material.

For example, the hepatic artery plays a dominant role in the blood supply of the liver tumour. By blocking the hepatic artery, the passage of essentials to support tumour growth is obstructed and therefore, the angiogenesis is retarded or even terminated. Another example is the atrial septal defect (ASD). ASD is a congenital heart disease wherein the septum between the left and right atrial is not integral, resulting in the blood flow between two compartments. The bilateral hydrogel expander can potentially be applied as a ‘plug’ to block the septal leakage. A double-headed umbrella-like/mushroom-like bilateral swelling expander, shown in Figure 6-14, may be applied in this case or other cases with similar settings.

In summary, future research can build on the current poly (VP-MMA) work, further understand the characterization of the die-drawn poly(VP-MMA) nature, and explore its performance in animal and clinical trials. In addition, we can target more extensive areas such as vascular

occlusion by applying this die-drawing technique on suitable hydrogel systems with shape memory potentials to achieve the bilateral swelling.

6 Appendix

6.1 Appendix I: Equations for Modelling ($A_r = A_g$)

6.1.1 2D-Bi Models

1) 2D-Bi-NA-#T

$$2\pi RL - 4RL = \left(2\pi - \frac{\pi}{2} - cos^{-1}\frac{R-r}{R+r} - cos^{-1}\frac{R}{R+r}\right) \times 2RL + 2RL + 2 \times 2\sqrt{Rr}L +$$

$$\left(2\,cos^{-1}\frac{R-r}{R+r} + 2\,cos^{-1}\frac{R}{R+r} - \pi\right)rL - 2\pi RL - 4RL \quad \text{Eq. 6.1}$$

$$\pi - 1 = (a - 1)\left(\theta_1 + \theta_2 - \frac{\pi}{2}\right) + 2\sqrt{a} \quad \text{Eq. 6.2}$$

2) 2D-Bi-NA-#TB

$$2\pi RL - 4RL = \left(2\pi - 2\,cos^{-1}\frac{R-r}{R+r} - 2cos^{-1}\frac{R}{R+r}\right) \times 2RL + 4 \times 2\sqrt{Rr}L - 2\pi RL - 4RL +$$

$$2 \times \left(2\,cos^{-1}\frac{R-r}{R+r} + 2\,cos^{-1}\frac{R}{R+r} - \pi\right)rL \quad \text{Eq. 6.3}$$

$$(a - 1)(\theta_1 + \theta_2) + 2\sqrt{a} = \frac{\pi}{2}a \quad \text{Eq. 6.4}$$

3) 2D-Bi-NA-#T-Single

$$a\left[\pi - \cos^{-1}\left(\sqrt{\frac{2}{a} + 1} - \frac{1}{a}\right)\right] - \sqrt{2\sqrt{2a + a^2} - 1 - 2a} = \pi - 2 \quad \text{Eq. 6.5}$$

4) 2D-Bi-NA-#TB-Single

$$a\left[\pi - cos^{-1}\left(\sqrt{\frac{2}{a} + 1} - \frac{1}{a}\right)\right] - \sqrt{2\sqrt{2a + a^2} - 1 - 2a} = \frac{\pi-2}{2} \quad \text{Eq. 6.6}$$

5) 2D-Bi-A-#T-Multiple

$$2n(r^2 - rh)\left[\pi - cos^{-1}\left(\frac{\sqrt{2Rr+r^2}-R}{r}\right)\right] + n\sqrt{2R\sqrt{2Rr+r^2} - 2Rr - R^2}\left(\sqrt{2Rr+R^2} - R\right) -$$

$$2hn\sqrt{2R\sqrt{2Rr+r^2} - 2Rr - R^2} = 2\pi RL - 4RL \quad \text{Eq. 6.7}$$

$$b\left\{-an\left[\pi - cos^{-1}\left(\sqrt{\frac{2}{a} + 1} - \frac{1}{a}\right)\right] + n\sqrt{2\sqrt{2\,a + a^2} - 2\,a - 1} + n(2\pi - 4) + 2 - \pi\right\} = (n - 1)\left\{\left[\pi - cos^{-1}\left(\sqrt{\frac{2}{a} + 1} - \frac{1}{a}\right)\right] a^2 + (\sqrt{2\,a + a^2} - 1)\sqrt{2\sqrt{2\,a + a^2} - 2\,a - 1}\right\} \quad \text{Eq. 6.8}$$

6) 2D-Bi-A-#TB –Multiple

$$\frac{1}{2}(2\pi RL - 4RL) = 2(n-1)\sqrt{2\sqrt{2Rr+r^2} - 2Rr - R^2}\left(\sqrt{2Rr+R^2} - R\right) +$$

$$2r[(n-1)r + nh]\left[\pi - cos^{-1}\left(\frac{\sqrt{2Rr+r^2}-R}{r}\right)\right] - 2hn\sqrt{2R\sqrt{2Rr+r^2} - 2Rr - R^2} \quad \text{Eq. 6.9}$$

$$b\left\{-an\left[\pi - cos^{-1}\left(\sqrt{\frac{2}{a} + 1} - \frac{1}{a}\right)\right] + n\sqrt{2\sqrt{2\,a + a^2} - 2\,a - 1} + n(\pi - 2) + 1 - \frac{\pi}{2}\right\} = (n - 1)\left\{\left[\pi - cos^{-1}\left(\sqrt{\frac{2}{a} + 1} - \frac{1}{a}\right)\right] a^2 + (\sqrt{2\,a + a^2} - 1)\sqrt{2\sqrt{2\,a + a^2} - 2\,a - 1}\right\} \quad \text{Eq. 6.10}$$

6.1.2 1D-Uni Models

7) 1D-Uni-NA-#T

$$\left[2\sqrt{H^2 + 2H\sqrt{2Rr - r^2}} + 2r + 2R + 2R\left(2\pi - tan^{-1}\sqrt{H^2 + 2H\sqrt{2Rr - r^2}} - tan^{-1}\frac{H+\sqrt{2Rr-r^2}}{R-r} - \frac{\pi}{2}\right) - 2\pi R - 4R\right]L = 2\pi RL - 4RL \quad \text{Eq. 6.11}$$

$$\sqrt{b^2 + 2b\sqrt{2a - a^2}} + a - tan^{-1}\sqrt{b^2 + 2b\sqrt{2a - a^2}} - tan^{-1}\frac{b+\sqrt{2a-a^2}}{1-a} = \frac{\pi}{2} - 1 \quad \text{Eq. 6.12}$$

8) 1D-Uni -NA-#TB

$$\left[4\sqrt{H^2+2H\sqrt{2Rr-r^2}}+4r+2R\left(2\pi-2\,tan^{-1}\sqrt{H^2+2H\sqrt{2Rr-r^2}}-\right.\right.$$

$$\left.\left.2tan^{-1}\frac{H+\sqrt{2Rr-r^2}}{R-r}\right)-2\pi R-4R\right]L=2\pi RL-4RL \qquad \text{Eq. 6.13}$$

$$\sqrt{b^2+2b\sqrt{2a-a^2}}+a=tan^{-1}\sqrt{b^2+2b\sqrt{2a-a^2}}+tan^{-1}\frac{b+\sqrt{2a-a^2}}{1-a} \qquad \text{Eq. 6.14}$$

9) 1D-Uni -A-#T-Single

$$2L(H-H_0)=2\pi RL-4RL \qquad \text{Eq. 6.15}$$

$$(m\ -\ 1)\ (1\ -\ \sqrt{2\ a\ -\ a^2})\ =\ \pi\ -\ 2 \qquad \text{Eq. 6.16}$$

10) 1D-Uni -NA-#TB-Single

$$4L(H-H_0)=2\pi RL-4RL \qquad \text{Eq. 6.17}$$

$$(m\ -\ 1)\ (1\ -\ \sqrt{2\ a\ -\ a^2})\ =\ \frac{\pi-2}{2} \qquad \text{Eq. 6.18}$$

11) 1D-Uni -A-#T -Multiple

$$2\pi rn(H-H_0)=2\pi RL-4RL \qquad \text{Eq. 6.19}$$

$$m\ =\ \frac{2n-1}{n(1-\sqrt{2\ a-a^2})}\times\frac{\pi-2}{\pi}+1 \qquad \text{Eq. 6.20}$$

12) 1D-Uni -A-#TB-Multiple

$$4\pi rn(H-H_0)=2\pi RL-4RL \qquad \text{Eq. 6.21}$$

$$m=\frac{2n-1}{n(1-\sqrt{2\ a-a^2})}\times\frac{\pi-2}{2\pi}+1 \qquad \text{Eq. 6.22}$$

6.1.3 3D-Iso Models (Sphere)

13) 3D- A-#T-Multiple

$$2\pi rn\left(\sqrt{2Rr+r^2}-R+r\right)-\pi n\left(\sqrt{2R\sqrt{2Rr+r^2}-2Rr-R^2}\right)^2=2(\pi-2)RL \quad \text{Eq. 6.23}$$

$$\pi n\left((a-1)\sqrt{2a+a^2}+a^2+\frac{1}{2}\right)=(\pi-2)\frac{L}{R} \quad \text{Eq. 6.24}$$

14) 3D- A-#TB-Multiple

$$2\left[2\pi rn\left(\sqrt{2Rr+r^2}-R+r\right)-\pi n\left(\sqrt{2R\sqrt{2Rr+r^2}-2Rr-R^2}\right)^2\right]$$

$$=2(\pi-2)RL \quad \text{Eq. 6.25}$$

$$\pi n\left((a-1)\sqrt{2a+a^2}+a^2+\frac{1}{2}\right)=(\pi-2)\frac{L}{2R} \quad \text{Eq. 6.26}$$

6.2 Appendix II: Supplementary Figures

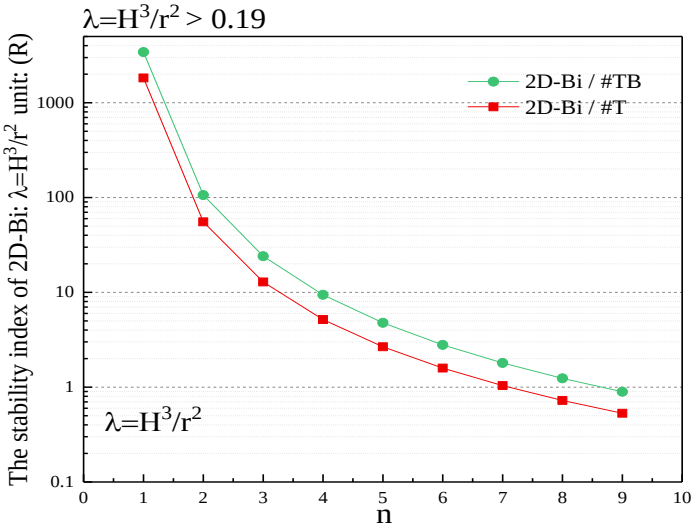

Figure 6-1 Stability index of 2D-Bi based on Brush equation, $\lambda = {H^3}/{r^2}$.

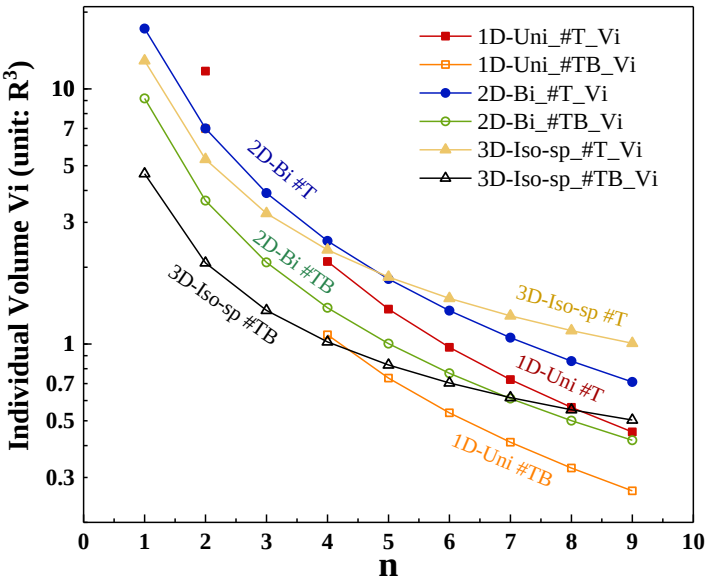

Figure 6-2 The required volume individual volume of each HTE (V_i) for all cases. Note that 2D-Bi represents 3D-Iso-cy(2D) and 1D-Uni represents 3D-Iso-cy(1D).

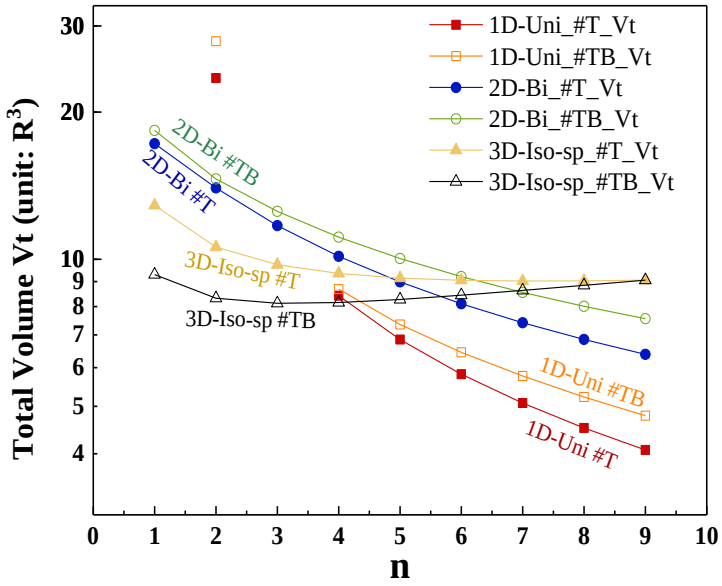

Figure 6-3 The required total HTEs volume (V_t) for all cases. Note that 2D-Bi represents 3D-Iso-cy(2D) and 1D-Uni represents 3D-Iso-cy(1D).

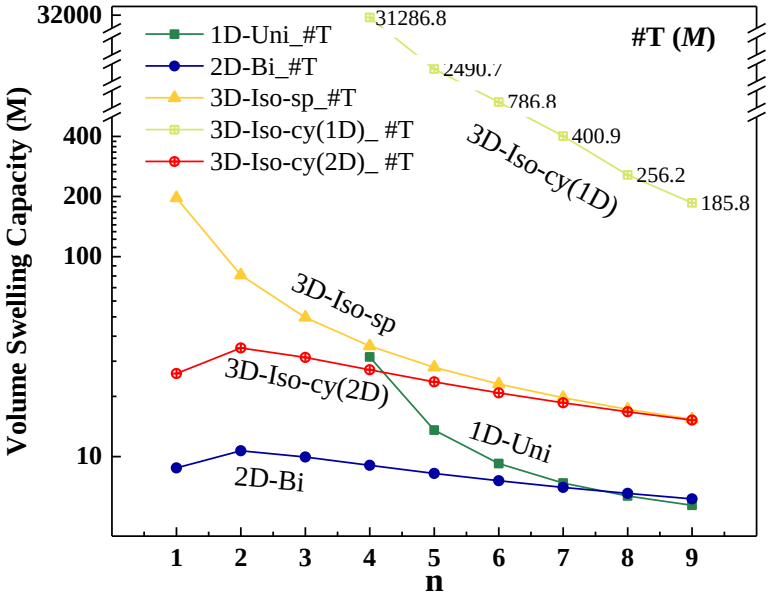

(b)

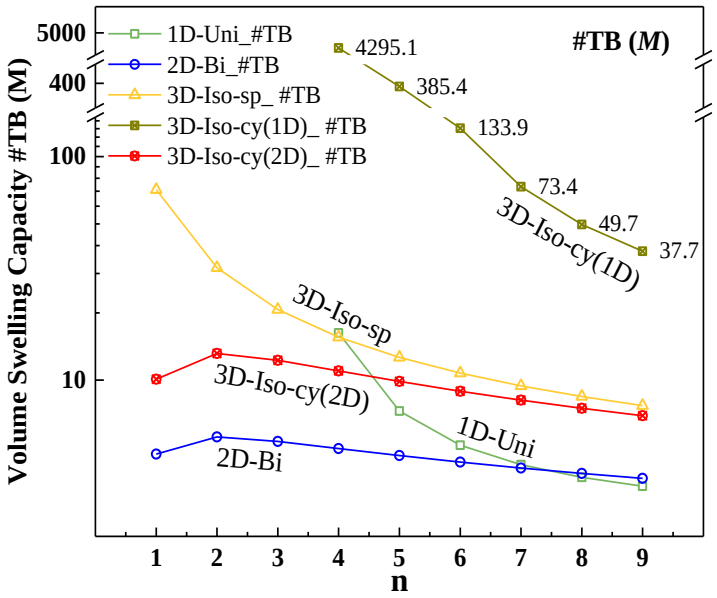

Figure 6-4 The required volume swelling capacity (M) for all (a) #T cases and (b) #TB cases.

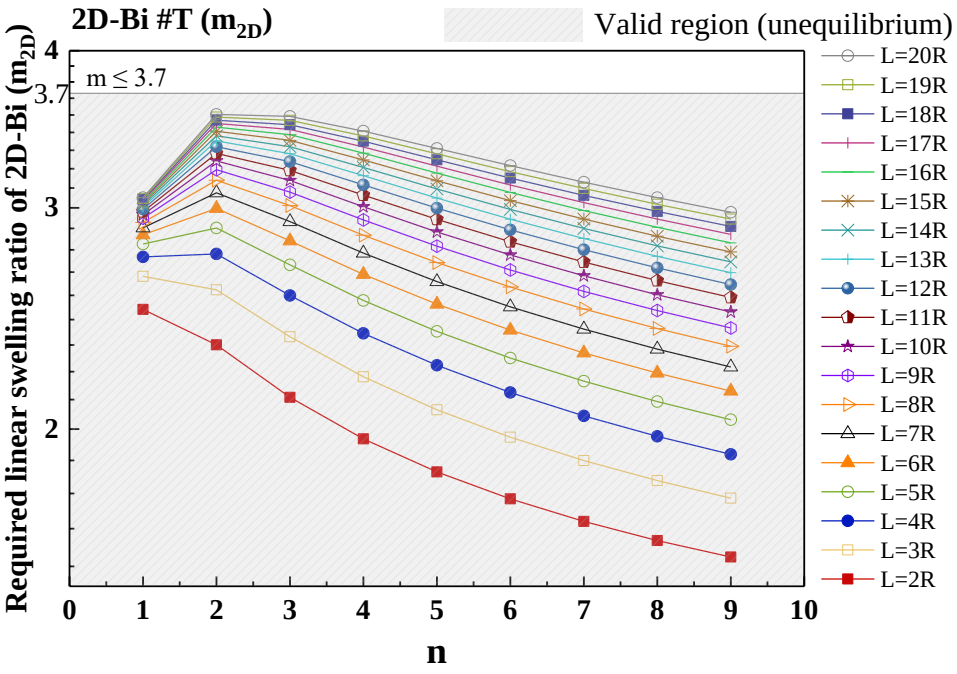

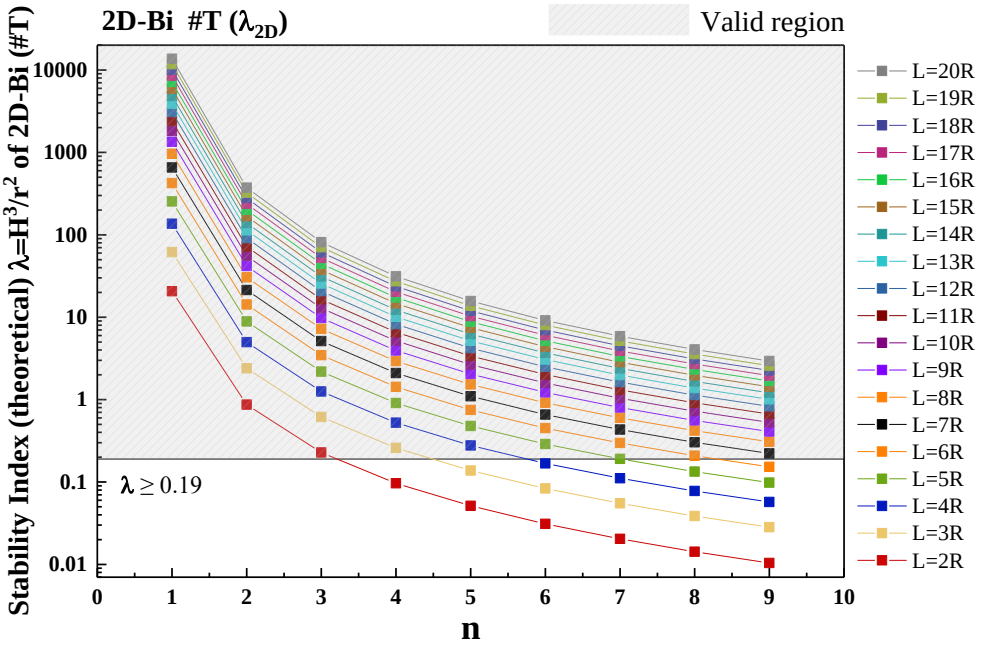
2D-Bi #T (λ_{2D})
Valid region
Stability Index (theoretical) $\lambda=H^3/r^2$ of 2D-Bi (#T)
$\lambda \geq 0.19$
n
L=20R
L=19R
L=18R
L=17R
L=16R
L=15R
L=14R
L=13R
L=12R
L=11R
L=10R
L=9R
L=8R
L=7R
L=6R
L=5R
L=4R
L=3R
L=2R

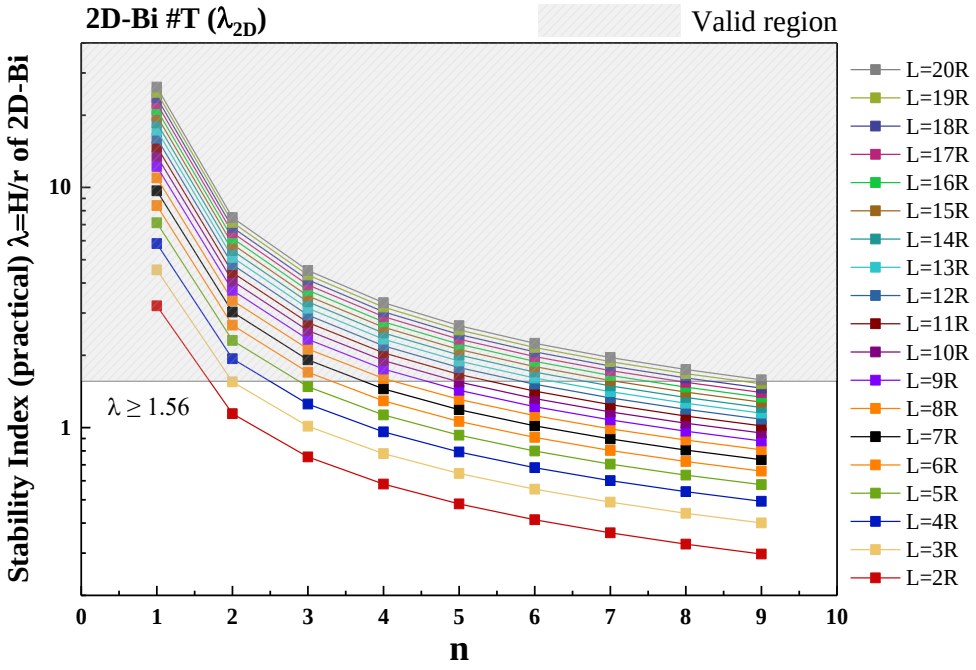
2D-Bi #T (λ_{2D})
Valid region
Stability Index (practical) $\lambda=H/r$ of 2D-Bi
$\lambda \geq 1.56$
n
L=20R
L=19R
L=18R
L=17R
L=16R
L=15R
L=14R
L=13R
L=12R
L=11R
L=10R
L=9R
L=8R
L=7R
L=6R
L=5R
L=4R
L=3R
L=2R

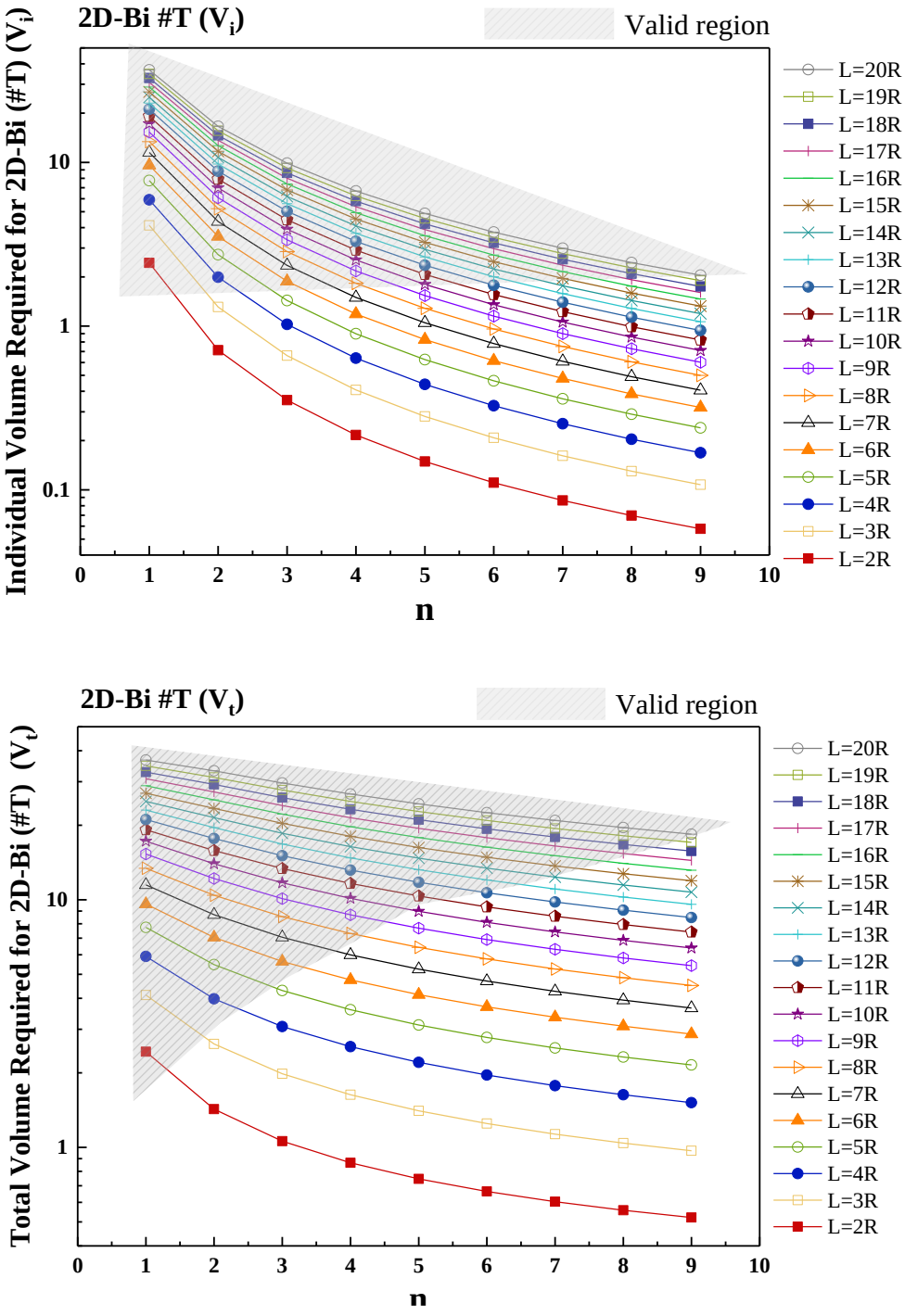

Figure 6-5 The L/R influence on m, λ, V_i, V_t of 2D-Bi (#T).

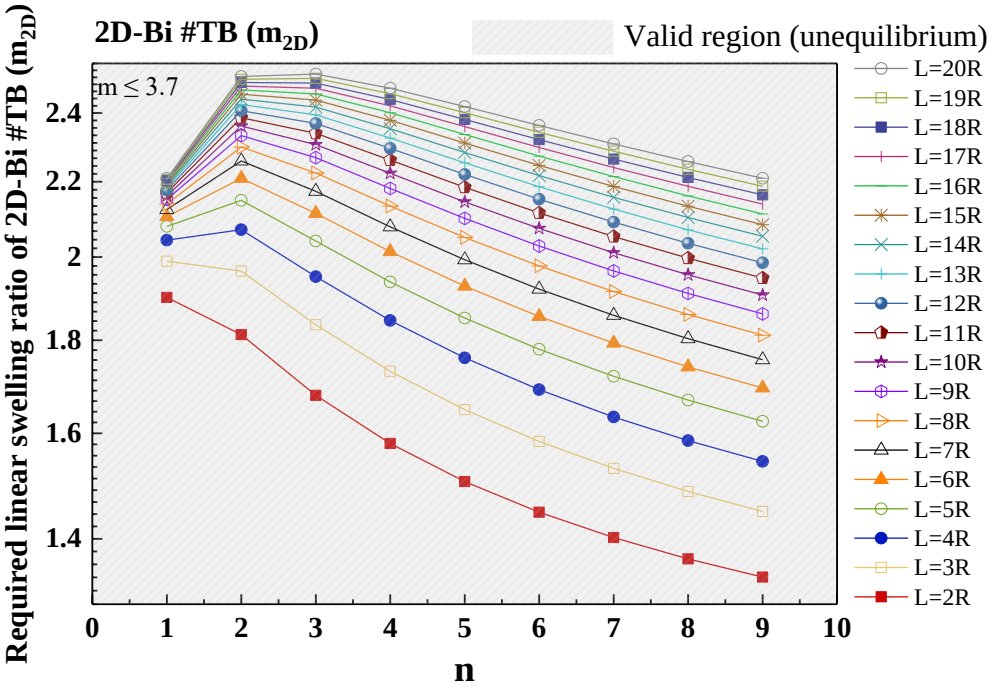
2D-Bi #TB (m_{2D})
Valid region (unequilibrium)
m ≤ 3.7
Required linear swelling ratio of 2D-Bi #TB (m_{2D})
n
L=20R
L=19R
L=18R
L=17R
L=16R
L=15R
L=14R
L=13R
L=12R
L=11R
L=10R
L=9R
L=8R
L=7R
L=6R
L=5R
L=4R
L=3R
L=2R

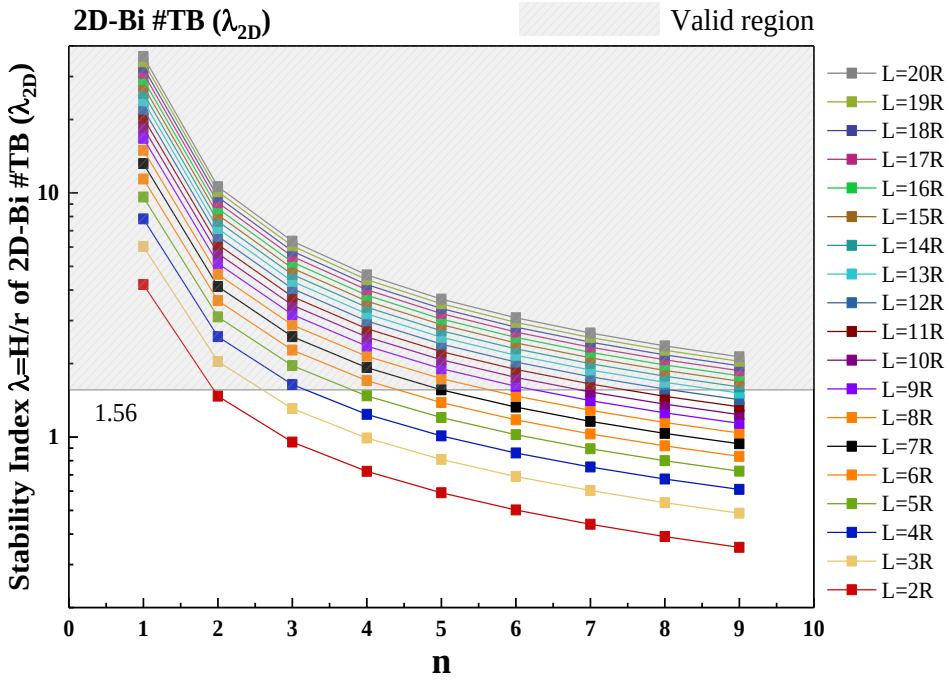
2D-Bi #TB (λ_{2D})
Valid region
1.56
Stability Index λ=H/r of 2D-Bi #TB (λ_{2D})
n
L=20R
L=19R
L=18R
L=17R
L=16R
L=15R
L=14R
L=13R
L=12R
L=11R
L=10R
L=9R
L=8R
L=7R
L=6R
L=5R
L=4R
L=3R
L=2R

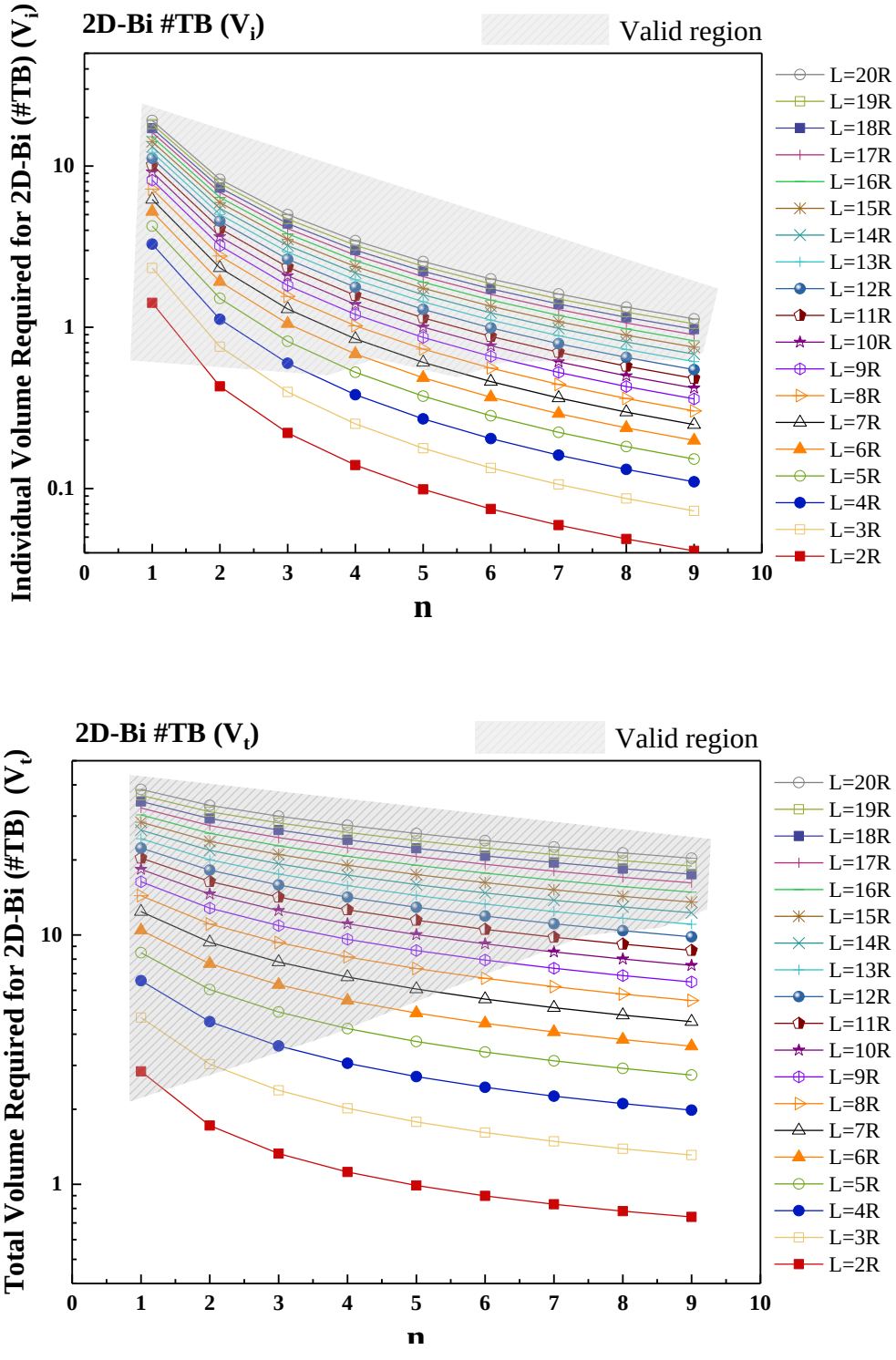

Figure 6-6 The L/R influence on m, λ, V_i, V_t of 2D-Bi (#TB).

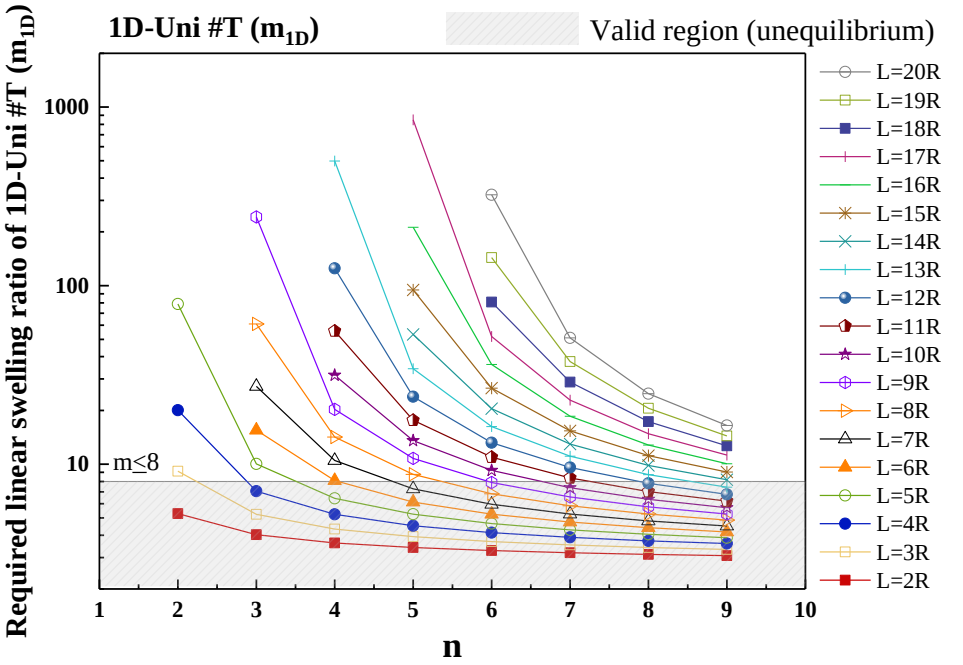
1D-Uni #T (m_{1D})
Valid region (unequilibrium)
Required linear swelling ratio of 1D-Uni #T (m_{1D})
1000
100
10
m≤8
1
2
3
4
5
6
7
8
9
10
n
L=20R
L=19R
L=18R
L=17R
L=16R
L=15R
L=14R
L=13R
L=12R
L=11R
L=10R
L=9R
L=8R
L=7R
L=6R
L=5R
L=4R
L=3R
L=2R

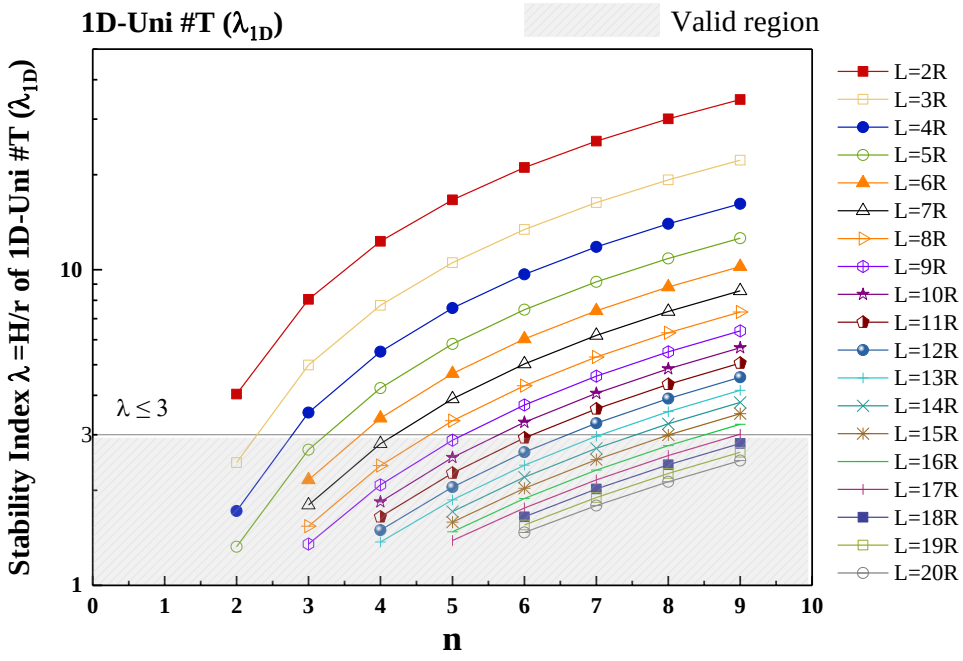
1D-Uni #T (λ_{1D})
Valid region
Stability Index λ=H/r of 1D-Uni #T (λ_{1D})
10
3
1
λ ≤ 3
0
1
2
3
4
5
6
7
8
9
10
n
L=2R
L=3R
L=4R
L=5R
L=6R
L=7R
L=8R
L=9R
L=10R
L=11R
L=12R
L=13R
L=14R
L=15R
L=16R
L=17R
L=18R
L=19R
L=20R

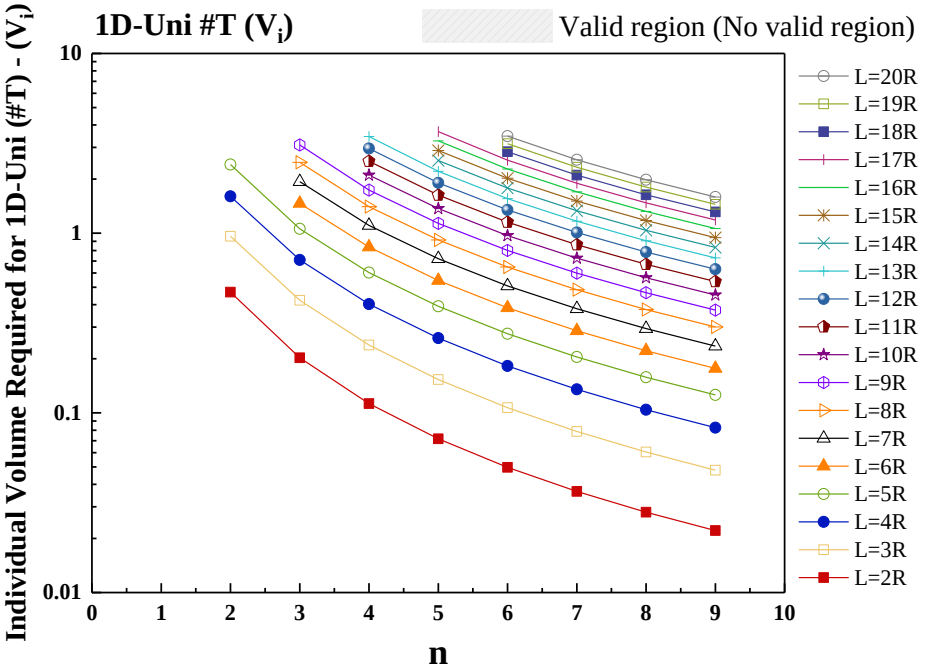

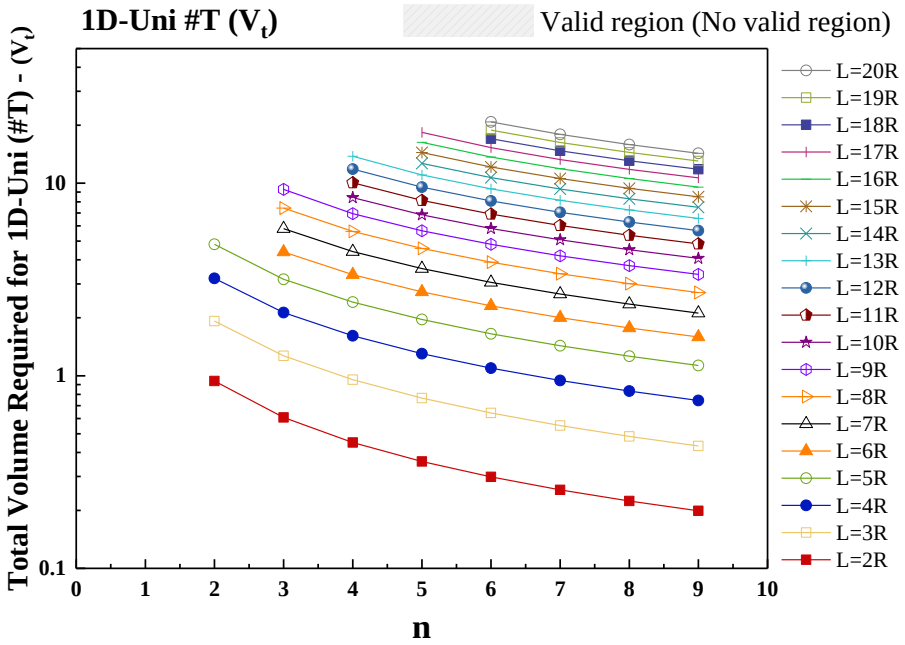

Figure 6-7 The L/R influence on m, λ, V_i, V_t of 1D-Uni (#T).

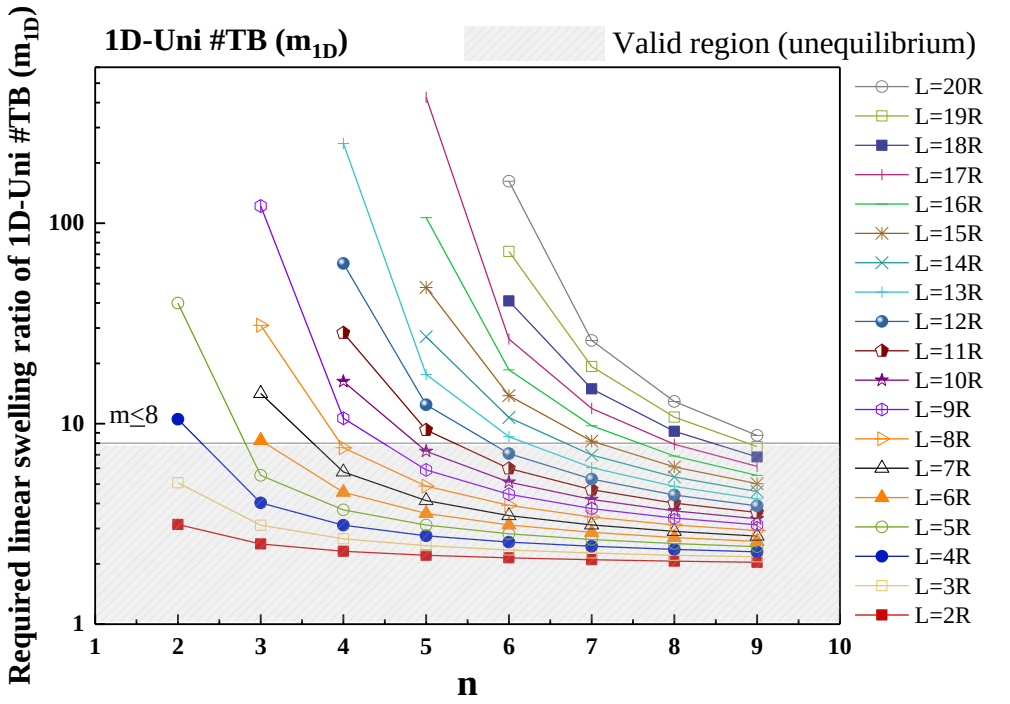
1D-Uni #TB (m_{1D})
Valid region (unequilibrium)
Required linear swelling ratio of 1D-Uni #TB (m_{1D})
m≤8
n
L=20R
L=19R
L=18R
L=17R
L=16R
L=15R
L=14R
L=13R
L=12R
L=11R
L=10R
L=9R
L=8R
L=7R
L=6R
L=5R
L=4R
L=3R
L=2R

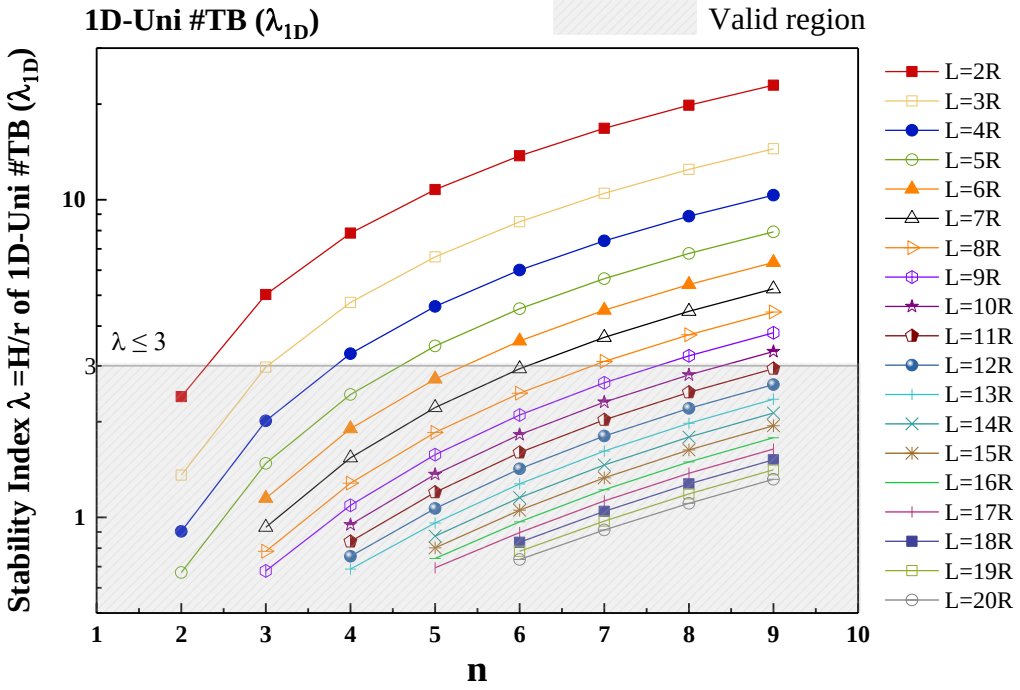
1D-Uni #TB (λ_{1D})
Valid region
Stability Index λ =H/r of 1D-Uni #TB (λ_{1D})
λ ≤ 3
n
L=2R
L=3R
L=4R
L=5R
L=6R
L=7R
L=8R
L=9R
L=10R
L=11R
L=12R
L=13R
L=14R
L=15R
L=16R
L=17R
L=18R
L=19R
L=20R

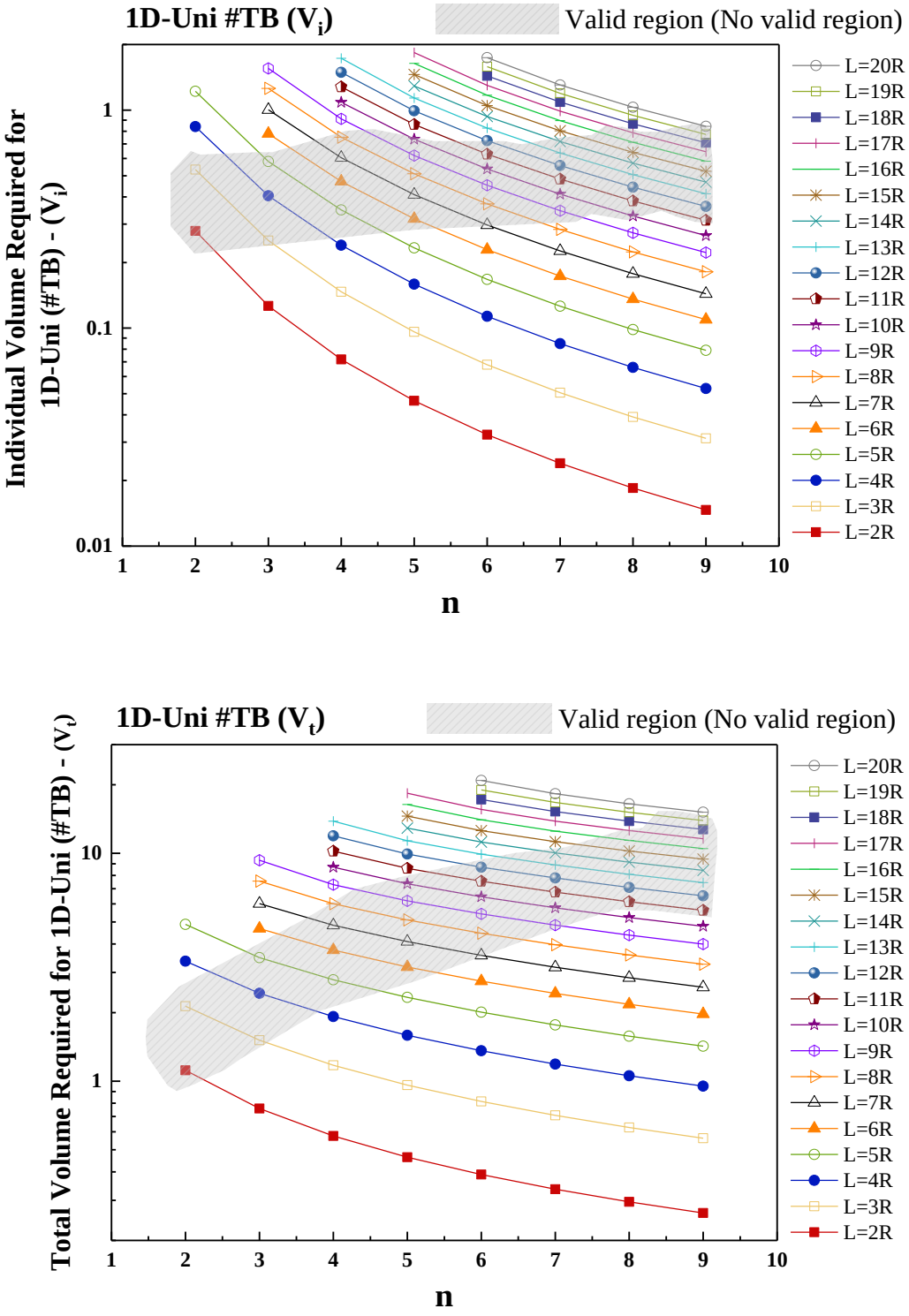

Figure 6-8 The L/R influence on m, λ, V_i, V_t of 1D-Uni (#TB).

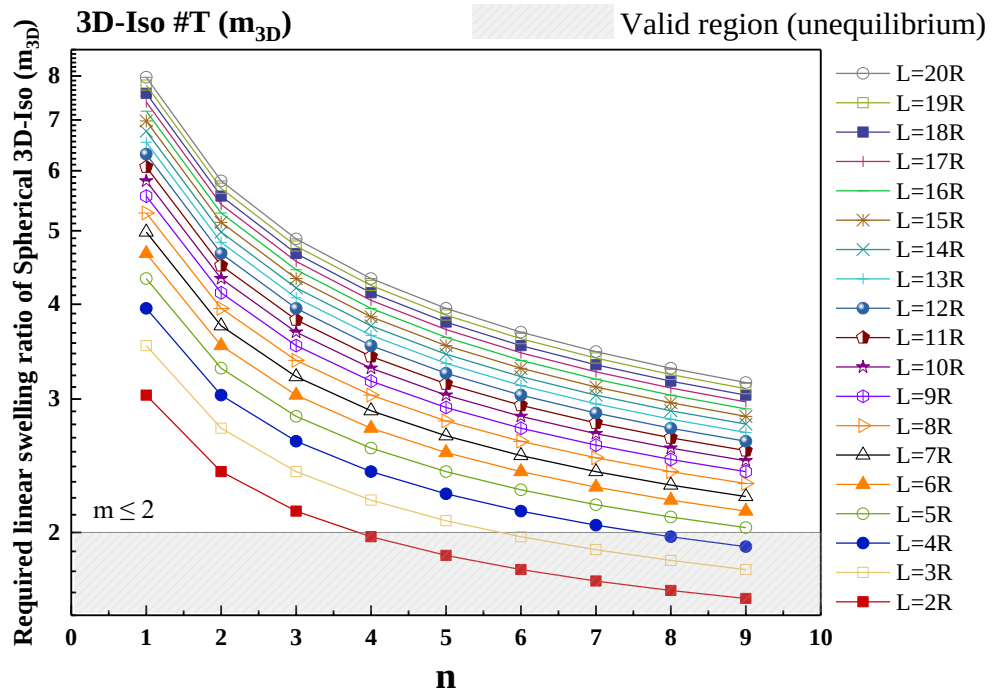
3D-Iso #T (m_{3D})
Valid region (unequilibrium)
Required linear swelling ratio of Spherical 3D-Iso (m_{3D})
m ≤ 2
n
L=20R
L=19R
L=18R
L=17R
L=16R
L=15R
L=14R
L=13R
L=12R
L=11R
L=10R
L=9R
L=8R
L=7R
L=6R
L=5R
L=4R
L=3R
L=2R

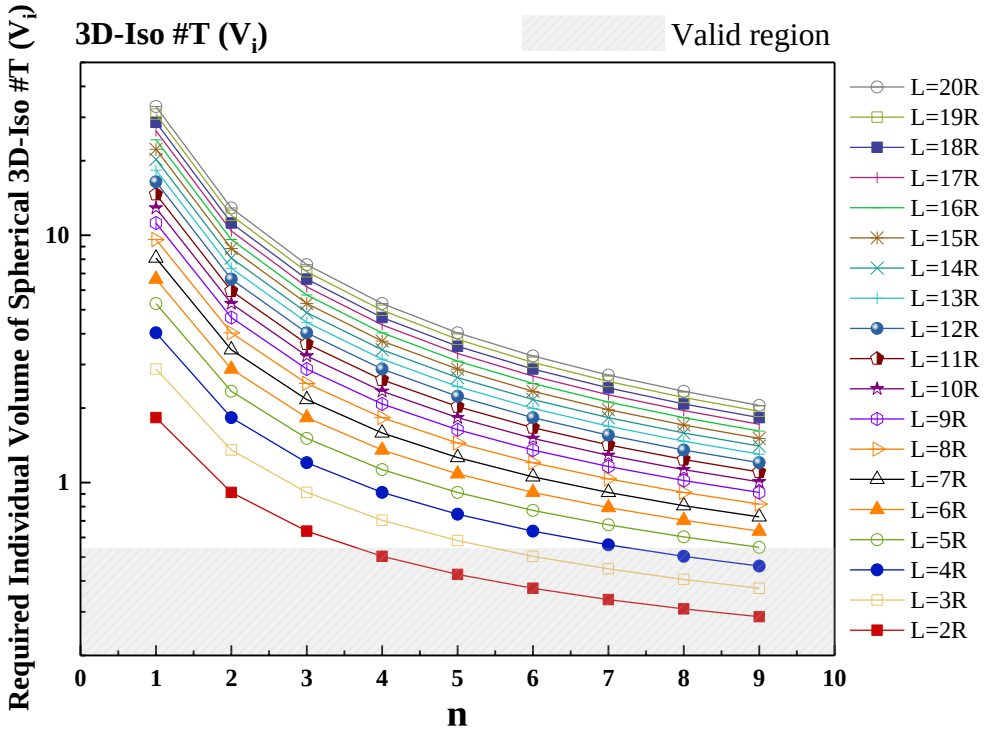
3D-Iso #T (V_i)
Valid region
Required Individual Volume of Spherical 3D-Iso #T (V_i)
n
L=20R
L=19R
L=18R
L=17R
L=16R
L=15R
L=14R
L=13R
L=12R
L=11R
L=10R
L=9R
L=8R
L=7R
L=6R
L=5R
L=4R
L=3R
L=2R

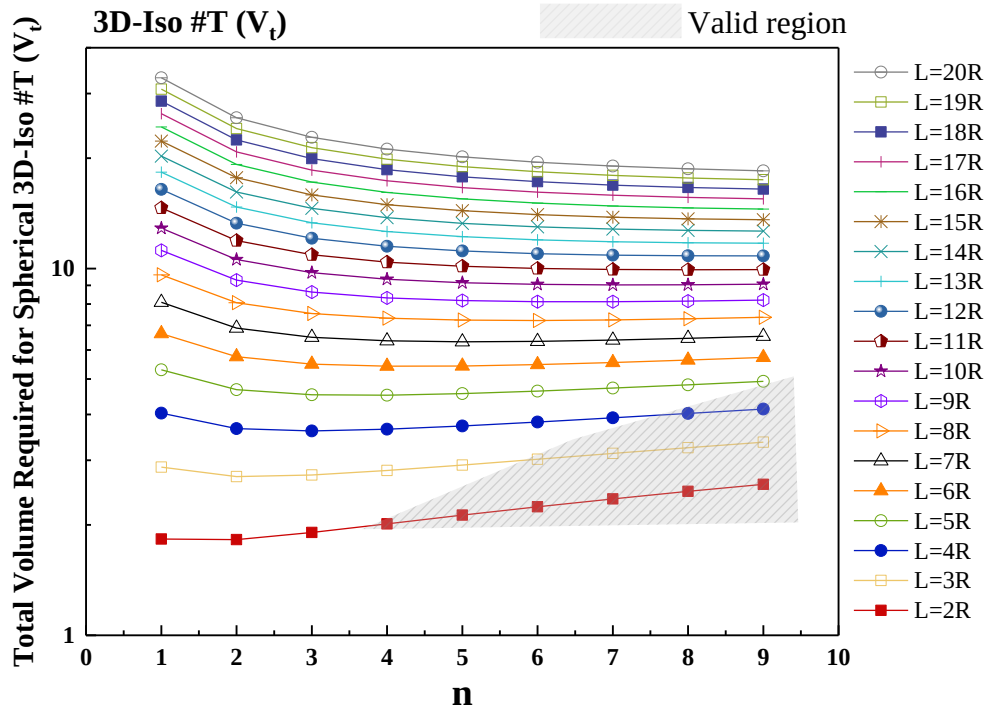

Figure 6-9 The L/R influence on m, λ, V_i, V_t of spherical 3D-Iso (#T).

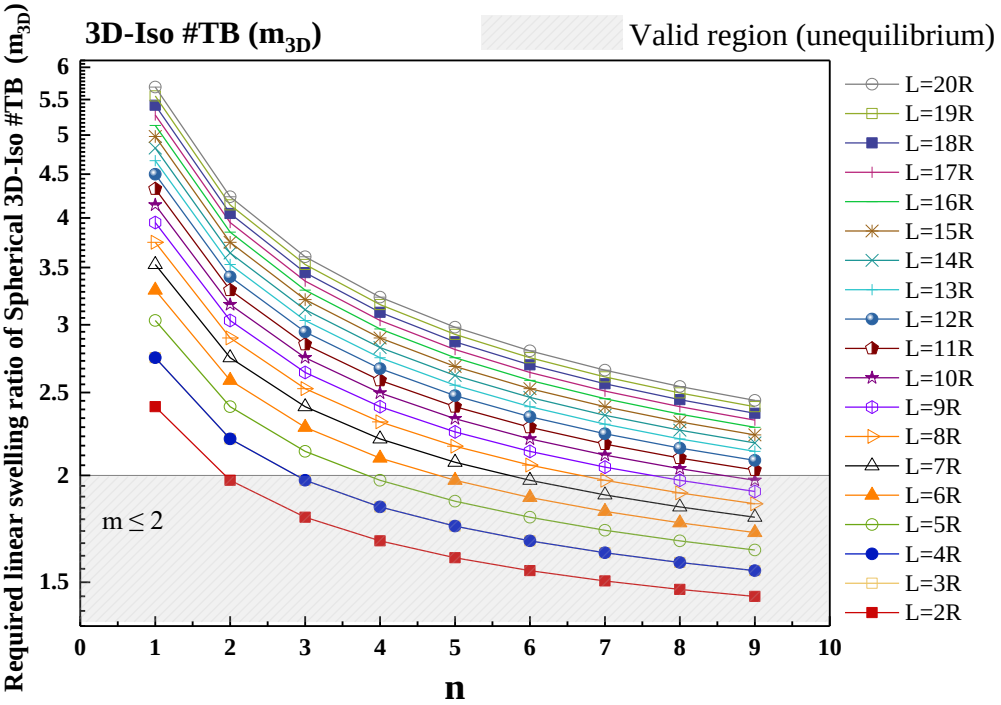

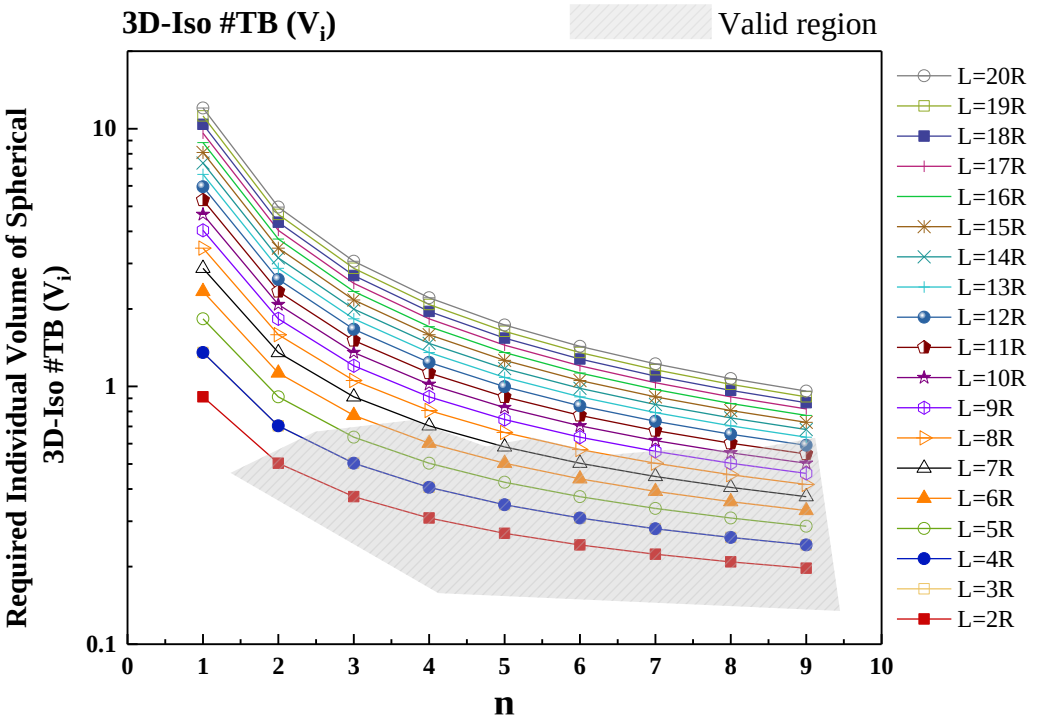

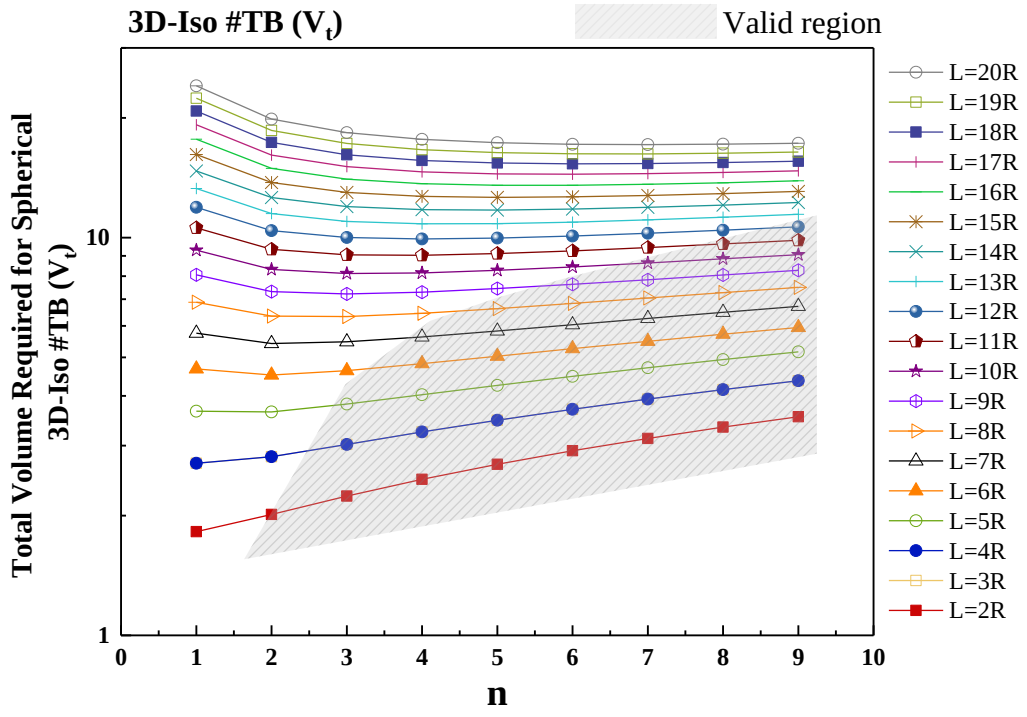

Figure 6-10 The L/R influence on m, λ, V_i, V_t of spherical 3D-Iso (#TB).

6.3 Appendix III: Supplementary Figures

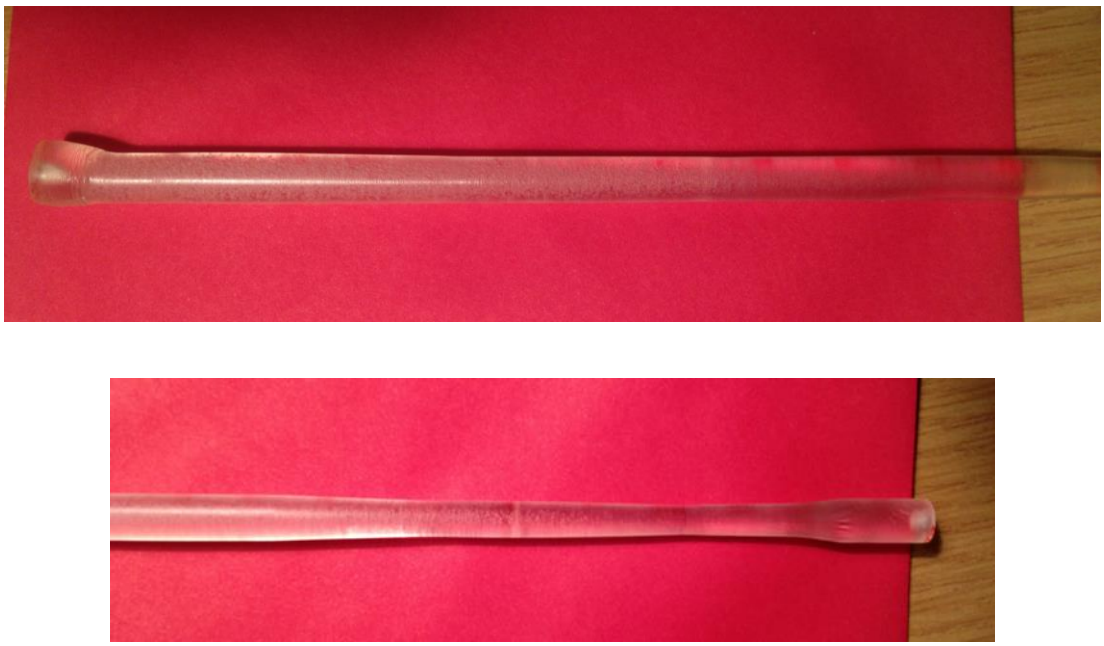

Figure 6-11 Raw photos of the die-drawn sample (#9.5).

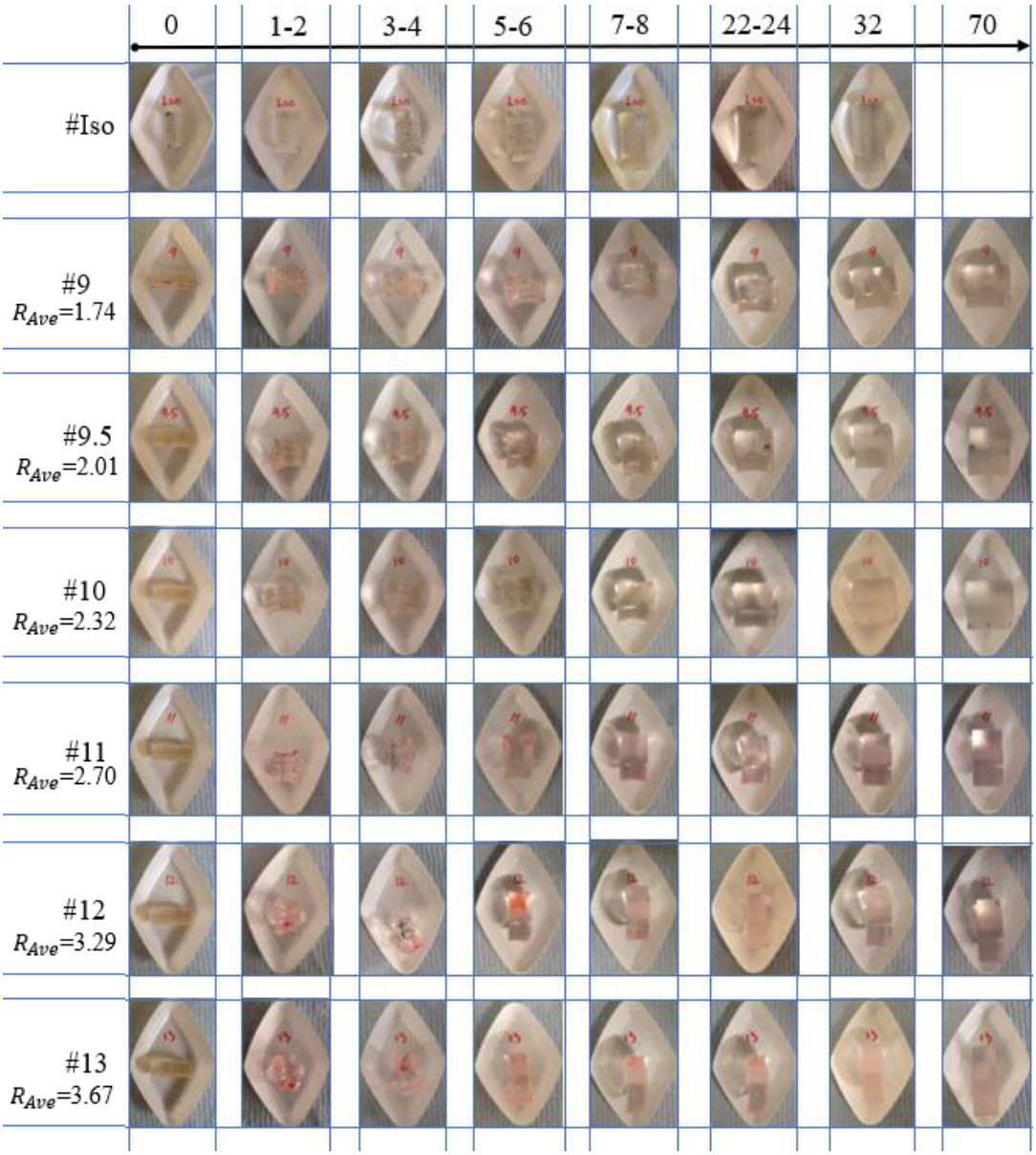

Figure 6-12 Photos (front view) of the swelling #Iso and #Die-drawn with various deformation ratios R_{Ave} at swelling time of 0, 1-2, 3-4, 5-6, 7-8, 22-24, 32, 72 hours.

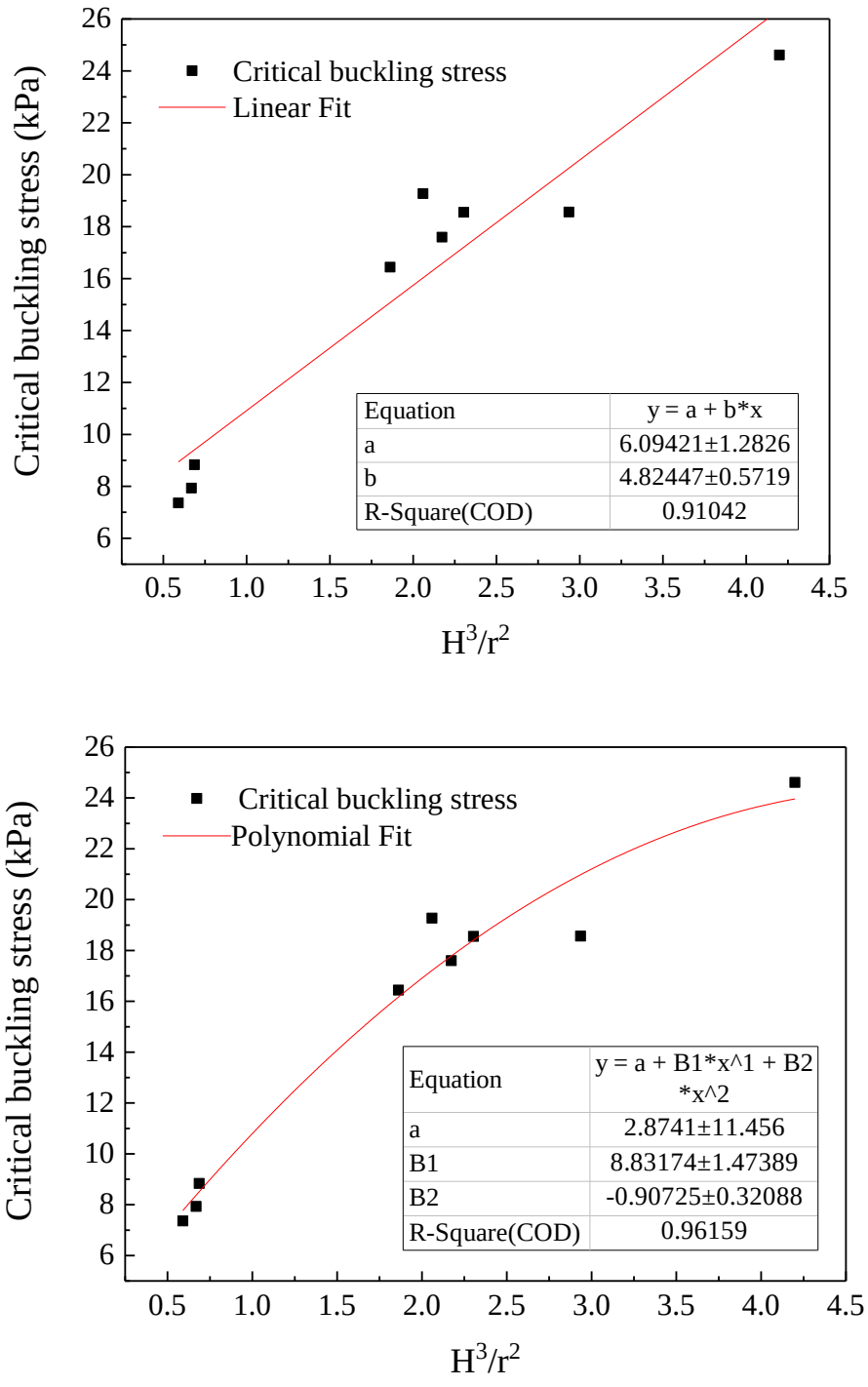

Figure 6-13 The relationship of critical buckling stress vs slenderness ratio (H^3/r^2) and (H/r)

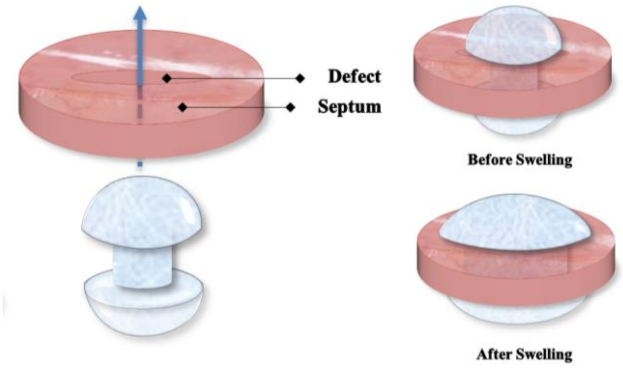

Figure 6-14 The application of bilateral swelling hydrogel expanders in ASD. Left: schematic of expander insertion; right: the comparison between before and after swelling.

7 REFERENCE

1. Keddie, G., *Symbolism and context: The world history of the Labret and cultural diffusion on the Pacific Rim*, in *Circum-Pacific Prehistory Conference*. 1989: Seattle, WA.

2. Waddington, R., *Mursi women and children*. 2012.

3. Codivilla, A., *On the means of lengthening, in the lower limbs, the muscles and tissues which are shortened through deformity.* Am. J. Orthop., 1905. **2**(4): p. 353-369.

4. Neumann, C.G., *The expansion of an area of skin by progressive distention of a subcutaneous balloon: Use of the method for securing skin for subtotal reconstruction of the ear.* Plast. Reconstr. Surg., 1957. **19**(2): p. 124-130.

5. Radovan, C. *Adjacent flap development using expandable silastic implant*. in *Annual Meeting of the American Society of Plastic and Reconstructive Surgeons*. 1976. Boston, Mass.

6. Radovan, C. *Reconstruction of the breast after radical mastectomy using a temporary expander*. in *Plast Surg Forum*. 1978.

7. Radovan, C. and R. Schulte, *Flap development device and method of progressively increasing skin area*, USPTO, Editor. 1980, Heyer Schulte Corporation.

8. Radovan, C., *Breast reconstruction after mastectomy using the temporary expander.* Plast. Reconstr. Surg., 1982. **69**(2): p. 195-208.

9. Austad, E.D., *Evolution of the concept of tissue expansion.* Facial Plast Surg, 1988. **5**(4): p. 277-9.

10. Radovan, C., *Development of adjacent flaps using a temporary expander*, in *Plast Surg Forum*. 1979. p. 62.

11. Iwuagwu, F.C., D. Wilson, and F. Bailie, *The use of skin grafts in postburn contracture release: A 10-year review.* Plast. Reconstr. Surg., 1999. **103**(4): p. 1198-1204.

12. Sullivan, M.A. and J.M. Adkinson, *A Systematic Review and Comparison of Outcomes Following Simple Syndactyly Reconstruction With Skin Grafts or a Dorsal Metacarpal Advancement Flap.* J Hand Surg Am, 2017. **42**(1): p. 34-40 e6.

13. Cherry, G.W., et al., *Increased survival and vascularity of random-pattern skin flaps elevated in controlled, expanded skin.* Plast. Reconstr. Surg., 1983. **72**(5): p. 680-7.

14. Marcus, J., D.B. Horan, and J.K. Robinson, *Tissue expansion: past, present, and future.* J Am Acad Dermatol, 1990. **23**(5 Pt 1): p. 813-25.

15. Manders, E.K., et al., *Soft-tissue expansion: concepts and complications.* Plast. Reconstr. Surg.,

1984. **74**(4): p. 493-507.

16. Antonyshyn, O., et al., *Tissue expansion in head and neck reconstruction.* Plast. Reconstr. Surg., 1988. **82**(1): p. 58-68.

17. Chun, J.T. and R.J. Rohrich, *Versatility of tissue expansion in head and neck burn reconstruction.* Ann. Plast. Surg., 1998. **41**(1): p. 11-6.

18. MacLennan, S.E., J.F. Corcoran, and H.W. Neale, *Tissue expansion in head and neck burn reconstruction.* Clin Plast Surg, 2000. **27**(1): p. 121-32.

19. Argenta, L.C., *Controlled tissue expansion in reconstructive surgery.* Br. J. Plast. Surg., 1984. **37**(4): p. 520-9.

20. LoGiudice, J. and A.K. Gosain, *Pediatric tissue expansion: indications and complications.* Plast Surg Nurs, 2004. **24**(1): p. 20-26.

21. Dickson, M.G. and D.T. Sharpe, *The complications of tissue expansion in breast reconstruction: a review of 75 cases.* Br. J. Plast. Surg., 1987. **40**(6): p. 629-35.

22. Antonyshyn, O., et al., *Complications of soft tissue expansion.* Br. J. Plast. Surg., 1988. **41**(3): p. 239-50.

23. Cordeiro, P.G. and C.M. McCarthy, *A single surgeon's 12-year experience with tissue expander/implant breast reconstruction: part I. A prospective analysis of early complications.* Plast. Reconstr. Surg., 2006. **118**(4): p. 825-831.

24. Cordeiro, P.G. and C.M. McCarthy, *A single surgeon's 12-year experience with tissue expander/implant breast reconstruction: part II. An analysis of long-term complications, aesthetic outcomes, and patient satisfaction.* Plast. Reconstr. Surg., 2006. **118**(4): p. 832-839.

25. Bennett, R.G. and M. Hirt, *A history of tissue expansion. Concepts, controversies, and complications.* J Dermatol Surg Oncol, 1993. **19**(12): p. 1066-73.

26. Gibstein, L.A., et al., *Tissue expansion in children: a retrospective study of complications.* Ann. Plast. Surg., 1997. **38**(4): p. 358-64.

27. Huang, X., X. Qu, and Q. Li, *Risk factors for complications of tissue expansion: a 20-year systematic review and meta-analysis.* Plast. Reconstr. Surg., 2011. **128**(3): p. 787-797.

28. Austad, E.D. and G.L. Rose. *Self-inflating implant for donor tissue augmentation*. in *Annual Meeting of the American Society of Plastic and Reconstructive Surgeons*. 1979. Toronto, Canada.

29. Austad, E.D., et al., *Histomorphologic evaluation of guinea pig skin and soft tissue after*

controlled tissue expansion. Plast. Reconstr. Surg., 1982. **70**(6): p. 704-10.

30. Austad, E.D. and G.L. Rose, *A self-inflating tissue expander.* Plast. Reconstr. Surg., 1982. **70**(5): p. 588-94.

31. Wee, S.S., S.E. Logan, and T.A. Mustoe, *Continuous versus intraoperative expansion in the pig model.* Plast. Reconstr. Surg., 1992. **90**(5): p. 808-14.

32. Downes, R., M. Lavin, and R. Collin, *Hydrophilic expanders for the congenital anophthalmic socket.* Adv. Ophthalmic. Plast. Reconstr. Surg., 1992. **9**: p. 57-61.

33. Wiese, K.G., *Osmotically induced tissue expansion with hydrogels: a new dimension in tissue expansion? A preliminary report.* J Craniomaxillofac Surg, 1993. **21**(7): p. 309-13.

34. Ronert, M.A., H. Hofheinz, and R.R. Olbrisch, *The beginning of a new era: self-filling tissue expander for defect coverage in a 3-year-old boy with a retroauricular nevus.* Plast. Reconstr. Surg., 2003. **112**(1): p. 189-91.

35. Obdeijn, M.C., J.P. Nicolai, and P.M. Werker, *The osmotic tissue expander: a three-year clinical experience.* J Plast Reconstr Aesthet Surg, 2009. **62**(9): p. 1219-22.

36. Mischkowski, R.A. and A.C. Kubler, *Correction of congenital nasal hypoplasia associated with Kallmann syndrome using self inflating injectable tissue expander pellets.* Plast. Reconstr. Surg., 2006. **118**(6): p. 1447-1452.

37. Ronert, M.A., et al., *The beginning of a new era in tissue expansion: self-filling osmotic tissue expander--four-year clinical experience.* Plast. Reconstr. Surg., 2004. **114**(5): p. 1025-31.

38. Chummun, S., P. Addison, and K.J. Stewart, *The osmotic tissue expander: a 5-year experience.* J Plast Reconstr Aesthet Surg, 2010. **63**(12): p. 2128-32.

39. Swan, M.C., et al., *Cleft palate repair with the use of osmotic expanders: a response.* J Plast Reconstr Aesthet Surg, 2008. **61**(2): p. 220-221.

40. Swan, M.C., *Anisotropic self-inflating tissue expanders in reconstructive palstic surgery*. 2007, Oxford University, UK.

41. Lee, J., *Development of an anisotropic swelling hydrogel for tissue expansion: control over the degree, rate and direction of hydrogel swelling*. 2008, Georgia Institute of Technology.

42. Zhu, Y. and J.T. Czernuszka, *Inter-penetrating polymer network hydrogel tissue expanders with controlled expansion and anisotropic properties.* J. med. bioeng., 2015. **4**(2).

43. Smith, J.R., Z. Radzi, and J.T. Czernuszka, *The effects of hot pressing on the swelling behavior of P(MMA-co-NVP) hydrogel discs.* Polymer Engineering and Science, 2015. **55**(6): p. 1290-

1295.

44. Swan, M.C., et al., *Development of a novel anisotropic self-inflating tissue expander: in vivo submucoperiosteal performance in the porcine hard palate.* Plast. Reconstr. Surg., 2012. **129**(1): p. 79-88.

45. Manssor, N.A., et al., *Characteristics and Young's Modulus of Collagen Fibrils from Expanded Skin Using Anisotropic Controlled Rate Self-Inflating Tissue Expander.* Skin Pharmacol Physiol, 2016. **29**(2): p. 55-62.

46. Lasheen, A.E., et al., *External tissue expansion successfully achieved using negative pressure.* Surg. Today, 2004. **34**(2): p. 193-6.

47. Lasheen, A.E., K. Saad, and M. Raslan, *External tissue expansion in head and neck reconstruction.* J Plast Reconstr Aesthet Surg, 2009. **62**(8): p. e251-4.

48. Nordström, R.E., M. Greco, and E. Raposio, *The" Nordstrom suture" to enhance scalp reductions.* Plast. Reconstr. Surg., 2001. **107**(2): p. 577-82; discussion 583.

49. Fan, J. and J. Wang, *The "silicone suture" for tissue expansion without an expander: a new device for repair of soft-tissue defects after burns.* Plast. Reconstr. Surg., 2004. **114**(2): p. 484-8; discussion 489-90.

50. Hussain, S.H., B. Limthongkul, and T.R. Humphreys, *The biomechanical properties of the skin.* Dermatol Surg, 2013. **39**(2): p. 193-203.

51. Child., G.V., *Microanatomy of Skin*. 2014.

52. Lorber, M. and S.A. Milobsky, *Stretching of the skin in vivo. A method of influencing cell division and migration in the rat epidermis.* J Invest Dermatol, 1968. **51**(5): p. 395-402.

53. Francis, A.J. and R. Marks, *Skin stretching and epidermopoiesis.* Br. J. Exp. Pathol., 1977. **58**(1): p. 35-9.

54. Squier, C.A., *The stretching of mouse skin in vivo: effect on epidermal proliferation and thickness.* J Invest Dermatol, 1980. **74**(2): p. 68-71.

55. Sasaki, G.H., *Intraoperative Sustained Limited Expansion (Isle) as an Immediate Reconstructive Technique.* Clinics in Plastic Surgery, 1987. **14**(3): p. 563-573.

56. De Filippo, R.E. and A. Atala, *Stretch and growth: the molecular and physiologic influences of tissue expansion.* Plast. Reconstr. Surg., 2002. **109**(7): p. 2450-62.

57. Wang, N., J.P. Butler, and D.E. Ingber, *Mechanotransduction across the Cell-Surface and through the Cytoskeleton.* Science, 1993. **260**(5111): p. 1124-1127.

58. Shyy, J.Y. and S. Chien, *Role of integrins in cellular responses to mechanical stress and adhesion.* Curr Opin Cell Biol, 1997. **9**(5): p. 707-13.

59. Schmidt, C., et al., *Mechanical stressing of integrin receptors induces enhanced tyrosine phosphorylation of cytoskeletally anchored proteins.* J Biol Chem, 1998. **273**(9): p. 5081-5.

60. Takei, T., et al., *Molecular basis for tissue expansion: clinical implications for the surgeon.* Plast. Reconstr. Surg., 1998. **102**(1): p. 247-58.

61. Rijken, P.J., et al., *Epidermal growth factor induces rapid reorganization of the actin microfilament system in human A431 cells.* J Cell Sci, 1991. **100 (Pt 3)**(3): p. 491-9.

62. Park, J.M., et al., *Stretch activates heparin-binding EGF-like growth factor expression in bladder smooth muscle cells.* Am. J. Physiol., 1998. **275**(5): p. C1247-54.

63. Yang, X.C. and F. Sachs, *Mechanically sensitive, nonselective cation channels.* EXS, 1993. **66**: p. 79-92.

64. Kirber, M.T., J.V. Walsh, Jr., and J.J. Singer, *Stretch-activated ion channels in smooth muscle: a mechanism for the initiation of stretch-induced contraction.* Pflugers Arch., 1988. **412**(4): p. 339-45.

65. Sachs, F., *Mechanical transduction by membrane ion channels: a mini review.* Mol. Cell. Biochem., 1991. **104**(1-2): p. 57-60.

66. Nakayama, K., *Calcium-dependent contractile activation of cerebral artery produced by quick stretch.* Am. J. Physiol., 1982. **242**(5): p. H760-8.

67. Laher, I., C. van Breemen, and J.A. Bevan, *Stretch-dependent calcium uptake associated with myogenic tone in rabbit facial vein.* Circ Res, 1988. **63**(3): p. 669-72.

68. Osol, G., I. Laher, and M. Cipolla, *Protein kinase C modulates basal myogenic tone in resistance arteries from the cerebral circulation.* Circ Res, 1991. **68**(2): p. 359-67.

69. Davis, M.J., J.A. Donovitz, and J.D. Hood, *Stretch-activated single-channel and whole cell currents in vascular smooth muscle cells.* Am. J. Physiol., 1992. **262**(4 Pt 1): p. C1083-8.

70. Davis, M.J., G.A. Meininger, and D.C. Zawieja, *Stretch-induced increases in intracellular calcium of isolated vascular smooth muscle cells.* Am. J. Physiol., 1992. **263**(4 Pt 2): p. H1292-9.

71. Diamond, S.L., F. Sachs, and W.J. Sigurdson, *Mechanically Induced Calcium Mobilization in Cultured Endothelial-Cells Is Dependent on Actin and Phospholipase.* J. Atheroscler. Thromb., 1994. **14**(12): p. 2000-2006.

72. Hill, M.A. and G.A. Meininger, *Calcium entry and myogenic phenomena in skeletal muscle arterioles.* Am. J. Physiol., 1994. **267**(3 Pt 2): p. H1085-92.

73. Dhivya, S., V.V. Padma, and E. Santhini, *Wound dressings - a review.* Biomedicine-Taiwan, 2015. **5**(4): p. 24-28.

74. Liang, Y.P., J.H. He, and B.L. Guo, *Functional Hydrogels as Wound Dressing to Enhance Wound Healing.* Acs Nano., 2021. **15**(8): p. 12687-12722.

75. Lawrence, E.L. and I.G. Turner, *Materials for urinary catheters: a review of their history and development in the UK.* Med Eng Phys, 2005. **27**(6): p. 443-453.

76. Johnson, J.R., P. Delavari, and M. Azar, *Activities of a nitrofurazone-containing urinary catheter and a silver hydrogel catheter against multidrug-resistant bacteria characteristic of catheter-associated urinary tract infection.* Antimicrob. Agents Chemother., 1999. **43**(12): p. 2990-5.

77. Hoffman, A.S., *Hydrogels for biomedical applications.* Adv. Drug. Deliv. Rev., 2012. **64**: p. 18-23.

78. Hamidi, M., A. Azadi, and P. Rafiei, *Hydrogel nanoparticles in drug delivery.* Adv. Drug. Deliv. Rev., 2008. **60**(15): p. 1638-49.

79. Sun, Z., et al., *Hydrogel-based controlled drug delivery for cancer treatment: a review.* Mol. Pharm., 2019. **17**(2): p. 373-391.

80. Lee, K.Y. and D.J. Mooney, *Hydrogels for tissue engineering.* Chem. Rev, 2001. **101**(7): p. 1869-1880.

81. Van Vlierberghe, S., P. Dubruel, and E. Schacht, *Biopolymer-based hydrogels as scaffolds for tissue engineering applications: a review.* Biomacromolecules, 2011. **12**(5): p. 1387-1408.

82. Klausner, E.A., et al., *Expandable gastroretentive dosage forms.* J Control Release, 2003. **90**(2): p. 143-62.

83. Bacskulin, A., et al., *New osmotically active hydrogel expander for enlargement of the contracted anophthalmic socket.* Graefes Arch Clin Exp Ophthalmol, 2000. **238**(1): p. 24-7.

84. Kallmes, D.F. and N.H. Fujiwara, *New expandable hydrogel-platinum coil hybrid device for aneurysm embolization.* AJNR Am J Neuroradiol, 2002. **23**(9): p. 1580-8.

85. Shi, Q., et al., *Bioactuators based on stimulus-responsive hydrogels and their emerging biomedical applications.* NPG Asia Mater., 2019. **11**(1): p. 1-21.

86. Shang, J., et al., *Trends in polymeric shape memory hydrogels and hydrogel actuators.* Polym.

Chem., 2019. **10**(9): p. 1036-1055.

87. Saini, K., *Preparation method, Properties and Crosslinking of hydrogel: a review.* PharmaTutor, 2017. **5**(1): p. 27-36.

88. Ahmed, E.M., *Hydrogel: Preparation, characterization, and applications: A review.* J Adv Res, 2015. **6**(2): p. 105-21.

89. Refojo, M.F., *Hydrophobic interaction in poly(2-hydroxyethyl methacrylate) homogeneous hydrogel.* J Polym Sci A1, 1967. **5**(12): p. 3103-13.

90. Lugão, A.B., S.O. Rogero, and S.M. Malmonge, *Rheological behaviour of irradiated wound dressing poly (vinyl pyrrolidone) hydrogels.* Radiat. Phys. Chem., 2002. **63**(3-6): p. 543-546.

91. Bercea, M., S. Morariu, and M. Teodorescu, *Rheological investigation of poly(vinyl alcohol)/poly(N-vinyl pyrrolidone) mixtures in aqueous solution and hydrogel state.* Journal of Polymer Research, 2016. **23**(7): p. 1-9.

92. Ooya, T. and N. Yui, *Polyrotaxanes: synthesis, structure, and potential in drug delivery.* Crit Rev Ther Drug Carrier Syst, 1999. **16**(3).

93. Okumura, Y. and K. Ito, *The polyrotaxane gel: a topological gel by figure-of-eight cross-links.* Adv. Mater., 2001. **13**(7): p. 485-487.

94. Sperling, L.H. and R. Hu, *Interpenetrating polymer networks*, in *Polymer blends handbook*. 2014, Springer. p. 677-724.

95. Klempner, D. and D. Sophiea, *Interpenetrating polymer networks*, in *Elastomer Technology Handbook*. 2020, CRC Press. p. 421-444.

96. Dragan, E.S., *Design and applications of interpenetrating polymer network hydrogels. A review.* Chem. Eng. J., 2014. **243**: p. 572-590.

97. Gun'ko, V.M., I.N. Savina, and S.V. Mikhalovsky, *Properties of water bound in hydrogels.* Gels, 2017. **3**(4): p. 37.

98. Behl, M. and A. Lendlein, *Shape-memory polymers.* Mater. Today, 2007. **10**(4): p. 20-28.

99. Liu, G.Q., et al., *Shape memory of hydrogen-bonded polymer network/poly(ethylene glycol) complexes.* Macromolecules, 2004. **37**(6): p. 2228-2232.

100. Mather, P.T., X.F. Luo, and I.A. Rousseau, *Shape Memory Polymer Research.* Annu. Rev. Mater. Sci., 2009. **39**: p. 445-471.

101. Liu, C., H. Qin, and P.T. Mather, *Review of progress in shape-memory polymers.* J. Mater.

Chem. A, 2007. **17**(16): p. 1543-1558.

102. Invernizzi, M., et al., *4D printed thermally activated self-healing and shape memory polycaprolactone-based polymers.* Eur Polym J, 2018. **101**: p. 169-176.

103. Sabzi, M., M. Babaahmadi, and M. Rahnama, *Thermally and Electrically Triggered Triple-Shape Memory Behavior of Poly(vinyl acetate)/Poly(lactic acid) Due to Graphene-Induced Phase Separation.* ACS Appl. Mater. Interfaces. , 2017. **9**(28): p. 24061-24070.

104. Gu, X.Z. and P.T. Mather, *Water-triggered shape memory of multiblock thermoplastic polyurethanes (TPUs).* RSC Adv., 2013. **3**(36): p. 15783-15791.

105. Osada, Y. and A. Matsuda, *Shape memory in hydrogels.* Nature, 1995. **376**(6537): p. 219.

106. Li, Y., Z.B. Hu, and Y.Y. Chen, *Shape memory gels made by the modulated gel technology.* J. Appl. Polym. Sci., 1997. **63**(9): p. 1173-1178.

107. Purnawali, H., et al., *Poly(methyl methacrylate) for active disassembly.* Smart Mater Struct, 2012. **21**(7): p. 075006.

108. Smith, J.R., *Developing P (MMA-co-NVP) hydrogels for use in self-inflating, anisotropic tissue expanders*. 2015, University of Oxford.

109. Ward, I.M., *Developments in oriented polymers, 1970-2004.* Plast, 2004. **33**(5): p. 189-194.

110. Allison, S.W. and I.M. Ward, *The cold drawing of polyethylene terephthalate.* J. Appl. Phys., 1967. **18**(8): p. 1151.

111. Andrews, J.M. and I.M. Ward, *The cold-drawing of high density polyethylene.* J. Mater. Sci., 1970. **5**(5): p. 411-417.

112. Takayanagi, M., S. Minami, and F. Nagatoshi, *Reports of the Association of Asahi Glass Company for the Advancement of Engineering Japan*. 1961: Japan. p. 127.

113. Imada, K., et al., *Crystal Orientation and Some Properties of Solid/State Extrudate of Linear Polyethylene.* J. Mater. Sci., 1971. **6**(6): p. 537-+.

114. Brew, B. and I.M. Ward, *Study of the production of ultra-high modulus polyoxymethylene by tensile drawing at high temperatures.* Polymer, 1978. **19**(11): p. 1338-1344.

115. Capaccio, G., T. Crompton, and I. Ward, *Drawing behavior of linear polyethylene. II. Effect of draw temperature and molecular weight on draw ratio and modulus.* J Polym Sci B Polym Phys, 1980. **18**(2): p. 301-309.

116. Coates, P.D. and I.M. Ward, *Neck Profiles in Drawn Linear Polyethylene.* J. Mater. Sci., 1980.

15(11): p. 2897-2914.

117. Dao, T.T., et al., *Capillary Rheometry: Analysis of Low-Viscosity Fluids, and Viscous Liquids and Melts at High Shear Rates.* American Laboratory, 2009. **41**(11): p. 14-+.

118. Williams, T., *Hydrostatically-Extruded Polypropylene.* J. Mater. Sci., 1973. **8**(1): p. 59-70.

119. Southern, J.H. and R.S. Porter, *The properties of polyethylene crystallized under the orientation and pressure effects of a pressure capillary viscometer.* J. Appl. Polym. Sci., 1970. **14**(9): p. 2305-2317.

120. Southern, J.H., et al., *Unique Polyethylene Morphologies Produced under Extrusion Conditions.* Die Makromolekulare Chemie, 1972. **162**(Ndec): p. 19-&.

121. Gibson, A.G., et al., *Hydrostatic Extrusion of Linear Polyethylene.* J. Mater. Sci., 1974. **9**(7): p. 1193-1196.

122. Coates, P.D. and I.M. Ward, *Drawing of Polymers through a Conical Die.* Polymer, 1979. **20**(12): p. 1553-1560.

123. Coates, P.D. and I.M. Ward, *Die Drawing - Solid-Phase Drawing of Polymers through a Converging Die.* Polymer Engineering and Science, 1981. **21**(10): p. 612-618.

124. Coates, P.D., et al., *Process structuring of polymers by solid phase orientation processing.* Sci China Chem, 2013. **56**(8): p. 1017-1028.

125. Coates, P.D. and I.M. Ward, *Hydrostatic Extrusion of Polyoxymethylene.* J Polym Sci B Polym Phys, 1978. **16**(11): p. 2031-2047.

126. Gibson, A.G. and I.M. Ward, *The manufacture of ultra-high modulus polyethylenes by drawing through a conical die.* J Mater, 1980. **15**(4): p. 979-986.

127. Rueda, D., et al., *Anisotropy of ultra-high modulus polymers drawn through a die.* J Mater, 1984. **19**(8): p. 2615-2621.

128. Kong, C., et al., *Structure and self-reinforcing mechanism of biaxially oriented polyethylene pipes produced by solid phase die drawing.* Polymer, 2019. **178**.

129. Gibson, A.G. and I.M. Ward, *High Stiffness Polymers by Die-Drawing.* Polym. Eng. Sci., 1980. **20**(18): p. 1229-1235.

130. Taraiya, A.K., A. Richardson, and I.M. Ward, *Production and Properties of Highly Oriented Polypropylene by Die Drawing.* J. Appl. Polym. Sci., 1987. **33**(7): p. 2559-2579.

131. Chaffey, C.E., A.K. Taraiya, and I.M. Ward, *Orientation in polypropylene sheets produced by*

die-drawing and rolling. Polym. Eng. Sci., 1997. **37**(11): p. 1774-1784.

132. Lyu, D., et al., *Die geometry induced heterogeneous morphology of polypropylene inside the die during die-drawing process.* Polym Test, 2019. **74**: p. 104-112.

133. Hope, P.S., A. Richardson, and I.M. Ward, *Manufacture of Ultrahigh-Modulus Poly(Oxymethylenes) by Die Drawing.* J. Appl. Polym. Sci., 1981. **26**(9): p. 2879-2896.

134. Taraiya, A.K., et al., *Production and properties of highly oriented polyoxymethylene by die-drawing.* J. Appl. Polym. Sci., 2003. **88**(5): p. 1268-1278.

135. Mohanraj, J., et al., *Physical and mechanical characterization of oriented polyoxymethylene produced by die-drawing and hydrostatic extrusion.* Polymer, 2006. **47**(16): p. 5897-5908.

136. Chapleau, N., et al., *Roll-drawing and die-drawing of toughened poly(ethylene terephthalate). Part 1. Structure and mechanical characterization.* Polymer, 2005. **46**(6): p. 1956-1966.

137. Richardson, A., P.S. Hope, and I.M. Ward, *The Production and Properties of Poly(Vinylidene Fluoride) Rods Oriented by Drawing through a Conical Die.* J Polym Sci B Polym Phys, 1983. **21**(12): p. 2525-2541.

138. Li, J.F., et al., *Structure and biocompatibility improvement mechanism of highly oriented poly(lactic acid) produced by solid die drawing.* Eur Polym J

2017. **97**: p. 68-76.

139. Li, J.F., et al., *Structure evolution and orientation mechanism of long-chain-branched poly (lactic acid) in the process of solid die drawing.* Eur Polym J

2017. **90**: p. 54-65.

140. Połeć, I., et al., *Die drawn wood polymer composites. I. Mechanical properties.* Compos Sci Technol, 2010. **70**(1): p. 45-52.

141. Kukureka, S.N., G. Craggs, and I.M. Ward, *Analysis and Modeling of the Die Drawing of Polymers.* J. Mater. Sci., 1992. **27**(12): p. 3379-3388.

142. Motashar, F.A., et al., *Analytical and Experimental-Study of the Die Drawing of Circular Rods through Conical Dies.* Polym. Eng. Sci., 1993. **33**(19): p. 1288-1298.

143. Mirza, M.S., et al., *Coupled thermomechanical simulation of the polymer die drawing process.* Proceedings of the Institution of Mechanical Engineers Part E-Journal of Process Mechanical Engineering, 2003. **217**(E2): p. 123-131.

144. Sweeney, J., et al., *Modelling the Mechanical and Strain Recovery Behaviour of Partially*

Crystalline PLA. Polymers (Basel), 2019. **11**(8).

145. Wu, P.P., et al., *Realizing simultaneous toughening and reinforcement in polypropylene blends via solid die-drawing.* Polymer, 2019. **161**: p. 109-121.

146. Hoffman, O. and G. Sachs, *Introduction to the Theory of Plasticity for Engineers*. 1953: McGraw-Hill.

147. Hope, P.S., A. Richardson, and I.M. Ward, *The Hydrostatic Extrusion and Die-Drawing of Glass-Fiber-Reinforced Polyoxymethylene.* Polymer Engineering and Science, 1982. **22**(5): p. 307-313.

148. Kvernmo, H.D. and J.R. Haugstvedt, *Treatment of congenital syndactyly of the fingers.* Tidsskr. Nor. Laegeforen., 2013. **133**(15): p. 1591-5.

149. Urschel, J.D., P.G. Scott, and H.T. Williams, *The effect of mechanical stress on soft and hard tissue repair; a review.* Br. J. Plast. Surg., 1988. **41**(2): p. 182-6.

150. Timmenga, E.J.F., et al., *The Effect of Mechanical-Stress on Healing Skin Wounds - an Experimental-Study in Rabbits Using Tissue Expansion.* British Journal of Plastic Surgery, 1991. **44**(7): p. 514-519.

151. Radzi, Z., in *Provided by Prof. Jan T. Czernuszka*, X.-r.o.s.f.l.w.t. expanders, Editor. 2015.

152. Dao, K.D., et al., *Surgical treatment of congenital syndactyly of the hand.* J Am Acad Orthop Surg, 2004. **12**(1): p. 39-48.

153. Odita, J.C., A.A. Okolo, and F. Ukoli, *Normal values for metacarpal and phalangeal lengths in Nigerian children.* Skeletal Radiol., 1991. **20**(6): p. 441-5.

154. Zhang, S., et al., *Normal values of metacarpo phalanxal length for Chinese children of five cities in China (in Chinese).* . Journal of Chinese Modern Pediatrics, 2009. **6**: p. 1-6.

155. Maneepairoj, P., *Investigation on the swelling mechanics of hydrogel tissue expanders using a skin-mimicking apparatus*. 2014, Oxford University, UK.

156. Brush, D.O., B.O. Almroth, and J.W. Hutchinson, *Buckling of bars, plates, and shells.* 1975: p. 208-221.

157. Javanmardi, Y., et al., *Quantifying cell-generated forces: Poisson's ratio matters.* Commun Phys, 2021. **4**(1): p. 237.

158. Jones, R.M., *Buckling of bars, plates, and shells*. 2006: Bull Ridge Corporation.

159. EngineeringToolBox. *Euler's Column Formula.* 2012; Available from:

https://www.engineeringtoolbox.com/euler-column-formula-d_1813.html.

160. EngineeringToolBox. *Euler column: end condition factors and buckling*. 2012; Available from: https://www.engineeringtoolbox.com/euler-column-formula-d_1813.html.

161. Aziz, J., et al., *AFM analysis of collagen fibrils in expanded scalp tissue after anisotropic tissue expansion.* Int J Biol Macromol, 2018. **107**(Pt A): p. 1030-1038.

162. Al-Majhali, S.H., et al., *Biomechanical Effects of Unidirectional Expansion Using Anisotropic Expanders in Horse Skin Tissue.* J. Equine Vet. Sci, 2021. **99**: p. 103399.

163. Swan, M.C., et al., *Synthesis and properties of a novel anisotropic self-inflating hydrogel tissue expander.* Acta Biomater., 2011. **7**(3): p. 1126-32.

164. Lyu, D., et al., *Advantage of preserving bi-orientation structure of isotactic polypropylene through die drawing.* Chinese J Polym Sci, 2021. **39**(1): p. 91-101.

165. Mohanraj, J., et al., *Analysis and design of profiled dies for the polymer wire die-drawing process.* Proceedings of the Institution of Mechanical Engineers Part E-Journal of Process Mechanical Engineering, 2007. **221**(E1): p. 47-60.

166. Wistreich, J.G., *Investigation of the mechanics of wire drawing.* Proceedings of the Institution of Mechanical Engineers, 1955. **169**(1): p. 654-678.

167. Hosford, W.F. and R.M. Caddell, *Metal forming: mechanics and metallurgy*. 2011: Cambridge university press.

168. Dieter, G.E. and D.J. Bacon, *Mechanical metallurgy*. Vol. 3. 1976: McGraw-hill New York.

169. Unknown. *Material Contact Properties Table*. 2008; Available from: http://atc.sjf.stuba.sk/files/mechanika_vms_ADAMS/Contact_Table.pdf.

170. Ward, I.M., P.D. Coates, and M.M. Dumoulin, *Solid phase processing of polymers*. 2000: Hanser Publishers Munich, Germany:.

171. Shrivastava, A., *Introduction to plastics engineering*. 2018: William Andrew.

172. Bouzidi, L., et al., *Use of first and second derivatives to accurately determine key parameters of DSC thermographs in lipid crystallization studies.* Thermochim. Acta, 2005. **439**(1-2): p. 94-102.

173. Vijaya, N., et al., *Structural, vibrational, thermal, and conductivity studies on proton-conducting polymer electrolyte based on poly (N-vinylpyrrolidone).* Ionics, 2012. **18**(1-2): p. 91-99.

174. Al-Zahra, A., A.Q. Abdullah, and A.S. Al-Kabbi, *EFFECT OF SUBSTRATE TEMPERATURE ON THE STRUCTURE AND OPTICAL PROPERTIES OF PVP:n-CdSe NANOCOMPOSITE THIN FILMS AND ITS SCHOTTKY DIODES PERFORMANCE.* Chalcogenide Letters, 2017. **14**(10): p. 457-464.

175. Vijaya, N., et al., *Proton conducting polymer electrolyte based on poly (N-vinyl pyrrolidone) doped with ammonium iodide.* Int. J. Electroactive Mater, 2015. **3**: p. 20-27.

176. Abasi, C.Y., D. Wankasi, and C. Dikio, *Adsorption study of lead (II) ions on poly (methyl methacrylate) waste material.* Asian J. Chem, 2018. **30**(4): p. 859-867.

177. Gaur, M.S., et al., *Improvement of dielectric properties of spin coated PMMA-ZnO nano hybrid thin film.* Ferroelectrics, 2017. **510**(1): p. 56-70.

178. Devikala, S., et al., *Structural morphological and electrochemical studies on PMMA/PVP blends.* Mater. Today -Proceedings, 2019. **14**: p. 630-639.

179. Mustoe, T.A., T.H. Bartell, and W.L. Garner, *Physical, biomechanical, histologic, and biochemical effects of rapid versus conventional tissue expansion.* Plast. Reconstr. Surg., 1989. **83**(4): p. 687-91.

180. Machida, B.K., et al., *Immediate versus chronic tissue expansion.* Ann. Plast. Surg., 1991. **26**(3): p. 227-31; discussion 232.